Extreme-Mass-Ratio Inspirals:
Modelling and Test of an
Alternative Theory of Gravity.

Priscil·la Cañizares Martínez

Memòria presentada per
Priscil·la Cañizares Martínez
per optar al grau de Doctora en Física.

Director:

Carlos Fernández Sopuerta.
Institut de Ciències de l'Espai (CSIC-IEEC).

Universitat Autònoma de Barcelona.
Departament de Física.
Programa de doctorat RD 778/98.
Tutor: Diego Pavón Coloma.

Bellaterra, Octubre del 2011.

a Diego

Acknowledgements

Here I wish to express my heartfelt thanks to all the people that I have had at my side during these years.

First and foremost, I would like express my sincerest gratitude to my supervisor Dr. Carlos F. Sopuerta, without his advise and unique support, this thesis would never had become a reality.

In particular, I would like to thank Prof. Alberto Lobo for his confidence, invaluable advises and good humour (even in the bad moments), and Dr. Ulrich Sperhake, who with our interesting and friendly coffee-discussions has made my days. Also I would like to thank Dr. Jonathan R. Gair for our collaboration and for hosting me at the Institute of Astronomy in Cambridge (UK), and Dr. José Luís Jaramillo for our collaboration and hospitality when I visited the Albert Einstein Institute in Postdam (Germany). Also, I would like to mention Dr. Pau Amaro for his support.

Of course, I would like to thank all my colleagues and friends from the Institute of Space Science, with whom I have had really fun moments. Specially I am very grateful to Anaïs González, who showed me another point of view about quotidian things and Dr. Ana Milonavović, who has a contagious joy and has always a kind word to me. Also I want to mention my group colleagues: Ivan Lloro, Ferran Gibert, Lluís Gesa, Marc Díaz, Dr. Miquel Nofraries, Ignacio Mateos, Nikolaos Karnesis and Victor Martín, and my PhD colleagues and office mates: Dr. Alina Hirschmann, Ane Garcés, Dr. Andreu Font, Antonio Jesús López, Dr. Diego Sáez, Dr. Elsa de Cea, Dr. Giovanna Pedaletti, Hector Gil, Jorge Carretero and Dr. Juan Carlos Morales.

Finally, I would like to thank Dr. Ulrich Sperhake and Dr. Leor Barack for contributing to this thesis with his corrections.

Thank you all for being always there.

Preface

In my parents' library there was a collection of books about modern and contemporary history. It included some volumes on art and science, and one of them was on modern physics. It contained a bit of nuclear physics and relativity, which seemed magical, and also had a picture of the 1927 Solvay Conference in Brussels, where the top scientists of the XX century gathered. It was my favourite book. I remember how I admired those scientists and the way they changed the world. I wanted to become like them and get an insight into the inner workings of Nature. The PhD has been a stage of my live which has showed me that the romantic picture of science that I had was in reality hard work, disappointments and sleepless nights to obtain little advances. However, I feel fortunate, since I have had the opportunity to witness and participate in the development of a new area of science such as Gravitational-Wave Astronomy.

This thesis presents the main achievements of my PhD, during this time I studied one of the main sources of Gravitational-Waves for the future spatial detector LISA, the so called Extreme-Mass-Ration Inspirals. These are binary systems which consist of a massive black hole and a stellar object, which is compact enough not to be torn apart by the strong gravitational field of its companion.

In the first years, I started to become familiar with EMRIs and the description of their dynamics. Due to the extreme difference between the masses of the black hole and the stellar object, EMRIs can be modelled as a particle orbiting a black hole. In this way, the orbit of the star can be described as a free fall motion which is deviated by a force. This study introduced me to one of the main problems that the scientific community encounters in modelling EMRI waveforms. Part of the work presented here consists of the development of a new method to compute that force. Its principal advantage is that it allows time-domain implementations of the system, since it avoids resolving the small star numerically. In this way, we can make the most of time-domain techniques for modelling EMRIs.

However, at some point along my PhD, I felt the need to learn about other aspects of these binaries. I wanted to focus on the discoveries and the new science that we shall be able to obtain from EMRI detections. Then, I had the

opportunity of starting another project and performing parameter estimations of EMRIs in order to see whether a spacial observatory like LISA could be able to determine which theory of Gravity governs these binaries, in particular to discriminate between the EMRIs is General Relativity or the Dynamical Chern-Simons alternative theory of Gravity. The development and outcome of this period of my PhD is presented in the second part or this thesis.

> *Science makes people reach*
> *selflessly for truth and objectivity;*
> *it teaches people to accept reality, with wonder and admiration,*
> *not to mention the deep awe and joy that the natural*
> *order of things brings to the true scientist*

Lise Meitner.

Notation and Acronyms

Along this thesis we follow the conventions of Misner, Thorne and Wheeler [Misner 1973]: Greek letters stand for spacetime indexes and Latin letters in the middle of the alphabet $i, j, ...$, stand for spatial indexes only. Partial derivatives are denoted by $\partial_\alpha h = \partial h / \partial x^\alpha = h_{,\alpha}$, while, for any quantity h, covariant derivatives are denoted by $\nabla_\alpha h = h_{;\alpha}$. The time derivative of a quantity Q is denoted with a dot: $dQ/dt = \dot{Q}$. Moreover, we shall use a bar to denote background quantities, complex conjugate and trace-reversed quantities and it will be made clear in the text which case we are dealing with. Symmetrisation and antisymmetrisation are denoted by parentheses and square bracket around the indices, respectively: $A_{(\mu\nu)} := [A_{\mu\nu} + A_{\nu\mu}]/2$ and $A_{[\mu\nu]} := [A_{\mu\nu} - A_{\nu\mu}]/2$. Along this work, $\mu = m/M_\bullet$ denotes the mass ratio of the EMRI/IMRI system, where m is the mass of the SCO and $M_\bullet$ the mass of the MBH. Finally, we use the Einstein summation convention and geometrised units, i.e. $G = c = 1$

Next, we list the different acronyms employed along this work:

AK:	Analytical Kludge.
BL:	Boyer-Lindquist.
CFL:	Courant-Friedrichs-Lax.
CS:	Chern-Simons.
DCSMG:	Dynamical Chern-Simons Modified Gravity.
EMRI:	Extreme-Mass-Ratio Inspiral.
EHS:	Extended Homogeneous Solution.
EOB:	Effective-One-Body.
FD:	Finite Diferences.
GR:	General Relativity.
GW:	Gravitational Wave.
IMRI:	Intermediate-Mass-Ratio Inspiral.
LISA:	Laser Interferometer Space Antenna.
LIGO:	Laser Interferometer Gravitational-Wave Observatory.
LSA:	Linearised-Signal Approximation.
LSO:	Last Stable Orbit.
MBH:	Massive Black Hole.

NK: Numerical Kludge.
ODE: Ordinary Differential Equation.
PDE: Partial Differential Equation.
PN: Post-Newtonian.
PSC: Pseudo-Spectral Collocation.
RHS: Right-Hand Side.
RR: Radiation Reaction.
SCO: Stellar Compact Object.
SSB: Solar System Baricenter.

Contents

List of Figures

List of Tables

Introduction

It is the theory that decides what can be observed.
Albert Einstein.

1.1 Gravitational-Wave Detection

In the next decades, Astronomy will undergo a revolutionary change which could be even bigger than that due to the detection of X-rays. This will be possible thanks to the huge effort of scientists around the world, which are pursuing the detection of Gravitational-Waves (GWs) and working in the development of a new kind of astronomy: The *GW Astronomy*. GWs are a phenomenon of Nature predicted by Einsteins's General Relativity (GR). Through their detection, we will have access to novel astrophysical discoveries that may change our way of understanding the nature of the Universe. Our research is encouraged by strong evidence of their existence, such as astrophysical scenarios whose dynamics and evolution can only be explained through GW emission. Up to date, the most relevant evidence has been established through the measurements of the orbital decay of the binary pulsar *PSR 1913+16* by Hulse and Taylor [Hulse 1975], which agrees with that expected in GR about 0.2% (see [Weisberg 2005, Weisberg 2010]). Hulse and Taylor [Hulse 1975] were awarded the 1993 Nobel prize in physics for the discover of this binary.

Einstein's field equations give a mathematical description of the Universe, where its content of matter and energy is closely related to its geometry. This relation is such that the stress-energy tensor of matter $T_{\mu\nu}$ and the curvature of spacetime, represented in terms of theRicci tensor $R_{\mu\nu}$ and scalar R, are related as (see, e.g. [Weinberg 1972]):

$$T_{\mu\nu} = \frac{1}{16\pi}\big\{2R_{\mu\nu} - g_{\mu\nu}R\big\}\,,\qquad\qquad(1.1)$$

where $g_{\mu\nu}$ are the spacetime metric components. The Ricci tensor is the trace of the Riemann tensor, $R_{\mu\nu} = R^{\alpha}{}_{\mu\alpha\nu}$, which is given by:

$$R^{\alpha}{}_{\gamma\beta\rho} = \Gamma^{\alpha}{}_{\beta\rho,\gamma} - \Gamma^{\alpha}{}_{\beta\gamma,\rho} + \Gamma^{\alpha}{}_{\mu\gamma}\,\Gamma^{\mu}{}_{\beta\rho} - \Gamma^{\alpha}{}_{\mu\rho}\,\Gamma^{\mu}{}_{\beta\gamma}\,, \tag{1.2}$$

where $\Gamma^{\gamma}{}_{\beta\mu}$ are the Christoffel symbols. These quantities are related with the spacetime metric and its derivatives through:

$$\Gamma^{\gamma}{}_{\beta\mu} = \frac{g^{\alpha\gamma}}{2}\left(g_{\alpha\beta,\mu} + g_{\alpha\mu,\beta} - g_{\beta\mu,\alpha}\right)\,. \tag{1.3}$$

Finally, the Ricci scalar R is the trace of the Ricci tensor, $R = g^{\mu\nu}R_{\mu\nu}$. When the spacetime curvature is weak, as in our solar system, one can reproduce the Newtonian gravity equations from Eq. (1.1) [Misner 1973, Weinberg 1972].

When the spacetime curvature oscillates, for example, due to strong collisions or relativistic orbital motions, there will appear ripples in the curvature of the spacetime or Gravitational-Waves (GWs). When a GW propagates across the Universe, it affects the spacetime geometry, which in turns affect the GW itself. Due to this non-linear relation, it is not possible to separate precisely the contributions of GWs from the average background curvature and find, in general, an exact general radiative solution of the Einstein field equations. However, since we expect to detect GWs from very distant cosmological sources, which do not carry enough energy and angular momentum to affect their own dynamics, the Einstein field equations can be linearised. In this *weak field approximation* or *linearised gravity* regime (see, e.g. [Misner 1973, Weinberg 1972]), a region of the spacetime smaller than the spacetime curvature can be considered flat and its metric described by the Minkowski metric: $\eta_{\mu\nu} = diag[-1, 1, 1, 1]$. When a GW passes through this locally flat region, it will produce little metric perturbations (ripples), $h_{\mu\nu}$, of the background geometry, $\eta_{\mu\nu}$ and, thus, the spacetime geometry of that region is given by:

$$g_{\mu\nu} = \eta_{\mu\nu} + h_{\mu\nu} + \mathcal{O}\left([h_{\mu\nu}]^2\right)\,, \tag{1.4}$$

where $|h_{\mu\nu}| \ll |\eta_{\mu\nu}|$.

In the weak field approximation, the field equations (1.1) are given in the linearised form:

$$h_{\mu\alpha,}{}^{\alpha}{}_{\nu} + h_{\nu\alpha,}{}^{\alpha}{}_{\mu} - h_{\mu\nu,}{}^{\alpha}{}_{\alpha} - h_{,\mu\nu} - \eta_{\mu\nu}\left\{h_{\alpha\beta,}{}^{\alpha\beta} - h_{,\alpha}{}^{\alpha}\right\} = 16\pi T_{\mu\nu} \tag{1.5}$$

with $h = h_{\mu}{}^{\mu}$ the trace of $h_{\mu\nu}$.

Introducing the *trace-reversed* form [Weinberg 1972]:

$$\bar{h}^{\mu\nu} \equiv h^{\mu\nu} - 1/2\eta^{\mu\nu}h\,, \tag{1.6}$$

we can write Eq. (1.5) in a more compact way:

$$\Box \bar{h}_{\mu\nu} + \eta_{\mu\nu}\bar{h}_{\alpha\beta,}{}^{\alpha\beta} - \bar{h}_{\nu\alpha,}{}^{\alpha}{}_{\mu} = -16\pi \bar{T}_{\mu\nu} \tag{1.7}$$

where $\Box \bar{h}_{\mu\nu} = \bar{h}_{\mu\nu,\alpha}{}^{\alpha}$ and the source term is given by $\bar{T}_{\mu\nu} = T_{\mu\nu} - \frac{1}{2}\eta_{\mu\nu}T^{\rho}{}_{\rho}$. In addition, in the linearised form of the weak field approximation, we have a gauge freedom, similar to that of electrodynamics, where we can adjust the potential term by adding the gradient of an arbitrary scalar, $A_{\mu} \to A_{\mu} - \partial_{\mu}S$, leaving the electromagnetic tensor field $F_{\mu\nu} = \partial_{\mu}A_{\nu} - \partial_{\nu}A_{\mu}$ unchanged (see, e.g. [Jackson 1999]). In GR, we have the gauge freedom that corresponds to the diffeomorphism invariance of the theory. In addition, in the linearised theory, we have the gauge freedom that corresponds to the mapping between the background and the perturbed spacetimes, which is described by a transformation of the type: $x^{\alpha} \to x^{\alpha} + \xi^{\alpha}$, with $\xi^{\alpha} \ll 1$. Under this transformation, $h_{\mu\nu}$ changes as: $h_{\mu\nu} \to h_{\mu\nu} - \partial_{\mu}\xi_{\nu} - \partial_{\nu}\xi_{\mu}$. One can see that this gauge transformation leaves the curvature tensor unchanged. Thus, in analogy with the electromagnetic case, we can take advantage of this gauge freedom to choose ξ^{α} in such a way that:

$$\bar{h}^{\mu\alpha}{}_{,\alpha} = 0 \,. \tag{1.8}$$

This is the so-called *Lorenz Gauge* condition and simplifies the linearised Einstein field equations (1.7), which take the wavelike form:

$$\Box \bar{h}_{\mu\nu} = -16\pi \bar{T}_{\mu\nu} \,. \tag{1.9}$$

This equation can be solved by using the method of the Green's function (see, e.g. [Flanagan 2005]), $G(\mathbf{x}, t; \mathbf{x}', t')$, which is the field produced by a delta function source. $G(\mathbf{x}, t; \mathbf{x}', t')$ gives us how much field is generated at the "field point" $(t, \mathbf{x})$ by a point source located at $(t', \mathbf{x}')$:

$$\Box G(\mathbf{x}, t; \mathbf{x}', t') = \delta(\mathbf{x} - \mathbf{x}')\delta(t - t') \,. \tag{1.10}$$

The form of the retarded Green's function associated with the wave operator $\Box$ is given by (see, e.g. [Jackson 1999]):

$$G(\mathbf{x}, t; \mathbf{x}', t') = \frac{\delta(t' - [t - |\mathbf{x} - \mathbf{x}'|])}{4\pi|\mathbf{x} - \mathbf{x}'|} \,, \tag{1.11}$$

where $|\mathbf{x} - \mathbf{x}'|$ is the distance from $\mathbf{x}$ to the source point $\mathbf{x}'$. Applying this result to Eq. (1.9), one finds the *retarded field*:

$$\bar{h}_{\mu\nu}(\mathbf{x}, t) = 4 \int d^3\mathbf{x}' \, \frac{\bar{T}_{\mu\nu}(t - |\mathbf{x} - \mathbf{x}'|, \mathbf{x})}{|\mathbf{x} - \mathbf{x}'|} \,. \tag{1.12}$$

The energy momentum tensor can be expressed as a sum of Fourier components:

$$\bar{T}_{\mu\nu}(\mathbf{x}, t) = \frac{1}{(2\pi)^2} \int d\omega \; d^3\boldsymbol{\kappa} \; \tilde{T}_{\mu\nu}(\omega, \boldsymbol{\kappa}) e^{i(\omega t - \boldsymbol{\kappa} \cdot \boldsymbol{x})} + c.c \,, \tag{1.13}$$

where *c.c.* means the complex conjugate of the preceding term.

Then, at distances from the source to the observer much larger than the dimensions of the source R, and also much larger than ωR^2 ($\omega R^2/c$ in general units) and $1/\omega$ (c/ω in general units), the denominator of Eq. (1.12) can be replaced by $r = |\mathbf{x}|$, and the exponent of Eq. (1.13) can be approximated by: $|\mathbf{x} - \mathbf{x'}| \simeq r - \mathbf{x'} \cdot \mathbf{x}/r$. As we are assuming that the term ωr is large far from their sources, the metric perturbations have fronts with radii of curvature much bigger than their wavelength λ [Weinberg 1972] and each single frequency component [Eq. (1.13)] of $\bar{h}_{\mu\nu}$ looks like a plane wave solution of Eq. (1.9):

$$\bar{h}_{\mu\nu}(\mathbf{x}, t) = A_{\mu\nu} e^{i\kappa_\mu x^\mu} + c.c. \,, \tag{1.14}$$

where $A_{\mu\nu}$ is the polarisation tensor of the plane wave, and the wave vector κ^μ determines the propagation direction of the waves and its frequency:

$$\begin{aligned} \boldsymbol{\kappa} &\equiv \omega \hat{\mathbf{n}} \,. \\ \kappa^0 &\equiv \omega \,, \end{aligned} \tag{1.15}$$

with $\hat{\mathbf{n}}$ the unitary vector that gives the direction of propagation of the wave and has components $\hat{\mathbf{n}} = (x/r, y/r, z/r)$, whereas the polarisation tensor $A_{\mu\nu}$ carries information about the amplitude and the polarisation of the waves.

Far away from the source, we are in an empty region of the spacetime, i.e. $T_{\mu\nu} = 0$, and Eq. (1.9) takes the wave-like form:

$$\Box \bar{h}_{\mu\nu} = 0 \,. \tag{1.16}$$

As a consequence of this equation, the wave vector κ^μ satisfies $\kappa_\mu \kappa^\mu = 0$ and the Lorenz gauge condition [Eq. (1.8)] implies:

$$A^{\mu\nu} \kappa_\nu = 0 \,. \tag{1.17}$$

However, the Lorenz gauge condition does not completely fix the gauge freedom of the linearised theory. In order to fix it, we employ the *Transverse Traceless* (TT) gauge [Misner 1973]:

$$h^\mu{}_\mu = 0 \; (\Rightarrow \bar{h}_{\mu\nu} = h_{\mu\nu}) \quad \text{and} \quad h_{\mu\nu} u^\nu = 0 \,, \tag{1.18}$$

where u^ν is the four-velocity dx^μ/dt of an inertial observer. Considering a reference frame at rest, i.e. with $u^\mu = (1, 0, 0, 0)$, these equations are equivalent to the algebraic conditions:

$$A_{\mu 0} = 0 \quad \text{and} \quad A^\nu{}_\mu = 0 \,, \tag{1.19}$$

which fix completely the gauge freedom and leave only two intrinsic degrees of freedom for the GW polarisation, i.e. $A_{\mu\nu}$, in GR. The counting of the $A_{\mu\nu}$ components goes as follows: 10 $(A_{\mu\nu})$ − 4 (Lorenz gauge conditions) − 1 (trace-free condition) − 3 (transverse condition) = 2. That is, only the spatial, transverse, and traceless components describe the spacetime perturbations in a gauge-invariant manner [Flanagan 2005, Hughes 2010].

In the case of a GW propagating along the z-direction, $\kappa^\mu = \omega(1, 0, 0, 1)$, only A_{xx}, A_{yy} and $A_{xy} = A_{yx}$ are nonzero and $A_{xx} = -A_{yy}$ from the trace-free condition. Under the TT gauge, we can write the polarisation amplitude $A_{\mu\nu}$ as a combination of the two polarisation states:

$$A^{\mu\nu} = h_+ \varepsilon_+^{\mu\nu} + h_\times \varepsilon_\times^{\mu\nu} \,, \tag{1.20}$$

where $h_+ \equiv h_{xx} = -h_{yy}$ and $h_\times \equiv h_{xy} = h_{yx}$, and where $\varepsilon_+^{\mu\nu}$ and $\varepsilon_\times^{\mu\nu}$ are the wave unit polarisation tensors defined by:

$$\varepsilon_+^{\mu\nu} \equiv \begin{pmatrix} 0 & 0 & 0 & 0 \\ 0 & 1 & 0 & 0 \\ 0 & 0 & -1 & 0 \\ 0 & 0 & 0 & 0 \end{pmatrix} \,, \quad \text{and} \quad \varepsilon_\times^{\mu\nu} \equiv \begin{pmatrix} 0 & 0 & 0 & 0 \\ 0 & 0 & 1 & 0 \\ 0 & 1 & 0 & 0 \\ 0 & 0 & 0 & 0 \end{pmatrix} \,, \tag{1.21}$$

From Eqs. (1.14) and (1.18) one obtains the expression for a GW propagating in a flat source-free spacetime:

$$h_{\mu\nu} \equiv \begin{pmatrix} 0 & 0 & 0 & 0 \\ 0 & h_+ & h_\times & 0 \\ 0 & h_\times & -h_+ & 0 \\ 0 & 0 & 0 & 0 \end{pmatrix} e^{i\kappa_\mu x^\mu} \,. \tag{1.22}$$

To estimate the order of magnitude of the strain h_{ij}, let us consider a binary system whose stars, of masses M_1 and M_2, are in a circular orbit with separation R. In the *quadrupole approximation*, the metric perturbation far from the source of GWs is given by (see [Misner 1973]):

$$h_{ij} = \frac{2\ddot{\mathcal{I}}_{ij}}{r} \,, \tag{1.23}$$
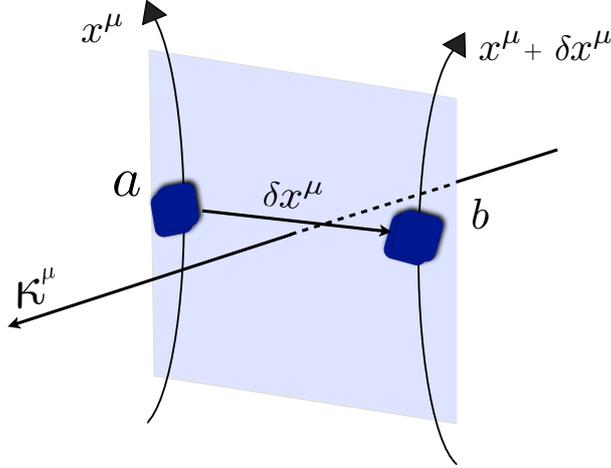
Figure 1.1: *Schematic diagram of two nearby test masses a and b, moving along geodesics $x^\mu(\tau)$ and $x^\mu(\tau) + \delta x^\mu(\tau)$ respectively. The test masses will experience a relative acceleration produced by the passage of a GW with propagation vector κ^μ.*

where r is the distance from the centre of mass of the source,

$$\mathcal{I}_{ij} = M_r \left(x_i x_j - R^2 \delta_{ij}/3 \right) , \tag{1.24}$$

is the inertia tensor of the source and $M_r = M_1 M_2/(M_1 + M_2)$ is the reduced mass. The second derivative of the quadrupole moment tensor can be written as (see, e.g. [Flanagan 2005]):

$$\ddot{\mathcal{I}}_{ij} = -2\Omega^2 M_r R^2 \begin{pmatrix} \cos(2\Omega t) & \sin(2\Omega t) & 0 \\ -\sin(2\Omega t) & \cos(2\Omega t) & 0 \\ 0 & 0 & 0 \end{pmatrix} , \tag{1.25}$$

with Ω the orbital angular velocity of the binary system. If we consider that the binary has equal masses, $M_r = M/2$, from Eq. (1.23) and Eq. (1.25), we obtain that the magnitude h of a typical non-zero component of $h_{\mu\nu}$ is:

$$h = \frac{2M^{5/3}\Omega^{2/3}}{r}. \tag{1.26}$$

Putting numbers to this expression for a common close binary white dwarf system in our galaxy, the amplitude of the GWs generated by the system is approximately:

$$h \simeq 10^{-22} \left(\frac{M}{2M_\odot} \right)^{5/3} \left(\frac{1\mathrm{h}\,\Omega}{2\pi} \right)^{2/3} \frac{10^3\,\mathrm{pc}}{r}. \tag{1.27}$$

The small magnitude, 10^{-22}, of this amplitude gives us an idea about the difficulty of detecting GWs.

One of the first things that we need to know for detecting GWs is which kind of effect we are looking for. To that end, we can consider two non-spinning free falling test masses a and b with mass m and which are moving along nearby geodesics $x_a^\mu(\tau)$ and $x_a^\mu(\tau) + \delta x^\mu(\tau)$, where $\delta x^\mu(\tau) = x_b^\mu - x_a^\mu$ is smaller than the scale on which the gravitational field varies (see Figure 1.1), and τ denotes the proper time of the particle ($g_{\mu\nu}u^\mu u^\nu = -1$, where $u^\mu = dx^\mu/d\tau$ is the velocity of the particle). The test masses will experience a relative acceleration induced by the passage of the GW that can be evaluated using the equation of geodesic deviation. This equation governs the evolution of $\delta x^\mu(\tau)$ and is given by (see, e.g. [Weinberg 1972]):

$$\frac{D^2 \delta x^\mu}{D\tau^2} = -R^\mu_{\ \nu\lambda\rho} \frac{dx^\nu}{d\tau} \frac{dx^\rho}{d\tau} \delta x^\lambda \,. \tag{1.28}$$

From this equation, we can see that, far away from the source, the Riemann tensor accounts for the change in the spacetime geometry produced by the GWs. In this regime, i.e. at linear order in $h_{\mu\nu}$, the Riemann tensor [Eq. (1.2)] is given by the second derivatives of the GW metric perturbations:

$$R_{\mu\nu\lambda\rho} = \frac{1}{2}(h_{\mu\rho,\lambda\nu} + h_{\nu\lambda,\rho\mu} - h_{\nu\rho,\lambda\mu} - h_{\mu\lambda,\rho\nu}) \,. \tag{1.29}$$

In the TT gauge [Eq. (1.19)] and at first order in the metric perturbation, the coordinate time coincides with the proper time $\tau = t$. In this way, the reference frame x^μ, which moves with the particle a, appears to be at rest and thus, the only non-zero components of the Riemann tensor are R_{i0j0}. Consequently, the pair of free falling test masses will exhibit a relative accelerated motion [Eq. (1.28)], revealing the presence of a gravitational field that can be viewed as the tidal effect produced by an effective force:

$$F_i = -mR_{i0j0}\delta x^j = \frac{m}{2} \frac{\partial^2 h_{ij}}{\partial t^2} \delta x^j \,. \tag{1.30}$$

If we consider that the test masses are initially set at relative rest ($d\delta x^\mu/dt = 0$) with respect to each other at a distance $\delta x^i \delta x_i = L^2$, due to the fact that any realistic GW is so weak that the changes in δx_i are very small compared with the distance to the origin, then δx_i can be regarded as essentially constant on the right-hand side of Eq. (1.30). Therefore, from Eqs. (1.28) - (1.30) one obtains [Hawking 1987]:

$$\Delta x_i = \frac{1}{2}h_{ij}\delta x^j \equiv \Delta L \,, \tag{1.31}$$

where here h_{ij} accounts for the dimensionless strain produced by the passing of a GW. From this relation one can see the effect produced by the plus and cross
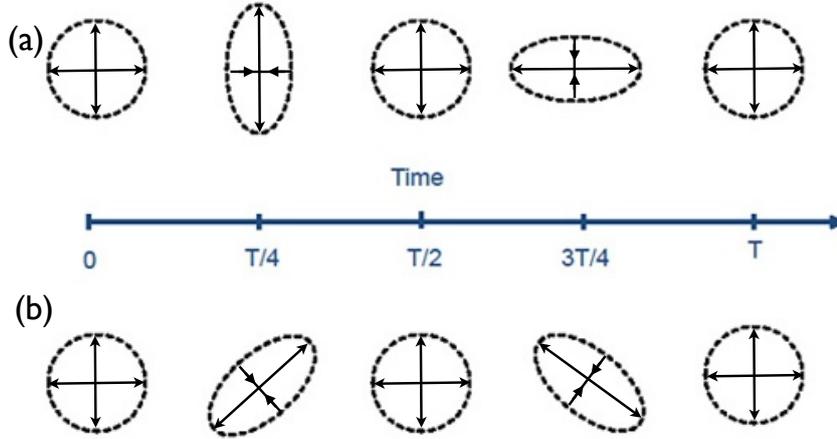
Figure 1.2: *The initial circular configuration of free falling test particles at rest is distorted towards an elliptical pattern by the passage of a GW. In (a) we can see the distortion produced by the plus polarisation, h_+, and in (b) the effect produced by the cross polarisation, $h_\times$.*

polarisations on a set of test masses initially arranged in a circular pattern: Thus, when a GW impinges perpendicular to the circle of particles, the plus polarisation changes the initial configuration to an elliptic one, making it oscillating between circular and elliptic configurations that preserve the initial area (see Figure 1.2 (a)). The equations describing those changes are given by [Hawking 1987]

$$\Delta \ddot{x} = \frac{1}{2}\ddot{h}_+ \delta x \tag{1.32}$$

$$\Delta \ddot{y} = -\frac{1}{2}\ddot{h}_+ \delta y, \tag{1.33}$$

where here the dots denote time derivatives. On the other hand, the cross polarisation produces the same effect but with a rotation of 45º with respect the main axes of the plus polarisation (see Figure 1.2 (b)), so that the changes in the circular distribution of particles are governed by the equations:

$$\Delta \ddot{x} = \frac{1}{2}\ddot{h}_\times \delta y \tag{1.34}$$

$$\Delta \ddot{y} = \frac{1}{2}\ddot{h}_\times \delta x. \tag{1.35}$$

These relations show how the passage of a GW affects the initial distribution of

the test masses, alternatively stretching and contracting the distance between them.

Due to the fact that GWs interact weakly with matter, their detection is a really technological challenge. However, it is precisely the weak interaction with matter that makes so attractive GWs, because it implies that the information that they carry is barely distorted along their way across the Universe. This is in contrast with the case of electromagnetic waves, which are easily absorbed and scattered. On the other hand, electromagnetic waves are generated by the emissions from individual atoms, molecules or other charged particles, whereas GWs are generated by the coherent motion of mass and/or energy. Then, due to the different nature of GWs, the astrophysical information about their generating sources is different from the one that we can obtain through electromagnetic detection. For this reason, not only will GW detection provide us with a new tool to learn about the nature of the Universe, but it will also offer a way to unveil objects and regions of space that otherwise would remain hidden and unknown (like strong gravitational field regions, which usually are surrounded by matter blocking out the electromagnetic waves coming from there). Besides, the detection of GWs is also likely to yield experimental tests of fundamental physics which cannot be done in any other way (see, e.g. [Schutz 1999]).
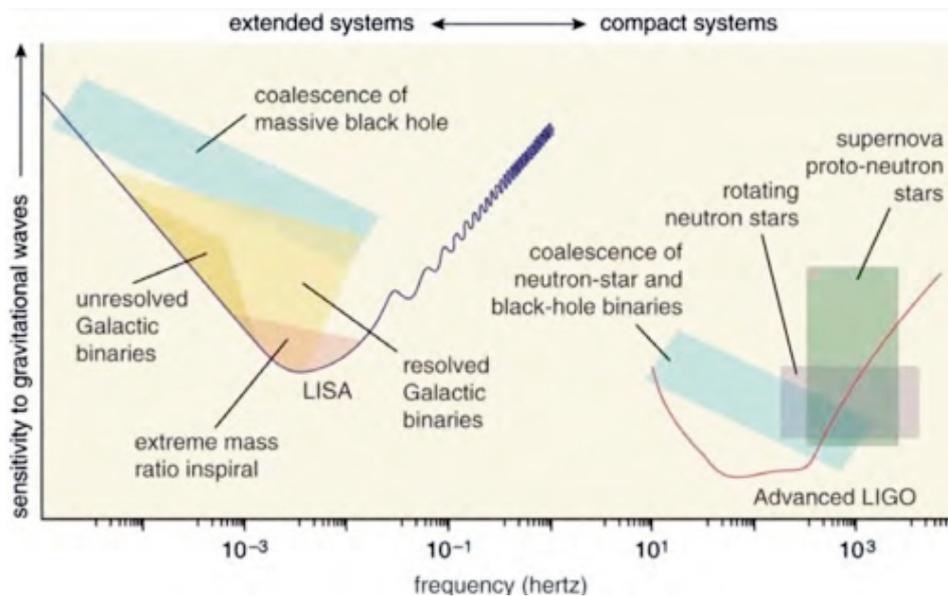
Figure 1.3: *Gravitational-wave sensitivities for LISA and Advanced LIGO. Each detector will detect in a different frequency range and, therefore, different kinds of astrophysical systems [credit ESA].*

Thanks to the development and improvement of GW detectors, in particular

of the ones based on laser interferometry, we have reached levels of sensitivity good enough to allow for GW detection. Up to date, the detectors constructed are on ground, for instance, in Europe we can find detectors like Virgo [Virgo], which is expected to detect GWs within the frequency band $10-6\times10^3$Hz or GEO600 [GEO600] whose frequency band is $50-1.5\times10^3$Hz. In the United States of America, we can find the Laser Interferometer GW Observatory (LIGO) [LIGO] whose frequency band is $40-10^4$Hz. Currently, Virgo and LIGO are being upgraded (advanced Virgo [AdVirgo] and advanced LIGO [AdLIGO]) to reduce the seismic noise and increase their sensitivities by about one order of magnitude in the whole detection band. This translates into an increase in volume of sky accessible of about a factor 10^3.

In order to avoid the seismic noise that heavily affects the measures of ground-based detectors and prevents the detection of low-frequency GWs, there are plans to develop a space-based detector: The Laser Interferometer Space Antenna (LISA) [LISA], which complements the measurements of ground-based detectors (see Figure 1.3), reaching different sources with a lot of interesting associated science. LISA is one of the *L-class mission* within the Cosmic Vision program (2015-2025) of the European Space Agency (ESA). LISA was meant to be a collaboration with the National Aeronautics and Space Administration (NASA). However, due to budgetary problems in NASA, the collaboration cannot comply with the planned schedule and ESA has decided to continue alone the program of L-class missions. This has lead to a redefinition of all these missions, including LISA, to adjust them to the ESA budget. The LISA redefinition is an ongoing study that will end around November 2011. For this reason in this thesis we use the sensitivity of the LISA mission establish in the *Yellow Book* [LISA International Science Team 2011], presented to the general public in February 2011.

1.2   The Laser Interferometer Space Antenna

The LISA mission consists in a constellation of three spacecrafts set in an equilateral triangular configuration, which exchange laser links in such a way that the system is equivalent to two Michelson interferometers. LISA lifetime is expected to be of 5 years. During this time it will orbit around the Sun, following the Earth at a distance of about 50×10^6 km (20º behind), to minimise the effects of its gravitational field, (see Figure 1.4), and the plane of the constellation is tilted 60º with respect to the plane of the ecliptic. The distance between spacecrafts is planed to be 5×10^6 km. Then, the constellation size will be small compared with the typical wavelengths of the

GWs emitted by the main sources of LISA. Inside each spacecraft, two proof masses will be kept in free-fall motion.

The arm length of LISA, i.e. the relative distances between test masses, will be modified by the tidal strain, h, of the GWs passing through. However, LISA measurements will be influenced by the effects of several noise contributions, both external and internal, which need to be eliminated (if possible), diminished to low levels, or controlled to obtain a signal of sufficient quality.
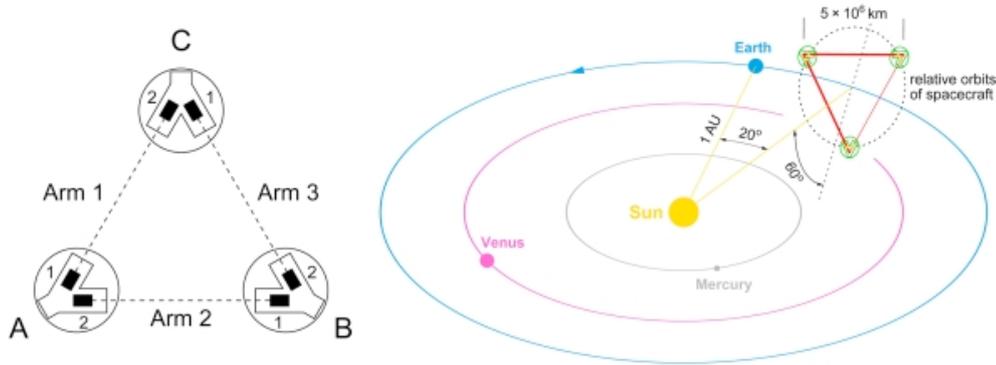
Figure 1.4: *Configuration of the LISA constellation (left) and the position of LISA in its orbit around the Sun (right) [credit ESA].*

The unperturbed triangular configuration of LISA will depend on the orbit of each spacecraft, which have been chosen to maintain as much as possible the triangular shape. LISA orbital motion will have two contributions, both with a period of a year: (1) An orbital motion around the Sun and (2) a cartwheel rotation around its mass centre, which will introduce modulations into the observed data that will help us to determine the location and orientation of the GW sources. In addition, since the noise will not vary periodically as the detector sweeps across the sky, whereas the signal will, the LISA motion will also help us to sort out the GW signals from the detected noise.
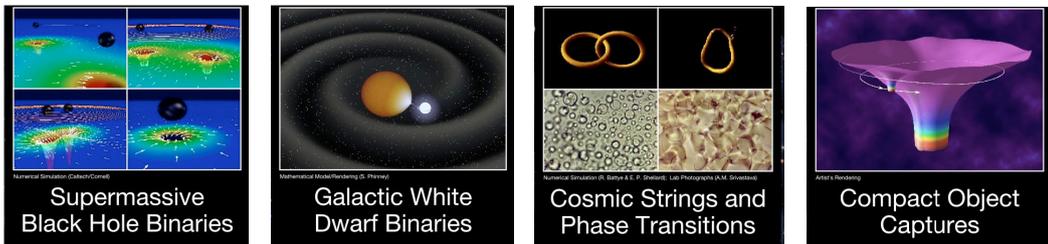
Figure 1.5: *Principal GW sources for LISA [credit NASA]*

The variety of sources scattered over all directions on the sky that LISA

will detect can be distinguished from each other through the different time evolution of their waveforms. In this regard, LISA will detect mainly GWs from (Figure 1.5):

(i) Massive Black Hole (MBH) mergers: From these sources we can figure out how MBH form, grow, and interact over the entire history of galaxy formation and learn about galaxy formation itself (see, e.g. [Sesana 2011]); we can also follow the inspiral and merger of MBH binaries and measure the MBH parameters. With this information, we may test General Relativity and the Kerr solution describing spinning BHs [Schutz 2009]. Moreover, coalescing MBH binaries can be used as "standard sirens" (see [Holz 2005]), i.e. the equivalent to "standard candles" in the electromagnetic spectrum, and may be employed to obtain precise estimates of some cosmological parameters. For example, in the case that we can distinguish an electromagnetic counterpart to a massive BH merger, we could obtain a good estimate of its redshift, which combined with the good estimation of the luminosity distance obtained from the GW detection, can be used to obtain the Hubble constant [Hughes 2003].

(ii) Galactic binaries: Among the myriad of compact binary stars in the galaxy forming a gravitational foreground, there are around thousands of them that will be resolvable for LISA. Their study will offer additional information about stellar evolution and about populations of compact objects through the galaxy. Moreover, there are several stellar mass binary systems, known from electromagnetic observations, whose gravitational radiation is ensured to be detected by LISA. These Galactic binaries, principally composed of white dwarfs, are known as *verification binaries* (see, e.g. [Stroeer 2006]) and they will give us an opportunity to study the physics of compact objects and should help us to understand the LISA detections [Stroeer 2006] (see [van der Sluys 2011] for a recent review on GWs from compact binaries).

(iii) Cosmic strings and phase transitions: These kind of GWs sources will give LISA a chance to find new phenomena of nature. For instance, LISA may be able to measure phase transitions associated with forces of nature or extra dimensions of space which may have caused explosive bubble growth and efficient GW production (see [Maggiore 2000] for an extensive review on inflation, string cosmology, phase transitions and cosmic strings employing GW detection).

(iv) Extreme-Mass-Ratio Inspirals (EMRIs): The existence of BHs is backed by observations of galactic X-ray binary systems, as ultraluminous X-ray sources, and active galactic nuclei (see, e.g. [Psaltis 2011]). Moreover, astrophysical observations carried out by space- and ground-based telescopes suggest the presence of a dark compact object, likely a MBH, at the centre of the majority of the observed galaxies (see [Amaro-Seoane 2007] and references therein). The mass range of the MBHs relevant for LISA is: $M_\bullet = 10^5 - 10^7 M_\odot$.

Surrounding the central MBH of a quiescent galaxy there are around $10^7 - 10^8$ stars forming a cusp/core (see e.g. [Amaro-Seoane 2011]). Due to mass segregation and large scattering encounters between stars in the cluster, the largest Stellar-Mass Compact Objects (SCOs), like neutron stars, $m \approx 1.4 M_\odot$, white dwarfs, $m \approx 0.6 M_\odot$, and stellar mass BHs, $m \approx 1 - 50 M_\odot$, are set in an orbit close enough to the MBH to get gravitationally bounded and form a binary system. All this suggests that the capture of a SCO by a MBH may be a frequent phenomon in the Universe.

Once the SCO is bounded to the MBH, it starts a slow inspiral due to the loss of energy and angular momentum of the system through the emission of GWs. In this process, mainly due to the fact that the mass of the SCO is much smaller than the mass of the MBH, the orbit of the SCO shrinks adiabatically (i.e. the orbital period is much shorter than the time needed for the orbit to shrink) and circularises, starting by emitting bursts of GWs near the pericentre and eventually emitting continuously at frequencies that will lie in the LISA bandwidth. These systems are referred to as Extreme-Mass-Ratio Inspirals since the mass ratios involved are very small, laying in the range $\mu = m/M_\bullet \sim 10^{-7} - 10^{-3}$.

The frequency of the gravitational radiation emitted by a binary system is determined by the mass of the bigger object. Then, the floor of the LISA noise curve ($\sim 3 \cdot 10^{-3} - 3 \cdot 10^{-2}$ Hz) gives a range for the MBH mass that LISA will be most sensitive to. In particular, the masses will correspond to MBHs with $M_\bullet$ between $10^5 M_\odot$ and $10^6 M_\odot$ [Gair 2004]. Moreover, it has been estimated that LISA could detect around a $1 - 10^3$ SCO-MBH binaries per year up to $z \lesssim 1$ [Hopman 2006, Gair 2004].

During the last year before plunge, an EMRI radiating at $3 \cdot 10^{-3}$ Hz will spend around $1/\mu \sim 10^5$ cycles orbiting inside the LISA band [Finn 2000]. During this time, the SCO tracks the strong field geometry in the vicinity of the MBH spacetime, mapping the (multipolar) structure of the MBH into the shape of the GWs emitted. In other

words, the orbit of the SCO depends on the geometry of the MBH (and the orbital parameters) and hence so do the GWs emitted. Moreover, as we shall see below, the detectability of these systems improves with the observation time. In this way, the sensitivity to the MBH parameters is enhanced with each detected cycle, making EMRIs a unique and invaluable tool to study and test MBHs.

(v) Intermediate-mass-ratio inspirals (IMRIs): There are are observations suggesting the existence of Intermediate-Mass Black Holes (IMBHs) i.e. BHs whose masses are lying in the range $M_\bullet = 10^2 - 10^4 M_\odot$ (see [Brown 2007b, Brown 2007a, Amaro-Seoane 2007, Miller 2009, Konstantinidis 2011] for information about the evidence of the existence of IMBHs and their relevance to GW Astronomy). These may form EMRI-like systems, either an IMBH-MBH inspiral or a (stellar BH)-IMBH system. LISA, and in general GW detectors, will be sensitive to the inspiral of an IMBH into a MBH whereas (advanced) ground detectors (such as Advanced LIGO and detectors of third generation like the EinsteinTelescope [ET]) will be sensitive to inspirals of SCOs into IMBHs. The mass ratio for IMRIs is in the range $\mu = 10^{-1} - 10^{-5}$.

LISA will be able to map the structure of the spacetime generated by isolated MBHs with high precision employing the information carried by EMRIs and or IMRIs waveforms. Thus, this will let us verify whether BHs are described by the Kerr metric as GR predicts (see, e.g. [Sopuerta 2010]). Besides, with these observations we can obtain a census of compact objects near galactic centres and also perform tests of galaxy formation models and measure cosmological parameters.

Although this thesis is mainly devoted to the study of EMRIs, great part of the work exposed here can also be applied to the study of IMRIs, since both systems exhibit the same physical properties and dynamics. In this sense, as it is follows from the discussion above, the work of this thesis may not only be useful for LISA, but it may also be of interest for advanced ground-based detectors like Advanced LIGO, Advanced VIRGO, or detectors of third generation like the EinsteinTelescope [ET].

1.3 Parameter Estimation Analysis

As we have seen in the last section, the LISA arms can be thought to be equivalent to two Michelson interferometers of arm-lengths $L_1 = L_2 = L$,

where the test masses play the role of the mirrors. In this way, when a GW impinges on the detector, it will push the masses back and forth relative to each other changing the arm-length difference, $\Delta L(t) = L_1 - L_2$.

A GW signal, $h_{ij}(t)$, produces a response on the detector that is given by (see, e.g. [Thorne 1997]):

$$h(t) \equiv \frac{\Delta L(t)}{L} = F_+(\theta, \phi, \psi)h_+(t) + F_\times(\theta, \phi, \psi)h_\times(t) , \qquad (1.36)$$

where the coefficients F_+ and $F_\times$ ($0 \leq |F_{+/\times}| \leq 1$) are the detector beam-pattern functions, which depend on the location of the source in the sky, (θ, ϕ), and the orientation ψ of the polarisation axes relative to the orientation of LISA. The GW polarisations h_+ and $h_\times$ are associated with the axes of the polarisation frame, described by the unit vectors $\hat{p}$ and $\hat{q}$ (see figure 1.6).
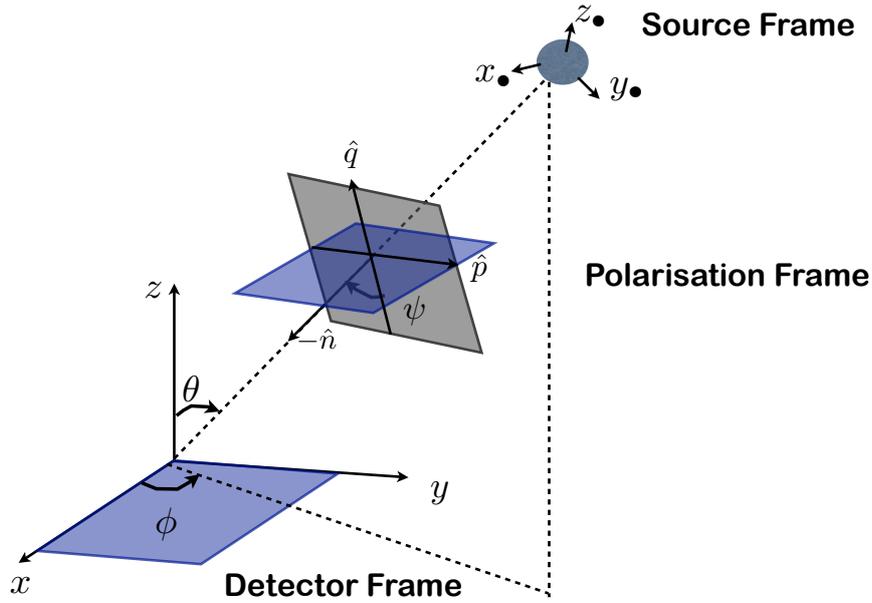
Figure 1.6: *Reference frames associated with the source, the GW and the detector.*

The time evolution of the strain $h(t)$ describes the waveform of the detected signal inducing an arm-length difference:

$$\Delta L(t) = Lh(t) , \qquad (1.37)$$

which, in turn, will produce a frequency shift in the laser beams (see [Hawking 1987, Abramovici 1992]) and the corresponding interference

pattern (or fringes), which will give rise to the final output signal of the detector:

$$\delta\Phi \simeq 2\frac{\Delta L}{\lambda} = 2\frac{h(t)L}{\nu\tau} , \qquad (1.38)$$

where λ and ν are the wavelength and frequency of the laser beam respectively, and τ is the time in which the light travels between two test masses.

In practice, the total interferometer output signal $s(t)$ will be made of two contributions: One produced by the true GW signal $h(t)$ and another one $n(t)$ accounting for the effect of different noise sources, which, in general, will be stronger than an EMRI signal:

$$s_\alpha(t) = h_\alpha(t) + n_\alpha(t) , \qquad (1.39)$$

with $\alpha = I, II$ labelling the two LISA interferometers. Then, it will be difficult to assert a priori if a detector output $s_\alpha(t)$ may contain the GW signal or may not.

The noise contribution will be the same independently of the arm length and, then, it will produce the same total displacement. In this way, the noise effects on the (GW amplitude) sensitivity of the detector scale as $n_\alpha \propto 1/L$. On the other hand, the noise is assumed to be Gaussian and stationary. Then, each of the components of its Fourier transform $\tilde{n}_\alpha(f)$ have Gaussian probability distribution and are uncorrelated between them and in both detectors, that is:

$$\langle \tilde{n}_\alpha(f)\tilde{n}_\beta(f')^* \rangle = \frac{1}{2}\delta(f - f')\delta_{\alpha\beta}S_n(f) , \qquad (1.40)$$

where $S_n(f)$ is the (one-sided) spectral density of the noise and "$\langle\ \rangle$" denotes the average over all possible realisations of the noise.

Since the sensitivity of any detector is determined by its level of noise, we start by looking at the power of the output signal to estimate the sensitivity of the detector [Cornish 2002]:

$$\langle s_\alpha^2(t) \rangle = \langle h_\alpha^2(t) \rangle + \langle n_\alpha^2(t) \rangle , \qquad (1.41)$$

with

$$\langle h_\alpha^2(t) \rangle = \frac{1}{T}\int_0^T |h_\alpha(t)|^2 dt = \int_{f=-\infty}^{f=\infty} |\tilde{h}_\alpha(f)|^2 df , \qquad (1.42)$$

where, in the first equality, we have used the fact that the noise is stationary in order to replace the average over noise realisations for average over time.

And in the second equality, we have used the Parseval's identity together with the definition for the Fourier transform of the signal:

$$h(t) = \sqrt{T} \int_{f=-\infty}^{f=\infty} \tilde{h}(f) e^{i2\pi ft} df \, , \tag{1.43}$$

where T is the total observation time and the normalisation factor, $\sqrt{T}$, is used to have the power spectrum roughly independent of time [Larson 2000]. In addition, the noise spectral density is related with the GW strain, $S_h(f) \equiv |\tilde{h}_\alpha(f)|^2$, by [Hawking 1987]:

$$S_h(f) = \frac{1}{L^2} S_n(f) \, . \tag{1.44}$$

A GW signal can be reliably detected if the interferometric response that it produces, $h_\alpha(t)$, is sufficiently above the noise level, $n_\alpha(t)$. In order to quantify this, we can compute the Signal-to-Noise Ratio (SNR), which basically tells us how much noise is corrupting the signal (a ratio higher than 1:1 indicates more signal than noise). To characterise the SNR for LISA, we assume that the signal is known and we want to figure out whether it is present or not. In order to do so, we start by defining the sensitivity of the interferometer as (from now on we omit the subscript α):

$$h_n(f) \equiv \sqrt{f S_n(f)} \, , \tag{1.45}$$

which has to be compared with the *characteristic amplitude*, $h_c(f)$, of the waves from a given source [Hawking 1987, Finn 2000]:

$$h_c = h_0 \sqrt{n} \, , \tag{1.46}$$

where $h_0^2 = \left[h_+^2 + h_\times^2\right]^{1/2}$, is the strain amplitude of the source, with h_+ and $h_\times$ the amplitudes for the plus and cross polarisations, and $n = fT$ is the number of cycles that the GWs spend at frequency f. Then, using Eq. (1.45), we can in principle define the SNR as:

$$\frac{S}{N} \cong \frac{h_c}{h_n(f)} = h_0 \sqrt{\frac{T}{S_n(f)}} \, . \tag{1.47}$$

Thus, the longer the EMRI keeps on emitting in a given frequency band, the more the signal is enhanced in comparison with the detector noise.

As we have seen, the detection of EMRI signals has to face several issues, principally related to the fact that their signals will be concealed among the different kind of noises affecting the signal output, like instrumental noise

and GW signals from the foreground (mainly from galactic binaries inside the EMRI frequency band). In this regard, matched filtering techniques can be employed to separate their signals from the total noise. With these methods, the signal power can be built up with each cycle, allowing for LISA detections. This in practice requires to have beforehand a bank of very accurate theoretical waveform templates to cross-correlate them with the detector data stream.

Matched filtering techniques will be used both to extract the EMRI signal from the noise, and to measure the parameters of the system associated with the signal. In order to do so, the data, $s(t)$, is filtered out, i.e. the detector output is cross-correlated with a filter $k(t)$, a modelled waveform that may match the desired signal [Cutler 1994a], by employing the following inner product, which is defined under the assumptions of stationarity and Gaussianity (recovering the subscript $\alpha = I, II$):

$$(\mathbf{s}|\mathbf{k}) = 4 \sum_\alpha \Re \int_0^\infty \frac{\tilde{s}_\alpha(f)\tilde{k}_\alpha(f)}{S_h(f)} df \ , \tag{1.48}$$

In other words, the filter projects the data stream $s(t)$, which consists in the true GW signal, $h(t)$, plus the contributions of the different noise sources, $n(t)$, with a best-guess waveform template $k(t)$ for the expected signal and weighs the result with the interferometer noise power spectral density $S_n(f)$. With this technique, when the filter matches the signal, there is a coherent contribution to the cross-correlation, since the noise contributes incoherently and is reduced in relation with the actual GW signal. Consequently, the value of the filtered data is bigger when the signal is present than when it is not. The weighting of the cross-correlation by the inverse of the spectral noise density enhances those frequencies to which the interferometer is most sensitive. In this way, signals thousands of cycles long whose unfiltered amplitude is only a few percent of the root mean square (rms) noise can be detected (see, e.g. [Owen 1999]).

Employing the inner product of signals given by Eq. (1.48), the probability for the Gaussian noise to have some realisation $\mathbf{n}_0$ is:

$$p\left(\mathbf{n} = \mathbf{n}_0\right) \propto e^{-(\mathbf{n}_0|\mathbf{n}_0)/2}. \tag{1.49}$$

Taking this into account, if the actual incident GW is $\mathbf{h}_{GW}$, the probability of measuring a signal $\mathbf{s}$ in the detector output is proportional to $e^{-(\mathbf{s}-\mathbf{h}|\mathbf{s}-\mathbf{h})/2}$. As a result, if the measured signal is $\mathbf{s}$, the waveform $\mathbf{h}$ that "best fits" the data should minimise the quantity: $(\mathbf{s} - \mathbf{h}|\mathbf{s} - \mathbf{h})$. If N is the number of source parameters, $\{\theta^i | i = 1, \ldots, N\}$, characterising the GW waveform templates then, the space of waveforms $\{h(\theta^i)\}$ is an N-dimensional manifold

embedded in the vector space of all possible signals S. In this way, the best-fit waveform $h(\theta^i_{bf})$ for a measured signal $\mathbf{s}$ is the point on $\{h(\theta^i)\}$ that lies closest to $\mathbf{s}$ with respect to the distance established by the inner product $(\cdot|\cdot)$, that is: $(\mathbf{s} - \mathbf{h}|\mathbf{s} - \mathbf{h})$. This criterion can be explained in geometric terms (see e.g. [Cutler 2007]) as in Figure 1.7. Correspondingly, the SNR ratio of the
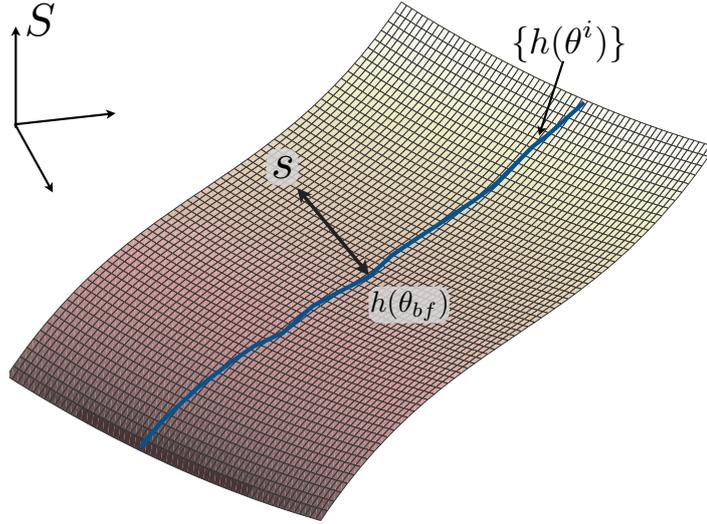
Figure 1.7: *Representation of the space of waveforms $\{h(\theta^i)\}$ embedded in an output signal space S. The best fit waveform $h(\theta^i_{bf})$ is the one that minimises the distance $(\mathbf{s} - \mathbf{h}|\mathbf{s} - \mathbf{h})$.*

actual value of the filtered output to its rms (root mean square) value in the presence of noise for an incident waveform $\mathbf{h}$, which is filtered by a perfectly matched template $\mathbf{h} = \mathbf{h}_{GW}$, is:

$$\text{SNR}[h] = \frac{(\mathbf{h}|\mathbf{h})}{rms\,(\mathbf{h}|\mathbf{n})} = (\mathbf{h}|\mathbf{h})^{1/2} \ , \tag{1.50}$$

where we have used: $rms(\mathbf{h}|\mathbf{n}) = (\mathbf{h}|\mathbf{h})^{1/2}$ to obtain the last equality.

From this discussion and taking into account that an EMRI expends thousands of cycles ($\sim \mathcal{O}(\mu)$) inside the LISA band, increasing the SNR of the detected data [Finn 2000], it has been estimated [Gair 2004] that we should be able to extract several thousands of cycles of an EMRI from the data by using matched filtering techniques.

Since the parameter vector of a signal $\theta^{\mathbf{i}}$ is not known in advance, it will be necessary to filter out the data with a family of templates located at various points in parameter space, for instance in a lattice, such that we make sure that any signal will lie close enough to at least one of the templates. Although

different realisations of the noise will give rise to different deviations from the best-fit parameters, for large SNR the distribution of best-fit parameters will be a Gaussian distribution centred around the correct values [Cutler 2007]. In other words, if θ^i_{tr} are the true system parameters, and $\theta^i_{bf}(\mathbf{n}) \equiv \theta^i_{tr} + \delta\theta^i(\mathbf{n})$ are the best-fit parameters, then for large SNR the parameter-estimation error $\delta\theta$ follows a Gaussian probability distribution function like:

$$p(\delta\theta^i) = \mathcal{N} e^{-\Gamma_{ij}\delta\theta^i \delta\theta^j/2} , \tag{1.51}$$

where $\mathcal{N} = \sqrt{det(\Gamma/2\pi)}$ is the normalisation factor and Γ_{ij} is the *Fisher information matrix* [Fisher 1935], defined by:

$$\Gamma_{ij} \equiv \left(\frac{\partial \mathbf{h}}{\partial \theta^i} \middle| \frac{\partial \mathbf{h}}{\partial \theta^j} \right) . \tag{1.52}$$

For large SNR, the variance-covariance matrix of the errors, which gives a measure of how much the errors $\delta\theta^i$ vary and how two errors change together in a set of data, is given by [Vallisneri 2008]:

$$\langle \delta\theta^i \delta\theta^j \rangle = (\Gamma^{-1})^{ij} + \mathcal{O}(\text{SNR}^{-1}) . \tag{1.53}$$

Then, the Fisher matrix carries information on the parameters errors and their covariance. If it is not diagonal (as it happens in our analysis), it means that the parameter estimations are correlated, that is, they have a similar effect on the data and it is difficult to quantify the contribution of each of them separately, independently of whether the parameters are or not physically related with each other.

As we can see [Eq. (1.52)], the Fisher matrix is built from the partial derivatives of the signal and then, it can only represent the true signal h_{GW} correctly if $h(\theta^i)$ is linear in all the parameters θ^i across ranges comparable to the expected parameter errors. This approximation is known as the *Linearised-Signal Approximation* (LSA). As the errors decrease, the SNR grows, and the LSA is expected to work better. In the regime where this approximation is valid, we can expand $h(\theta^i)$ around $h_{GW} = h(\theta^i_0) \equiv h_0$, i.e. $\theta^i = \theta^i_0 + \delta\theta^i$ with $\delta\theta^i$ being a small deviation in the parameters comparable with the parameter error estimation, and where $h(\theta^i)$ is a certain waveform template family:

$$h(\theta^k) = h_0 + \delta\theta^i \partial_i h|_{\theta^k=0} + \frac{\delta\theta^i \delta\theta^j}{2} \partial^2_{ij} h|_{\theta^k=0} + \dots . \tag{1.54}$$

Then, the likelihood [Eq. (1.51)] can be approximated as:

$$p(n) \propto \exp \left\{ -(n,n)/2 + \delta\theta^i \delta\theta^j (\partial_i h, \partial_j h)/2 + \delta\theta^j (\partial_j h, n) \right\} . \tag{1.55}$$

The use of the Fisher matrix for parameter estimation is limited by the high-SNR condition, in the sense that it can be a poor predictor of the amount of information obtained from waveforms with several parameters and relatively low expected SNR. In this regard, Vallisneri [Vallisneri 2008] provides a criterion to determine when the SNR is high enough, which is given by the following ratio r of the LSA likelihood [Eq. (1.55)] to the exact likelihood [Eq. (1.49)]:

$$| \log r(\delta\theta^k, \mathrm{SNR})| = (\delta\theta^i \partial_i h + \Delta h(\delta\theta^k) | \delta\theta^j \partial_j h - \Delta h(\delta\theta^k))/2 \ , \qquad (1.56)$$

this relation is usually called *maximum-mismatch criterium*, here $\Delta h(\delta\theta^k) = h(\delta\theta^k) - h(\theta)$, $SNR = \sqrt{(h(\theta)|h(\theta))}$, $\delta\theta^i$ is the error. The product in Eq. (1.56) represents the noise weighted-norm of the contributions to $h(\delta\theta^k)$ above the linear terms, expanded around the true source parameters θ. Then, the idea behind the criterium is to choose an isoprobability surface as predicted by the Fisher Matrix, and explore it to verify the mismatching between the LSA and exact likelihood is smaller than a fiducial value, i.e. ratios r below this fiducial value are considered acceptable. In this way, we can believe that the LSA is predicting a reliable surface to begin with the parameter estimation.

1.4 Overview

As we have seen along this introduction, EMRIs are one of the main sources of GWs for LISA. They emit long and complex GW signals in the strong field regime of the MBHs, which encode the MBH structure. For this reason, EMRI GW signals are a valuable tool to study the MBHs located in the galactic centres and the science related with them.

In this thesis, we study two different aspects of EMRIs. The first part of the thesis is devoted to the modelling of EMRIs. To produce the GW waveforms needed for EMRI detections, we have to know how the gravitational field of the SCO affects its own trajectory and deviates it from geodesic motion. In this regard, due to the extreme mass-ratio of the system, we can consider the SCO as a structureless particle orbiting in a geodesic of the exact MBH geometry. In this picture, the inspiral of the SCO around the MBH is described through the action of a local self-force, which alters the geodesic motion of the particle. However, the implementation of this mechanism presents several difficulties, mainly due to the point-like description of the SCO, which introduces Dirac delta distributions. This in practice means that one has to deal with very different spatial scales, one associated with the modelling of the SCO and another associated with the MBH. Moreover, the extreme mass ratio of these

systems implies that we have to deal with two different time scales in the dynamics of the system, one associated with the orbital evolution of the SCO and another associated with the evolution of its orbit due to GW emission. We present a new method that provides very efficient and accurate computations of the self-force in the time-domain, which makes our technique amenable for the intensive computations required in the astrophysically relevant scenarios. The key point of our scheme is that it does not need to resolve the SCO. Instead, we avoid its presence in the computational domain by substituting the Dirac delta distributions by boundary conditions. Consequently, we have just to provide the numerical resolution to describe the field near the SCO, but not the SCO itself.

In the second part of the thesis we investigate whether we can use EMRI observations to test a particular theory of Gravity, namely *Dynamical Chern-Simons Modified Gravity* (DCSMG) theory. The idea is that the SCO orbits are deep inside the MBH gravitational potential, that is, EMRI systems emit GWs from the strong field region of the MBH. In this way, the shape and timing of the GWs emitted by the system have encoded the structure of the MBH spacetime and the way in which the characteristic frequencies of the system evolve. This information allows us to perform tests of GR and even of other theories of gravity. We perform this study using Fisher matrix analysis.

The distribution of chapters in this thesis is the following: In Chapter 2, we introduce EMRI systems and the main issues related with their modelling, in particular the model that we employ as a proof-of-principle in our simulations. Next, in Chapter 3, we present our time-domain method to model EMRIs, which we call the *P*article-without-Particle (PwP) method, describing the mathematical foundations and the implementation. Later, in Chapter 4 and Chapter 5, we apply our method to compute the self-force acting on EMRIs in circular and in eccentric motion around a non-rotating MBH. On the other hand, in Chapter 6 we introduce the DCSMG and describe the dynamics of EMRI in this theory. Finally, in Chapter 7, we present results on the capability of LISA to distinguish this theory using EMRI detections.

Part I

Modelling Extreme-Mass-Ratio Inspirals

Extreme-Mass-Ration Inspirals

Science... never solves a problem without creating ten more.
George Bernard Shaw.

2.1 The Physical Scenario

Modelling EMRIs implies to deal with a two-body problem in General Relativity, where the spacetime geometry is a dynamical entity: The SCO evolution generates GWs that modify the spacetime geometry determined by the MBH. EMRI waveforms are very rich and complex signals, which are quite sensitive to the physical parameters of the system. Without taking into account the spin of the SCO, they depend on 14 different parameters (see Table 7.1). During the last year before plunge, an EMRI system will perform around $1/\mu = M_\bullet/m$ cycles [Finn 2000], all of them within the LISA band, i.e. for an EMRI with a MBH of $M_\bullet = 10^6 M_\odot$ and a SCO of mass $m = 10 M_\odot$ the number of cycles during this last year is about 10^5. Then, we would need a huge number of waveform templates to cover the EMRI signal space and perform a fully matched filter search of the parameters of the system [Gair 2004]. In turn, this will translate into a huge demand of computational resources, making necessary the obtention and computation of EMRI waveforms in an efficient and quick way.

The GW emission leads to a loss of energy and angular momentum of the system, which changes the SCO orbital parameters and makes its orbit non periodic. In fact, to determine the influence of the GW emission on the SCO motion, i.e. the gravitational *Radiation Reaction* (RR) or *backreaction*, is a long standing problem (see, e.g. [Barack 2009]), which can become more complicated due to the effect of *transient resonances*. Recently, it has been shown [Flanagan 2010] that transient resonances may appear for a given combination of the EMRI parameters, when the SCO is deep in the strong field

potential of the MBH. This effect makes the EMRI dynamics even more sensitive to initial conditions in this region. Consequently, it is very difficult to find an analytical solution to the EMRI equations of motion and to obtain accurate waveform templates. For this reason, the use and development of new numerical techniques to compute the EMRI dynamics without employing many simplifications becomes necessary.

The fact that the MBH mass is orders of magnitude bigger than the one of the SCO ($\mu \ll 1$) is used to justify the use of approximative methods to model EMRIs, since it implies that the field of the SCO can be treated as a linear perturbation of the MBH gravitational field (see, e.g. [Drasco 2006]). In other words, the coupling between the field of the SCO and that of the MBH is very small. On the other hand, the geodesic motion around a Kerr (spinning) MBH is characterised by three constants of motion, namely: energy E, angular momentum along the spin axis (usually taken to be the z axis) L_z, and Carter constant Q (for a non-rotating Schwarzschild BH it does not play any role). However, since the SCO is going to be subjected to GW emission, these constants of motion are going to evolve. Nevertheless, the motion of the SCO, on short time scales (orbital time scales), is well approximated by geodesic of the MBH background, since the time scale of change of these constants, the inspiral time scale $T_{inspiral}$, is much larger than the typical orbital time scale $T_{orbital}$: $T_{orbital}/T_{inspiral} \sim \mu \ll 1$.

This clear separation of time scales has motivated the so called *adiabatic approximation* (see for instance [Mino 2003a, Pound 2005, Pound 2008a, Mino 2008, Hinderer 2008]), where the inspiral can be described by a flow through a sequence of geodesic orbits. This can be handled by using the method of *osculating orbits*, where at each instant the worldline of the SCO is assumed to lie tangent to a reference geodesic, called an osculating orbit, such that the worldline evolves smoothly from one such geodesic to the next [Pound 2008b]. One can further approximate the inspiral treatment by assuming that only dissipative effects (those due to GW emission and that changes, for instance, the intrinsic orbital parameters) are relevant, neglecting conservative effects (which do not change the constants of motion on average, but change the phase). We can call this approximation the *radiative approximation*, which has been developed and used by a number of authors [Hughes 2005, Drasco 2006, Sago 2005, Ganz 2007]. However, it is not clear that this approximation is enough to produce accurate EMRI waveforms for the purposes of a space detector like LISA, as it has been suggested recently [Hinderer 2008]. In addition, we can model EMRIs employing the *black hole perturbation theory*, where the internal structure of the SCO is not taken into account and then, it can be pictured as a particle (particle limit),

and where the spacetime metric $g_{\mu\nu}$ is expanded in powers of the mass-ratio μ of the system (see [Pound 2010] and references therein). In this approximation, we consider that the particle orbits the MBH while generating metric perturbations $\delta g_{\mu\nu}$ and, since the particle is small compared with the background curvature scale, these perturbations can be linearised (see Section 1.1). Taking into account these considerations, at leading order in BH perturbation theory, the spacetime of the system is given by an exact MBH geometry $g_{\mu\nu}$ plus linear perturbations $h_{\mu\nu}$ generated by the particle, i.e. the particle moves on a geodesic of the MBH spacetime and simultaneously emits GWs. From the point of view of energy conservation arguments this picture is not consistent, because it implies that the particle will ever move on a geodesic of the MBH while the GWs carry off energy and angular momentum. However, including higher powers in the mass-ratio, we can reproduce the inspiral of the particle. In this context, the inspiral trajectory of the SCO can be seen from two points of view: (i) The particle follows a geodesic in a perturbed smooth spacetime: $\bar{g}_{\mu\nu} = g_{\mu\nu} + h_{\mu\nu}$, where here $h_{\mu\nu} \equiv h_{\mu\nu}^{\mathcal{R}}$ is the regular part of the metric perturbation, whose meaning will be made clear later, or (ii) the particle moves in a non-geodesic orbit of the MBH geometry. In BH perturbation theory, the RR is described as the action of an effective force that pushes the particle away from geodesic motion around the MBH in the picture of (ii) or makes it move along geodesics of a perturbed spacetime in the picture of (i). This is similar to what happens in electrodynamics with accelerated charged particles [Barut 1980, Jackson 1999], but in our case we deal with a *gravitational self-force* [Poisson 2005, Mino 1997, Quinn 1997] (see also [Detweiler 2003b, Poisson 2004a, Gralla 2008]).

In curved spacetimes the self-force has two different contributions. On the one hand the self-force has a term that emulates the effect of the RR and requires knowledge to the different orders in the mass ratio μ. This term is associated with dissipative effects. On the other hand, the self-force contains also a conservative component. The dissipative component leads to a secular change in the intrinsic orbital parameters, such as the constants of motion E, L_z and Q [Mino 2003a] and the RR effects can be characterised by their time evolution. Whereas the conservative component leads to a small shift in the instantaneous values of the orbital parameters, altering the time dependence of the orbital phases (see, e.g. [Sago 2008] and reference therein).

Although, the theoretical formalism to compute the self-force has been fully developed, the mathematical tools needed to implement that formalism has not been fully developed yet and, hence, the self-force computation is still an open problem (see [Barack 2009] for an extended review on the status of self-force computations). In this regard, there has been a step forward to

solve this problem by Barack and Sago [Barack 2010]. In their work they have computed the gravitational self-force (in the Lorenz gauge) for a particle in a generic (bound) geodesic in a Schwarzschild geometry. Now, the next challenge is to extend these computations to the case of a Kerr MBH. In this sense, the techniques for constructing templates good enough for EMRI detection and parameter extraction have not been yet fully developed.

2.2 The Self-Force Problem

As we have seen in the last section, to model accurately the strong field orbital evolution of the SCO, it is necessary to employ the self-force approach to the EMRI dynamics. A key development for the formulation of the gravitational self-force was done by Mino, Sasaki and Tanaka [Mino 1997] and Quinn and Wald [Quinn 1997], who derived, in the Lorenz gauge, the equations of motion for both a small BH and a particle in a curved background spacetime at linear order in μ. These equations are known as the *MiSaTaQuWa* equations of motion (see, e.g. [Rosenthal 2006, Galley 2009] for recent work towards $O(\mu^2)$ calculations). Nevertheless, they only provide a formal expression of the gravitational self-force (see [Detweiler 2003b, Poisson 2004a, Gralla 2008]). The difficulties in computing the self-force originate from the singular character of the particle description, because the metric perturbations become singular at its location and one is required to introduce a regularisation method. In this regard, the mode sum regularisation scheme [Barack 2000b, Barack 2000a, Barack 2001a, Mino 2003b, Barack 2002a, Barack 2002b, Detweiler 2003a, Haas 2006], which has been formulated only in the Lorenz gauge (see Section 1.4), tells us how to subtract, mode by mode, the singular part of the perturbations that do not contribute to the self-force and the problem is reduced to compute the full retarded solution of the perturbative equations.

On the other hand, the field equations associated with the perturbative EMRI problem are a set of ten linear partial differential equations (PDEs) for the metric perturbations that can only be decoupled in certain gauges, like the *Regge-Wheeler gauge* [Regge 1957]. The fact that the self-force is obtained in the Lorenz gauge, whereas the metric perturbations are better decoupled in other gauges puts another obstacle in the way towards the self-force computation, which is known as the *gauge problem*. In this regard, there have been several advances towards the gravitational self-force computation employing a *radiation gauge* [Keidl 2010, Shah 2011], which is closer to the Regge-Wheeler gauge in the sense that it is also an algebraic gauge.

Next, following closely [Poisson 2004a], we are going to review briefly three different physical models where a particle is subject to a self-force generated by different physical fields, namely: (i) A scalar field (Section 2.2.1); (ii) an electromagnetic field (Section 2.2.2); and (iii) a gravitational field (Section 2.2.3). This will help us to introduce the equations of motion for a small, structureless and non spinning object moving in a curved spacetime, and in particular the equations for the dynamics of a SCO orbiting a MBH. We will also use this discussion to introduce and justify the EMRI model that we study in this thesis.

2.2.1   Scalar Case

We start considering the motion of a point scalar charge q of mass m orbiting in a generic spacetime whose geometry is described by the non-dynamical metric $g^{\mu\nu}$. The particle generates a scalar field $\Phi(x)$, which satisfies the following wave equation:

$$(\Box - \upsilon R)\,\Phi = -4\pi\rho \,, \tag{2.1}$$

where $\Box = g^{\alpha\beta}\nabla_\alpha\nabla_\beta$; υ is a coupling constant between the field and the spacetime geometry and the source term is given by:

$$\rho = -4\pi q \int_\gamma d\tau\, \delta_4(x, z(\tau)) \,, \tag{2.2}$$

where $\delta_4(x, z(\tau))$ is the invariant Dirac delta distribution defined by the relation:

$$\int_\gamma \sqrt{-g(x)}f(x)\delta_4(x, x')d^4x = f(x') \,. \tag{2.3}$$

Due to the appearance of the $\delta_4(x, x')$ in the source term of Eq. (2.1), it is clear that ρ has only support on the particle worldline. The retarded solution Φ_{ret} to the wave equation is given by:

$$\Phi_{ret}(x) = q \int_\gamma G_+(x, z)d\tau \,, \tag{2.4}$$

where, G_+ is the retarded Green's function associated with Eq. (2.1)

The RR that undergoes the scalar particle can be seen as an "external" self-force that deviates the particle from geodesic motion (and drives its inspiral when the spacetime metric is the one of a BH). This self-force is generated by the retarded field, Φ_{ret}, and is given by (see e.g. [Poisson 2004a]):

$$ma^\mu = q(g^{\mu\nu} + u^\mu u^\nu)\nabla_\nu\Phi_{ret} \,, \tag{2.5}$$

where $a^\mu = u^\mu \nabla_\alpha u^\alpha$ is the covariant 4-acceleration of the particle and

$$u^\mu = \frac{dz^\mu}{d\tau} \, , \tag{2.6}$$

is its particle 4-velocity.

Although the retarded field is not invariant under time reversal, we could preserve this invariance introducing the advanced solution Φ_{adv} of a time symmetric evolution giving rise to a "reverse playback picture", i.e. an outward inspiralling particle and an ingoing radiation. Then, the following linear superposition:

$$\Phi_{\mathcal{S}} = \frac{1}{2} \left(\Phi_{ret} + \Phi_{adv} \right) + \frac{q}{2} \int_\gamma H(x, z) d\tau \, , , \tag{2.7}$$

where the two-point function $H(x, z)$ is introduced specifically to cure non-causal effects due to the spacetime curvature [Poisson 2004b]. It is invariant under time reversal, since both incoming and outgoing radiation would be equally present. Consequently, $\Phi_{\mathcal{S}}$ would be generated by a point charge that does not undergo any RR or any self-force.

Regardless of the fact that $\Phi_{\mathcal{S}}$, Φ_{ret} and Φ_{adv} gives rise to different particle dynamics, they satisfy the same wave equation with the same singular source term [see Eq. (2.2)]. Then, the three fields diverge at the location of the particle. In other words, due to the singularity of the source term, the force Eq. (2.5) diverges at the particle location losing its physical meaning. Nevertheless, we can obtain a well behaved solution $\Phi_{\mathcal{R}}$ near the particle worldline by just subtracting $\Phi_{\mathcal{S}}$ to Φ_{ret}, since both share the same singularities [Detweiler 2003b]. The resulting *regular field* is then given by:

$$\Phi_{\mathcal{R}} = \Phi_{ret} + \Phi_{\mathcal{S}} \, , \tag{2.8}$$

and fulfils the homogeneous wave equation:

$$\left(\Box - \upsilon R \right) \Phi_{\mathcal{R}} = 0 \, , \tag{2.9}$$

where the gradient of the radiative field, $\Phi_{\mathcal{R}}$, evaluated on the worldline is given by [Quinn 2000, Poisson 2004a]:

$$\nabla_\mu \Phi_{\mathcal{R}} = -\frac{q}{12} \left(1 - 6\upsilon \right) R \, u_\mu + \frac{1}{6} q \left(g_{\mu\nu} + u_\mu u_\nu \right) R^\nu_\lambda u^\lambda + \nabla_\mu \Phi^{tail} \, , \tag{2.10}$$

where all the quantities in this expression are evaluated at $z(\tau)$, the current position of the particle on the worldline, and the last term is given by:

$$\nabla_\mu \Phi^{tail}(z(\tau)) = q \int_{-\infty}^{\tau^-} \nabla_\mu G_+(z(\tau), z(\tau')) \, d\tau' \, , \tag{2.11}$$

where $z(\tau')$ represents a previous position of the particle. This integration is cut at $\tau' = \tau^- \equiv \tau - \varepsilon$ $(0 < \varepsilon \ll 1)$, to avoid the singular behaviour of the retarded Greens function at the particle location.

By introducing Eq. (2.11) into Eq. (2.5) we obtain the equation of motion of the point scalar charge [Poisson 2004a]:

$$ma^{\mu} = \mathcal{F}_{\mathcal{R}}^{\mu} , \tag{2.12}$$

where the correction term $\mathcal{F}_{\mathcal{R}}^{\mu} = \nabla_{\mu}\Phi_{\mathcal{R}}$, which gives rise to the self-force:

$$\mathcal{F}_{\mathcal{R}}^{\mu} = \frac{1}{6}q^2 \left(\delta_{\nu}^{\mu} + u^{\mu}u_{\nu}\right) R_{\lambda}^{\nu}u^{\lambda} + F_{\mu}^{tail} . \tag{2.13}$$

The *tail* part of the field $F_{\mu}^{tail} = q\nabla_{\mu}\Phi^{tail}$ represents the radiation that, after being emitted and scattered on the spacetime curvature, impacts on the particle itself and, hence, is the contribution that we need to find to obtain the self-force. Notice that due to this field contribution, the self-force depends upon the entire past history of the particle.

2.2.2 Electromagnetic Case

We consider now a charged point q of mass m in a generic curved spacetime $\mathrm{g}^{\mu\nu}$. The radiative field equations for the charged particle can be formulated in the same way as in the scalar case exposed above but, in this case, the particle generates a retarded vector field, A_{ret}^{μ}, which in the Lorenz gauge, $\nabla_{\mu}A_{ret}^{\mu} = 0$ satisfies the wave-like equations [Poisson 2004a]:

$$\Box A_{ret}^{\mu} - R_{\ \beta}^{\mu}A_{ret}^{\beta} = -4\pi j^{\mu} , \tag{2.14}$$

where the source term is given by the current density $j^{\alpha}(x)$:

$$j^{\alpha}(x) = q \int_{\gamma} \mathrm{g}_{\mu}^{\alpha}(x,z)u^{\mu}(z)\delta_4(x,z)\,d\tau . \tag{2.15}$$

The retarded solution can be written as:

$$A_{ret}^{\mu}(x) = 4q \int_{\gamma} G_{+\ \nu}^{\mu}(x,z)u^{\nu}(z)\,d\tau , \tag{2.16}$$

Since the retarded field A_{ret}^{β} is singular on the world line of the particle, it can be regularised following the same procedure as for the scalar charged case, i.e by subtracting the singular part of the field $A_{\mathcal{S}}^{\beta}$ from the retarded one A_{ret}^{β}. The resulting regular vector potential $A_{\mathcal{R}}^{\beta}$ is then given by:

$$A_{\mathcal{R}}^{\beta} = A_{ret}^{\beta} + A_{\mathcal{S}}^{\beta} \tag{2.17}$$

and satisfies the homogeneous equation:

$$\Box A^{\beta}_{\mathcal{R}} - R^{\mu}{}_{\beta} A^{\beta}_{\mathcal{R}} = 0 \, . \tag{2.18}$$

On the other hand, the acceleration that $A^{\beta}_{\mathcal{R}}$ produces on the particle is given by:

$$m a_{\mu} = \mathcal{F}^{\mathcal{R}}_{\mu\nu} u^{\nu} \, , \tag{2.19}$$

where the last term is the self-force acting on the charge [Poisson 2004a]:

$$\mathcal{F}^{\mathcal{R}}_{\mu\nu} u^{\nu} = \frac{1}{3} q^2 \left(g_{\mu\nu} + u_{\mu} u_{\nu} \right) R^{\nu}{}_{\lambda} u^{\lambda} + q F^{tail}_{\mu\nu} u^{\nu} \, , \tag{2.20}$$

where the tail part is given by:

$$q F^{tail}_{\mu\nu} u^{\nu} = 2 q^2 u^{\mu} \int_{\infty}^{\tau^{-}} \nabla_{[\mu} G_{+\ \nu]\beta}(z(\tau), z(\tau')) u^{\beta}(z(\tau')) \, d\tau' \, . \tag{2.21}$$

2.2.3 Gravitational Case

In what follows, we consider a gravitating point mass m (in contrast with a test mass) moving on a worldline of a MBH spacetime geometry with metric $g_{\mu\nu}$. In this study we are interested in the dynamics of a small particle and the nature of the gravitational perturbations that its movement generates, which is essential to obtain and understand the nature of the gravitational self-force. Then, in this case, the point mass produces small metric perturbations $h_{\mu\nu}$ ($|h^{\mu\nu}| \ll |g^{\mu\nu}|$) during its orbit, and it is the "smallness" of $h_{\mu\nu}$ that lets us deal with the particle in an analogous way to the scalar and vectorial cases exposed in Section 2.2.1 and Section 2.2.2 respectively.

The spacetime metric of the system particle-MBH, $g_{\mu\nu}$, can be approximately written as a contribution of two terms: The MBH spacetime metric $\bar{g}_{\mu\nu}$ plus the metric perturbations $h_{\mu\nu}$ generated by the particle,

$$g_{\mu\nu} = \bar{g}_{\mu\nu} + h_{\mu\nu} \, . \tag{2.22}$$

In order to obtain the equations of motion for the particle, we start writing the gravitational perturbations in a trace-reversed form [Eq. (1.6)]

$$\tilde{h}_{\mu\nu} = h_{\mu\nu} - \frac{1}{2} \left(\bar{g}^{\alpha\beta} h_{\alpha\beta} \right) \bar{g}_{\mu\nu} \, , \tag{2.23}$$

which in the Lorenz gauge [Eq. (1.8)],

$$\bar{\nabla}_{\mu} \tilde{h}^{\mu\beta} = 0 \, , \tag{2.24}$$

satisfies the equations:

$$\bar{g}^{\alpha\beta}\bar{\nabla}_\alpha\bar{\nabla}_\beta\tilde{h}_{\mu\nu} + 2\bar{R}_\alpha{}^\mu{}_\beta{}^\nu\tilde{h}^{\alpha\beta} = -16\pi T^{\mu\nu} . \tag{2.25}$$

Here, the stress-energy tensor of the system is due to the point mass particle:

$$T^{\mu\nu} = m \int \frac{d\tau}{\sqrt{-g}} u^\mu u^\nu \delta^4\left(x - z(\tau)\right) . \tag{2.26}$$

The retarded solution is given by:

$$\tilde{h}_{ret}^{\alpha\beta}(x) = 4m \int_\gamma G_{+\,\mu\nu}^{\alpha\beta}(x, z(\tau)) u^\mu(z(\tau)) u^\nu(z(\tau)) \, d\tau , \tag{2.27}$$

where $G_{+\,\mu\nu}^{\alpha\beta}(x, z)$ is the retarded Green function associated with Eq. (2.25) (see [Poisson 2004a]). Notice that the perturbation $h_{\mu\nu}$ can be recovered by inverting Eq. (2.23).

In order to obtain the equations of motion for the small mass, we demand a geodesic motion in the perturbed spacetime [Eq. (2.34)]. This translates into an accelerated motion in the MBH background spacetime [Poisson 2004a]:

$$a^\mu = -\frac{1}{2}\left(\bar{g}^{\mu\nu} + u^\mu u^\nu\right)\left(2\bar{\nabla}_\beta h_{\nu\alpha} - \bar{\nabla}_\nu h_{\alpha\beta}\right) u^\alpha u^\beta . \tag{2.28}$$

Due to the singular character of the source, the metric perturbations diverge at the particle location, and then Eq. (2.28) is not meaningful. We remove the singular contribution to the metric perturbations, $\tilde{h}_\mathcal{S}^{\mu\nu}$, from the retarded one, $\tilde{h}_{ret}^{\mu\nu}$, obtaining a radiative field, $\tilde{h}_\mathcal{R}^{\mu\nu}$. This regular field ($h_\mathcal{R}^{\mu\nu}$) satisfies the homogeneous wave equation associated with our problem and drives the inspiral of the particle into the MBH.

On the particle worldline the radiative field is given by:

$$\bar{\nabla}_\alpha\tilde{h}_{\mu\nu}^\mathcal{R} = -4m\left(u_{(\mu} R_{\nu)\beta\alpha\gamma} + R_{\mu\beta\nu\gamma}u_\alpha\right) u^\beta u^\gamma + \bar{\nabla}_\alpha\tilde{h}_{\mu\nu}^{tail} , \tag{2.29}$$

where the corresponding expression for the tail term is:

$$\bar{\nabla}_\gamma\tilde{h}_{\mu\nu}^{tail} = 4m \int_{-\infty}^{\tau^-} \bar{\nabla}_\gamma\left(G_{+\,\mu\nu\mu'\nu'} - \frac{1}{2}\bar{g}_{\mu\nu}G_{+\,\rho\mu'\nu'}^\rho\right) u^{\mu'} u^{\nu'} \, d\tau' , \tag{2.30}$$

where unprimed indices refer to objects evaluated at $z(\tau)$ and primed indices to objects evaluated at $z(\tau')$. Introducing Eq. (2.29) in Eq. (2.28) we obtain the celebrated MiSaTaQuWa equations of motion [Mino 1997, Quinn 1997]:

$$a^\mu = -\frac{1}{2}\left(\bar{g}^{\mu\nu} + u^\mu u^\nu\right)\left(2\bar{\nabla}_\beta h_{\nu\alpha}^{tail} - \bar{\nabla}_\nu h_{\alpha\beta}^{tail}\right) u^\alpha u^\beta . \tag{2.31}$$

This equation describes the motion of a gravitational body in a curved space-time, whenever we can ignore its internal structure [Mino 1997]. They also apply for non-rotating small black holes which are of interest for modelling EMRIs (see also [Mino 1997] for a derivation using a small non-rotating BH and the method of matched asymptotic expansions).

Notice that the MiSaTaQuWa equations are not gauge invariant, since the metric perturbations are derived under the Lorenz gauge condition. In particular, we could find a gauge transformation were $a^\mu = 0$ and, consequently, with any self-force [Barack 2001b]. Hence, in the perturbative context, the gravitational self-force can be regarded as a pure gauge entity [Barack 2001a]. Nevertheless, one can in principle construct gauge invariant quantities associated with the motion of the particle [Sago 2008]. Moreover, the gravitational waveforms emitted by the system (which have to be constructed at second order in perturbation theory) are gauge invariant objects.

2.3 MBH Perturbation Theory for EMRIs

Following the gravitational EMRI model introduced in the previous section, we focus on obtaining the equations for the gravitational perturbations generated by a mass particle orbiting around a MBH. The main reason for this exposition is to compare the evolution equations for the gravitational perturbations with the ones for the field generated by a charged scalar particle. This will be done in Section 2.4, where we discuss the similarities between the two models and justify the use of the scalar field-particle system as a test-bed for the techniques to model EMRIs that we develop in this thesis.

For a Schwarzschild BH spacetime, the one that we are going to deal with in this first part of the thesis and which has a geometry given by the line element:

$$ds^2 = f(-dt^2 + dr^{*2}) + r^2 d\Omega^2 \,, \tag{2.32}$$

where:

$$d\Omega^2 = d\theta^2 + \sin^2\theta d\varphi^2 \,, \tag{2.33}$$

and $x^\mu = (t, r, \theta, \varphi)$ are the Schwarzschild coordinates; we can derive a single *master* evolution equation to deal with the odd parity sector of the metric perturbations [Regge 1957] and another one for the even parity one [Zerilli 1970b]. These equations are called master equations because they

decouple from the rest of the metric perturbations, simplifying their computation [Regge 1957, Vishveshwara 1968, Zerilli 1970a, Moncrief 1974].

We start by considering an EMRI system consisting of a particle of mass m moving in a world line of a Schwarzschild spacetime. The metric of the system has two contributions, one from the non-rotating MBH metric $\bar{g}_{\mu\nu}$ and another one from the small linear metric perturbations generated by the particle, $h_{\mu\nu}$:

$$g_{\mu\nu} = \bar{g}_{\mu\nu} + h_{\mu\nu} \, . \tag{2.34}$$

Due to the fact that a Schwarzschild black hole is spherically symmetric, the background manifold is given by the warped product of a two-dimensional Lorenzian manifold, M^2, and the two-sphere, S^2. Defining the coordinate system on M^2 as $x^A = (t, r)$ and that of S^2 as $x^a = (\theta, \phi)$, we can write the 4-dimensional spacetime metric as:

$$\bar{g}_{\mu\nu} = \begin{pmatrix} \bar{g}_{AB} & 0 \\ 0 & r^2 \sigma_{ab} \end{pmatrix} \, , \tag{2.35}$$

where $r = r(x^A)$ is the radial areal coordinate, defined as a function on M^2. In addition, we have (in Schwarzschild coordinates):

$$\bar{g}_{AB} dx^A dx^B = -f dt^2 + f^{-1} dr^2 \, , \tag{2.36}$$

with

$$f = 1 - \frac{2M_\bullet}{r} \, , \tag{2.37}$$

and (in standard spherical coordinates):

$$\sigma_{ab} dx^a dx^b = d\theta^2 + \sin^2\theta d\phi^2 \, . \tag{2.38}$$

Since M^2 and S^2 are different manifolds, we denote the covariant derivative on M^2 with a vertical bar ($g_{AB|C} = 0$) and define the antisymmetric covariant unit tensor is: ε_{AB}. Moreover, the covariant derivative on S^2 are denoted with a colon, then $\sigma_{ab:c} = 0$, and the respective antisymmetric covariant unit tensor as ε_{ab}. The antisymmetric tensors ε_{AB} and ε_{ab}, satisfy the following relations:

$$\varepsilon_{AB|C} = \varepsilon_{ab:c} = 0 \, , \tag{2.39}$$

$$\varepsilon_{AB} \varepsilon^{BC} = -\delta_A^C \, , \tag{2.40}$$

$$\varepsilon_{ab} \varepsilon^{bc} = -\delta_a^c \, . \tag{2.41}$$

Any covariant derivative acting on the 4-dimensional spacetime can be written in terms of the covariant derivatives on M^2 and on S^2, plus terms that contain the warp factor r^2 and its derivatives.

The metric linear perturbations can be decomposed in scalar, vector and tensor spherical harmonics (see, e.g. [Gerlach 1979, Gerlach 1980]):

- The scalar harmonics $Y^{\ell m}$ are eigenfunctions of the Laplace operator on the two sphere (see Appendix A for our conventions on the definition of the $Y^{\ell m}$):

$$\sigma^{ab} Y^{\ell m}_{:ab} = -\ell(\ell+1) Y^{\ell m}. \tag{2.42}$$

- The vector spherical harmonics, which are defined for $\ell \geqslant 1$, are given by:

$$Y^{\ell m}_a \equiv Y^{\ell m}_{:a} \qquad \text{polar parity}, \tag{2.43}$$

$$S^{\ell m}_a \equiv \varepsilon_a{}^b Y^{\ell m}_b \qquad \text{axial parity}, \tag{2.44}$$

where the $Y^{\ell m}_a$ have *polar* or *even* parity, i.e. under a parity transformation, $(\theta, \phi) \to (\pi - \theta, \phi + \pi)$, they transform as: $Y^{\ell m}_a \to (-1)^\ell Y^{\ell m}_a$; whereas $S^{\ell m}_a$ have *axial* or *odd* parity, i.e. they transform as $S^{\ell m}_a \to (-1)^{\ell+1} S^{\ell m}_a$.

- The basis of symmetric 2nd-rank tensor spherical harmonics, which are defined for $\ell \geqslant 2$, are given by (see App. A):

$$Y^{\ell m}_{ab} \equiv Y^{\ell m} \sigma_{ab}, \qquad \text{polar parity}, \tag{2.45}$$

$$Z^{\ell m}_{ab} \equiv Y^{\ell m}_{:ab} + \frac{\ell(\ell+1)}{2} Y^{\ell m} \sigma_{ab} \qquad \text{polar parity}, \tag{2.46}$$

$$S^{\ell m}_{ab} \equiv S^{\ell m}_{a:b} \qquad \text{axial parity}. \tag{2.47}$$

Employing these expressions, the metric perturbations can be split into polar parity perturbations $h^{\ell m, polar}_{\mu\nu}$ and axial parity perturbations $h^{\ell m, axial}_{\mu\nu}$:

$$h_{\mu\nu} = \sum_{\ell, m} h^{\ell m, axial}_{\mu\nu} + h^{\ell m, polar}_{\mu\nu}, \tag{2.48}$$

where:

$$h^{\ell m, axial}_{\mu\nu} = \begin{pmatrix} 0 & q^{\ell m}_A S^{\ell m}_a \\ * & q^{\ell m}_2 S^{\ell m}_{ab} \end{pmatrix}, \tag{2.49}$$

and

$$h_{\mu\nu}^{\ell m,polar} = \begin{pmatrix} h_{AB}^{\ell m} Y^{\ell m} & h_A^{\ell m} Y_a^{\ell m} \\ * & r^2 \left(K^{\ell m} Y^{\ell m} + G^{\ell m} Z_{ab}^{\ell m} \right) \end{pmatrix} . \tag{2.50}$$

Here the asterisk denotes the symmetry of the tensors. Moreover, $K^{\ell m}$ and $S^{\ell m}$ are scalar perturbations, $q_2^{\ell m}$, and $h_A^{\ell m}$ are vector perturbations and $h_{AB}^{\ell m}$ are tensorial ones.

On the other hand, the energy-momentum tensor of a particle [Eq. (2.26)] can be decomposed into spherical harmonics, obtaining that the polar components are described in terms of the following quantities (here, a bar denotes complex conjugation):

$$Q_{\ell m}^{AB} = 8\pi \int_{S^2} d\Omega\, T^{AB} \bar{Y}^{\ell m} , \tag{2.51}$$

$$_y Q_{\ell m} = 8\pi r^2 \int_{S^2} d\Omega\, T^{ab} \bar{Y}_{ab}^{\ell m} , \tag{2.52}$$

$$Q_{\ell m}^A = \frac{16\pi r^2}{\ell(\ell+1)} \int_{S^2} d\Omega\, T^{Aa} \bar{Y}_a^{\ell m} , \tag{2.53}$$

$$_z Q_{\ell m} = 32\pi r^4 \frac{(\ell-2)!}{(\ell+2)!} \int_{S^2} d\Omega\, T^{ab} \bar{Z}_{ab}^{\ell m} . \tag{2.54}$$

In the same way, the axial components are described in terms of the following quantities:

$$P_{\ell m}^A = \frac{16\pi r^2}{\ell(\ell+1)} \int_{S^2} d\Omega\, T^{Aa} \bar{S}_a^{\ell m} , \tag{2.55}$$

$$P_{\ell m} = 16\pi r^4 \frac{(\ell-2)!}{(\ell+2)!} \int_{S^2} d\Omega\, T^{ab} \bar{S}_{ab}^{\ell m} . \tag{2.56}$$

2.3.1 Metric Perturbations in the Regge-Wheeler Gauge

The Regge-Wheeler gauge [Regge 1957] is given by:

$$h_A^{\ell m} = G^{\ell m} = 0 , \qquad q_2^{\ell m} = 0 . \tag{2.57}$$

The axial sector of the perturbed Einstein equations decouples for the master function of Regge and Wheeler [Regge 1957] and also for the one introduced by Cunningham, Price and Moncrief [Cunningham 1978]:

$$\Psi_{\ell m}^{CPM} = \frac{2r}{(\ell+2)(\ell-1)} \varepsilon^{AB} \left(q_{B|A}^{\ell m} - \frac{2}{r^2} r_{|A} q_B^{\ell m} \right) , \tag{2.58}$$

and the polar sector decouples employing the Zerilli-Moncrief master functions [Zerilli 1970a]:

$$\Psi_{\ell m}^{ZM} = \frac{2r}{\ell(\ell+1)} \left[K^{\ell m} + \frac{1}{\Lambda_\ell r^2} \left(h_{AB}^{\ell m} r^{|A} r^{|B} - r^2 r^{|A} K_{|A}^{\ell m} \right) \right] , \qquad (2.59)$$

where $\Lambda_\ell = (\ell+2)(\ell-1)/2 + 3M/r$. The complex functions $\Psi_{\ell m}^{RW}$ and $\Psi_{\ell m}^{ZM}$ satisfy the master wave-like equations:

$$\left[-\partial_t^2 + \partial_{r*}^2 - V_\ell^{CPM/ZM}(r) \right] \Psi_{\ell m}^{CPM/ZM} = f \, S_{\ell m}^{CPM/ZM} , \qquad (2.60)$$

where r^* is the so-called *tortoise* coordinate:

$$r^* = r + 2M_\bullet \ln \left(\frac{r}{2M_\bullet} - 1 \right) . \qquad (2.61)$$

The curvature-induced potential barrier for the axial modes, V_ℓ^{CPM}, is given by:

$$V_\ell^{CPM}(r) = \frac{f}{r^2} \left[\ell(\ell+1) - \frac{6M_\bullet}{r} \right] , \qquad (2.62)$$

whereas for the polar modes, their potential term is given by:

$$V_\ell^{ZM}(r) = \frac{2f}{r^2 \Lambda_\ell^2} \left[\lambda_\ell^2 \left(1 + \lambda_\ell + \frac{3M_\bullet}{r} \right) + 9 \frac{M_\bullet^2}{r^2} \left(\lambda_\ell + \frac{M_\bullet}{r} \right) \right] , \qquad (2.63)$$

where $\lambda_\ell = (\ell+2)(\ell-1)/2$.

On the other hand, the source term for axial modes is given by:

$$S_{\ell m}^{CPM} = \frac{2r}{\ell(\ell+1)} \varepsilon^{AB} P_{A|B}^{\ell m} , \qquad (2.64)$$

and the one for the polar modes is:

$$\begin{aligned} S_{\ell m}^{ZM} = {} & \frac{2}{\Lambda_\ell r} \left(r_{|A} Q_{\ell m}^A - {}_z Q_{\ell m} \right) \\ & - \frac{r^2}{(1+\lambda_\ell)\Lambda_\ell} \left\{ \frac{r^{|C}}{r} \mathrm{g}_{AB} Q_{\ell m|C}^{AB} - \frac{6M}{r^4 \Lambda_\ell} r_{|A} r_{|B} Q_{\ell m}^{AB} \right. \\ & \left. - \frac{f}{r} {}_y Q_{\ell m} - \frac{1}{r\Lambda_\ell} \left[\lambda_\ell(\lambda_\ell - 1) + \frac{3M}{r} (2\lambda_\ell - 3) + 21 \frac{M^2}{r^2} \right] \mathrm{g}_{AB} Q_{\ell m}^{AB} \right\} . \end{aligned} \qquad (2.65)$$

The source terms for both axial and polar modes take the following form when we are dealing with a particle [i.e. when we substitute Eq. (2.26) into Eqs. (2.51)-(2.56), and these ones into Eqs. (2.64) and (2.66)]:

$$S^{\ell m} = G(t,r)\delta[r - r_p(t)] + F(t,r)\delta'[r - r_p(t)] , \qquad (2.66)$$

where δ' is the Dirac delta derivative, and $G(t,r)$ and $F(t,r)$ are known functions that are determined once the orbital motion of the particle is specified (see, e.g. [Martel 2004, Sopuerta 2006b]). Here, the function $r_p(t)$ denotes the radial location of the particle, which is determined by the geodesic equations of the background spacetime.

As we can see from the structure of the source term [Eq. (2.66)], the gravitational perturbations in the Regge-Wheeler gauge involve terms proportional to the Dirac delta and its derivative. Consequently, the solutions to the wave equations are not smooth and turn out discontinuous across the radial location of the particle $r = r_p(t)$. Once we know the value of these discontinuities, we can design a numerical scheme in which the value of this jumps across the particle location could be enforced (see [Sopuerta 2006b]).

2.3.2 Metric Perturbations in the Lorenz Gauge

The metric perturbations generated by the particle can also be described using the Lorenz gauge [see Eq. (2.24)]. For Schwarzschild black holes, this choice preserves the local isotropic nature of the particle singularity (see [Barack 2005]). In this gauge, rather than working with $h_{\mu\nu}$, it is more convenient to work with its trace-reversed form introduced in Eq. (2.23) [Barack 2005]. We can also decompose $\tilde{h}_{\mu\nu}$ into spherical harmonics, so that the axial sector is given by:

$$\tilde{h}_{\mu\nu}^{\ell m,axial} = \begin{pmatrix} 0 & \xi_A^{\ell m} S_a^{\ell m} \\ * & \xi^{\ell m} S_{ab}^{\ell m} \end{pmatrix} , \qquad (2.67)$$

and the polar one is given by:

$$\tilde{h}_{\mu\nu}^{\ell m,polar} = \begin{pmatrix} \phi_{AB}^{\ell m} Y^{\ell m} & \phi_A^{\ell m} Y_a^{\ell m} \\ * & \chi^{\ell m} Y^{\ell m} + \lambda^{\ell m} Z_{ab}^{\ell m} \end{pmatrix} , \qquad (2.68)$$

where $(\tilde{h}_{AB}^{\ell m}, \tilde{h}_A^{\ell m}, \chi^{\ell m}, \lambda^{\ell m})$ and $(\xi_A^{\ell m}, \xi^{\ell m})$ are the unknowns to be determined by solving the resulting perturbative equations. Once they are determined, we can recover the metric perturbations through Eqs. (2.49)-(2.50) [Sopuerta 2006a]:

$$h_{AB}^{\ell m} = \phi_{AB}^{\ell m} - \tfrac{1}{2}(\bar{g}^{CD}\phi_{CD}^{\ell m} + \tfrac{2}{r^2}\chi^{\ell m})\bar{g}_{AB} ,$$

$$h_A^{\ell m} = \phi_A^{\ell m} , \qquad\qquad\qquad q_A^{\ell m} = \xi_A^{\ell m} ,$$

$$K^{\ell m} = -\tfrac{1}{2}g^{AB}\phi_{AB}^{\ell m} , \qquad\qquad G^{\ell m} = \tfrac{\lambda}{r^2} , \qquad\qquad q^{\ell m} = \xi^{\ell m} .$$

For convenience we rescale the axial and polar perturbations. The polar ones are redefined as:

$$\hat{\phi}_t^{\ell m} = \frac{r^2}{f^2}\sqrt{\ell(\ell+1)}\phi_t^{\ell m}, \quad \hat{\phi}_{tt}^{\ell m} = \frac{r^2}{\sqrt{2}f}\phi_{tt}^{\ell m}, \quad \hat{\phi}_{tr}^{\ell m} = r\phi_{tr}^{\ell m}, \quad (2.69)$$

$$\hat{\phi}_r^{\ell m} = r^2\sqrt{\ell(\ell+1)f}\phi_r^{\ell m}, \quad \hat{\phi}_{rr}^{\ell m} = \frac{rf}{\sqrt{2}}\phi_{rr}^{\ell m}, \quad (2.70)$$

$$\hat{\chi}^{\ell m} = \frac{1}{r}\chi^{\ell m} \quad (2.71)$$

$$\hat{\lambda}^{\ell m} = \frac{1}{2r}\sqrt{\frac{(\ell+2)!}{(\ell-2)!}}\lambda^{\ell m}. \quad (2.72)$$

whereas the axial ones are changed as follows:

$$\hat{\xi}_t^{\ell m} = \frac{r^2}{f^2}\sqrt{\ell(\ell+1)}\xi_t^{\ell m}, \quad \hat{\xi}_r^{\ell m} = r^2\sqrt{\ell(\ell+1)f}\xi_r^{\ell m}, \quad (2.73)$$

$$\hat{\xi}^{\ell m} = \frac{1}{2r}\sqrt{\frac{(\ell+2)!}{(\ell-2)!}}\xi^{\ell m}. \quad (2.74)$$

With these definitions, the perturbative field equations [Eqs. (2.25)] can be written in the following form [Sopuerta 2006a]:

$$\Box_*\mathbf{U} + \mathbb{A}\,\partial_t\mathbf{U} + \mathbb{B}\,\partial_{r^*}\mathbf{U} + \mathbb{C}\,\mathbf{U} = \mathbf{F}\delta[r - r_p(t)], \quad (2.75)$$

where:

$$\Box_* = -\partial_t^2 + \partial_{r^*}^2, \quad (2.76)$$

and the vector $\mathbf{U}$ contains the polar and axial perturbative variables:

$$\mathbf{U} \equiv \begin{cases} \mathbf{U}_{polar}^{\ell m} = \left(\hat{\phi}_{tt}^{\ell m}, \hat{\phi}_{tr}^{\ell m}, \hat{\phi}_{rr}^{\ell m}, \hat{\phi}_t^{\ell m}, \hat{\phi}_r^{\ell m}, \hat{\chi}^{\ell m}, \hat{\lambda}^{\ell m}\right) \\ \\ \mathbf{U}_{axial}^{\ell m} = \left(\hat{\xi}_t^{\ell m}, \hat{\xi}_r^{\ell m}, \hat{\xi}^{\ell m}\right) \end{cases}. \quad (2.77)$$

Here, the "coefficients" $\mathbb{A}$, $\mathbb{B}$, and $\mathbb{C}$ are symmetric matrices that depend on (t, r) and the vector $\mathbf{F}$ contains the contributions from the energy-momentum of the particle, i.e. it depends on the trajectory of the particle.

In addition to the field equations [Eq. (2.75)], we have the equations given by the Lorenz gauge conditions, which have been assumed to be fulfilled along this development and represent four more constrains to be satisfied by the fields. Although this is true at the analytic level, in the sense that the Lorenz gauge conditions are preserved by the evolution dictated by the field equations,

at the numerical level, due to the round off errors, these gauge conditions can not be exactly satisfied leading to numerical instabilities. In order to fix this, we can introduce combinations of the Lorenz gauge conditions to keep the evolution stable. In practice this has been shown to work for perturbations in a Schwarzschild spacetime [Barack 2005, Barack 2007b, Barack 2010]. This method was first applied in the context of numerical relativity and using a generalised harmonic gauge (similar to the Lorenz gauge) [Pretorius 2005a, Pretorius 2005b].

Up to now we have seen that the metric perturbations can be computed in the Lorenz gauge and in the Regge-Wheeler gauge. Both formulations have their advantages and disadvantages. For instance, in the Lorenz gauge, the sources do not contain derivatives of the Dirac delta distribution, which improves the accuracy of the field computations, in contrast to the Regge-Wheeler gauge, where we found also the derivative of the Dirac delta distribution. Consequently, the solutions in the Lorenz gauge are C^0, i.e. they are continuous everywhere but not differentiable at the particle location, whereas in the Regge-Wheeler gauge, we expect, in general, discontinuities in the solutions. On the other hand, the integration of the perturbative field equations Eq. (2.66) is much easier in the Regge-Wheeler gauge, where the equations can be decoupled, than in the Lorenz gauge. However, the metric perturbation reconstruction in the Regge-Wheeler gauge is singular when we are dealing with massive particles [Hopper 2010]. Finally, and more important, up to now the regularisation procedures to obtain the self-force have only been obtained in the Lorenz gauge [Barack 2000b, Barack 2001a, Mino 2003b, Barack 2002a, Barack 2002b]. In addition, working in the Lorenz gauge, the field equations can take a fully hyperbolic form, which makes them especially suitable for time-domain integrations.

2.4   The Scalar EMRI Problem

In Section 2.2, we have reviewed three different EMRI physical models, corresponding to a scalar charged particle (Section 2.2.1), a vector charged particle (Section 2.2.2), and a mass particle orbiting a MBH (Section 2.2.3). The orbital motion of the particle in all these cases is governed by the same dynamics, that is, the particle, which is moving in a curved geometry, undergoes a RR deviating it from a geodesic motion and driving the inspiral. What makes these cases different between them is the type of field that generates the self-force.

On the other hand, In Section 2.3, we have presented, for a Schwarzschild

MBH spacetime, the equations for the metric perturbations both in the Regge-Wheeler and in the Lorenz gauge. We have also seen that in both gauges, solving for the metric perturbations implies dealing with wave-like equations. The main difference is that these wave-like equations can be decoupled in the Regge-Wheeler gauge, whereas a scheme for regularising them has only been constructed in the Lorenz gauge. Nevertheless, the type of numerical techniques employed to solve for them is similar for both gauges.

The master equations for the axial perturbations in the Regge-Wheeler gauge can be generalised to the cases of a scalar and vector test fields in Schwarzschild spacetime. For all these cases, the form of the master equation is the same as Eq. (2.60)], but instead of using the potential of Eq. (2.62), we have to use the following generalised potential:

$$V_\ell = \frac{f}{r^2}\left[\ell(\ell+1) + \frac{2M_\bullet(1-s^2)}{r}\right], \qquad (2.78)$$

where s is the spin of the field, that for the gravitational case is $s = 2$, for the electromagnetic (vector) case is $s = 1$, and for the scalar case is $s = 0$.

The main conclusion of this discussion is that any numerical techniques developed for the computation of the self-force for one of the physical models discussed above can be transferred to the other cases. For this reason, and since the *scalar EMRI* model contains all the physical ingredients that characterise the gravitational one, in the first part of this thesis we use the scalar EMRI model. We use it as a proof of principle of the new methods for self-force computations that we are going to present.

Following the discussion of Section 2.2.1, the scalar field equation of a scalar particle orbiting a Schwarzschild MBH is given by [we restrict ourselves to the case where the scalar field is not coupled to the MBH curvature i.e. Eq. 2.1 with $\upsilon = 0$]:

$$\Box\Phi_{ret}(x) = -4\pi q \int_\gamma d\tau\, \delta_4(x, z(\tau))\,. \qquad (2.79)$$

The Schwarzschild metric is given by:

$$ds^2 = f(-dt^2 + dr^{*2}) + r^2 d\Omega^2\,, \qquad (2.80)$$

where $f = f(r)$ is given in Eq. (2.37) and

$$d\Omega^2 = d\theta^2 + \sin^2\theta d\phi^2\,. \qquad (2.81)$$

The coordinates $(x^\mu) = (t, r, \theta, \phi)$ are the so-called Schwarzschild coordinates.

In order to solve the field equations for the scalar field Eq. (2.79), it is convenient to take advantage of the spherical symmetry of the Schwarzschild spacetime and decompose Φ_{ret} into scalar spherical harmonics, $Y^{\ell m}(\theta, \varphi)$ (see App. A),

$$\Phi_{ret}(x) = \sum_{\ell=0}^{\infty} \sum_{m=-\ell}^{\ell} \Phi_{ret}^{\ell m}(t, r) Y^{\ell m}(\theta, \phi), \tag{2.82}$$

where the harmonic numbers (ℓ, m) take the usual values: $\ell = 0, 1, 2, ..., \infty$, and $m = -\ell, -\ell+1, ..., \ell-1, \ell$.

Since geodesic motion takes place on a plane in the Schwarzschild spacetime, we shall assume, without loss of generality, that this plane is given by $\theta = \pi/2$. Moreover, we parameterise the motion of the particle in terms of the coordinate time t, instead of proper time τ. That is, the particle world-line, γ, will be given by $(t, r(t), \pi/2, \varphi(t))$. Taking this into account, we introduce the expansion (2.82) into the scalar field equation (2.79), finding that the equations for the different harmonic coefficients $\Phi_{ret}^{\ell m}$ decouple and have the form of a $1+1$ wave-type equation:

$$\left[-\frac{\partial^2}{\partial t^2} + \frac{\partial^2}{\partial r^{*2}} - V_\ell(r) \right] (r \, \Phi_{ret}^{\ell m}) = S^{\ell m} \delta(r - r(t)), \tag{2.83}$$

which has to be solved for each field mode $\Phi_{ret}^{\ell m}$. This equation has the same structure as the wave-like master equations that appear in the Regge-Wheeler gauge. This equations has different parts, namely: It has a $1+1$ wave operator $-\partial^2/\partial t^2 + \partial^2/\partial r^{*2}$, a singular source term,

$$S^{\ell m} = -\frac{4\pi q f(r)^2}{r u^t} \bar{Y}^{\ell m} (\theta = \pi/2, \phi(t)), \tag{2.84}$$

where a bar denotes complex conjugation. Finally, the potential term V_ℓ is given by:

$$V_\ell = \frac{f}{r^2} \left[\ell(\ell+1) + \frac{2M_\bullet}{r} \right], \tag{2.85}$$

which corresponds to the case $s = 0$ of the generalised potential Eq. (2.78).

On a hypersurface $\{t = t_o\}$, we can prescribe initial data for $\Phi_{ret}^{\ell m}$ $(\Phi_{ret}^{\ell m}(t_o, r), \partial_t \Phi_{ret}^{\ell m}(t_o, r))$, and then find the corresponding solution at later times. Given that Φ_{ret} satisfies a wave-type equation, the problem is well-posed. This solution will be finite and continuous at the particle location but, due to the singular character of the source term, it will not be differentiable in this point, in the sense that the radial derivative from the left and from

the right of the particle yield different values (see Chapter 3). Moreover, the sum of the multipole coefficients over ℓ will diverge there. This can be fixed by regularising the scalar retarded field. In order to do so we use the mode-sum regularisation scheme [Barack 2000b]. We are interested in applying this scheme to the gradient of the scalar field, which is the quantity that we need to compute the self-force.

The multipolar decomposition of the gradient of the retarded field can be written as (for clarity of notation we remove the label ret) :

$$\Phi_\alpha(x^\mu) = \sum_{\ell=0}^{\infty} \nabla_\alpha \sum_{m=-\ell}^{\ell} \Phi^{\ell m}(t,r)\,Y^{\ell m}(\theta,\phi)\,, \qquad (2.86)$$

where we have defined $\Phi_\alpha \equiv \nabla_\alpha \Phi$. The mode-sum scheme is applied to each ℓ harmonic, and for this reason we rewrite this equation as:

$$\Phi_\alpha(x^\mu) = \sum_{\ell=0}^{\infty} \Phi_\alpha^\ell(x^\mu)\,, \qquad (2.87)$$

with

$$\Phi_\alpha^\ell(x^\mu) \equiv \nabla_\alpha \sum_{m=-\ell}^{\ell} \Phi^{\ell m}(t,r)\,Y^{\ell m}(\theta,\phi)\,. \qquad (2.88)$$

Due to the singularity introduced by the source term, one can see that $\Phi_\alpha(x^\mu)$ also diverges at the particle worldline, although the different ℓ-modes Φ_α^ℓ are finite. Then, the gradient of Φ, and hence the self-force, are regularised by subtracting from the full retarded field the singular contribution, $\Phi_\alpha^{\mathcal{S}}$, (see Section 2.2.1), which is known in a neighbourhood of the particle worldline. In particular, the multipoles of the singular part of the gradient of the scalar field, $\Phi_\alpha^{\mathcal{S},\ell}$, at the particle worldline have an analytical expression [Barack 2000b, Barack 2000a, Barack 2001a, Barack 2002a, Barack 2002b, Barack 2003, Mino 2003b]:

$$\lim_{x^\mu \to z^\mu(\tau)} \Phi_\alpha^{\mathcal{S},\ell} = q\left[\left(\ell + \frac{1}{2}\right)A_\alpha + B_\alpha + \frac{C_\alpha}{\ell + \frac{1}{2}} - \frac{2\sqrt{2}D_\alpha}{(2\ell-1)(2\ell+3)} + ...\right]\,, \tag{2.89}$$

where A_α, B_α, C_α, D_α, ... are regularisation parameters, which are independent of ℓ, but depend on the particle dynamics. The singular part of the field corresponds to the first three terms, A_α, B_α, and C_α, which, when we sum over ℓ, lead to to quadratic, linear, and logarithmical divergences respectively.

The sum over the remaining terms form a convergent series that does not contribute to the self-force, in other words, they sum up to zero individually. These remaining terms accelerate the convergence of the series as we increase the number of multipoles included. In our computations we only include the D_α term to produce this effect, as it is the only one quoted in the literature for generic orbits.

The resulting regular field, $\Phi_\alpha^{\mathcal{R}} = \Phi_\alpha - \Phi_\alpha^{\mathcal{S}}$, at the particle location is given by:

$$\Phi_\alpha^{\mathcal{R}}(z^\mu(\tau)) = \lim_{x^\mu \to z^\mu(\tau)} \sum_{\ell=0}^{\infty} \left(\Phi_\alpha^\ell(x^\mu) - \Phi_\alpha^{\mathcal{S},\ell}(x^\mu) \right) , \tag{2.90}$$

from which the self-force is obtained:

$$\mathcal{F}_\alpha = q\, \Phi_\alpha^{\mathcal{R}}(z^\mu(\tau)) , \tag{2.91}$$

and the equation of motion for the particle is given by [Quinn 2000]:

$$u^\alpha \nabla_\alpha(m u^\mu) = \mathcal{F}^\mu = q \nabla^\mu \Phi^{\mathcal{R}} . \tag{2.92}$$

This equation has a non-vanishing component along the 4-velocity $dx^\alpha/d\tau$, which is responsible for the change of the inertial mass of the particle:

$$\frac{dm}{d\tau} = -q\, u_\alpha \nabla^\alpha \Phi^{\mathcal{R}} = -u_\mu \mathcal{F}^\mu . \tag{2.93}$$

As it has been discussed in [Warburton 2010], for radial circular periodic orbits, like the ones that we are going to be interested in this thesis, we do not expect net mass changes over a radial period and then, it can be taken as constant. Therefore we are left with an equation of motion that is orthogonal to the 4-velocity of the particle:

$$m a^\mu = q(\mathrm{g}^{\mu\nu} + u^\mu u^\nu) \nabla_\nu \Phi^{\mathcal{R}} , \tag{2.94}$$

where we recall that the acceleration $a^\mu = u^\nu \nabla_\nu u^\mu$.

Using the fact that τ is proper time along the worldline, i.e. $u^\mu u_\mu = -1$ and then $u^\nu \nabla_\nu(u^\mu u_\mu) = 0$, we can see that multiplying Eq. (2.92) with u_μ:

$$u_\mu \mathcal{F}^\mu = 0 , \tag{2.95}$$

and thus, the four components of the self-force are not fully independent. For instance, restricting ourselves to the particular case of a scalar particle in circular orbits ($\mathcal{F}^r = \mathcal{F}^\theta = 0$), we have:

$$u^t \mathcal{F}_t + u^\phi \mathcal{F}_\phi = 0 , \tag{2.96}$$

This agrees with the fact that, in the circular case, the field Φ^{R} is constant along the orbit and has symmetry that satisfies the *helical condition*:

$$u^t \nabla_t \Phi^{\mathrm{R}} + u^\phi \nabla_\phi \Phi^{\mathrm{R}} = 0 \,, \qquad (2.97)$$

or equivalently:

$$u^\alpha \nabla_\alpha \Phi = 0 \,, \qquad (2.98)$$

The method to compute the self-force developed here has been applied to two different kind of orbits (both bound orbits), namely circular and generic eccentric orbits. Since the scalar field generated by the charged particle depends on the kind of orbit that it performs, the regularisation coefficients appearing in the singular field are different in both cases. In order to compute them, we have employed the derivations for circular and eccentric orbits found in the literature, which are summarised in Appendix B. In particular, for circular orbits, where the non-vanishing regularisation parameters are only the radial ones: A_r, B_r, and D_r, we have employed the coordinate-based expressions derived by Detweiler et al [Detweiler 2003a] and Barack and Ori [Barack 2002b, Barack 2000b]. We have also employed the results of Haas and Poisson [Haas 2006], which are computed employing a tetrad basis (see Appendix B). On the other hand, for generic eccentric orbits, we also employ two different kinds of developments, the one by Haas and Poisson [Haas 2006] (based on a tetrad formalism) and the one developed by Barack and Ori [Barack 2002b] and also Kim [Kim 2004]), who employ a co-ordinate formalism. However, the last derivation, in the case of generic orbits, does not include an expression for the D_α coefficient. In this way, confronting the results obtained with the different expressions for the singular field, we have a way of checking the performance of our method.

2.4.1 Motion of a Scalar Particle in a Schwarzschild Spacetime

The geodesic equations for a particle in Schwarzschild spacetime can be completely separated. Using Schwarzschild coordinates and taking $\theta = \pi/2$ as the orbital plane, they are given by:

$$\frac{dt}{d\tau} = \frac{E}{f}\,, \qquad \frac{d\phi}{d\tau} = \frac{L}{r^2}\,, \qquad \left(\frac{dr}{d\tau}\right)^2 = E^2 - V(L, r)\,, \qquad (2.99)$$

where the constants of motion $E = -u_t$ and $L = u_\phi$ are, respectively, the energy and angular momentum of the particle; the factor f is given in Eq. (2.37);

and the potential term is given by:

$$V(L, r) = f \left(1 + \frac{L^2}{r^2} \right) . \tag{2.100}$$

Since we are interested in bound orbits ($E^2 < 1$), the trajectory will have turning points in the radial motion that can be obtained from the condition $dr/d\tau = 0$ and the last relation of Eq. (2.99). This results in a cubic polynomial equation, $V(L, r) = E^2$, or its equivalent form $(r - r_{peri})(r - r_{apo})(r - r_3) = 0$. The three roots are designated as: $r_3 < r_{peri} < r_{apo}$, where r_{peri} (the pericenter) and r_{apo} (the apocenter) are the turning points between which the movement of the particle takes place, whereas the solution $r = r_3$ corresponds to a plunging geodesic (see, e.g. [Cutler 1994b]).

On the other hand, the orbits of the particle can be characterised either by the constants of motion (E, L) or by the orbital elements (e, p), where p is the semilatus rectum, measuring the size of the orbit, and e is the eccentricity, measuring the degree of non-circularity of the orbit, where $0 \leqslant e < 1$. Both parameters can be defined in the usual way:

$$r_{peri} = \frac{pM_\bullet}{1 + e}, \qquad r_{apo} = \frac{pM_\bullet}{1 - e} . \tag{2.101}$$

From these equations we can obtain an expression for e and p in terms of the turning points:

$$e = \frac{r_{apo} - r_{peri}}{r_{apo} + r_{peri}}, \qquad p = \frac{2r_{apo}r_{peri}}{M_\bullet(r_{apo} + r_{peri})} . \tag{2.102}$$

Moreover, from Eq. (2.99) and the relation obtained for the potential at the turning points $dr/d\tau = 0$, i.e. $V(L, r_{apo}) = V(L, r_{peri}) = E^2$, one can find the energy and angular momentum of the particle, which in terms of the orbital parameters (e, p) are:

$$E^2 = \frac{(p - 2 - 2e)(p - 2 + 2e)}{p(p - 3 - e^2)}, \qquad L^2 = \frac{p^2 M_\bullet^2}{p - 3 - e^2} . \tag{2.103}$$

To compute numerically the motion of the particle, we integrate the geodesic equations [Eq. (2.99)] eliminating τ from the system and choosing instead the coordinate time t as the integration parameter. In this way, we solve the geodesic equations for $r(t)$ and $\phi(t)$. The inconvenience of this procedure is that the variable $r(t)$ is a multivaluated function of the trajectory and, consequently, the radial motion has two branches: (i) The motion from r_{peri} to r_{apo} and (ii) the motion from r_{apo} back to r_{peri}. Then, to avoid the (multi-valuate)

turning points in the integration of the radial coordinate, we introduce the angle variable χ (a monotonically increasing phase), which is related to the radial coordinate of the particle as:

$$r(t) = \frac{pM_\bullet}{1 + e\cos\chi(t)}\,,\tag{2.104}$$

where $\chi(t)$ is single-valued along the orbit. The quantity $\cos\chi(t)$ ranges from -1 to 1 as $r(t)$ goes from r_{peri} to r_{apo}, and ranges from 1 to -1 as $r(t)$ goes from r_{apo} back to r_{peri}.

When the particle undergoes RR and looses energy and angular momentum, the semilatus rectum p of its orbit continually decreases and the particle eventually plunges into the MBH. This occurs when:

$$p < 6 + 2e.\tag{2.105}$$

Then, stable bound orbits in the Schwarzschild spacetime can be represented by those points in the $p - e$ plane which satisfy $0 \leqslant e < 1$, $p \geqslant 6 + 2e$. The boundary,

$$p = 6 + 2e\,,\tag{2.106}$$

is called the *separatrix* and the points along it represent marginally unstable orbits.

On the other hand, the geodesic equations (2.99) can be expressed in terms of the variables $\chi(t)$ and $\phi(t)$ by employing the relations Eq. (2.103) together with Eq. (2.104):

$$\frac{d\chi}{dt} = \frac{(p - 2 - 2e\cos\chi)\sqrt{p - 6 - 2e\cos\chi}(1 + e\cos\chi)^2}{M_\bullet p^2\sqrt{(p-2)^2 - 4e^2}}\,,\tag{2.107}$$

$$\frac{d\phi}{dt} = \frac{(p - 2 - 2e\cos\chi)(1 + e\cos\chi)^2}{M_\bullet p^{3/2}\sqrt{(p-2)^2 - 4e^2}}\,.\tag{2.108}$$

These are the relations that we employ to evolve the particle motion in our computations. On the other hand, they can be alternatively formulated in terms of the χ derivatives:

$$\frac{dt}{d\chi} = \frac{M_\bullet p}{p - 2 - 2e\cos\chi}\sqrt{\frac{(p - 2 - 2e)(p - 2 + 2e)}{(1 + e\cos\chi)(p - 6 - 2e\cos\chi)}}\,,\tag{2.109}$$

$$\frac{d\phi}{d\chi} = \sqrt{\frac{p}{p - 6 - 2e\cos\chi}}\,.\tag{2.110}$$

Finally, the radial proper velocity of the particle u^r is given by:

$$u^r = \frac{dr}{d\tau} = eE\sin\chi\sqrt{\frac{p - 6 - 2e\cos\chi}{(p - 2 - 2e)(p - 2 + 2e)}} \,. \tag{2.111}$$

These equations determine the motion of the particle in a generic eccentric orbit around a Schwarzschild BH.

The Particle-without-Particle Scheme

Methods and means cannot be separated from the ultimate aim
Emma Goldman.

3.1 Introduction

The regularisation scheme needed to compute the self-force tells us how to subtract, mode by mode the singular part of the perturbations that do not contribute to the self-force. Then, to obtain the self-force through this method, one needs to compute the full retarded solution of the perturbative equations. To solve them we need to resort to numerical methods. In this regard frequency methods were the only method of choice in the past [Davis 1972, Detweiler 1978, Detweiler 1979, Cutler 1994b, Poisson 1995, Poisson 1997], and it was found that they provide accurate results for EMRIs with moderate eccentricities. However, the frequency-domain approach presents several disadvantages. In particular, one has to sum over a large number of modes to obtain a good accuracy for highly eccentric orbits, which are of interest for LISA. Recently, Warburton and Barack [Warburton 2010] presented work where they compute the scalar self-force acting on a particle performing eccentric (up to $e \sim 0.7$) equatorial orbits around a Kerr BH. In addition, frequency-domain techniques can not be incorporated easily in a scheme that evolves the orbit self-consistently under the self-force effect (see e.g., [Dolan 2011]).

On the other hand, time-domain methods are typically more flexible and are not much affected by the eccentricity of the orbit, being more efficient for the case of high-eccentricity EMRIs. Moreover, they can, in principle, be easily adapted to incorporate the self-force in a self-consistent way. In the last years, there has been an intense activity on this front,

both for a nonrotating BH [Martel 2004, Barack 2005, Sopuerta 2006b, Haas 2006, Haas 2007, Vega 2008, Barack 2007b], and for a rotating (Kerr) BH [Burko 2007, Sundararajan 2007, Sundararajan 2008a].

The main drawbacks of time-domain methods have two origins and both translate into high-computational cost: (i) The fact that one has to resolve very different physical scales (both spatial and temporal) present in the problem due to the extreme mass ratios involved (see, e.g. [Sopuerta 2006c]). That is, using a standard numerical discretisation of the problem we are led to resolve the typical gravitational wavelengths (comparable or bigger than the size of the MBH) and, at the same time, scales in the vicinity of the SCO, which are crucial for evaluating the self-force. (ii) The fact that the SCO is described as a point-like object. This introduces Dirac delta distributions in the SCO energy-momentum expression that lead to loss of differentiability in the solution of the perturbative field equations. This fact can degrade the convergence properties of the numerical algorithms used. Moreover, such a localised distribution of matter can also introduce spurious high-frequency modes that contaminate the numerical solution and, in consequence, degrade its accuracy (see for instance [Jaramillo 2011]).

There have been different proposals to improve the performance of time domain methods. Barack and Goldbourn [Barack 2007a] have introduced a new technique to compute the scalar field generated by a point-like scalar charge orbiting a Kerr BH. This technique consists in subtracting from each azimuthal mode (in the Kerr geometry the field equations are not fully separable in the time domain and one has to tackle them in $2 + 1$ dimensions) of the retarded field a piece that describes the singular behaviour near the particle. This is done through a careful analytical study of the scalar field near the particle, using a *puncture* scheme which resembles the puncture model used for simulations in numerical relativity [Brandt 1997, Campanelli 2006, Baker 2006]. On the other hand, Vega and Detweiler [Vega 2008] have introduced another new method for regularising the solution of the field equations. Their approach has been tested with a simplified model of a charged particle orbiting a nonrotating BH, where the retarded field is regularised by identifying and removing first, in an analytical way, its singular part. This alternative approach to the mode-sum regularisation scheme yields a finite and differentiable remainder from which the self-force can be computed. This remainder is the solution to a field equation with a nonsingular source, which avoids the problem (ii) above. More recently, this approach has been applied to $3 + 1$ evolutions of a scalar charged particle [Vega 2009]. Finally, Lousto and Nakano [Lousto 2008] have also introduced an analytical technique to remove the particle's singular behaviour. Their method is global and also produces a well behaved source

for the field equations.

Whereas these new techniques help in dealing with problem (ii) above, they do not completely solve the problem (i) since the regular source terms that these new schemes produce still have associated with them a length scale. From the numerical point of view, this length scale implies special spatial resolution requirements in order to describe accurately the SCO. Recently, Dolan et al. [Dolan 2011] developed a scheme based on the puncture method and Finite Difference (FD) discretization of the field equations, to compute the self-force generated by a scalar particle in circular equatorial orbits in the Kerr geometry. Their method alleviates the problem (ii), since they only have to deal with small inaccuracies in the numerical evaluation of an effective source near the particle location.

In this thesis, we introduce the PwP scheme to compute the self-force. We test this method with the computation of the scalar self-force in a nonrotating BH geometry. Our method eliminates completely any length scale associated with the SCO. This is done by using multiple subdomains and replacing the particle by boundary conditions at the interface between two of them. In this way, the Dirac delta distributions do not appear in our equations and, as a consequence, we are solving wave-type equations with smooth solutions, avoiding the problems described in (ii). Moreover, we employ a *PseudoSpectral Collocation* (PSC) method to discretise our spatial computational domain (which will be introduced in Section 3.6). Regarding (i), we just need to provide the numerical resolution to describe the field near the particle, but not the particle itself, which makes the computation much more efficient.

In this chapter we are going to introduce the ingredients of the PwP method. To begin with, we shall introduce their mathematical foundations and, subsequently, we shall discuss the particular formulation employed to discretise the dynamical equations that govern our EMRI system and its numerical implementation. As we have discussed in the last Chapter (see Section 2.4), this simplified model contains all the ingredients of a generic EMRI and, consequently, the transition from this case to the gravitational one is a pure computational task, since all the ingredients of our method can be transferred directly.

3.2 Foundations of the PwP Method

The singular structure of the source term in Eq. (3.2) implies the existence of discontinuities at the particle location. Outside this point, the solution is smooth provided we prescribe smooth initial data.

The one-dimensional spatial domain corresponding to the radial direction (either parameterised by r or r^*) where the particle is moving can be divided into two different and disjoint regions or subdomains. The subdomain to the left of the particle location $r^* = r_p^*(t)$[1], that is $r^* < r_p^*$, and the subdomain to the right of the particle $r^* > r_p^*$. The boundaries at the interface or junction between the two subdomains are identified. Then, our spatial domain can be expressed as:

$$r^* \in (-\infty, \infty) = (-\infty, r_p^*) \cup (r_p^*, +\infty) \,. \tag{3.1}$$

Inside each subdomain, we evolve the associated $1+1$ homogeneous wave-like equations of Eq. (3.123):

$$\left[-\partial_t^2 + \partial_{r^*}^2 - V_\ell(r) \right] (r \, \Phi^{\ell m}) = 0 \,, \tag{3.2}$$

In this way, all the computational issues associated with the presence of a distributional source term $S^{\ell m}$ [Eq. (2.84)] are avoided. Then, the problem is reduced to finding the junction conditions for the field and its derivatives across the particle location, i.e. across the interface.
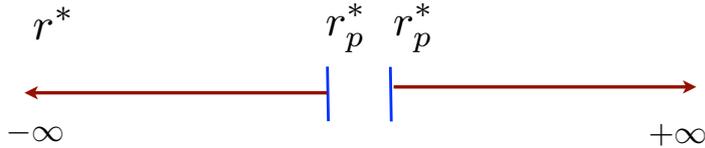
Figure 3.1: *Structure of the one-dimensional spatial domain, which has been divided into two subdomains: one to the right, $(r_p^*, +\infty)$, and the other one to the left, $(-\infty, r_p^*)$, of the particle radial location.*

It is well-known (see, e.g. [Courant 1953a]) that discontinuities in hyperbolic equations (like wave equations) can only appear and propagate along characteristics. In this regard, to find and analyse the junction conditions across the

---

[1]For simplicity, in the following discussion, we omit the time dependence of the radial motion and write simply r_p^*

characteristics, it is convenient to adopt a first-order formulation of Eq. (3.2). The hyperbolic reduction of the scalar field equation can be done by introducing the following set of variables:

$$\psi^{\ell m} \;=\; r\,\Phi^{\ell m}\,, \tag{3.3}$$

$$\phi^{\ell m} \;=\; \partial_t \psi^{\ell m}\,, \tag{3.4}$$

$$\varphi^{\ell m} \;=\; \partial_{r^*} \psi^{\ell m}\,, \tag{3.5}$$

which are adapted to the hyperbolic character of the underlying equation, as we are going to see later. Arranging these field variables in a vector:

$$\boldsymbol{U} = (\psi^{\ell m}, \phi^{\ell m}, \varphi^{\ell m}) = (r\,\Phi^{\ell m}\,, \partial_t \psi^{\ell m}\,, \partial_{r^*}\psi^{\ell m})\,, \tag{3.6}$$

the evolution equations for a given harmonic (ℓ, m) are a system of PDEs, which in matrix form are:

$$\partial_t \boldsymbol{U} = \mathbb{A} \cdot \partial_{r^*}\boldsymbol{U} + \mathbb{B} \cdot \boldsymbol{U} + \boldsymbol{S}\,. \tag{3.7}$$

The matrices $\mathbb{A}$ and $\mathbb{B}$ are given by:

$$\mathbb{A} = \begin{pmatrix} 0 & 0 & 0 \\ 0 & 0 & 1 \\ 0 & 1 & 0 \end{pmatrix}\,, \quad \mathbb{B} = \begin{pmatrix} 0 & 1 & 0 \\ -V_\ell & 0 & 0 \\ 0 & 0 & 0 \end{pmatrix}\,. \tag{3.8}$$

where the vector $\boldsymbol{S}$ contains the distributional source term:

$$\boldsymbol{S} = \left(0, -\frac{S^{\ell m}}{f_p}\delta(r^* - r_p^*), 0\right)\,, \tag{3.9}$$

and $f_p = f(r_p)$ [Eq. (2.37)] and we recall that $r_p^* = r^*(t)$. Then, one can show that Eq. (3.7) constitutes a first-order symmetric hyperbolic system. This essentially means that it has a complete set of characteristics and characteristic fields and that the matrix that describes the principal part of the system, matrix $\mathbb{A}$, is symmetric or can be symmetrised (see for instance [Courant 1953b]).

In order to find the evolution equations at each side of the particle location and the junction conditions of the field variables at the boundaries between subdomains, we divide the global solution of Eq. (3.7) following the division of the spatial domain, that is, we split the solution into two contributions, one to the left and one to the right of the particle. In mathematical terms this can be expressed as follows:

$$\mathbf{U}(t, r^*) = \mathbf{U}_-(t, r^*)\Theta_- + \mathbf{U}_+(t, r^*)\Theta_+\,, \tag{3.10}$$

where $\Theta_- = \Theta(r_p^* - r^*)$ and $\Theta_+ = \Theta(r^* - r_p^*)$, and Θ is the Heaviside step function. Then $\mathbf{U}$ is restricted in the subdomanin to the left of the particle

to the smooth function $\boldsymbol{U}_-$, and in the subdomain to the right to the smooth function $\boldsymbol{U}_+$.

In order to introduce the global solution (3.38) into the global equation (3.7) we need to make use of the following properties of the Heaviside step function and its derivatives:

$$
\begin{aligned}
\partial_{r^*}\Theta_+ &= \partial_{r^*}\Theta(r^* - r_p^*) = \delta(r^* - r_p^*) & (3.11) \\
\partial_{r^*}\Theta_- &= \partial_{r^*}\Theta(r_p^* - r^*) = -\delta(r^* - r_p^*) \,, \\
\partial_t\Theta_+ &= \partial_t\Theta(r^* - r_p^*) = -\dot{r}_p^* \delta(r^* - r_p^*) \,, \\
\partial_t\Theta_- &= \partial_t\Theta(r_p^* - r^*) = \dot{r}_p^* \delta(r^* - r_p^*) \,.
\end{aligned}
$$

Moreover, we denote the jumps of the field variables at the particle location using the following definition:

$$
[\lambda]_p = \lim_{r^* \to r_p^*} \lambda_+(t, r^*) - \lim_{r^* \to r_p^*} \lambda_-(t, r^*) \,. \tag{3.12}
$$

where λ is any field variable. With the help of these expressions, we can now analyse the consequences of the global equation (3.7). For each variable we obtain homogeneous evolution equations valid at each side of the particle and the corresponding jump conditions (to simplify the notation we have dropped the harmonic indexes ℓ and m):

- For the retarded field variable ψ:

$$
\begin{aligned}
\{\partial_t\psi_\pm - \phi_\pm\}\Theta_\pm &= 0 \,, & (3.13) \\
\dot{r}_p^*[\psi]_p \delta(r^* - r_p^*) &= 0 \,. & (3.14)
\end{aligned}
$$

Then, the condition to be imposed at the interface between the subdomains is that the field variable ψ must be continuous across the particle location, i.e.:

$$
[\psi]_p = 0 \,. \tag{3.15}
$$

- For the retarded field variable ϕ we get the following set of equations:

$$
\begin{aligned}
\{\partial_t\phi_\pm - \partial_{r^*}\varphi_\pm - V\psi_\pm\}\Theta_\pm &= 0 \,, & (3.16) \\
\left\{[\phi]_p \dot{r}_p^* + [\varphi]_p - S\right\}\delta(r^* - r_p^*) &= 0 \,. & (3.17)
\end{aligned}
$$

Then, at the particle location the jump on ϕ is given by:

$$
[\phi]_p = \frac{S - [\varphi]_p}{\dot{r}_p^*} = -\frac{\dot{r}_p^* S}{(1 - \dot{r}_p^{*2})f_p} \,, \tag{3.18}
$$

Thus, ϕ has a discontinuity at the particle location that depends on the velocity of the particle. The condition to be imposed is, thus, given by this jump.

- Finally, for the field variable φ we obtain the following set of equations:

$$\{\partial_t \varphi_\pm - \partial_{r^*} \phi_\pm\} \Theta_\pm \;=\; 0 \,, \tag{3.19}$$

$$\left\{[\varphi]_p \dot{r}_p^* + [\phi]_p\right\} \delta(r^* - r_p^*) \;=\; 0 \,. \tag{3.20}$$

Consequently, the field variable φ has a jump at the particle location, which is given by:

$$[\varphi]_p = -\frac{[\phi]_p}{\dot{r}_p^*} \quad \Longrightarrow \quad [\varphi]_p = \frac{S}{(1 - \dot{r}_p^{*2})f_p} \tag{3.21}$$

Then, φ is also discontinuous at the particle location and dependent on the velocity of the particle. This is the jump condition to be imposed for this variable at the boundaries between subdomains.

From these relations, the jumps on the radial and time derivatives of the retarded field satisfy the following advection-like equation:

$$\left[\phi - \dot{r}_p^* \varphi\right]_p = 0 \,. \tag{3.22}$$

In summary, the homogeneous equations Eq. (3.14), Eq. (3.17), and Eq. (3.20) determine the evolution of the field variables at the two sides of the particle, which can be written in the following compact form:

$$\partial_t \boldsymbol{U}_\pm = \mathbb{A} \cdot \partial_{r^*} \boldsymbol{U}_\pm + \mathbb{B} \cdot \boldsymbol{U}_\pm \,. \tag{3.23}$$

In addition, the set of equations Eq. (3.15), Eq. (3.18), and Eq. (3.21) give the values of the jump of the field variables at the particle location, and hence the boundary conditions that we need to prescribe during the evolution.

3.3 Hyperbolic Structure and Characteristic Fields

As we have mentioned in the last section, the discontinuities in hyperbolic PDEs evolve along the characteristics curves. Then, the jump conditions, Eq. (3.15), Eq. (3.18), and Eq. (3.21) have to be imposed on the characteristic curves of our scalar EMRI problem. In this sense, one can also employ the associated characteristic fields instead of the field variables to find the jumps.

The field equations [Eq. (3.23)] have principal part given by:

$$\boldsymbol{\Pi}\,\boldsymbol{U} \equiv (\partial_t - \mathbb{A} \cdot \partial_{r^*})\boldsymbol{U}(t, r^*) \,, \tag{3.24}$$

where for each field component takes the form:

$$\mathbf{\Pi}\,\boldsymbol{U} = \left(\partial_t \psi, \partial_t \phi - \partial_{r^*}\varphi, \partial_t \varphi - \partial_{r^*}\phi\right). \tag{3.25}$$

The hyperbolic structure of our problem can be analysed in an algebraic way (see [Courant 1953b] for details). To that end we introduce the $1+1$ vector, $\boldsymbol{\kappa} = (\kappa_t, \kappa_{r^*})$, that is orthogonal to the characteristic lines along which the characteristic fields propagate. Then, in order to find the characteristic lines, we perform the substitution $(\partial/\partial_t, \partial/\partial_{r^*}) \to (\kappa_t, \kappa_{r^*})$ in the equations $\mathbf{\Pi}\,\boldsymbol{U} = 0$. The result can be written as:

$$\kappa_t \psi^{\ell m} = 0 , \tag{3.26}$$
$$\kappa_t \phi^{\ell m} - \kappa_{r^*}\varphi^{\ell m} = 0 , \tag{3.27}$$
$$\kappa_t \varphi^{\ell m} - \kappa_{r^*}\phi^{\ell m} = 0 . \tag{3.28}$$

In order to solve for this system we have to consider the following two different cases (see Figure 3.2 for a graphical representation of the characteristic lines and fields of our system of equations):

- [i] $\kappa_t = 0$: In this case $\boldsymbol{\kappa} = (0, \kappa_{r^*})$, which means that the characteristic lines are the lines tangent the vector $\partial/\partial t$ and the characteristic field is $\boldsymbol{U} = (\psi^{\ell m}, 0, 0)$. In other words, the characteristic surfaces (orthogonal to the characteristic lines) are the $t = const.$ surfaces whose normal vector is:

$$\mathbf{n} = \left(0, 1\right). \tag{3.29}$$

- [ii] Case $\psi^{\ell m} = 0$: The characteristic surfaces are found by solving the following determinant (to avoid the trivial solution $\phi^{\ell m} = \varphi^{\ell m} = 0$):

$$\begin{vmatrix} \kappa_t & -\kappa_{r^*} \\ -\kappa_{r^*} & \kappa_t \end{vmatrix} = 0 , \tag{3.30}$$

which leads to null characteristic surfaces:

$$\kappa_t = \pm\kappa_{r^*} , \tag{3.31}$$

whose normal vectors are given by:

$$\mathbf{n} = \left(\pm 1, 1\right) , \tag{3.32}$$

Using Eqs. (3.26)-(3.28) and Eq. (3.31), we obtain the associated characteristics fields:

$$
\begin{aligned}
V^{\ell m} &= \phi^{\ell m} + \varphi^{\ell m} \,, \\
U^{\ell m} &= \phi^{\ell m} - \varphi^{\ell m} \,.
\end{aligned}
\tag{3.33}
$$

Then, it follows that the characteristic surfaces for the characteristic field $U^{\ell m}$ correspond to $t - r^* = \text{const.}$, and those for $V^{\ell m}$ corresponds to $t + r^* = \text{const.}$
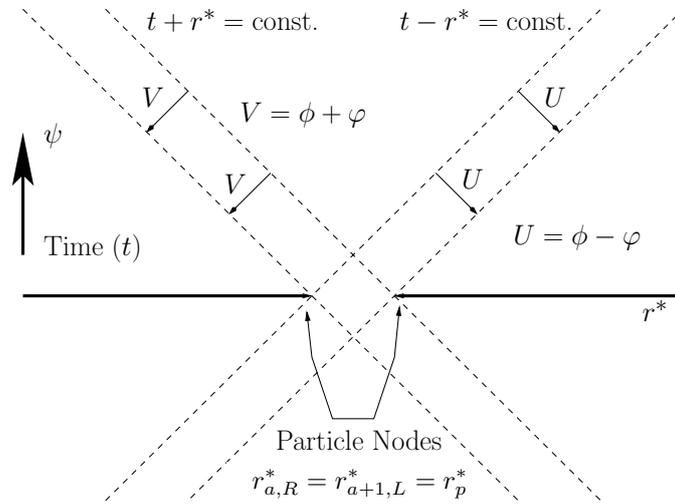
Figure 3.2: *Characteristic structure of the field equations. The picture shows the characteristic surfaces ($t \pm r^* = \text{const.}$) of the hyperbolic system of PDEs in Eq. (3.7), the characteristic fields ($\psi^{\ell m}$, $U^{\ell m} = \phi^{\ell m} - \varphi^{\ell m}$, and $V^{\ell m} = \phi^{\ell m} + \varphi^{\ell m}$), and their propagation directions (characteristic lines).*

At this point, we present an alternative description of our problem, which is based on the characteristic fields we have just derived. That is, instead of working with the vector of field variables in Eq. (3.6), we employ the characteristic field variables:

$$
\boldsymbol{N} = (\psi^{\ell m}, U^{\ell m}, V^{\ell m}) \,.
\tag{3.34}
$$

Thus, the global system of evolution equations for a given harmonic (ℓ, m) is a system of PDEs that takes the following matrix form:

$$
\partial_t \boldsymbol{N} = \mathbb{C} \cdot \partial_{r^*} \boldsymbol{N} + \mathbb{D} \cdot \boldsymbol{N} + \boldsymbol{S} \,.,
\tag{3.35}
$$

where the matrices $\mathbb{C}$ and $\mathbb{D}$ are

$$\mathbb{C} = \begin{pmatrix} 0 & 0 & 0 \\ 0 & -1 & 0 \\ 0 & 0 & 1 \end{pmatrix} , \quad \mathbb{D} = \begin{pmatrix} 0 & 1/2 & 1/2 \\ -V_\ell & 0 & 0 \\ -V_\ell & 0 & 0 \end{pmatrix} , \tag{3.36}$$

and the distributional source term is contained in the source vector:

$$\boldsymbol{S} = \left(0, -\frac{S^{\ell m}}{f_p} \delta(r^* - r_p^*), 0 \right) . \tag{3.37}$$

As we can see, Eq. (3.35) constitutes a first-order symmetric hyperbolic system.

As we did before, we can find the evolution equations for the characteristic fields at each of the two subdomains around the particle location and also the junction conditions at the interface between them. To that end, we also split the global solution $\boldsymbol{N}$ [Eq. (3.34)] into two contributions, one to the left and one to the right of the particle location:

$$\boldsymbol{N}(t, r^*) = \boldsymbol{N}_-(t, r^*)\Theta_- + \boldsymbol{N}_+(t, r^*)\Theta_+ , \tag{3.38}$$

Then, by introducing this expression into Eq. (3.35) and employing Eqs. (3.11) and Eq. (3.12), one obtains the following set of homogeneous equations for the characteristic field variables:

$$\partial_t \boldsymbol{N}_\pm = \mathbb{C} \cdot \partial_{r^*} \boldsymbol{N}_\pm + \mathbb{D} \cdot \boldsymbol{N}_\pm , \tag{3.39}$$

together with the corresponding jumps at the particle location:

$$\left[\psi^{\ell m} \right]_p = 0 , \tag{3.40}$$

$$\left[U^{\ell m} \right]_p = -\frac{S^{\ell m}}{(1 - \dot{r}_p^*)f_p} , \tag{3.41}$$

$$\left[V^{\ell m} \right]_p = \frac{S^{\ell m}}{(1 + \dot{r}_p^*)f_p} . \tag{3.42}$$

Notice that we could also have obtained these expressions for the jumps on the characteristic fields from Eq. (3.33) and Eqs. (3.15)- (3.21).

Putting things together, the formulation of the PwP scheme could be summarised in the following way: By splitting the physical domain from the particle location, as in Eq. (3.1), we introduce, in a natural way, the splitting in the dynamical variables $\boldsymbol{U}$ [Eq. (3.38)], and the equivalent one for the characteristic variables $\boldsymbol{N}$ [Eq. (3.34)]. By doing so, we restrict the global variables to the subdomains to the left of the particle, $(-\infty, r_p^*)$, and to the right of the

particle, $(r_p^*, +\infty)$, $\boldsymbol{U}_+$ $(\boldsymbol{N}_+)$ and $\boldsymbol{U}_-$ $(\boldsymbol{N}_-)$ respectively. These fields satisfy homogeneous hyperbolic equations given by Eq. (3.23) (or Eq. (3.43) for the field variables) inside each subdomain since we have got rid of the distributional source term appearing in Eq. (3.7). Finally, to introduce the presence of the particle in our computations, we use the boundary conditions given by Eq. (3.15), Eq. (3.18) and Eq. (3.21), or Eq. (3.15), Eq. (3.41) and Eq. (3.42) for the characteristic variables.

3.4   Enforcing the Junction Conditions

As we have just seen, the homogeneous field equations obtained for each subdomain are communicated employing jump conditions. However, we have not mentioned yet how these conditions are introduced in our system of equations and how are they going to be enforced. In what follows, we are going to describe the two methods that we employ to enforce the analytic jumps on the variables, namely the *penalty method* (see, e.g. [Hesthaven 2000a]) and the *direct communication of the characteristic fields*.

3.4.1   The Penalty Method

The penalty method is a well-known technique and has been applied to several numerical schemes to solve PDEs. The basic idea behind it is to modify the field equations by adding extra terms that are proportional to the conditions that we want to enforce, let us call them $\boldsymbol{P}$:

$$\partial_t \boldsymbol{N}_\pm = \mathbb{C} \cdot \partial_{r^*} \boldsymbol{N}_\pm + \mathbb{D} \cdot \boldsymbol{N}_\pm + \tau_{\boldsymbol{N}}^\pm \cdot \boldsymbol{P}\,, \qquad (3.43)$$

where $\tau_{\boldsymbol{N}}^\pm$ are the *penalty* coefficients and, as before, the plus and minus indexes are employed to differentiate the penalty terms employed with the equations at the left of the particle from the ones employed with the equations at the right of the particle. The same can be done for the evolution equations in terms of the field variables $\boldsymbol{U}$ [Eq. (3.38)]. By choosing these extra terms $\tau_{\boldsymbol{N}}^\pm \cdot \boldsymbol{P}$ in a convenient way that will be made precise later, we can dynamically drive the system to a state in which the junction conditions are satisfied (see [Hesthaven 2000b] and references therein). In our case, the quantities $\boldsymbol{P}$ are proportional to the junction conditions, i.e. the jumps, on the field variables given by Eqs. (3.15)-(3.21) for the field variables $\boldsymbol{U}$, or by Eqs. (3.15)-(3.42) for the characteristic variables $\boldsymbol{N}$. Then, the penalty terms guide dynamically the system to satisfy a set of conditions that are not

part of the original system of evolution equations (like in the case in which we have constraints or boundary conditions on the variables that have to be satisfied for all times). The strength of the driving terms is controlled by the penalty coefficients $\tau_N^{\pm}$, which determine the weight of the penalty terms in the evolution equations.

Since the characteristic field $U^{\ell m}$ propagates from left to right along $t + r^* = const.$ (that is across $t - r^* = const.$), we need to introduce a penalty enforcing the jump of $U^{\ell m}$ from the subdomain at the right to the one at the left of the particle. Then, the evolution equations at the boundary belonging to the subdomain to the left of the particle $(-\infty, r_p^*)$ (see Figure 3.2) can be driven in the following way (to simplify the notation we have dropped the harmonic indexes ℓ and m):

$$\partial_t \psi_+ = \frac{1}{2} \left[\left(1 + \dot{r}_p^*\right) V_+ + \left(1 - \dot{r}_p^*\right) U_+ \right] - \tau_\psi^+ [\psi]_p , \qquad (3.44)$$

$$\partial_t V_+ = \left(1 + \dot{r}_p^*\right) \partial_{r^*} V_+ - V(r) \psi_+ , \qquad (3.45)$$

$$\partial_t U_+ = -\left(1 - \dot{r}_p^*\right) \partial_{r^*} U_+ - V(r) \psi_+ - \tau_U^+ \left(U_+ - U_+ - [U]_p\right) \qquad (3.46)$$

The same reasoning can be applied to the characteristic variable V, which propagates from right to left along $t - r^* = const.$ (across $t + r^* = const.$). In this case, we only need a penalty term enforcing the jump of V from the subdomain to the left of the particle to the one to the right of the particle (see Figure 3.2). Then, the evolution equations at the boundary belonging to the subdomain to the right of the particle $(r_p^*, +\infty)$ are:

$$\partial_t \psi_- = \frac{1}{2} \left[\left(1 + \dot{r}_p^*\right) V_- + \left(1 - \dot{r}_p^*\right) U_- \right] - \tau_\psi^- [\psi]_p , \qquad (3.47)$$

$$\partial_t V_- = \left(1 + \dot{r}_p^*\right) \partial_{r^*} (V^a)_N - V(r) \psi_- - \tau_V^- \left(V_- - V_+ + [V]_p\right) \qquad (3.48)$$

$$\partial_t U_- = -\left(1 - \dot{r}_p^*\right) \partial_{r^*} (U^a)_N - V(r) \psi_- , \qquad (3.49)$$

In practice, the jump conditions inside the penalty terms are evaluated as the difference between the analytic expressions of the jumps (Eqs. (3.40)-(3.42)) and the numerical jumps (computed as the difference between the numerical values of the fields from the right to the left of the particle, e.g. $V_+ - V_-$. In this way, these terms, and their error, depend on the accuracy with which we can numerically compute the field variables, since the more accurate are the solutions of the fields, the closer to zero these terms are.

3.4.2 Direct Communication of the Characteristic Fields

An alternative to the penalty method is to use the direct communication of the characteristic fields, a method that takes advantage of the symmetric hyper-

bolic structure of our system of PDEs. It consists in passing the characteristic fields through their corresponding characteristics curves. This process is illustrated in Figure 3.2. In the case that the interface does not contain the particle, at the right boundary of the left subdomain we only need to evolve Eq. (3.43) for $(\psi_-^{\ell m}, U_-^{\ell m})$ while $V_-^{\ell m}$ is obtained by just copying the value of $V_+^{\ell m}$ from the other subdomain. Moreover, at the left boundary of the right subdomain we only need to evolve Eq. (3.43) for $(\psi_+^{\ell m}, V_+^{\ell m})$ while $U_+^{\ell m}$ is obtained by copying the value of $U_-^{\ell m}$ from the other subdomain. However, when the particle is found at the interface, we cannot just copy the values of the characteristic fields, instead we have pass them in a way that enforces the junction conditions of Eq. (3.41) and Eq. (3.42). That is, we communicate the $V^{\ell m}$ field by doing:

$$V_-^{\ell m} = V_+^{\ell m} - \left[V^{\ell m} \right]_p ,\tag{3.50}$$

and the $U^{\ell m}$ field by doing:

$$U_+^{\ell m} = U_-^{\ell m} + \left[U^{\ell m} \right]_p .\tag{3.51}$$

In practice, the numerical implementation of the direct communication of the characteristic fields, $\boldsymbol{N}$, can be performed in two different ways. One that implements directly Eq. (3.50) and Eq. (3.51), and the other one is using the method of lines, which incorporates the boundary matching conditions into the evaluation of the RHS. Hence, for this second method we need the derivatives of Eq. (3.50) and Eq. (3.51):

$$\frac{dV_-^{\ell m}}{dt} = \frac{dV_+^{\ell m}}{dt} - \frac{d\left[V^{\ell m} \right]_p}{dt} ,\tag{3.52}$$

$$\frac{dU_+^{\ell m}}{dt} = \frac{dU_-^{\ell m}}{dt} + \frac{d\left[U^{\ell m} \right]_p}{dt} ,\tag{3.53}$$

3.5   Initial and Boundary Conditions

In order to evolve the ODEs of the system Eq. (3.7), we prescribe *zero initial data*, that is (the following argument is formally equivalent for the field variables $\boldsymbol{U}$):

$$\psi^{\ell m}(t_o, r^*) = V^{\ell m}(t_o, r^*) = U^{\ell m}(t_o, r^*) = 0 ,\tag{3.54}$$

These initial conditions can be employed whenever we communicate the solutions employing jumps. However, they are not valid with the method of

lines exposed above. This is due to the fact that the method of lines evolve the time derivatives of the jumps given in Eq. (3.52) and Eq. (3.53) and it is necessary to provide initial values for them that are consistent with the values of the jumps themselves.

The numerical evolution of the field equations with zero initial data [Eq. (3.54)] produces an initial unphysical burst. This is due to the fact that zero initial data is not compatible with the existence of a particle. More specifically, zero initial data means that at an initial time t_o we have a source term, the particle, but not the radiation that the orbiting particle produced in the past to the initial time. This is clearly not consistent and the way the system has to adapt to the situation is by the emission of an initial radiation burst. This unphysical radiation may contaminate the solution producing not reliable results. In order to avoid this and obtain physically relevant results, we wait for several orbital periods (typically 1-3) until the initial unphysical radiation has propagated away and its contribution to the solution can be considered negligible. In this regard, we have explored in [Jaramillo 2011] (see also [Field 2010]) a way of mitigating even more the negative effects that the initial burst may produce. This consists in gradually introducing the presence of the particle in the system, i.e. we *switch on* the particle during a certain time (comparable with the typical orbital period). In order to do this in practice, the source terms (in our case the jumps) are multiplied by a suitable function of time, which varies from zero to unity. In this way, we have tested that the initial burst of radiation is significantly reduced with respect to the case in which the particle is introduced instantaneously. This technique, in certain numerical implementations [in particular in implementations that use Eqs. (3.50) and (3.51) instead of Eqs. (3.52) and (3.53) for the communication of the characteristic fields], can improve the accuracy in the calculation of the self-force by reducing the high-frequency noise (see [Jaramillo 2011] for details) introduced by the presence of the particle.

This initial unphysical burst, produced in the numerical computations, has been the subject of controversy, since it has been claimed in [Field 2010] that certain components of this burst, which have been called *Jost junk* solutions, can persists in time as junk radiation, compromising the accuracy of time-domain techniques. Nevertheless, in a recent study [Jaramillo 2011], the possible appearance of Jost junk radiation solutions in relation with the imposition of zero initial data has been analysed in detail. It has been shown that the Jost solutions can always be avoided as long as the source terms (associated with the particle) are correctly implemented at late times. Indeed, it was concluded that the junk radiation appears as a consequence of enforcing the jumps through an infinitesimal condition in time, like e.g. $d[V]_p/dt$, without

simultaneously imposing the correct initial value of the jump itself, i.e. $[V]_p$. In conclusion, we can use the initial zero data condition as long as we provide the value of the derivatives of the jumps (see also [Canizares 2010]).

On the other hand, we need to prescribe suitable boundary conditions for the field variables at the outer boundaries, i.e. near spatial infinity, $r^* = r^*_\text{I}$ (with $r^*_\text{I} \to \infty$) and near the MBH horizon, $r^* = r^*_\text{H}$ (with $r^*_\text{H} \to -\infty$). In this regard, we employ Sommerfeld outgoing boundary conditions, sometimes known as absorbing boundary conditions, to prevent incoming signals from outside the physical domain:

$$\phi^{\ell m}(t, r^*_\text{H}) - \varphi^{\ell m}(t, r^*_\text{H}) = 0 = U^{\ell m}(t, r^*_\text{H}), \qquad (3.55)$$

$$\phi^{\ell m}(t, r^*_\text{I}) + \varphi^{\ell m}(t, r^*_\text{I}) = 0 = V^{\ell m}(t, r^*_\text{I}). \qquad (3.56)$$

Note that these conditions are only valid when they are applied exactly at $r^* \to \infty$ and $r^* \to -\infty$. At other locations they are approximate boundary conditions. This means that after sufficiently long time the solution could be contaminated by the inaccuracy in the prescription of these boundary conditions. However, this can be avoided by setting the boundaries out of causal contact with the particle location, where we want to estimate the self-force, for the whole duration of our evolutions.

3.6 Numerical Implementation

In what follows, we are going to describe the numerical algorithms, both for the spatial and temporal discretisation, that we use in this first part of the thesis to solve the PDEs of our EMRI model.

We first introduce the pseudospectral Collocation method that we use for the spatial discretisation of the evolution equations of our scalar EMRI problem. To that end, we start by considering an arbitrary system of PDEs defined in some domain $\Omega \subset \mathbb{R}^d$:

$$L[U](x) = S(x) \qquad x \in \Omega, \qquad (3.57)$$

where L is a differential operator acting on the unknowns $\boldsymbol{U}$ and S is the source term. The boundary conditions of the problem are given by:

$$H[U](x) = 0 \qquad x \in \partial\Omega, \qquad (3.58)$$

where H is the operator defining the boundary conditions and $\partial\Omega$ denotes the boundary of Ω.

In spectral methods, the solution $U(x)$ of Eq. (3.57) is approximated by a truncated series in some suitable basis of functions $\{\phi_i\}$, $(i = 0, ..., N)$:

$$U(x) \approx U_N(x) \equiv \sum_{i=0}^{N} a_i\, \phi_i(x), \qquad (3.59)$$

where a_i are the *spectral coefficients* of the expansion. We can also see U_N as the interpolating approximation to the solution U. Given certain smoothness conditions on the operators L and H and with an appropriate choice of the basis functions $\{\phi_i\}$, it is possible in many cases to show that the approximation $U_N(x)$ converges exponentially towards the solution $U(x)$ as we increase N. The selection of the basis of functions usually depends on the boundary conditions imposed on the variables. For instance, Fourier series or an expansion in spherical harmonics are suitable to approximate the solution of periodic problems. On the other hand, for non-periodic problems, the eigenfunctions of singular Sturm-Liouville operators are more convenient, for instance Chebyshev or Legendre polynomials.

Given a spectral approximation [Eq. (3.59)] to the solution of our system of PDEs [Eq. (3.57)], we need a criterium to decide in a quantitative way when the approximated expansion U_N is *close* to the exact solution U. Or equivalently, since we do not know a priori the exact solution, we need a criterium to establish the level of accuracy to which the approximation U_N satisfy the system of PDEs of Eq. (3.57). Most criteria are based on the *residual* R_N associated with the PDEs, which is defined as

$$R_N(x) = L[U_N(x)] - S(x)\,. \qquad (3.60)$$

Then, assuming that by construction the approximation U_N satisfies the boundary conditions Eq. (3.58), we say that the function $U_N(x)$ approaches a solution of the system of PDEs in Eq. (3.57) when, by increasing the number of functions included in the spectral expansions, the residual becomes smaller. The conditions that one imposes on the residuals to make them as close as possible to zero in Ω characterises the type of spectral method employed. In fact, the specification of the residuals provides the way to determine uniquely the spectral coefficients a_i.

In the case of the PSC method (see [Boyd 2001] for an exhaustive presentation of the PSC method), one imposes that the approximate solution U_N agrees with the exact one U at a set of $N + 1$ *collocation points* x_i $(i = 0, ..., N)$. In other words, we choose as an error minimisation condition to make the residuals zero at each x_i, that is:

$$U_N(x_i) \;=\; U(x_i)\,, \qquad (3.61)$$
$$L[U_N](x_i) \;=\; S(x_i)\,. \qquad (3.62)$$

In the PSC method, we can obtain another expression/representation for the approximate solution U_N by employing the *Lagrange Cardinal functions* [Boyd 2001], $\mathcal{C}_i(x)$ $(i = 0, ..., N)$, associated with the basis functions $\{\phi_i\}$, $(i = 0, ..., N)$. The Cardinal functions are characterised by the conditions:

$$\mathcal{C}_i(x_j) = \delta_{ij} \, , \tag{3.63}$$

and the expression for U_N is:

$$U_N(x) = \sum_{i=0}^{N} U_i \, \mathcal{C}_i(x) \, . \tag{3.64}$$

This is very convenient to impose the PSC conditions on the residuals, that is, the $(N + 1)$ conditions $R_N(x_i) = 0$, which tell us that

$$U_i = U(x_i) \, . \tag{3.65}$$

The expansion of Eq. (3.64) is called the *physical* representation of the solution. As a result, when the basis functions belong to a class of polynomials (for instance Chebyshev polynomials) the functions $U_N(x)$ are fitted by a polynomial (*Lagrangian interpolant*) of degree N at each collocation (or interpolation) point x_i.

In an interval $[a, b]$ containing the point x and the set of collocation points $\{x_i\}$, the error in interpolating a function $U(x)$ by the Lagrangian interpolant $U_N(x)$ is given by:

$$U(x) - U_N(x) = \frac{1}{(N + 1)!} U^{(N+1)}(\xi) \prod_{i=0}^{N} (x - x_i) \, . \tag{3.66}$$

where the point ξ (belonging to the interval $[a, b]$) depends on the specific function being approximated upon, the number of collocation points N, x, and upon the location of the collocation points [Boyd 2001]. Given a fixed number of collocation points, the *Cauchy interpolation error*, Eq. (3.66), can only be controlled by changing the location of the collocation points x_i through the term:

$$\prod_{i=0}^{N} (x - x_i) \, , \tag{3.67}$$

which depends on the choice of collocation points, i.e. the numerical grid. It has been shown (see, e.g. [Boyd 2001]) that the set of collocation points that

minimises the Cauchy interpolation error (when the interval $[a, b]$ is taken to be $[-1, 1]$, which can always be achieved by a simple linear transformation of the coordinate x) corresponds to the zeros of the Chebyshev polynomial of order $N+1$, usually called $T_{N+1}(x)$. Therefore, this is an important argument in favour of these polynomials for non-periodic problems.

In what follows we describe some techniques related with the PSC method that are useful for practical calculations and at the same time illustrate the potential of the method. We start with the applications of spectral method to the computation of integrals. Given $N + 1$ arbitrary collocation points $\{x_i\}$ defined on an interval $[-1, 1]$, we can always find constants (weights) ω_i such that for any polynomial of degree N, $U_N(x)$, the Gauss quadrature integral is exact:

$$\int_{-1}^{1} U_N(x) \ dx = \sum_{i=0}^{N} \omega_i U_N(x_i), \qquad i = 0, ..., N \ . \tag{3.68}$$

Imposing this formula for the different powers of x up to order N, we obtain a linear system whose resolution give us the weights ω_i.

On the other hand, in the case that the collocation points $\{x_i\}$ are the zeros of $N + 1$ orthonormal polynomials $\{\phi_i\}$ with respect to the weight function $\omega(x)$, or in other words:

$$\langle \phi_i, \phi_j \rangle = \int_{-1}^{1} \omega(x)\phi_i(x)\phi_j(x) \ dx = \delta_{ij}\nu_i^2 \ , \tag{3.69}$$

where $\nu = \sqrt{\langle \phi_i, \phi_j \rangle}$, then, for any polynomial $U(x)$ of at most degree $2N+1$, Eq. (3.68) leads to the *Gauss-Jacobi integration* rule:

$$\int_{-1}^{1} \omega(x)U(x) \ dx = \sum_{i=0}^{N} \omega_i U(x_i), \qquad i = 0, ..., N \ , \tag{3.70}$$

where ω_i are the quadrature weights that can be found by solving the linear system:

$$\sum_{i=0}^{N} (x_i)^k \omega_i = \int_{-1}^{1} \omega(x)x^k \ dx, \qquad k = 0, ..., N \ . \tag{3.71}$$

Or alternatively by:

$$\omega_i = \int_{-1}^{1} \mathcal{C}_i(x) \ dx \ , \tag{3.72}$$

where $\mathcal{C}_i(x)$ denotes the cardinal functions Eq. (3.63) associated with the zeros of $\{\phi_i\}$.

The integration rule Eq. (3.70) can also be defined for a polynomial made up of a combination of the basis of functions $\{\phi_i\}$, giving rise to the so called Gauss integration formulas. The orthogonality defined by the polynomials $\{\phi_i\}$ in the continuum case [Eq. (3.69)] together with the Gauss integration formulas leads to the following discrete inner product:

$$[u,v] = \sum_{i=0}^{N} \omega_i u(x_i) v(x_j) \ , \tag{3.73}$$

which preserves the orthogonality of $\{\phi_i\}$. Then, the inner product Eq. (3.69) is discretised as:

$$[\phi_i, \phi_j] = \sum_{i=0}^{N} \omega_i \phi(x_i) \phi(x_j) = \delta_{ij} \nu_i^2 \ . \tag{3.74}$$

We can apply these techniques to the PSC method to obtain the spectral coefficients a_i of Eq. (3.59) once the coefficients U_i of the physical representation [Eq. (3.64)] are known:

$$a_i = \frac{[U, \phi_i]}{[\phi_i, \phi_i]} = \frac{[U, \phi_i]}{|\phi_i|} = \frac{1}{\nu_i^2} \sum_{i=0}^{N} \omega_i U(x_i) \phi_i(x_i) = \frac{1}{\nu_i^2} \sum_{i=0}^{N} \omega_i U_i \phi_i(x_i) \ , \tag{3.75}$$

and the inverse process is given by:

$$U_i = U(x_i) = \sum_{i=0}^{N} a_i \, \phi_i(x_i) \, . \tag{3.76}$$

From Eq. (3.75) and Eq. (3.76), it follows that in the PSC method we can transform easily from the discrete space of the solutions $\{U(x_i)\}$ (*physical space*) to the discrete space of the coefficients $\{a_i\}$ of their spectral expansions (*spectral space*). In this way, we may use as unknowns either the spectral coefficients a_i or the function grid point values $U(x_i)$. This is an important remark, since this freedom to jump back and forth between the $\{a_i\}$ and $\{U(x_i)\}$ representations of $U(x)$ is essential to deal with the derivatives associated with our problem, and also it is very useful to deal with non-linear terms (in the case of non-linear PDEs).

Introducing Eq. (3.64) in Eq. (3.57), we get the following matrix representation of our system of PDEs:

$$\mathbb{L}^P \cdot \mathbf{U} = \mathbf{S}, \tag{3.77}$$

where $\mathbb{L}^P$ is a matrix with components:

$$L_{ij}^P = L[\mathcal{C}_j](x_i) \,, \tag{3.78}$$

$\mathbf{U}$ is a vector with components $U_i = U(x_i)$, and $\mathbf{S}$ is the source vector with components $\mathbf{S}_i = S(x_i)$. Moreover, the approximated solution in the spectral picture is given by the spectral basis function representation of Eq. (3.59). Thus, we end up with the following spectral matrix problem:

$$\mathbb{L}^S \cdot \mathbf{a} = \mathbf{S}, \tag{3.79}$$

where the components of $\mathbb{L}^S$ are:

$$\mathbb{L}_{ij}^S = L[\phi_j](x_i) \,, \tag{3.80}$$

and $\mathbf{a}$ is a vector containing the spectral coefficients $\mathbf{a}_i = a_i$. Consequently, from Eq. (3.75), the relationship between the grid points values and the spectral coefficients, i. e. between the physical and spectral pictures, can be written in a matrix form which is equivalent to Eq. (3.75):

$$\mathbb{M} \cdot \mathbf{U} = \mathbf{a} \,, \tag{3.81}$$

and where the transformation matrix $\mathbb{M}$ has components:

$$M_{ij} = \frac{\phi_i(x_j)\omega_j}{[\phi_i, \phi_i]} = \frac{\phi_i(x_j)\omega_j}{\nu_i^2} \,. \tag{3.82}$$

Combining Eq. (3.77), Eq. (3.79) and Eq. (3.81), we establish the following relation:

$$\mathbb{L}^S \cdot \mathbb{M} = \mathbb{L}^P \,. \tag{3.83}$$

Moreover, the inverse of Eq. (3.81) is given by Eq. (3.76) and, consequently, the components of the inverse of $\mathbb{M}$ are given by

$$M_{ij}^{-1} = \phi_j(x_i) \,, \tag{3.84}$$

which leads to:

$$\mathbf{U} = \mathbb{M}^{-1} \cdot \mathbf{a} \,. \tag{3.85}$$

As a result, using Eqs. (3.81) and (3.85) we can move back and forth between the physical and the spectral representation employing this matrix multiplication transformation.

The m-th derivative of U_N admits an expansion similar to Eq. (3.59), given by:

$$\frac{d^m U_N}{dx^m}(x_i) = \sum_{i=0}^{N} U_N^{(m)}(x_i)\mathcal{C}_i(x) \ , \tag{3.86}$$

where the coefficients $U_N(x_i)$ and $U_N^{(m)}(x_i)$ can be related through a differentiation matrix D_{ij}^m of order m:

$$U_N^m(x_i) = \sum_{j=0}^{N} D_{ij}^{(m)} U_N(x_j) \ , \tag{3.87}$$

and the matrix D_{ij}^m is obtained in terms of the associated Cardinal functions $\mathcal{C}_i(x)$:

$$D_{ij}^{(m)} = \frac{d^m \mathcal{C}_j}{dx^m}(x_j) \ . \tag{3.88}$$

On the other hand, the spectral expansion of the first derivative of U can be written as

$$\frac{dU_N}{dx}(x) = \sum_{j=0}^{N} b_j \phi_j(x) \ , \tag{3.89}$$

where the spectral coefficients b_j are given by the recurrence relation:

$$
\begin{aligned}
b_i &= b_{i+2} + 2(i+1)a_{i+1} \ , \\
b_0 &= \frac{1}{2}b_2 + a_1 \ ,
\end{aligned}
\tag{3.90}
$$

with $a_{N+1} = a_N = 0$. In the same way, the spectral coefficients of the second-order derivative of U:

$$\frac{d^2 U_N}{dx^2}(x) = \sum_{j=0}^{N} d_j \phi_j(x) \ , \tag{3.91}$$

are obtained by a similar recurrence relation, or by applying Eq. (3.90) twice (see, e.g. [Boyd 2001]).

We have seen that within the PSC method our solutions U can be approximated employing a suitable basis of functions [Eq. (3.59)] and also using an expansion using a set of collocation points. But up to now, we have not mentioned any particular basis of functions nor any particular set of collocation

points $\{x_i\}$. In what follows we are going to introduce and justify the basis and the numerical grid employed in our numerical computations.

The basis of functions employed to expand the field solutions must cover the computational necessities of our physical problem. In this regard, since our problem has no spatial periodicity and taking into account the result of the minimisation of the Cauchy interpolation error described above, we discretise the field variables using an expansion in a basis of Chebyshev polynomials, $T_n(X)$, which are defined as:

$$T_n(X) = \cos\left(n \cos^{-1}(X)\right), \qquad X \in [-1, 1] . \tag{3.92}$$

where $|T_n(X)| \leq 1$, and n is the degree of the polynomial. Chebyshev polynomials can be employed to interpolate any analytical function and they provide exponential convergence for smooth functions, independently of the boundary conditions satisfied by them [Boyd 2001]. Moreover, Chebyshev polynomials are defined in a finite interval, $X \in [-1, 1]$, which can always be mapped to the (finite) spatial domain (or subdomain) of our problem. In addition, as we have already mentioned, the Chebyshev polynomial T_{N+1} is the one that has the smallest maximum on the interval $[-1, 1]$ of all polynomials of degree $N + 1$ with leading coefficient (X^{N+1}) equal to unity, $\{P_{N+1}\}$. This can be expressed as [Boyd 2001]:

$$\max_{P_{N+1}} \left\| P_{N+1}(X) \right\| \geq \max \left\| \frac{T_{N+1}(X)}{2^N} \right\| = \frac{1}{2^N} . \tag{3.93}$$

In addition, since any polynomial of degree N can be factored into the product of linear factors of the form $(x - x_i)$, where the $\{x_i\}$ are the roots of the polynomial and, we can write

$$\frac{1}{2^N} T_{N+1}(X) = \prod_{i=0}^{N} (X - X_i) . \tag{3.94}$$

where $\{X_i\}$ are the roots of T_{N+1} and $X \in (-1, 1)$. Taking into that this Chebyshev polynomial minimises the error in the Cauchy remainder of Eq. (3.66), the optimal collocation points are the roots of the Chebyshev polynomial of degree $(N+1)$. This set of roots/collocation points are usually called the Gauss-Chebyshev grid. One can see that this grid does not include the boundary points $X = 1$ and $X = -1$, and hence it may not be a convenient grid for problems in which we need to prescribe boundary conditions exactly at the boundary points. An alternative grid which shares the same properties as the Gauss-Chebyshev grid but that includes the boundary points $X = \pm 1$ is the so-called Lobatto-Chebyshev grid, which are given by the roots of

$$(1 - X^2)T_N'(X) = 0 . \tag{3.95}$$

where the prime indicates differentiation with respect to X. In this way, the Lobatto-Chebyshev grid includes the extrema of the Chebyshev polynomial $T'_N(X)$ and the end points $X = \pm 1$. The explicit expression of these collocation points is:

$$X_i = -\cos\left(\frac{\pi i}{N}\right) \qquad (i = 0, 1, \ldots, N)\,. \qquad (3.96)$$

Notice that we can always map any (physical) interval $[a, b]$ to the (spectral or collocation) interval $[-1, 1]$ and find optimal interpolation points as the roots of a Chebyshev polynomial of order $N + 1$, or alternatively the Lobatto-Chebyshev collocation points.

The distance between the collocation points X_i goes as N^{-1} near the centre of the interval, whereas near the ends of the interval it goes as N^{-2}. Therefore, the density of collocation points is bigger at the ends of the interval than around the centre. This is very convenient for our computations, since, to compute the self-force, we need more resolution near the particle location that in the rest of the spatial domain and this is granted by employing a Chebyshev-Lobatto grid.

Focusing now in the Chebyshev PSC method with the Lobatto-Chebyshev grid, the expansion of the solutions at each collocation point leads to the spectral representation (real) space of the solutions:

$$U_i \equiv U_N(X_i) = \sum_{k=0}^{N} a_k T_k(X_i)\,. \qquad (3.97)$$

The cardinal functions associated with the Chebyshev-Lobatto collocation grid are:

$$\mathcal{C}_i(X) = \frac{(1 - X^2)T'_N(X)}{(1 - X_i^2)(X - X_i)T''_N(X_i)} \qquad i = 0, \ldots, N\,. \qquad (3.98)$$

Taking into account the properties of the spectral quadratures formulae given above, the Chebyshev polynomials fulfil the following discrete orthogonality relation:

$$[T_j, T_k] = \frac{2}{N\bar{c}_k} \sum_{i=0}^{N} \frac{1}{\bar{c}_i} T_j(X_i)\, T_k(X_i) = \delta_{nm}\,. \qquad (3.99)$$

The degree of the polynomials is given by the number of collocation points (their roots), $k, j = 0, \ldots, N$, and $\bar{c}_i$ are normalisation coefficients given by:

$$\bar{c}_i = \begin{cases} 2 & \text{for } i = 0, N\,, \\ 1 & \text{otherwise}\,. \end{cases} \qquad (3.100)$$

Using this, we can invert Eq. (3.97) to find:

$$a_j = \frac{2}{N\bar{c}_i} \sum_{i=0}^{N} \frac{U_i}{\bar{c}_i} T_j(X_i),$$ (3.101)

Consequently, since there is the same number of grid values U_i and spectral coefficients a_k, this equation provides the one-to-one mapping between $\{U_i\}$ and $\{a_k\}$.

On the other hand, as we can see from Eq. (3.92), a Chebyshev series is a Fourier cosine series with just a change of variable given by the mapping:

$$X: \qquad [0, 2\pi] \longrightarrow [-1, 1]$$ (3.102)
$$\theta \longrightarrow X(\theta) = \cos(\theta),$$ (3.103)

so that

$$T_n(X) = \cos(n\theta).$$ (3.104)

Since Chebyshev expansions can be translated into Fourier expansions, they also have to admit a FFT algorithm to perform the matrix multiplication needed to change from the spectral to the physical representation and the converse. Then, the following two series are equivalent under the transformation of Eq. (3.103):

$$U(X) = \sum_{n=0}^{\infty} a_n T_n(X) \iff U(\cos\theta) = \sum_{n=0}^{\infty} a_n \cos(n\theta).$$ (3.105)

and, the coefficients of $U(X)$ as a Chebyshev series are identical with the Fourier coefficients of $U(\cos\theta)$. Moreover, since $U(\cos\theta)$ is periodic, its Fourier series must have exponential convergence, unless $U(X)$ is singular for $X \in [-1, 1]$. Hence, it does not matter whether $U(X)$ has singularities for real X outside $[-1, 1]$ nor does it matter whether $U(X)$ is periodic in X.

Then, the matrix multiplications of Eq. (3.97) and Eq. (3.101) can be performed using a FFT algorithm (we use the routines of the FFTW library [Frigo 2005]) employing a number of operations $\mathcal{O}(N \ln N)$ instead of $N \times N$ operations needed in a direct matrix multiplication. As we shall see in the next chapters, the kind of operations needed to solve numerically the PDEs associated with our problem involve a change of representation between the physical and the spectral picture. An example of this is differentiation. In this regard, since differentiation is easier in the spectral representation, it is convenient to compute the derivatives there. To that end, one has to follow the next steps: (i) Transform from the physical to the spectral picture,

(ii) compute the derivatives in the spectral domain, and finally (iii) transform back to the physical picture. Then, for an implementation of the PSC method employing Chebyshev polynomials, the differentiation process can be described by the following scheme:

$$\partial_{r^*} : \{U_i\} \xrightarrow{FFT} \{a_n\} \xrightarrow{\partial_{r^*}} \{b_n\} \xrightarrow{FFT} \{(\partial_{r^*}U)_i\},\qquad (3.106)$$

where $\{b_n\}$ are the spectral coefficients associated with the spatial derivative in Eq. (3.90) (see, e.g. [Boyd 2001]).

In our computations, a spectral filter is employed to reduce the spurious (of non-physical origin) high-frequency components of our numerical solutions (see Section 3.5). The filter is applied after every time step (see below for the numerical evolution algorithm). We choose a filter of the exponential type, whose action on the spectral coefficients $\{a_n\}$ is given by:

$$a_n \;\longrightarrow\; \tilde{a}_n \quad\text{with}\quad \tilde{a}_n = \sigma\left(\frac{n}{N}\right) a_n,\qquad (3.107)$$

where $\sigma(n/N)$ is the exponential filter defined as:

$$\sigma\left(\frac{n}{N}\right) = \begin{cases} 1 & \text{for } 0 \leqslant n \leqslant N_c, \\ \exp\left[-\alpha\left(\frac{n-N_c}{N-N_c}\right)^\gamma\right] & \text{for } N_c < n \leq N. \end{cases}\qquad (3.108)$$

Here N_c is the cut-off mode number, γ is the order of the filter (typically chosen to be of the order of the number of collocation points, N), and α is the machine accuracy parameter, which is related to the machine accuracy, ε_M, by $\alpha = -\ln\varepsilon_M$. For a 32 bit machine and double precision we have: $\varepsilon_M = 2^{-52}$, and hence $\alpha \simeq 36.0437$. The process of filtering the solution can be summarised schematically as:

$$\{U_i\} \xrightarrow{FFT} \{a_n\} \xrightarrow{\text{Filter}} \{\tilde{a}_n\} \xrightarrow{FFT} \{\tilde{U}_i\},\qquad (3.109)$$

where $\{U_i\}$ are the values of the solutions at the collocation points after an evolution time step; $\{a_n\}$ are their corresponding spectral components; $\{\tilde{a}_n\}$ are the filtered spectral components; and $\{\tilde{U}_i\}$ are the filtered values of the solution at the collocation points.

The typical numeric error introduced when implementing the PSC method to our fields is due to the fact that we have a truncated expansion in Chebyshev polynomials, at a given number that coincides with the number of collocation points, i.e. $N+1$. This error can be estimated using the well-known *truncation error*:

$$\text{Error} = \log_{10}|a_N|.\qquad (3.110)$$

Notice that with the PSC method, in practice we discretise a set of PDEs for the field variables $\boldsymbol{U}$ [Eq. (3.6)], (or $\boldsymbol{N}$ [Eq. (3.34)] for the characteristic fields), and the result is a set of equations for a set of time-dependent variables at each collocation point x_i or, in other words, we obtain a system of ODEs for either the grid values of our variables $\{\boldsymbol{U}_i(t)\}$ at each collocation point x_i or the spectral coefficients $\{a_k(t)\}$. We have seen before how to change the representation, i.e. how to obtain $\{a_k(t)\}$ from $\{\boldsymbol{U}_i(t)\}$ and the converse.

The situation after the spatial discretisation with the PSC method is that we have $N+1$ unknowns which are fully determined inside each subdomain by a set of ODEs (an ODE at each collocation point) that come from Eq. (3.77). To solve these ODEs we use the method of lines (see, e.g. [Gustafsson 1995]) the well-known Runge-Kutta 4 (RK4) time stepping algorithm. Assuming the ODEs have the following general form (method of lines),

$$\frac{d\boldsymbol{U}}{dt} = \boldsymbol{F}(t, \boldsymbol{U})\,, \tag{3.111}$$

the RK4 algorithm to evolve from time t_n to time t_{n+1} is given by the following expressions:

$$(t_n, \boldsymbol{U}_n) \quad \longrightarrow \quad (t_{n+1}, \boldsymbol{U}_{n+1}) \tag{3.112}$$

$$\boldsymbol{U}_{n+1} = \boldsymbol{U}_n + \frac{1}{6}\left(\boldsymbol{K}_1 + 2\boldsymbol{K}_2 + 2\boldsymbol{K}_3 + \boldsymbol{K}_4\right)\,, \tag{3.113}$$

where

$$\boldsymbol{K}_1 = \Delta t\,\boldsymbol{F}\left(t_n, \boldsymbol{U}_n\right)\,, \tag{3.114}$$

$$\boldsymbol{K}_2 = \Delta t\,\boldsymbol{F}\left(t_n + \frac{\Delta t}{2}, \boldsymbol{U}_n + \frac{\boldsymbol{K}_1}{2}\right)\,, \tag{3.115}$$

$$\boldsymbol{K}_3 = \Delta t\,\boldsymbol{F}\left(t_n + \frac{\Delta t}{2}, \boldsymbol{U}_n + \frac{\boldsymbol{K}_2}{2}\right)\,, \tag{3.116}$$

$$\boldsymbol{K}_4 = \Delta t\,\boldsymbol{F}\left(t_n + \Delta t, \boldsymbol{U}_n + \boldsymbol{K}_3\right)\,, \tag{3.117}$$

where Δt is the time step. In this sense, it is important to mention that we have a restriction in the choice of the time step due to causality restrictions due to the fact that the domain of dependence of the system of hyperbolic equations evolve at a certain velocity (see [Courant 1953b]). This restriction is called the Courant-Friedrichs-Lax (CFL) condition. In Finite Differences schemes it imposes a condition of the time $\Delta t_{CFL} \propto N^{-1}$ whereas in the case of pseudospectral computations it is given by

$$\Delta t_{CFL} \sim \frac{\pi^2|b-a|}{4N^2}\,. \tag{3.118}$$

where $|b - a|$ is the size of the physical interval $[a, b]$ (or, in our case, subdomain) [Boyd 2001].

Finally, our numerical code is implement using the C programming language, the GNU Scientific Library [Galassi 2006], mainly for calculations with special functions, and the FFTW library [Frigo 2005] for performing FFTs.

3.7 A First Test of the PwP Implementation

In what follows, we are going to present a first test of the techniques developed to implement the PwP method. To that end, we are going to evolve a Gaussian function in a multi-domain framework constructed using the machinery introduced along this chapter.

As a first test of the numerical setup, we study the wave propagation of a moving Gaussian packet in $1 + 1$ flat space. Then, the PDE that we study is given by:

$$\left\{ -\frac{\partial^2}{\partial t^2} + \frac{\partial^2}{\partial r^{*2}} \right\} F = 0 \,. \tag{3.119}$$

This example corresponds to Eq. (3.123) with no source $\mathcal{S}^{\ell m} = 0$ nor potential term (choosing the case with $\ell = m = 0$ and $M_\bullet = 0$). An exact solution of this equation for a moving Gaussian packet can given as:

$$F(t, r^*) = A \exp\left(-\frac{[t - (r^* - r_0^*)]^2}{2\sigma^2} \right) \,, \tag{3.120}$$

where A the amplitude, r_0^* the initial position of the centre, and σ is the width of the Gaussian. From here we construct initial data for our evolutions:

$$F(0, r^*) = A \exp\left(-\frac{(r^* - r_0^*)^2}{2\sigma^2} \right) \,, \tag{3.121}$$

$$\partial_t F(0, r^*) = \frac{A(r^* - r_0^*)}{\sigma^2} \exp\left(-\frac{(r^* - r_0^*)^2}{2\sigma^2} \right) \,. \tag{3.122}$$

The Gaussian is evolved through a multidomain grid, like the one showed in Figure 4.1 below, which is discretised using PSC methods. We perform several evolutions of the Gaussian packet by increasing the number of collocation points per subdomain, N. Then, we study the convergence of the solution computing the truncation error [using Eq. (3.110)] in the subdomain where the Gaussian packet is present at a chosen time.

In Figure 3.3, we show the convergence plot for a simulation that uses two subdomains distributed as: $r^* \in [-550, 0] \cup [0, 550] M_\bullet$. The solution has been communicated across the subdomains by using the penalty method. In our simulation we have used a Gaussian packet with $A = 0.1$, $\sigma = 20$ and $r_0^* = 200$. As we can see, the truncation error decreases exponentially with the number of collocation points [Canizares 2009]. This result is not surprising, since the PSC should provide this kind of convergence for smooth solutions.
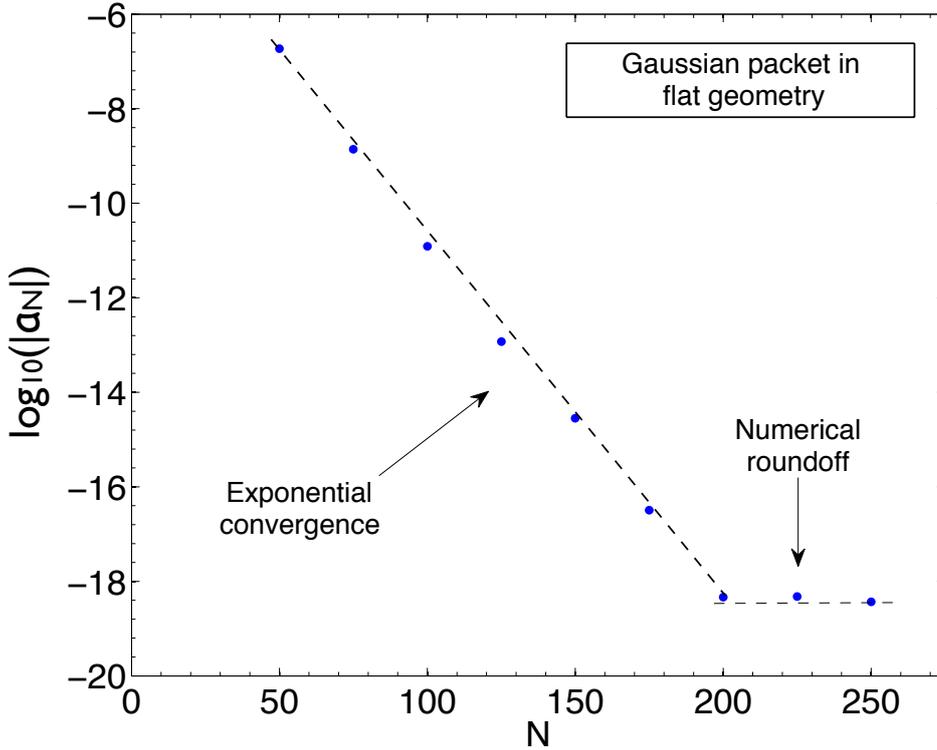
Figure 3.3: *Truncation error for the evolution of the wave equation [Eq. (3.123)], for an initially moving Gaussian packet on flat spacetime. The plot shows the dependence of the truncation error [Eq. (3.110)] associated with the field F with respect to the number of collocation points. The data indicates the exponential convergence of the numerical method.*

As a second test, we perform the same type of simulation but with the Gaussian wave packet propagating on a (curved) Schwarzschild background. This corresponds to: $\ell = m = 0$ and $q = 0$. Then the evolution equation is given by:

$$\left\{ -\frac{\partial^2}{\partial t^2} + \frac{\partial^2}{\partial r^{*2}} + f\frac{2M_\bullet}{r^3} \right\} F = 0 \,, \tag{3.123}$$

where f is given by Eq. (2.37). As before, we perform several evolutions of the Gaussian packet in our multidomain grid, with the same type of initial data, increasing the number of collocation points per subdomain, N, in each evolution. In this way, we estimate the convergence of the solution by computing the truncation error through Eq. (3.110) [Canizares 2009]. In Figure 3.4, we show the convergence plot for a simulation that uses two subdomains, $r^* - r_p^* \in [-550, 0] \cup [0, 550] M_\bullet$, where the solution again has been connected by using the penalty method. As we can see, the truncation error decreases exponentially with the number of collocation points. This result is also expected, since the mathematical structure of the equation is essentially the same in the sense that the equation has the same differential properties.
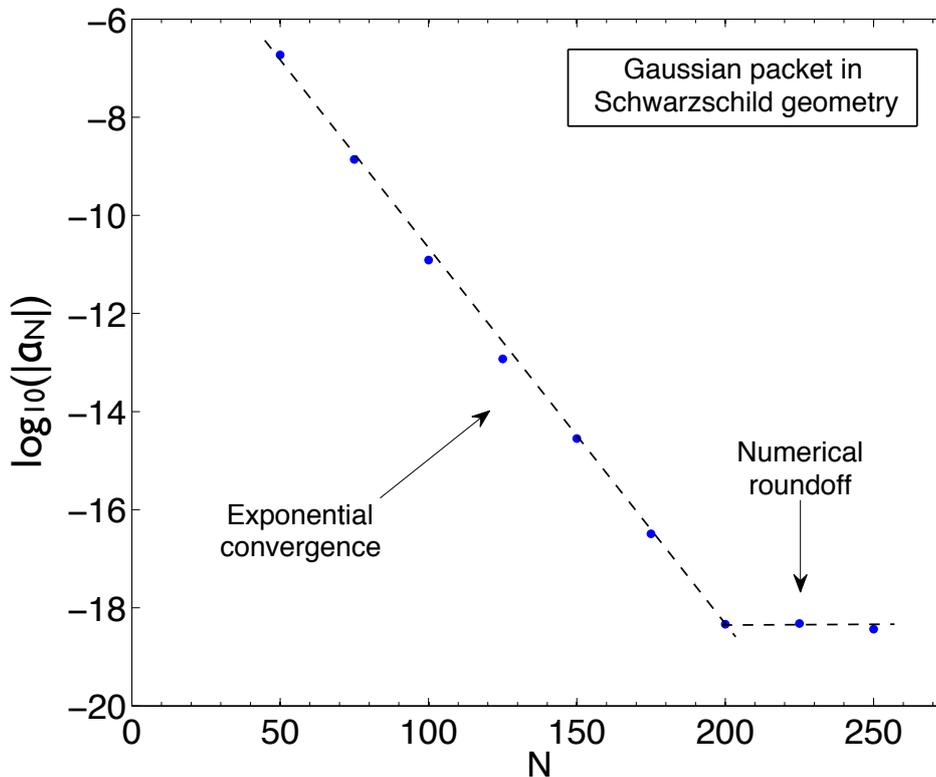
Figure 3.4: *Truncation error for the evolution of a moving Gaussian packet propagating on a Schwarzschild background. We can see the dependence of the truncation error associated with the field F with respect the number of collocation points. The data indicates the exponential convergence of the numerical method.*

3.8   Counting the Number of Evolutions

To obtain the self-force acting on the scalar particle one needs, in principle, to compute the different harmonic modes of the retarded field decomposition Eq. (2.82) up to a given ℓ_{max}. But, since the source term in the evolution equation Eq. (2.84) is complex, both the real and imaginary parts of the (ℓ, m) harmonic components of the retarded field $\Phi^{\ell m}$ are needed in the calculation of the self-force. However, if we can avoid computing some of these field modes, the time required in a full self-force computation can be made significantly smaller and, consequently, it would improve the efficiency of our implementation of the PwP scheme. For this reason, we use the fact that Φ is a real scalar function and then, the relation $\bar{\Phi}^{\ell -m} = (-1)^m \Phi^{\ell m}$ holds for each (ℓ, m). In this way, we do not need to compute the modes with $m < 0$. Moreover, taking into account that the orbits take place in the equatorial plane $\theta = \pi/2$, where the spherical harmonics in the particle source term are evaluated, and the fact that for any (ℓ, m), we have:

$$Y^{\ell m}(\pi/2, \varphi) = 0 \quad \text{for } \ell + m \text{ odd} , \tag{3.124}$$

the corresponding field modes are exactly zero. Taking into account all these considerations, the total number of evolutions needed in terms of ℓ_{max} is:

$$N_{\text{evolutions}} = \frac{(\ell_{\text{max}} + 1)\,(\ell_{\text{max}} + 2)}{2} . \tag{3.125}$$

EMRIs in Circular Motion

If you can't be a good example, then you'll just have to serve as a horrible warning
Catherine Aird.

4.1 Introduction

The goal of this chapter is to show the potential of the PwP method to perform time-domain self-force computations. We shall see that this method is easily adapted to the requirements of the system, allowing for precise and, at the same, time-efficient computations. Finally, we validate our numerical code by studying the convergence of the solutions and comparing results for the self-force components with other works in the literature.

4.2 Multidomain Structure

As it has already been mentioned, the self-force is a local force that acts only at the particle location (see Section 2.2). Then, in practice, we only need to have high resolution for the field modes around the particle. In what follows we show how we discretise the spatial domain, i.e how we choose the number of collocation points N, the number of subdomains D and how we distribute them. This has obvious direct implications in the resolution of the field modes and the computational time needed in our simulations.

In order to implement the PwP scheme numerically, we start defining the physical computational spatial domain of our problem. It comprises the region defined between the MBH horizon and the spatial infinity, which in tortoise coordinates [Eq. (2.61)] is given by:

$$r^* \in (-\infty, +\infty), \tag{4.1}$$

where $r_{\textrm{H}}^* \to -\infty$ corresponds to the location of the MBH horizon and $r_\infty^* \to +\infty$ corresponds to spatial infinity. Since we are going to use standard Chebyshev polynomials we have to truncate the spatial domain [Boyd 2001] as follows:

$$\Omega = [r_{\textrm{H}}^*, r_I^*] \, , \tag{4.2}$$

and we impose the Sommerfeld boundary conditions Eq. (3.55) and Eq. (3.56). Notice that these conditions are only valid for a flat spacetime, i.e they are exact conditions only when $V_\ell = 0$ or $r_{\textrm{H}}^* \to -\infty$ and $r_{\textrm{I}}^* \to +\infty$. However, we set the outer boundaries far enough from the particle, in such a way that they are not in causal contact with the particle itself during the evolution time $t_f - t_o$. In this way, we avoid the possible contamination from the fields originated at the outer boundaries.

Once the spatial computational domain is defined, the following step is to divide it into a number D of subdomains (see Figure 4.1):

$$\Omega = \bigcup_{a=1}^{D} \Omega_a \, , \tag{4.3}$$

where

$$\Omega_a = \left[r_{a,\textrm{L}}^*, r_{a,\textrm{R}}^* \right] \, , \tag{4.4}$$

and $r_{a,\textrm{L}}^*$ and $r_{a,\textrm{R}}^*$ are the left and right boundaries of each subdomain Ω_a. We discretise each subdomain independently, using the PSC method introduced in Section (3.6). The subdomains are disjoint intervals, whose boundaries or
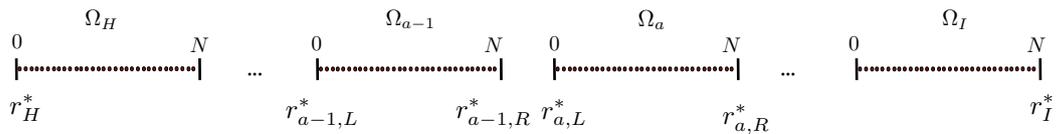
Figure 4.1: *Structure of the truncated one-dimensional spatial grid and the division intp subdomains.*

interfaces are identified:

$$r_{a-1,\textrm{R}}^* = r_{a,\textrm{L}}^* \, . \tag{4.5}$$

In the PwP scheme the particle is located at one interface between two subdomains, say $\Omega_{\textrm{P}}$ and $\Omega_{\textrm{P}+1}$. Then the radial coordinate of the particle is:

$$r_{\textrm{P},\textrm{R}}^* = r_{\textrm{P}+1,\textrm{L}}^* = r_p^* \, . \tag{4.6}$$

In addition, the physical domain, for the circular case studied in this chapter, is implemented employing a comoving tortoise coordinate:

$$r_c^* = r^* - r_p^*, \tag{4.7}$$

in this way the particle location is always at $r_c^* = 0$ (see Figure 4.2).
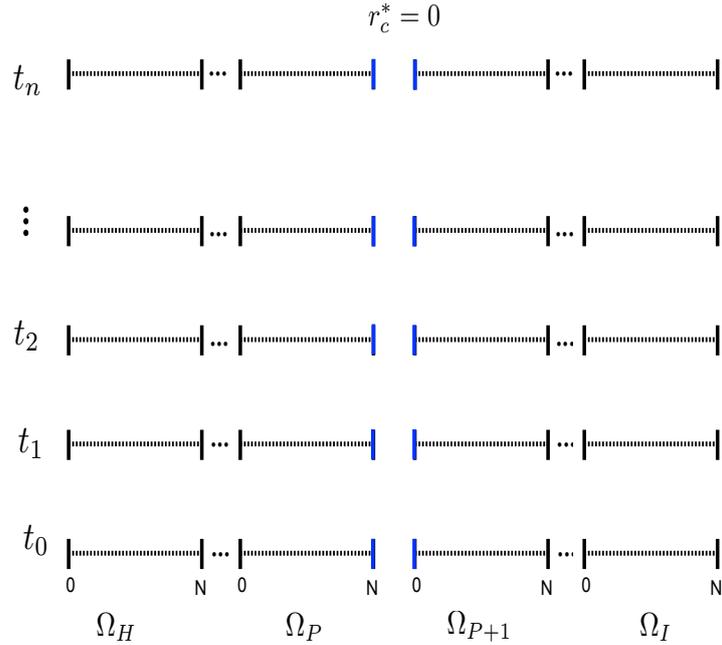
Figure 4.2: *Structure of the physical computational domain, which has been divided into several subdomains. The particle is set at the boundaries between two subdomains: Ω_P and Ω_{P+1}. For a circular orbit, it remains at the same radial location along the whole evolution.*

The field variables have independent expansions in Chebyshev polynomials in each subdomain Ω_a. To communicate them during the evolution, we employ the jump conditions dictated by the evolution equations (see Section 3.4). Thus, since we work with several subdomains and the particle is located at the interface between two of them, we find two possible situations for communicating the fields at a given interface:

(i) The particle is not located there: In this case, we only have to impose the continuity of the solutions. This corresponds to imposing zero RHS to the junction conditions for the field variables Eqs. (3.15)-(3.21), or for the characteristic fields Eq. (3.41) and Eq. (3.42) (i.e. setting there $S^{\ell m} = 0$).

(ii) The particle is located there: In this case, we have to impose the junction conditions Eqs. (3.15)-(3.21) (or for the characteristic fields Eqs. (3.40) - (3.42)), with $\dot{r}_p^* = 0$ since we are dealing with a a circular orbit case:

$$\left[\psi^{\ell m}\right]_p = 0 \,, \quad \left[\phi^{\ell m}\right]_p = 0 \,, \quad \left[\varphi^{\ell m}\right]_p = \frac{S^{\ell m}}{f_p} \,, \tag{4.8}$$

and for the characteristic fields:

$$\left[\psi^{\ell m}\right]_p = 0 \,, \quad \left[U^{\ell m}\right]_p = -\frac{S^{\ell m}}{f_p} \,, \quad \left[V^{\ell m}\right]_p = \frac{S^{\ell m}}{f_p} \,. \tag{4.9}$$

Here it is worth remarking that the matching conditions are imposed at the boundaries of each subdomain to enforce the continuity of the field modes and also to account for the presence of the particle when needed.

We have seen that the field modes are expanded in a basis of Chebyshev polynomials [Eq. (3.97)], and the solution $\mathbf{U}_N$ are defined in a physical subdomain $r^* \in \left[r_{a,\text{L}}^*, r_{a,\text{R}}^*\right]$, whereas the basis of Chebyshev polynomials T_n are defined in the spectral domain, i.e. the space where the arguments of the Chebyshev polynomials are defined, $X \in [-1, 1]$. Moreover, in our analysis we need to change between the physical and the spectral representations. To that end, we project the physical radial space $\{r^*\}$ into the spectral space $\{X\}$ by employing a linear mapping:

- For a given physical subdomain $\Omega_a = \left[r_{a,\text{L}}^*, r_{a,\text{R}}^*\right]$ $(a = 0, \ldots, D)$ the mappings to the spectral space are given by:

$$
\begin{aligned}
X_a \;: \quad \mathbb{T} \times \left[r_{a,\text{L}}^*, r_{a,\text{R}}^*\right] \quad &\longrightarrow \quad \mathbb{T} \times [-1, 1] \\
(t, r^*) \quad &\longmapsto \quad (T, X_a)
\end{aligned}
\tag{4.10}
$$

where $\mathbb{T} = [t_o, t_f]$ is the evolution time interval and

$$
\begin{aligned}
T(t) \;&=\; t \,, \\
X_a(r^*) \;&=\; \frac{2r^* - r_{a,\text{L}}^* - r_{a,\text{R}}^*}{r_{a,\text{R}}^* - r_{a,\text{L}}^*} \,.
\end{aligned}
\tag{4.11}
$$

- The inverse mappings, i.e. from the spectral domain to the physical ones Ω_a, are defined by:

$$
\begin{aligned}
r^*|_{\Omega_a} \;: \quad \mathbb{T} \times [-1, 1] \quad &\longrightarrow \quad \mathbb{T} \times \left[r_{a,\text{L}}^*, r_{a,\text{R}}^*\right] \\
(T, X) \quad &\longmapsto \quad (t, r^*)
\end{aligned}
\tag{4.12}
$$

where

$$t(T) = T\,,$$

$$r^*(X)|_{\Omega_a} = \frac{r^*_{a,\mathrm{R}} - r^*_{a,\mathrm{L}}}{2} X + \frac{r^*_{a,\mathrm{L}} + r^*_{a,\mathrm{R}}}{2}\,. \tag{4.13}$$

Notice that, since we discretise each subdomain independently and since the spectral domains are always in the interval $[-1, 1]$, there are as many mappings as subdomains.

4.3   Discretisation of the Field Equations

In Chapter 3, we introduced two different ways for solving the field equations, namely using the field variables $\boldsymbol{U}$ or using the characteristic variables $\boldsymbol{N}$. In addition, it was shown that the jump conditions at the boundaries between subdomains can be enforced employing the penalty method or the direct communication of the characteristic fields. The results presented in this chapter have been obtained employing the evolution of the field variables $\boldsymbol{U} = (\psi, \phi, \varphi)$, and the communication across subdomains has been enforced with the penalty method. In what follows we describe the structure of the evolution equations that we implement in our computations.

The structure of the field equations depends on whether the subdomain involved contains the particle at one boundary (see the discussion at the end of Section 4.2) and, if so, on whether it is located at the right boundary or at the left boundary of that subdomain. In other words, if the subdomain in question is located to the left (Ω_{P}) or to the right ($\Omega_{\mathrm{P}+1}$) of the particle. Furthermore, as we mentioned in Section 3.6, our ODEs are solved at each collocation point X_i. Then, the structure of the field equations depends also on whether the variables are associated with collocation points at the boundaries or inside a given subdomain.

Let us consider first the field variables $\boldsymbol{U}_N$ at the subdomains Ω_{P} and $\Omega_{\mathrm{P}+1}$. The equations at the inner points, $\{X_i\}$ ($i = 1, \ldots, N$) are just given by Eq. (3.23).

$$\partial_T \psi_i = \phi_i\,, \tag{4.14}$$

$$\partial_T \phi_i = \partial_{r^*}\varphi_i - V_\ell^i\,\psi_i \tag{4.15}$$

$$\partial_T \varphi_i = \partial_{r^*}\phi_i \tag{4.16}$$

On the other hand, the evolution equations at the nodes of the interfaces, $r^*_{\mathrm{P},\mathrm{R}}$ ($X_{\mathrm{P}} = 1$) and $r^*_{\mathrm{P}+1,\mathrm{L}}$ ($X_{\mathrm{P}+1} = -1$), are modified in the following way:

(i) Equations valid at the right boundary of Ω_{P} (we have simplified the notation by dropping the harmonic indices ℓ and m)

$$\partial_T \psi_{\text{P,N}} = \phi_{\text{P,N}} - \tau_\psi^{\text{P,R}} \left(\psi_{\text{P,N}} - \psi_{\text{P+1,0}} \right) , \tag{4.17}$$

$$\partial_T \phi_{\text{P,N}} = (\partial_{r^*} \varphi_{\text{P}})_{\text{N}} - V_\ell^{\text{P,N}} \psi_{\text{P,N}} \tag{4.18}$$
$$- \frac{\tau_\phi^{\text{P,R}}}{2} \left[\phi_{\text{P,N}} + \varphi_{\text{P,N}} - \left(\phi_{\text{P+1,0}} + \varphi_{\text{P+1,0}} \right) + [\varphi]_p^{\text{P,P+1}} \right] ,$$

$$\partial_T \varphi_{\text{P,N}} = (\partial_{r^*} \phi_{\text{P}})_{\text{N}} \tag{4.19}$$
$$- \frac{\tau_\varphi^{\text{P,R}}}{2} \left[\phi_{\text{P,N}} + \varphi_{\text{P,N}} - \left(\phi_{\text{P+1,0}} + \varphi_{\text{P+1,0}} \right) + [\varphi]_p^{\text{P,P+1}} \right] ,$$

where $\tau_\psi^{\text{P,R}}$, $\tau_\phi^{\text{P,R}}$, and $\tau_\varphi^{\text{P,R}}$, are penalty (constant) coefficients associated with the evolution of the field variables $\psi_{\text{P,N}}$, $\phi_{\text{P,N}}$, and $\varphi_{\text{P,N}}$ respectively. The quantities $[\phi]_p^{\text{P,P+1}}$ and $[\varphi]_p^{\text{P,P+1}}$ are the jumps across the subdomains Ω_{P} and $\Omega_{\text{P+1}}$, given in Eq. (3.18) and Eq. (3.21); and $\psi_{\text{P+1,0}}$, $\phi_{\text{P+1,0}}$, and $\varphi_{\text{P+1,0}}$ are the values of the solutions obtained at the node to the right of the particle, whose evolution equations are given in what follows.

(ii) Equations valid at the left boundary of $\Omega_{\text{P+1}}$:

$$\partial_T \psi_{\text{P+1,0}} = \phi_{\text{P+1,0}} - \tau_\psi^{\text{P+1,L}} \left(\psi_{\text{P+1,0}} - \psi_{\text{P,N}} \right) , \tag{4.20}$$

$$\partial_T \phi_{\text{P+1,0}} = \left(\partial_{r^*} \varphi_{\text{P+1}} \right)_0 - V_\ell^{\text{P+1,0}} \psi_{\text{P+1,0}} \tag{4.21}$$
$$- \frac{\tau_\phi^{\text{P+1,L}}}{2} \left[\phi_{\text{P+1,0}} - \varphi_{\text{P+1,0}} - \left(\phi_{\text{P,N}} - \varphi_{\text{P,N}} \right) + [\varphi]_p^{\text{P,P+1}} \right] ,$$

$$\partial_T \varphi_{\text{P+1,0}} = \left(\partial_{r^*} \phi_{\text{P+1}} \right)_0 \tag{4.22}$$
$$+ \frac{\tau_\varphi^{\text{P+1,L}}}{2} \left[\phi_{\text{P+1,0}} - \varphi_{\text{P+1,0}} - \left(\phi_{\text{P,N}} - \varphi_{\text{P,N}} \right) + [\varphi]_p^{\text{P,P+1}} \right] ,$$

where $\tau_\psi^{\text{P+1,L}}$, $\tau_\phi^{\text{P+1,L}}$, and $\tau_\varphi^{\text{P+1,L}}$ are the penalty coefficients associated with the evolution of the field variables $\psi_{\text{P+1,0}}$, $\phi_{\text{P+1,0}}$, and $\varphi_{\text{P+1,0}}$ respectively. The fields $\psi_{\text{P,N}}$, $\phi_{\text{P,N}}$, and $\varphi_{\text{P,N}}$ are the solutions obtained at the boundary node to the left of the particle, whose equations are given above. We recall that the boundaries of the adjacent subdomains are identified [Eq. (4.5)].

Regarding the field variable ψ, which is continuous at the particle location, we have also experimented with an alternative way to pass the information of its evolution from one subdomain to another. This consists in evolving first ϕ and φ and subsequently use the result to evolve ψ. In this way, ψ can be seen as a *subsidiary* variable and instead of employing the penalty method to impose its continuity, we can just replace the right-hand sides of Eq. (4.17) and Eq. (4.20) by the expressions:

$$\partial_T \psi_{\mathrm{P},N} = (\phi_{\mathrm{P},N} + \phi_{\mathrm{P+1},0})/2\,, \tag{4.23}$$

$$\partial_T \psi_{\mathrm{P+1},0} = (\phi_{\mathrm{P},N} + \phi_{\mathrm{P+1},0})/2\,, \tag{4.24}$$

which, by construction, ensure the continuity of ψ up to machine precision.

Finally, the outgoing (global) boundary conditions implemented at the outer subdomains are given by (see Eq. (3.55) and Eq. (3.56)):

- At the horizon $r^* = r^*_{\mathrm{H}}$:

$$\partial_T \psi_{1,\mathrm{H}} = \phi_{1,\mathrm{H}}\,, \tag{4.25}$$

$$\partial_T \phi_{1,\mathrm{H}} = \partial_T \varphi_{1,\mathrm{H}}\,, \tag{4.26}$$

$$\partial_T \varphi_{1,\mathrm{H}} = (\partial_{r^*}\phi_1)_{\mathrm{H}}\,, \tag{4.27}$$

- At spatial infinity $r^* = r^*_{\mathrm{I}}$:

$$\partial_T \psi_{\mathrm{D,I}} = \phi_{\mathrm{D,I}}\,, \tag{4.28}$$

$$\partial_T \phi_{\mathrm{D,I}} = -\partial_T \varphi_{\mathrm{D,I}}\,, \tag{4.29}$$

$$\partial_T \varphi_{\mathrm{D,I}} = (\partial_{r^*}\phi_{\mathrm{D}})_{\mathrm{I}}\,, \tag{4.30}$$

  where the subindex 1 refers to the first subdomain and D to the last one.

Due to the structure of our equations the penalty term is taken to be positive, i.e. $\tau_U^\pm > 0$. The values of the penalty coefficients were chosen inspired by studies in numerical analysis of the advection equation (see [Hesthaven 2000b]), which suggest that the penalty coefficients should be proportional to N^{-2}, i.e. proportional to τ_{CFL}, where τ_{CFL} is the maximum time step that we can employ in the integration of the evolution equations [Eq. (3.118)].

4.4 Improving the Resolution of the Fields

The different subdomains are distributed along the spatial computational domain with their sizes increasing from the particle location towards the

boundaries. The sizes of the subdomains at both sides of the particle play a decisive role. Indeed, the degree of resolution achieved depends on how well we can resolve all the field modes involved in their computation. In this section, we are going to introduce a criterium to choose the size of the subdomains, $\Delta r^* \equiv r_{a,N}^* - r_{a,0}^*$, and the number of collocation points N (see [Canizares 2011]).

In order to address this question, we look at the harmonic field modes generated by the charged particle in circular motion. They behave like *forced* oscillators, whose source term oscillates like $\exp\{im\,\omega_p t\}$ (where $\omega_p = \sqrt{M_\bullet/r_p^3}$ is the orbital angular velocity of the particle) [see Eq. (2.84)]. Moreover, the potential V_ℓ decays quite fast away from the location of its maximum, so that the field looks like a monochromatic wave in the regions where the potential is weak. On the other hand, the wavelength of the different field modes is controlled by the harmonic number m and are given by $\lambda_m = \lambda_1/m$, where $\lambda_1 = 2\pi/\omega_p$ is the wavelength of the $m = 1$ modes. Therefore, in a given domain Ω_a of (coordinate) size Δr^*, modes with different harmonic number m require different resolutions, understood as the ratio $\Delta r^*/N$. For instance, given two modes $\Phi^{\ell m}$ and $\Phi^{\ell' m'}$ such that $m < m'$, i.e. with $\lambda_m > \lambda'_m$, we can fit more wavelengths of the mode $\Phi^{\ell' m'}$ inside Ω_a than of the mode $\Phi^{\ell m}$. In practice, this means that the lower modes can be resolved with a smaller amount of collocation points. To achieve a similar degree of accuracy for the higher modes, we can proceed mainly in two ways: (i) Diminishing Δr^*, which in turn means to change the number of subdomains D that cover the computational domain (if we reduce Δr^* we need more domains and the converse), and (ii) increasing the number of collocation points N. From our simulations we have found that adjusting the size of the domains to the wavelength size, i.e. $\Delta r^* \simeq \lambda_m$, the values of the retarded field modes converge and are resolved using a minimum N that is given by:

$$N \sim \Delta r^*/(2M_\bullet) + 25\,. \tag{4.31}$$

This provides a rule of thumb for the choice of Δr^* and N as a function of m:

$$\Delta r^*(m) \sim \lambda_m \qquad \text{and} \qquad N(m) = [\Delta r^*/(2M_\bullet) + 25]\,, \tag{4.32}$$

where $[x]$ here denotes the integer closest to x. In turn, by adapting the resolution for each m-mode varying Δr^*, we adapt the computational time step, since the CFL condition on the allowed size of the time step is given by [Eq. (3.118)] :

$$\Delta t_{CFL} \sim \pi^2 |r_R^* - r_L^*|/(4N^2)\,, \tag{4.33}$$

which is set by the size of the smaller subdomain employed. Consequently, the number of time steps required, T_{ns}, for a simulation is going to be proportional to m as:

$$T_{ns}^m = m \, T_{ns}^{m=1} \, . \tag{4.34}$$

This assume that we use the same number of subdomains for all the field modes, but it is clear that modes with low m (would) need less subdomains than modes with high m. Then, this is another source of reduction of computational time.

In order to further investigate this question, we conducted a series of simulations to study the behaviour of the field modes $\Phi^{\ell m}$ under changes of Δr^* and N. In particular, we employ the modes $\Phi^{8,2}$ and $\Phi^{8,8}$, and the results at the particle location are shown in Figure 4.3 for $t = 500 M_\bullet$. As we can see, it is crucial to choose carefully Δr^* for a fixed value of N, otherwise we can find ourselves in one of the following situations: Either Δr^* is too big and then we need a high number N of collocation points to resolve all the modes, or Δr^* is too small and we are using too many collocation points, i.e. we are performing unnecessary computations to resolve the modes.

4.5 Validation of the Numerical Code

In general, the presence of a singular source term in the evolution equations implies that the global solution (the solution in the whole computational domain) is not smooth and one would not expect exponential convergence for our solutions. However, as we have seen in Chapter 3, the PwP scheme avoids dealing with the Dirac delta distribution by replacing the particle with a set of boundary conditions, actually jump conditions, between subdomains. In this way, the PwP scheme preserves the exponential convergence of the PSC method and we have tested this in our numerical evolutions (see Section 3.6).

In order to test whether the convergence of the numerical implementation of the PwP scheme is indeed exponential, we consider a fixed number of (different) subdomains and we perform simulations increasing N gradually. In particular, we have employed $D = 7$ with the following distribution:

$$
\begin{aligned}
\frac{(r^* - r_p^*)}{M_\bullet} \ \in \ & [-550, -12.6] \cup [-12.6, -2.6] \cup [-2.6, 2.6] \cup [2.6, 0.0] \\
& \cup [0.0, 12.4] \cup [12.4, 17.4] \cup [17.4, 500.0] \, .
\end{aligned}
\tag{4.35}
$$
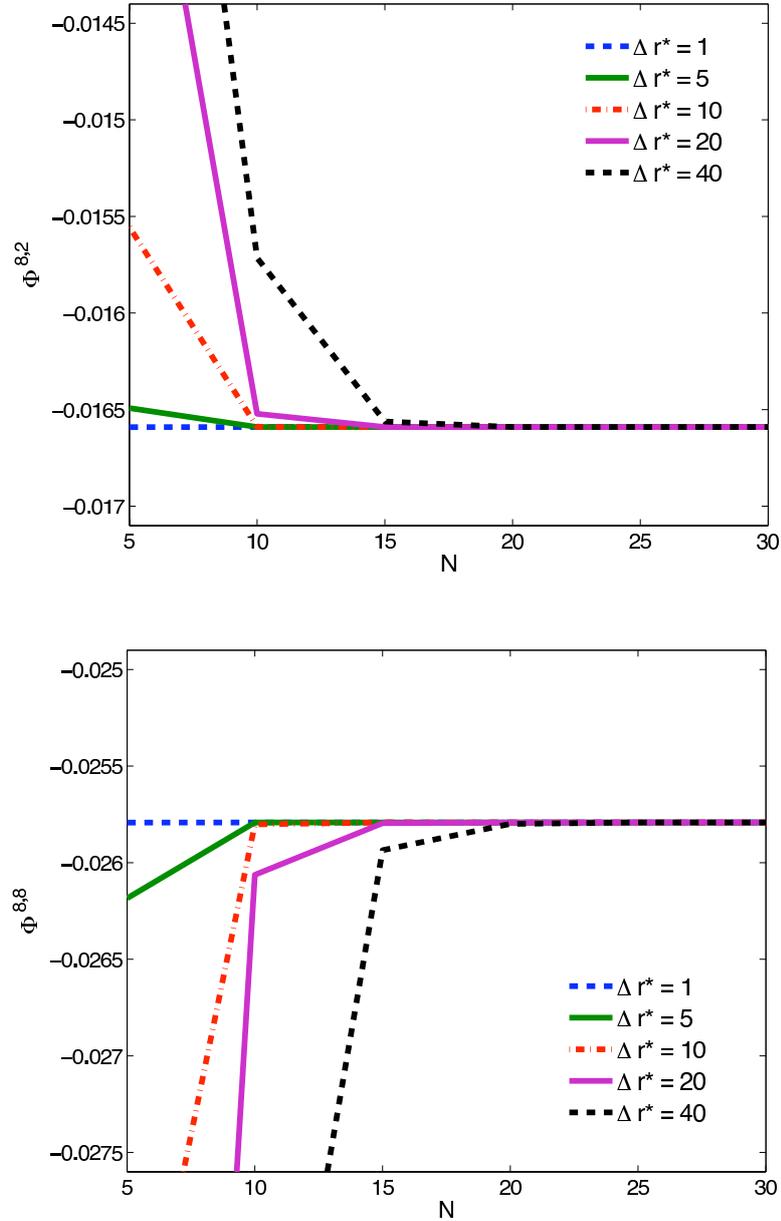
Figure 4.3: *Values of the $\Phi^{8,2}$ (top) and $\Phi^{8,8}$ (bottom) modes of the retarded field at the particle location, as computed from the domain to the right of it, Ω_P, with respect to the number of collocation points N. Each line correspond to a different coordinate size of the domain where the calculations are done: $\Delta r^*/M_\bullet = 1, 5, 10, 20, 40$. The plot shows how the values of the modes converge as Δr^* is decreased and N is increased. It is remarkable to realise that for small coordinate size the convergence is reached with few collocation points.*
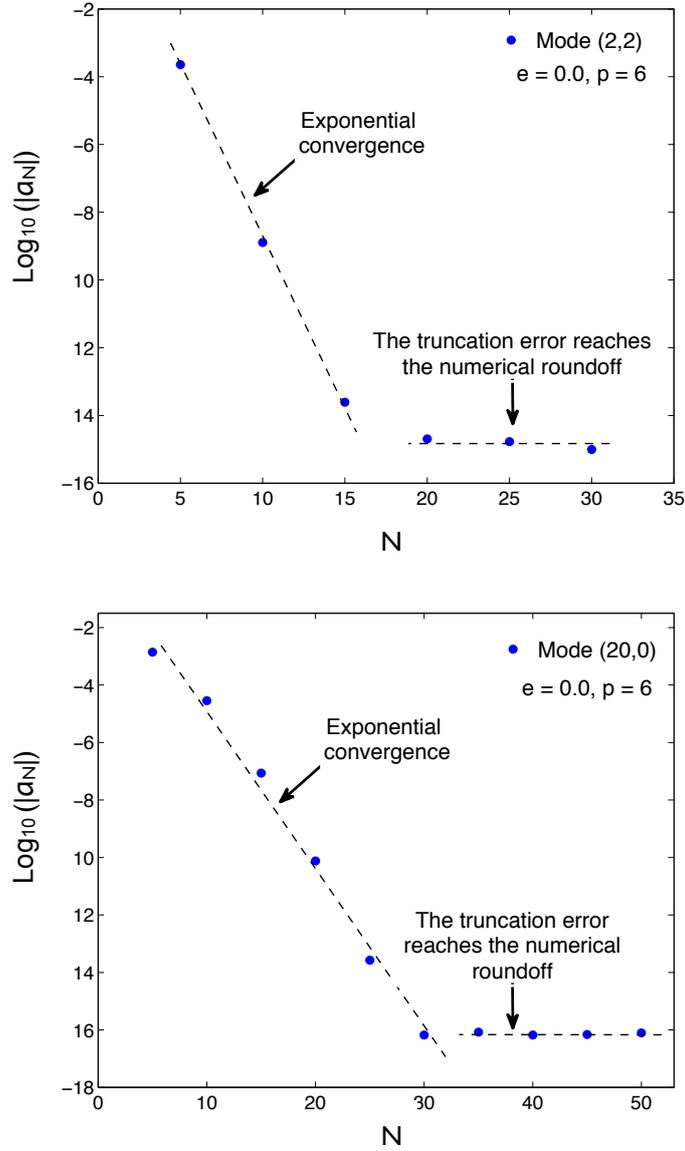
Figure 4.4: *Convergence plots ($\log_{10} |a_N|$ versus N) for the variable $\psi^{\ell m} = r \, \Phi^{\ell m}$. The figures show the results for different field harmonic modes generated by a particle in a circular orbit with $r = 6M_\bullet$ (last stable orbit). In particular, the top figure corresponds to the mode $(\ell, m) = (2, 2)$ and the bottom figure to the mode $(\ell, m) = (20, 0)$. The data has been obtained from the domain to the right of the particle, whose coordinate size, $\Delta r^* = 5M_\bullet$. We can see how exponential convergence is achieved until machine roundoff is reached.*

With this setup, we compute the field modes: $(\ell, m) = (2, 2)$ and $(\ell, m) = (20, 0)$ and their truncation error [Eq. (3.110)]. As one can see from Figure 5.3, the truncation error decreases exponentially by increasing the number of col-

location points. Then, we can conclude that our PwP scheme indeed provide solutions smooth enough to preserve the *a priori* exponential convergence of the PSC method [Canizares 2011].

In Figure 4.5, we present snapshots of the field mode with $\ell = m = 2$ obtained when the particle is at the Last Stable Orbit (LSO). These simulations used 7 subdomains and 50 collocation points per subdomain, and the snapshots have been taken after a substantial time has passed ($t = 650M_\bullet$) and a number of wave cycles have been generated. The figure includes insets of the different variables, ($\psi^{2,2}, \phi^{2,2}, \varphi^{2,2}$), near the particle location. These snapshots illustrate the ability of our method to capture the structure of the solution near the particle, and in particular the ability of resolving the jump in the radial derivative of the field mode (this information is encoded in the variable $\varphi^{\ell m}$) [Eq. (3.21)].

Notice that it is not the same having a number N of collocation points inside D domains that having $N \cdot D$ points in one single domain, since these two possibilities have very different computational cost (associated with the computation of the FFT). Moreover, the smaller the size of a subdomain, the bigger the density of collocation points and, in turn, the higher the field resolution. This is an important fact and has to be considered in a situation where the need for resolution comes only from some isolated regions of the computational domain. Like in our problem, where we only need more resolution around the particle. On the other hand, from the point of view of the evolution, it is important to take into account that the CFL condition with PSC methods [Eq. (4.33)] is more stringent than in FD schemes. Since in the former Δt_{CFL} goes like $1/N^2$, whereas in FD schemes it goes like $1/N$. Hence, increasing the number of subdomains for a fix total number of collocation points can help in having a bigger Δt_{CFL}, that is in performing faster computations.

In addition, the multidomain scheme can be seen as a way of implementing numerical adaptivity, in the sense that we can construct small subdomains for the regions that need to be well resolved, essentially near the particle, and large subdomains for the regions that do not need to have high resolution, essentially far away from the particle.

In order to illustrate how the multidomain structure of our numerical framework works, we have performed simulations with a fixed number of collocation points but increasing the number of subdomains [Canizares 2009]. The goal is to show how the field resolution improves by adding new subdomains. As we have seen, the waveforms of the field modes are in principle easy to resolve, but for modes with high ℓ and m the wavelength gets reduced since we have
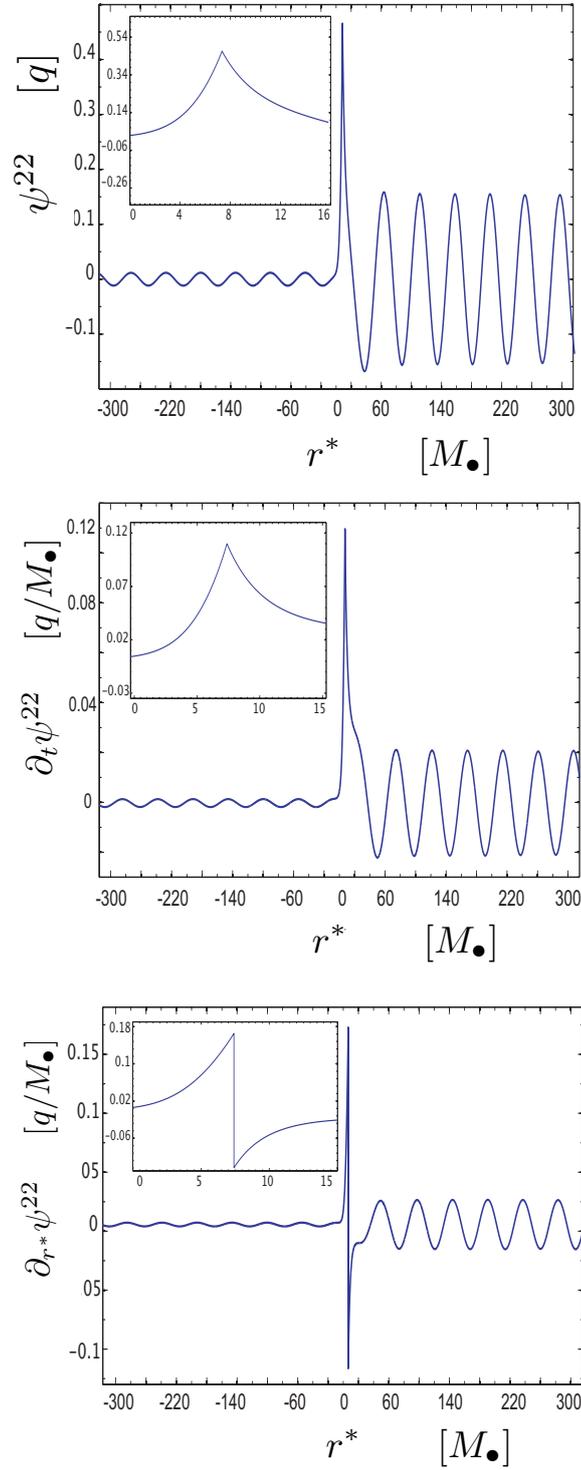
Figure 4.5: *Snapshots corresponding to the mode $\ell = m = 2$ of the scalar field, generated during the evolution of the scalar charged particle in circular motion at the LSO ($r_p^* = 7.4 M_\bullet$). They show the evolution of the variables $\psi^{\ell m}$ (top), $\phi^{\ell m}$ (center), and $\varphi^{\ell m}$ (botton).*
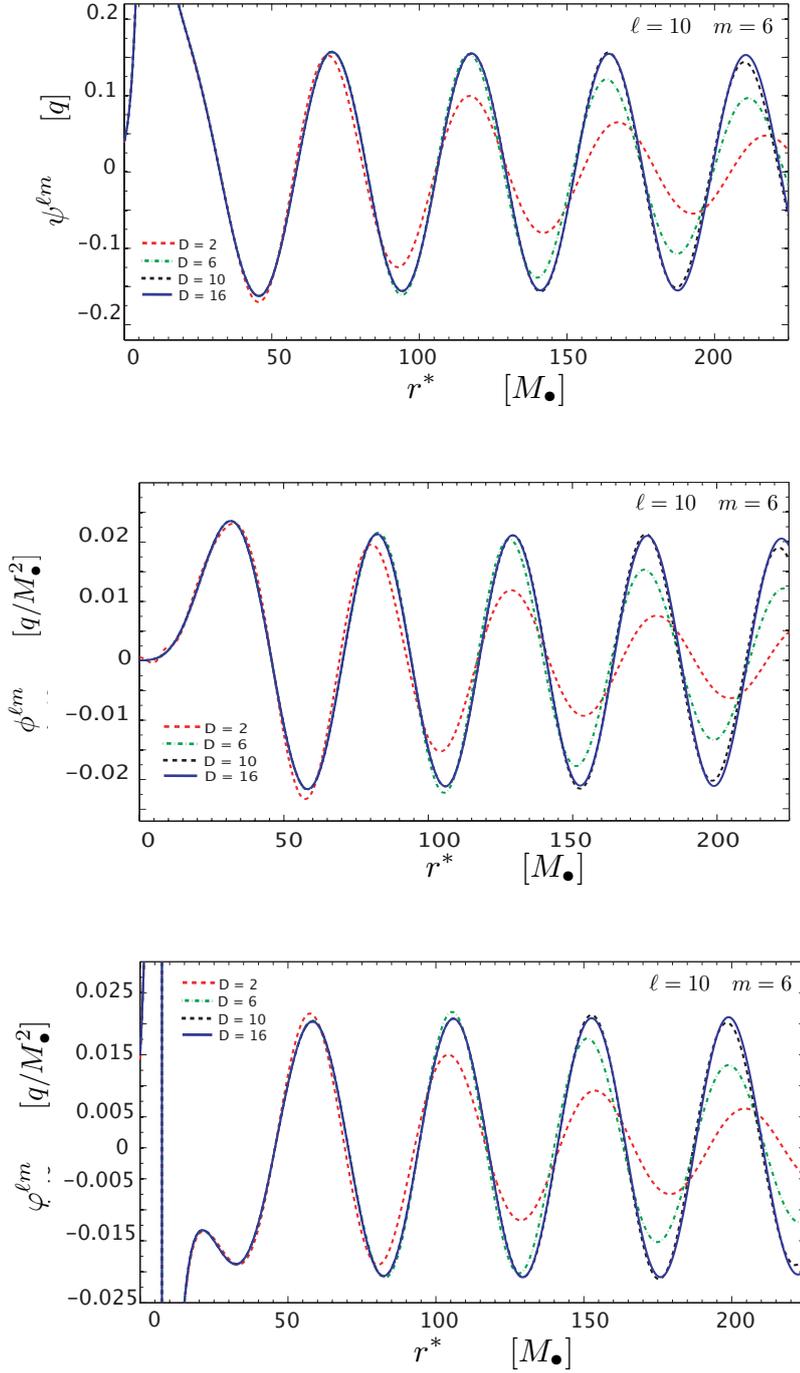
Figure 4.6: *Snapshot of the evolution of the scalar charged particle in circular orbital motion at the LSO for the mode $\ell = 10$ and $m = 6$. Each plot shows different evolutions of the variables $\psi^{\ell m}$ (top), $\phi^{\ell m}$ (centre), and $\varphi^{\ell m}$ (bottom), for a fixed number of collocation points ($N = 50$), but for different numbers of subdomains ($D = 2, 6, 10, 16$). The snapshots has been taken at $t = 500 M_\bullet$.*

higher density of waves that for low m. These waves are moving away and need to be resolved. In Figure 4.6, we show snapshots of evolutions with 50 collocation points per subdomain, but with different number of subdomains, namely from $D = 2$ to $D = 16$ (half of them to the left of particle and the other half to the right). The figure shows the mode $\ell = 10$ and $m = 6$ (so that the period of the waves is $\pi/(3\Omega_p)$) for the three retarded fields (ψ, ϕ, φ). We can see how with few subdomains the waves are unresolved, and that by increasing the number of subdomains the solutions converge and we obtain better accuracy (we can see how the waves get better resolved) with a much less computational cost as if we would have increase the number of collocation points in a single domain.

In conclusion, the multidomain structure is a very useful tool that provides adaptivity to achieve accurate results with a reasonable computational cost. The key point is to realise what is the optimal number of subdomains, their size, and their distribution over the whole computational domain. Given that in our case the period of the waves changes with the harmonic number m, the optimal strategy for setting the subdomain is to adapt the multidomain structure to the value of m.

4.6   Scalar Self-Force Results

We present some self-force results obtained with the PSC implementation of the PwP, where we have employed both the penalty method and the direct communication of the characteristic fields (see Section 3.4). Since both techniques lead to implementations of the PwP scheme which are different enough to be considered as different numerical codes, this provides us with a good cross-check for the numerical results in the self-force computations.

Our numerical code provides results for the gradient of the regular field, which give rise to the self-force components [see Eq. (2.91)]:

$$\mathcal{F}_t = q\Phi_t^{\mathrm{R}}, \quad \mathcal{F}_r = q\Phi_r^{\mathrm{R}}, \quad \mathcal{F}_\phi = q\Phi_\phi^{\mathrm{R}}. \tag{4.36}$$

These self-force components have been evaluated at $r = r_{LSO} := 6M_\bullet$, $\theta_p = \pi/2$ and $\phi_p = 0$ ($\phi_p := \sqrt{M_\bullet/r_p^3}\,t$ for circular orbits). For these simulations we have used the penalty method (Section 3.4.1) to communicate the field modes across the subdomains boundaries and, thus, two values of the self-force components are obtained: One from the subdomain to the left (Ω_{P}) $\mathcal{F}_\alpha^{\mathrm{R},-} = \mathcal{F}_\alpha^{\mathrm{R}}(r_{\mathrm{P},N}^*)$, and the other one from the subdomain to the right $(\Omega_{\mathrm{P}+1})$, $\mathcal{F}_\alpha^{\mathrm{R},+} = \mathcal{F}_\alpha^{\mathrm{R}}(r_{\mathrm{P}+1,0}^*)$. This also provides us with a test for the numerical calculations,

Table 4.1: *Values of the regular field at the particle location, $(\Phi_\alpha^{R,-}, \Phi_\alpha^{R,+})$, computed at $\phi_p = 0$. These results correspond to the subdomains where the particle is located and for the LSO [Canizares 2009]. We compare them with the results obtained with a time-domain method in [Haas 2007], and with a frequency-domain method in [Diaz-Rivera 2004] and [Haas 2006].*

Component of Φ_α^R	Estimate using the PwP Method	Estimate from Frequency-domain	Estimate from Time-domain
$(\Phi_t^{R,-}, \Phi_t^{R,+}) M_\bullet^2/q$	$(3.60777, 3.60778) \cdot 10^{-4}$	$3.609072 \cdot 10^{-4}$	$3.60339 \cdot 10^{-4}$
$(\Phi_r^{R,-}, \Phi_r^{R,+}) M_\bullet^2/q$	$(1.67364, 1.67362) \cdot 10^{-4}$	$1.67728 \cdot 10^{-4}$	$1.6767 \cdot 10^{-4}$
$(\Phi_\phi^{R,-}, \Phi_\phi^{R,+}) M_\bullet/q$	$(-5.30422, -5.30438) \cdot 10^{-3}$	$-5.304231 \cdot 10^{-3}$	$-5.30424 \cdot 10^{-3}$

since both values have to agree to a high degree of precision. We have used $N = 50$, and a number of subdomains that ranges from $D = 12$ to $D = 34$. The outer boundaries have been set between $r^* = \pm(500 - 700)M_\bullet$ and we have truncated the multipolar expansion of the fields at $\ell_{\max} = 20$, i.e. we have to compute 231 evolutions [see Eq. (3.125)].

In the Table 4.1, we present the results obtained with the PwP scheme for a scalar particle in the last stable circular orbit around a Schwarzschild MBH [Canizares 2009]. Our results are compared with two types of calculations in the literature: (i) Calculations based on a time-domain method that employ a numerical scheme based on the characteristic formulation of the scalar field equations [Haas 2006]; (ii) calculations based on an accurate frequency-domain method [Diaz-Rivera 2004]. As we can see, we get a good numerical approximation to the self-force components using a modest amount of computational resources. In particular, we have computed the field modes up to $\ell_{\max} = 20$, with $N = 50$ collocation points per subdomain, and a number of subdomains between $D = 12 - 32$. The smaller subdomains, as measured in terms of the tortoise coordinate, have size $\Delta r^* = 20 M_\bullet$ and are located at both sides of the particle, i.e the particle is set at the interface between these subdomains. The average time for a full self-force calculation of the type just described in a computer with two Quad-Core Intel Xeon processors at $2.8\,\mathrm{GHz}$ is always in the range $20 - 30$ minutes. The relative error in the radial component of the self-force (the one that needs to be regularised) to frequency-domain calculations in (ii) is 0.2% and the one to time-domain calculations in (i) is 0.18%. Finally, it is easy to check that the self-force results obtained agree with the helical condition of Eq. (2.97).

On the other hand, we have also performed simulations with a different setup, namely with $D = 43$ and $N = 50$. In this case, the size of the subdomains where the particle is located are adjusted to the wavelength of the higher mode

employed in our computations ($\ell = 40$), which corresponds to $\Delta r_p^* \sim 2M_\bullet$, and the rest of the radial space has been covered with subdomains of increasing size from $|\Delta r^*| = 50M_\bullet$ to $|\Delta r^*| = 100M_\bullet$. Here we quote the self-force results obtained employing the direct communication of the characteristic fields (see Section 3.4.2) to match the solutions at the subdomain interfaces:

$$\Phi_t^{\text{R}} = 3.609002 \times 10^{-4} \frac{q}{M_\bullet^2}, \tag{4.37}$$

$$\Phi_r^{\text{R}} = 1.677282 \times 10^{-4} \frac{q}{M_\bullet^2}, \tag{4.38}$$

$$\Phi_\phi^{\text{R}} = -5.304233 \times 10^{-3} \frac{q}{M_\bullet}, \tag{4.39}$$

By construction the direct communication of the characteristic fields (Section 3.4.2) provides identical values at both nodes associated with the particle. For this reason, the self-force values are the same up to machine precision. Comparing the value obtained for Φ_r with that obtained in [Diaz-Rivera 2004] using frequency-domain methods (see Table 4.1), the fractional error obtained is of $5 \cdot 10^{-5}\%$. Moreover, a full self-force calculation like this, in a computer with two Quad-Core Intel Xeon processors at 2.8 GHz, is always in the range of 10 to 15 minutes instead of 30 minutes for computations without adjusting the subdomains size, like the ones showed in Table 4.1.

Summarising, in this chapter we have shown that the PwP scheme provides accurate self-force results in the time-domain. This is a direct consequence of the fact that this method "erases" the particle from the computational domain and, consequently, we do not resolve the (artificial) numerical scale that other methods need to account for. In addition, the solutions obtained have exponential convergence, since the properties of the PSC method used to discretise in space are preserved within the PwP scheme.

EMRIs in Eccentric Motion

We've only played two games, and we've improved from the first game and hopefully we'll improve every time.
Sidney Nozaki.

5.1   Introduction

In the previous chapter, we have shown that the PwP technique is able to perform efficient time-domain computations of the self-force for scalar EMRI with circular orbits. Also, it was shown that it is a flexible technique allowing for adjustments and further improvements. In this regard, the next natural step is to modify the PwP scheme to allow for modelling EMRIs with generic (bound) orbits. In what follows, we are going to show how the PwP technique can be adapted to cope with these motions. Of relevant importance is the redefinition of the mapping between the physical and spectral domains, since it is going to play a key roll in keeping the particle at a fixed interface between two subdomains.

5.2   From Circular to Eccentric Orbits

The centerpiece of the PwP scheme is to set the particle at one of the interfaces and replace its presence in the field equations by a set of boundary conditions. When the particle is performing circular orbits this can be done by construction, since the radial location of the particle remains constant along the whole time evolution, as it is shown in Figure 5.1. However, things are very different when the particle moves in an eccentric, since it would cross inside the subdomains spoiling the essence of the PwP technique. To circumvent this situation, we modify the linear mapping given by Eqs. (4.10) - (4.12), so that it becomes a time-dependent mapping between the physical $r_p^* = r_p^*(t)$

and spectral coordinates $X(t, r^*)$. In this way, the structure of the physical domain is similar to the one introduced in Section 4.2, but now the particle is located at a dynamic interface, i.e. at the boundaries of two subdomains that will move with the particle as it is shown in Figure 4.2. That is, the boundaries are commoving with the particle in the radial direction.
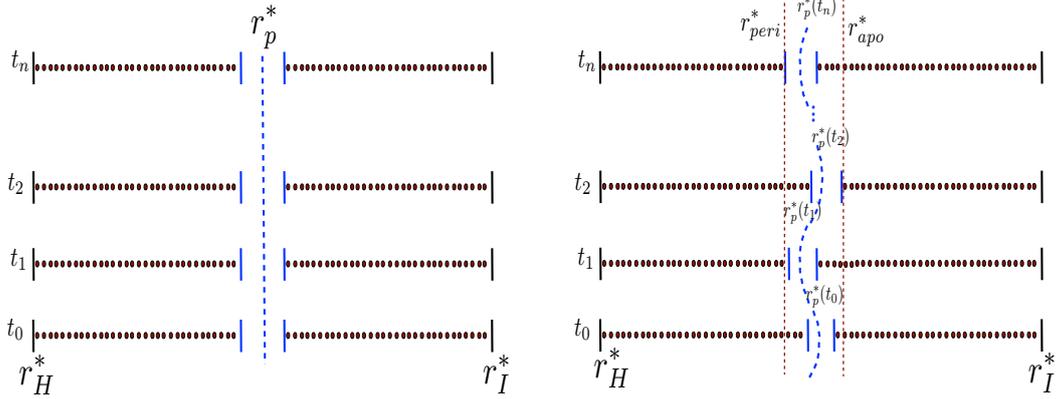
Figure 5.1: *Structure of the (discretised) one-dimensional spatial grid for circular orbits (left), where the particle remains at the same radial position and eccentric orbits (right), where the particles moves between the pericentre and and the apocentre.*

The way in which we modify the mappings of Eq. (4.10) and Eq. (4.12) is given by the following expressions:

$$X_a \quad : \quad \mathbb{T} \times \left[r^*_{a,\mathrm{L}}, r^*_{a,\mathrm{R}}\right] \quad \longrightarrow \quad \mathbb{T} \times [-1, 1]$$
$$(t, r^*) \quad \longmapsto \quad (T, X_a) \tag{5.1}$$

where $\mathbb{T} = [t_o, t_f]$ is the evolution time interval and:

$$T(t) \quad = \quad t \,,$$
$$X_a(t, r^*) \quad = \quad \frac{2r^* - r^*_{a,\mathrm{L}} - r^*_{a,\mathrm{R}}}{r^*_{a,\mathrm{R}} - r^*_{a,\mathrm{L}}} \,. \tag{5.2}$$

Here, the time dependence in X_a comes from the time dependence of the boundary location $r^*_{a,\mathrm{L}}(t)$ and/or $r^*_{a,\mathrm{R}}(t)$.

On the other hand, the inverse mappings from the spectral domain to each of the subdomains Ω_a are given by:

$$r^*|_{\Omega_a} \quad : \quad \mathbb{T} \times [-1, 1] \quad \longrightarrow \quad \mathbb{T} \times \left[r^*_{a,\mathrm{L}}, r^*_{a,\mathrm{R}}\right]$$
$$(T, X) \quad \longmapsto \quad (t, r^*) \tag{5.3}$$

and

$$
\begin{aligned}
t(T) &= T, \\
r^*(T,X)|_{\Omega_a} &= \frac{r^*_{a,\mathrm{R}} - r^*_{a,\mathrm{L}}}{2} X_{a,i} + \frac{r^*_{a,\mathrm{L}} + r^*_{a,\mathrm{R}}}{2}.
\end{aligned}
\tag{5.4}
$$

Here $X_{a,i}$ is the i-th collocation point at the domain Ω_a, given by Eq. (3.96).

From the relations above, we can compute the following derivatives which are going to be useful for later developments:

$$
(\partial_{r^*} X_a)_i = \frac{2}{r^*_{a,\mathrm{R}} - r^*_{a,\mathrm{L}}}.
\tag{5.5}
$$

$$
(\partial_t X_a)_i = -\frac{\dot{r}^*_p}{r^*_{a,\mathrm{R}} - r^*_{a,\mathrm{L}}} \left\{ \delta^{a,\mathrm{L}}_p + \delta^{a,\mathrm{R}}_p + \left(\delta^{a,\mathrm{R}}_p - \delta^{a,\mathrm{L}}_p \right) X_{a,i} \right\},
\tag{5.6}
$$

$$
\delta^{a,\mathrm{L}}_p = \begin{cases} 1 & \text{if } r^*_p = r^*_{a,\mathrm{L}}, \\ 0 & \text{otherwise,} \end{cases} \qquad \delta^{a,\mathrm{R}}_p = \begin{cases} 1 & \text{if } r^*_p = r^*_{a,\mathrm{R}}, \\ 0 & \text{otherwise.} \end{cases}
\tag{5.7}
$$

In practice, we do not need that all the subdomains change with time. Then, both dynamical and non-dynamical subdomains are employed at the same time, according to whether or not any of their boundary nodes evolves with time. We restrict ourselves to the case in which only two subdomains, namely those containing the particle (Ω_{P} and $\Omega_{\mathrm{P}+1}$), are dynamical, in other words, only $r^*_{\mathrm{P,R}}$ and $r^*_{\mathrm{P}+1,\mathrm{L}}$ are time dependent, as it is shown in Figure 5.1.

At this point, it is worth making the following two remarks:
(i) The time-dependent mappings of Eq. (5.2) and Eq. (5.4) maintain the particle exactly at the boundary between two subdomains and prevent it from entering inside the spatial subdomains. To that end, in the setup that we use here only the boundaries $r^*_{\mathrm{P,R}}$ and $r^*_{\mathrm{P}+1,\mathrm{L}}$ evolve with the particle, leaving the rest fixed. Consequently, the sizes of the subdomains Ω_{P} and $\Omega_{\mathrm{P}+1}$ will change periodically along the time evolution. This will affect the density of collocation points, say $N/\Delta r^*$, of that subdomains and, in turn, the resolution of the field modes near the particle location. For this reason, for a fixed N, we a priori expect that the PwP scheme provides better results when dealing with orbits with moderate eccentricity, i.e. $0 < e \leqslant 0.5$, than when considering high eccentric orbits $e \geqslant 0.5$.
(ii) Although the size of the corresponding physical subdomains change with time, the time-dependent mappings do not affect the size of the "spectral subdomains", i.e. always $X \in [-1,1]$. In this way, we can keep employing the PSC method for the numerical implementation of the PwP scheme.

5.3 High Eccentric Orbits in the PwP Scheme

As we have mentioned before, along this thesis we are only considering the case in which the movement of the particle affects the two subdomains located immediately to its left Ω_{P} and to its right $\Omega_{\text{P}+1}$. This is enough to deal with generic orbits with moderate eccentricity. However, if one wants to model EMRIs with higher eccentricities employing this multidomain framework, the accuracy of the results could be compromised (see the comments on this in the last section). In what follows, we propose a way to circumvent this problem by dealing with an arbitrary number of dynamical subdomains that are all around the particle as it is shown in Figure 5.2. This set of subdomains follows the particle along its evolution absorbing among all of them the total change in the physical (coordinate) size. In this way the change in numerical resolution due to the particle motion is not as abrupt as it would be in the case of having only two dynamical subdomains.

To begin with, let us consider the situation where we have N_d dynamical domains on each side of the particle, $2N_d$ in total (Figure 5.2 shows the case $N_d = 3$), and that the first dynamical domain is $\Omega_m = [r^*_{m,\text{L}}, r^*_{m,\text{R}}]$, which means that $\text{P} = m + N_d$, that is:

$$
\begin{aligned}
\Omega \;=\; & [r^*_{\text{H}}, r^*_{1,\text{R}}] \cup \cdots \cup [r^*_{m,\text{L}}, r^*_{m,\text{R}}] \cup \cdots \cup [r^*_{m+N_d-1,\text{L}}, r^*_p] \cup [r^*_p, r^*_{\text{P},\text{R}}] \\
& \cup \;\cdots\cup [r^*_{\text{P}+N_d-1,\text{L}}, r^*_{\text{P}+N_d-1,\text{R}}] \cup \cdots \cup [r^*_{d,\text{L}}, r^*_{\text{I}}] .
\end{aligned}
\tag{5.8}
$$

Following Figure 5.2, the criterium that we use to determine the motion of the dynamical domains is to demand that all of them to the left of the particle have the same coordinate size (in terms of the radial tortoise coordinate) at any given time, and the same for those to the right of the particle. This completely determines the evolution of the dynamical subdomains. The motion of the dynamical nodes to the left of the particle is described by the following set of equations $(a = m, \ldots, m + N_d - 1)$:

$$
r^*_{a,\text{L}} \;=\; r^*_{m,\text{L}} + (a - m)\frac{r^*_p - r^*_{m,\text{L}}}{N_d} ,
\tag{5.9}
$$

$$
r^*_{a,\text{R}} \;=\; r^*_{m,\text{L}} + (a - m + 1)\frac{r^*_p - r^*_{m,\text{L}}}{N_d} ,
\tag{5.10}
$$

and the motion of the nodes to the right of the particle by $(a = \text{P}, \ldots, \text{P} +$
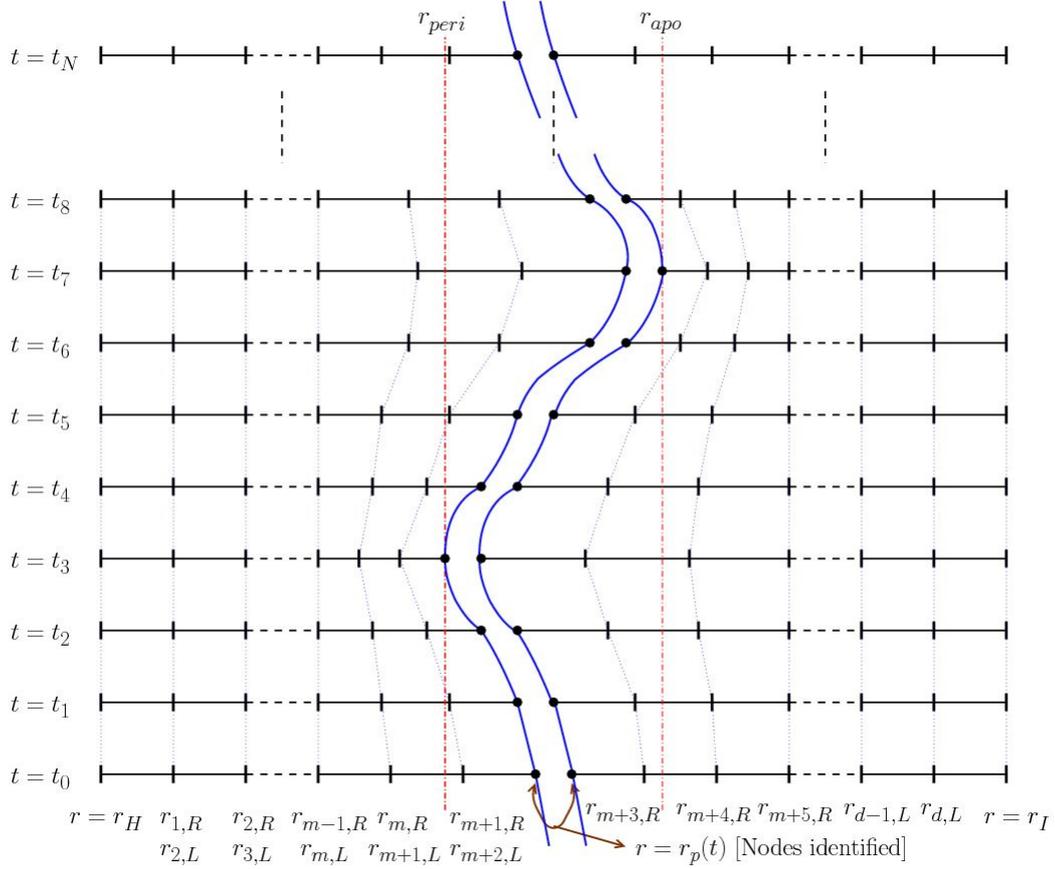
Figure 5.2: *Structure of the one-dimensional spatial computational domain for a generic orbit. The trajectory is restricted to the interval between the pericentre (r_{peri}) and the apocentre (r_{apo}). In the setup shown there are three dynamical domains to the left and right of the particle, namely $[r^*_{m,L}, r^*_{m,R}] \cup [r^*_{m+1,L}, r^*_{m+1,R}] \cup [r^*_{m+2,L}, r^*_{m+2,R}]$ (left) and $[r^*_{m+3,L}, r^*_{m+3,R}] \cup [r^*_{m+4,L}, r^*_{m+4,R}] \cup [r^*_{m+5,L}, r^*_{m+5,R}]$ (right) with $r^*_{m+2,R} = r^*_{m+3,L} = r^*_p$. The figure illustrates how the dynamical subdomains change their coordinate size to adapt to the particle motion.*

$N_d - 1$):

$$r^*_{a,\mathrm{L}} = r^*_p + (a - \mathrm{P})\frac{r^*_{\mathrm{P}+N_d-1,\mathrm{R}} - r^*_p}{N_d}, \qquad (5.11)$$

$$r^*_{a,\mathrm{R}} = r^*_p + (a - \mathrm{P} + 1)\frac{r^*_{\mathrm{P}+N_d-1,\mathrm{R}} - r^*_p}{N_d}, \qquad (5.12)$$

where $r^*_{m,\mathrm{L}}$ and $r^*_{\mathrm{P}+N_d-1,\mathrm{R}}$ are fixed boundary nodes that separate the static from the dynamical domains. The r^*-coordinate size of the dynamical domains changes according to the motion of the particle, as illustrated in Figure 5.2.

5.4 Evolution with Moderate Eccentricity

To compute the retarded field generated by a particle in a generic orbit with moderate eccentricity, we have employed the two sets of variables, $\boldsymbol{U}$ and $\boldsymbol{N}$. Then, the jumps have been enforced by employing the penalty method for both sets of variables, where the direct communication of the characteristic fields has been only employed for the variables $\boldsymbol{N}$ [see Chapter 3]. Here we present results for the following two implementations: (a) The penalty method to communicate solutions of the field variables $\boldsymbol{U} = (\psi^{\ell m}, \phi^{\ell m} \varphi^{\ell m})$, and (b) the direct communication of the characteristic fields to communicate the characteristic variables $\boldsymbol{N} = (\psi^{\ell m}, U^{\ell m}, V^{\ell m})$. Regarding the global boundary conditions, we employ the same ones prescribed for the circular case in Eq. (3.55) and in Eq. (3.56), i.e. outgoing boundary conditions, since the outer boundaries are not affected by the particle motion.

As it was mentioned before, in this work, we consider only two dynamical subdomains: Ω_{P} and $\Omega_{\mathrm{P}+1}$, and the particle is set at their interface $r^*_p = r^*_{\mathrm{P,R}} = r^*_{\mathrm{P}+1,\mathrm{L}}$, with $r^*_{\mathrm{P,R}} = r^*_{\mathrm{P,N}}$ and $r^*_{\mathrm{P}+1,\mathrm{L}} = r^*_{\mathrm{P}+1,0}$. Then, for a given subdomain one encounters two possible situations:

(i) The particle is not located at the interface: In this case we only have to impose the continuity of the solutions. This would correspond to imposing zero RHS to the junction conditions for the field variables $\boldsymbol{U}$, Eqs. (3.15)-(3.21), or for the characteristic fields $\boldsymbol{N}$, Eqs. (3.41)-(3.42). That is, we set $S^{\ell m} = 0$ in these expressions for the jumps.

(ii) The particle is located at the interface: In this case, we have to impose the junction conditions, Eqs. (3.15)-(3.21) for the variables $\boldsymbol{U}$, or Eqs. (3.40)-(3.42) for the characteristic variables $\boldsymbol{N}$, where in these expressions $S^{\ell m}$ is given in Eq. (2.84).

In the remainder of this section, we are going to describe the evolution equations that we need to implement (i) and (ii).

5.4.1   The Penalty Method

Here, we are going to look at the detailed expressions for the evolution equations associated with the penalty method (see Section 3.4.1) and the form of their RHSs that determine the evolution of the field variables $\boldsymbol{U}$.

The algorithm to compute the field generated by a particle in an eccentric orbit only differs from those of the circular orbit case (Section 4.3) when we are dealing with the subdomains where the particle is located. For these subdomains we have to distinguish between four different kinds of situations:
(i) Computations at the interior points for the subdomain to the left of the particle, i.e. in Ω_{P};
(ii) Computations at the interior points for the subdomain to the right of the particle, i.e. in $\Omega_{\mathrm{P}+1}$;
(iii) Computations at the left boundary node of $\Omega_{\mathrm{P}+1}$;
(iv) Computations at the right boundary node of Ω_{P}.

In what follows, we describe the equations for implementing the computations described above (to simplify the notation, in what follows we have dropped the harmonic indices ℓ and m):

(i) The equations for interior points ($i = 1, \ldots, N-1$) valid at the dynamical subdomain to the left of the particle are:

$$\partial_T \psi_{\mathrm{P},i} \;=\; \dot{r}_p^* \frac{1 + X_{\mathrm{P},i}}{2}\, \varphi_{\mathrm{P},i} + \phi_{\mathrm{P},i}\,, \tag{5.13}$$

$$\partial_T \phi_{\mathrm{P},i} \;=\; \dot{r}_p^* \frac{1 + X_{\mathrm{P},i}}{2}\, (\partial_{r^*}\phi_{\mathrm{P}})_i + (\partial_{r^*}\varphi_{\mathrm{P}})_i - V_\ell^{\mathrm{P},i}\, \psi_{\mathrm{P},i}\,, \tag{5.14}$$

$$\partial_T \varphi_{\mathrm{P},i} \;=\; \dot{r}_p^* \frac{1 + X_{\mathrm{P},i}}{2}\, (\partial_{r^*}\varphi_{\mathrm{P}})_i + (\partial_{r^*}\phi_{\mathrm{P}})_i\,, \tag{5.15}$$

where for any quantity $\mathcal{A}$ we compute the spatial derivatives as

$$(\partial_{r^*}\mathcal{A}_{\mathrm{P}})_i = (\partial_{r^*} X_{\mathrm{P}})_i\, (\partial_X \mathcal{A}_{\mathrm{P}})_i\,, \tag{5.16}$$

and $(\partial_{r^*} X_{\mathrm{P}})_i$ is given in Eq. (5.5). Notice that $\partial_X \mathcal{A}_{\mathrm{P}}$ is, indeed, the numerical derivative that we compute. It is performed by changing between the physical and spectral representations, according to Eq. (3.106), see Section 3.6.

(ii) Equations for interior points at the dynamical subdomain to the right of the particle:

$$\partial_T \psi_{P+1,i} = \dot{r}_p^* \frac{1 - X_{P+1,i}}{2} \varphi_{P+1,i} + \phi_{P+1,i} , \tag{5.17}$$

$$\partial_T \phi_{P+1,i} = \dot{r}_p^* \frac{1 - X_{P+1,i}}{2} \left(\partial_{r^*} \phi_{P+1}\right)_i + \left(\partial_{r^*} \varphi_{P+1}\right)_i$$
$$- V_\ell^{P+1,i} \psi_{P+1,i} , \tag{5.18}$$

$$\partial_T \varphi_{P+1,i} = \dot{r}_p^* \frac{1 - X_{P+1,i}}{2} \left(\partial_{r^*} \varphi_{P+1}\right)_i + \left(\partial_{r^*} \phi_{P+1}\right)_i . \tag{5.19}$$

The equations at the interior points of any non-dynamical subdomain are obtained by setting $\dot{r}_p^* = 0$ either at the set of Eqs. (5.13)-(5.15) or at the set of Eqs. (5.17)-(5.19).

(iii) Equations valid at the right boundary of the dynamical subdomain to the left of the particle, that is, at $r^* = r_{P,N}^* = r_p^*(t)$:

$$\partial_T \psi_{P,N} = \dot{r}_p^* \varphi_{P,N} + \phi_{P,N} - \tau_\psi^{P,R} \left(\psi_{P,N} - \psi_{P+1,0}\right) , \tag{5.20}$$

$$\partial_T \phi_{P,N} = \dot{r}_p^* \left(\partial_{r^*} \phi_P\right)_N + \left(\partial_{r^*} \varphi_P\right)_N - V_\ell^{P,N} \psi_{P,N}$$
$$- \frac{\tau_\phi^{P,R}}{2} \left[\phi_{P,N} + \varphi_{P,N} - \left(\phi_{P+1,0} + \varphi_{P+1,0}\right)\right.$$
$$+ \left. [\phi]_p^{P,P+1} + [\varphi]_p^{P,P+1}\right] , \tag{5.21}$$

$$\partial_T \varphi_{P,N} = \dot{r}_p^* \left(\partial_{r^*} \varphi_P\right)_N + \left(\partial_{r^*} \phi_P\right)_N$$
$$- \frac{\tau_\varphi^{P,R}}{2} \left[\phi_{P,N} + \varphi_{P,N} - \left(\phi_{P+1,0} + \varphi_{P+1,0}\right)\right.$$
$$+ \left. [\phi]_p^{P,P+1} + [\varphi]_p^{P,P+1}\right] , \tag{5.22}$$

where $\tau_\psi^{P,R}$, $\tau_\phi^{P,R}$, and $\tau_\varphi^{P,R}$, are (constant) penalty coefficients associated with the evolution of $\psi_{P,N}(T)$, $\phi_{P,N}(T)$, and $\varphi_{P,N}(T)$ respectively. The quantities $[\phi]_p^{P,P+1}$ and $[\varphi]_p^{P,P+1}$ are the jumps across the subdomains Ω_P and Ω_{P+1}, given in Eq. (3.18) and Eq. (3.21).

(iv) Equations valid at the left boundary of the dynamical subdomain to the

right of the particle, i.e. at $r^* = r^*_{\mathrm{P+1,0}} = r^*_p(t)$:

$$\partial_T \psi_{\mathrm{P+1,0}} = \dot{r}^*_p \varphi_{\mathrm{P+1,0}} + \phi_{\mathrm{P+1,0}} - \tau_\psi^{\mathrm{P+1,L}} \left(\psi_{\mathrm{P+1,0}} - \psi_{\mathrm{P,N}} \right) , \quad (5.23)$$

$$\begin{aligned}
\partial_T \phi_{\mathrm{P+1,0}} = {} & \dot{r}^*_p \left(\partial_{r^*} \phi_{\mathrm{P+1}} \right)_0 + \left(\partial_{r^*} \varphi_{\mathrm{P+1}} \right)_0 - V_\ell^{\mathrm{P+1,0}} \psi_{\mathrm{P+1,0}} \\
& - \frac{\tau_\phi^{\mathrm{P+1,L}}}{2} \left[\phi_{\mathrm{P+1,0}} - \varphi_{\mathrm{P+1,0}} - \left(\phi_{\mathrm{P,N}} - \varphi_{\mathrm{P,N}} \right) \right. \\
& \left. - \left[\phi \right]_p^{\mathrm{P,P+1}} + \left[\varphi \right]_p^{\mathrm{P,P+1}} \right] , \qquad\qquad (5.24)
\end{aligned}$$

$$\begin{aligned}
\partial_T \varphi_{\mathrm{P+1,0}} = {} & \dot{r}^*_p \left(\partial_{r^*} \varphi_{\mathrm{P+1}} \right)_0 + \left(\partial_{r^*} \phi_{\mathrm{P+1}} \right)_0 \\
& + \frac{\tau_\varphi^{\mathrm{P+1,L}}}{2} \left[\phi_{\mathrm{P+1,0}} - \varphi_{\mathrm{P+1,0}} - \left(\phi_{\mathrm{P,N}} - \varphi_{\mathrm{P,N}} \right) \right. \\
& \left. - \left[\phi \right]_p^{\mathrm{P,P+1}} + \left[\varphi \right]_p^{\mathrm{P,P+1}} \right] , \qquad\qquad (5.25)
\end{aligned}$$

where again $\tau_\psi^{\mathrm{P+1,L}}$, $\tau_\phi^{\mathrm{P+1,L}}$, and $\tau_\varphi^{\mathrm{P+1,L}}$ are penalty coefficients associated with the evolution of $\psi_{\mathrm{P+1,0}}(T)$, $\phi_{\mathrm{P+1,0}}(T)$, and $\varphi_{\mathrm{P+1,0}}(T)$ respectively. At this point we comment on the equation for $\psi^{\ell m}$. Here, we are enforcing the continuity of this variable via a penalty term. However, there is an alternative to this option, as it has been discussed in Section 4.3 for the circular orbit case. This consists in taking a sort of average of the RHS of the equation for $\psi^{\ell m}$ over the two subdomains that we are trying to communicate. The alternative equation for $\psi^{\ell m}$ would then look as follows:

$$\partial_T \psi_{\mathrm{P+1,0}} = \frac{1}{2} \dot{r}^*_p \left(\varphi_{\mathrm{P,N}} + \varphi_{\mathrm{P+1,0}} \right) + \frac{1}{2} \left(\phi_{\mathrm{P,N}} + \phi_{\mathrm{P+1,0}} \right) , \qquad (5.26)$$

and the same applies to the equation for $\psi_{\mathrm{P,N}}$. In this way, ψ is continuous, to machine precision, by construction.

Notice that we can recover the evolution equations for a particle in a circular orbit (see Section 3.4.1), just by setting $\dot{r}^*_p = 0$ in these expressions.

5.4.2 Direct Communication of the Characteristic Fields

The second implementation of the PwP method is based on the evolution of the characteristic fields $\boldsymbol{N}$. In this case, the solution of the evolution equations is naturally matched by employing the direct communication of the characteristic fields which, as we have seen in Section 3.4.2, requires the computation of the derivatives of the jumps in the case that we want to evolve using the method of lines. In order to obtain the jump time derivatives we use

the expressions of the jumps in Eqs. (3.41)-(3.42) together with the geodesic equations Eq. (2.99), obtaining:

$$
\begin{aligned}
\frac{d\left[U^{\ell m}\right]_p}{dt} =\ & \beta_m \left[-\left\{\rho_p \dot{r}_p^* - \frac{r_p\,\ddot{r}_p^*}{1-\dot{r}_p^*}\Re[Y^{\ell m}] + m\frac{L_p f_p}{E_p r_p}\,\Im[Y^{\ell m}]\right\}\right. \\
& \left. +\ i\left\{\left[\rho_p \dot{r}_p^* - \frac{r_p \ddot{r}_p^*}{1-\dot{r}_p^*}\right]\Im[Y^{\ell m}] - m\frac{L_p f_p}{E_p r_p}\,\Re[Y^{\ell m}]\right\}\right],
\end{aligned}
$$
(5.27)

$$
\begin{aligned}
\frac{d\left[V^{\ell m}\right]_p}{dt} =\ & \beta_p \left[\left\{\rho_p \dot{r}_p^* + \frac{r_p\,\ddot{r}_p^*}{1+\dot{r}_p^*}\,\Re[Y^{\ell m}] + m\frac{L_p f_p}{E_p r_p}\,\Im[Y^{\ell m}]\right\}\right. \\
& \left. -\ i\left\{\left[\rho_p \dot{r}_p^* - \frac{r_p \ddot{r}_p^*}{1+\dot{r}_p^*}\right]\Im[Y^{\ell m}] - m\frac{L_p f_p}{E_p r_p}\,\Re[Y^{\ell m}]\right\}\right],
\end{aligned}
$$
(5.28)

where we have defined $\beta_m = 4\pi q f_p/(E_p r_p^2(1-\dot{r}_p^*))$, $\beta_p = 4\pi q f_p/(E_p r_p^2(1+\dot{r}_p^*))$, and $\rho_p = \left(1-4M_\bullet/r_p\right)$; $\Re[Y^{\ell m}]$ and $\Im[Y^{\ell m}]$ denote the real and imaginary parts of the scalar spherical harmonic $Y^{\ell m}$; and $\dot{r}_p^*$ and $\ddot{r}_p^*$ are given by the geodesic equations:

$$
\dot{r}_p^* = \sqrt{1 - \frac{f_p}{E_p^2}\left(1+\frac{L_p^2}{r_p^2}\right)},
$$
(5.29)

and

$$
\ddot{r}_p^* = -\frac{f_p}{r_p E_p^2}\left\{\frac{M}{r_p} - \frac{L_p^2}{r_p^2}\left(1-\frac{3M}{r_p}\right)\right\}.
$$
(5.30)

In practice, the implementation of the evolution and communication of the characteristic fields requires us to deal with the equations of the fields at the different collocation points in a particular order. In what follows we outline an algorithm that describes step by step the procedure that has to be followed (again we drop the harmonic indices ℓ and m):

(i) For each subdomain Ω_a $(a = 1, \ldots, D)$, we evolve the variable U at the interior points and at the right boundary node, $r^* = r_{a,\mathrm{N}}^*$, according to the following evolution equation:

$$
\partial_T U_{a,i} = -\left[1 + \frac{(\partial_t X_a)_i}{(\partial_{r^*} X_a)_i}\right](\partial_{r^*} U_a)_i - V_\ell^{a,i}\,\psi_{a,i},
$$
(5.31)

where $(\partial_{r^*} X_a)_i$ and $(\partial_t X_a)_i$ are given in Eq. (5.5) and Eq. (5.6) respectively, and $i = 1, \ldots, N$.

(ii) The next step is: For each subdomain Ω_a $(a = 1, \ldots, D)$, we evolve the variable V at the interior points and at the left boundary node, $r^* = r^*_{a,0}$, according to the following evolution equation:

$$\partial_T V_{a,i} = \left[1 - \frac{(\partial_t X_a)_i}{(\partial_{r^*} X_a)_i} \right] (\partial_{r^*} V_a)_i - V_\ell^{a,i} \, \psi_{a,i} \,, \tag{5.32}$$

where $i = 0, \ldots, N - 1$.

(iii) We evolve the variable V at all the right boundary nodes according to Eq. (3.50) or its time derivative (for the method of lines), Eq. (3.52). Here we distinguish between two situations:

- For boundary nodes that do no contain the particle, we just pass the value of this variable (or its time derivative) to the left (see Section 3.4.2).

- For boundary nodes containing the particle, we either use Eq. (3.50) or Eq. (3.52) in the case of using the method of lines, that is, we need to use (see Section 3.4.2):

$$\frac{dV_{\text{P},\text{N}}}{dT} = \frac{dV_{\text{P}+1,0}}{dT} - \frac{d\,[\,V\,]_p^{\text{P},\text{P}+1}}{dT} \,. \tag{5.33}$$

(iv) We evolve the variable U at all the left boundary nodes according to Eq. (3.51) or its time derivative (for the method of lines), Eq. (3.53). Again, we distinguish between two situations:

- For boundary nodes that do not contain the particle, we just pass the value of this variable or its time derivative to the right (see Section 3.4.2).

- For boundary nodes containing the particle, we either use Eq. (3.51) or Eq. (3.53) in the case of using the method of lines, that is, we need to use (see Section 3.4.2):

$$\frac{dU_{\text{P}+1,0}}{dT} = \frac{dU_{\text{P},\text{N}}}{dT} + \frac{d\,[\,U\,]_p^{\text{P},\text{P}+1}}{dT} \,, \tag{5.34}$$

(v) Instead of the Sommerfeld outgoing boundary conditions, Eq. (3.55) and Eq. (3.56), we evolve the characteristic variables U and V at the global boundaries following the method of lines. Then, at horizon $r^* = r^*_{\text{H}}$, we use the equations:

$$\partial_T U_{0,\text{H}} \;=\; 0 \,, \tag{5.35}$$

$$\partial_T V_{0,\text{H}} \;=\; (\partial_{r^*} V_0)_{\text{H}} - V_\ell^{0,\text{H}} \psi_{0,\text{H}} \,, \tag{5.36}$$

and, at the spatial infinity $r^* = r_{\rm I}^*$:

$$\partial_T U_{\rm D,I} = -(\partial_{r^*} U_{\rm D})_{\rm I} - V_\ell^{\rm D,I} \psi_{\rm D,I} \,, \qquad (5.37)$$

$$\partial_T V_{\rm D,I} = 0 \,. \qquad (5.38)$$

(vi) The last step consists in evolving the variable ψ at the collocation points of all domains according to the equation:

$$\partial_T \psi_{a,i} = \frac{1}{2}\left(U_{a,i} + V_{a,i}\right) + \frac{1}{2}\frac{(\partial_t X_a)_i}{(\partial_{r^*} X_a)_i}\left(U_{a,i} - V_{a,i}\right) \,, \qquad (5.39)$$

where $i = 0, \ldots, N$, and $a = 1, \ldots, D$. As for the penalty case, we can obtain the equations for a particle on a circular orbit just by setting $\dot{r}_p^* = 0$ and in the expressions for the jumps Eq. (3.41) and (3.42).

Finally, it is important to comment on the implementation of the communication of the characteristic fields when employing the method of lines. In other to communicate the solutions at two different boundaries we use the expressions containing the derivatives of the jumps in (U, V), Eqs. (3.53) and (3.52). This requires to impose initially the values of the jumps, Eqs. (3.41) and (3.42), since during the evolution the only input about them is the information on their derivatives. Therefore, in this case, we cannot just use the *zero* initial data that we used in the case of the evolution of the field variables $\boldsymbol{U}$, namely $\boldsymbol{U}_o = \boldsymbol{U}(t = t_o, r) = (\psi^{\ell m}(t_o, r), \phi^{\ell m}(t_o, r), \varphi^{\ell m}(t_o, r)) = \boldsymbol{0}$, but a modification of it, at least at the nodes where the particle is located. All these options have been implemented in our numerical code, and in this way we avoid the appearance of the Jost junk solutions discussed in Section 3.4.2.

5.5   Validation of the Numerical Code

Thanks to the flexibility of the PwP scheme, it can be adjusted to the type of problem that we are dealing with. In particular, for the computation of the self-force acting on an EMRI with eccentric orbits, the subdomains containing the particle are made time dependent. However, we have not study yet how this affect the accuracy of the solution and, in principle, since the number of collocation points remains fixed whereas the size of the subdomains vary with time, one can think that the exponential convergence of the PwP scheme could be compromised.

In order to check the performance of the PwP scheme for eccentric orbits, we start by studying the convergence of our numerical code. Thus, as in
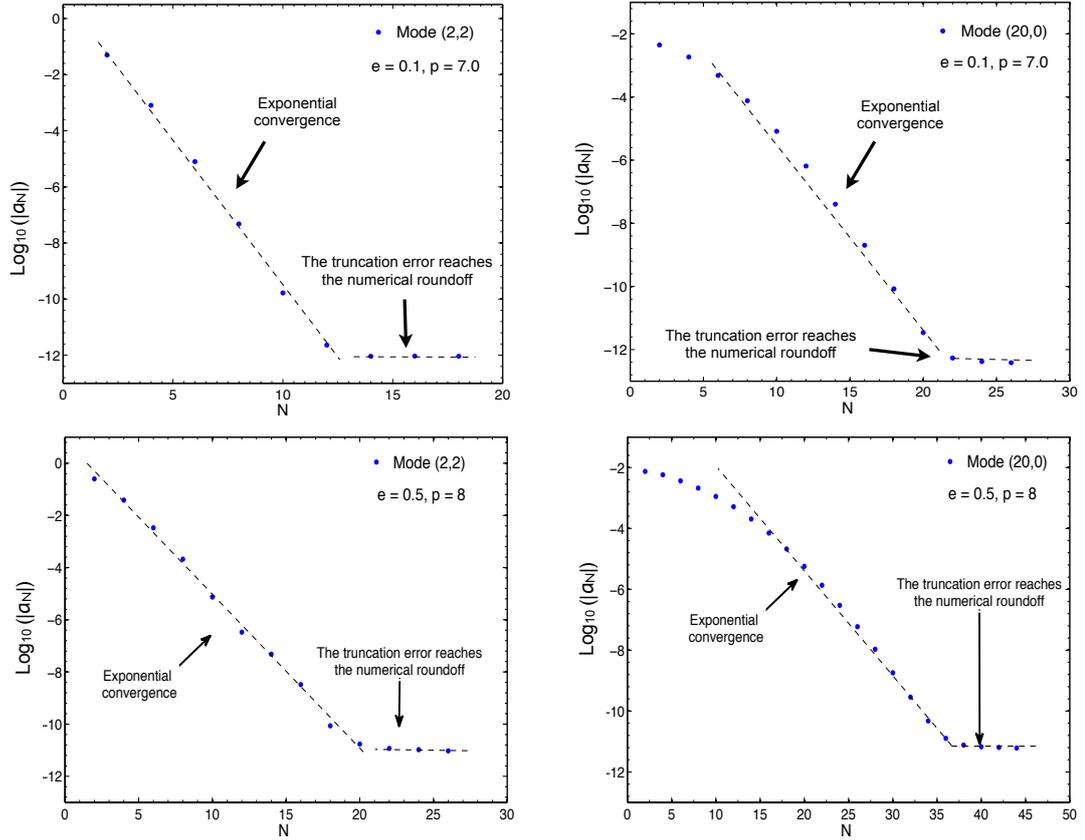
Figure 5.3: *Dependence of the truncation error, as estimated from the quantity $\log_{10}|a_N|$, on the number of collocation points, N, for evolutions of the harmonic modes $\ell = m = 2$ (left column) and $\ell = 20$, $m = 0$ (right column) of the field variable $\psi^{\ell m}$.   These results correspond to $t = 500M_\bullet$.   From top to bottom, we show the truncation error for: (i) $(e,p) = (0.2, 7.0)$ and (ii) $(e,p) = (0.5, 8.0)$. The plots correspond to the solutions on the subdomain to the right of the particle. The tortoise radial coordinate size of this subdomain, i.e. $|r^*_{P+1,N} - r^*_p(t)|$, is in the range $2 - 15\, M_\bullet$. The good fit of the data to a straight line confirms the exponential convergence of the numerical computations.*

Section 5.5, we compute the field modes increasing the number of collocation points and compute the truncation error [Eq. (3.110)]. In particular, we have studied the evolution of two harmonic modes, the low harmonic mode $(\ell, m) = (2, 2)$ and the high harmonic mode $(\ell, m) = (20, 0)$. These have been generated for two different generic eccentric orbits with orbital parameters: (i) $(e, p) = (0.2, 7.0)$ and (ii) $(e, p) = (0.5, 8.0)$.

In Figure 5.3, we show the truncation error obtained by increasing the number of collocation points. As we can see from the plot, the truncation error decreases exponentially with the number of collocation points N. This confirms that the PwP scheme also provides smooth solutions for moderately eccentricities, preserving, in this way, the exponential convergence of the PSC method. The values showed in the figure have been obtained from the subdomain to the right of the particle, i.e. at Ω_{P+1}, whose size $|r_{\mathrm{P}+1}^* - r_p^*(t)|$ has been adjusted in such a way that, at the pericenter it is $\mathcal{O}(\lambda_{\max})$. Then, $|r_{\mathrm{P}+1}^* - r_p^*(t)|$ was varying in the range $2 - 4M_\bullet$ for the case (i) and within the range $1 - 15M_\bullet$ for the case (ii) [Canizares 2011].

5.6   Scalar Self-Force Results

Here we present some self-force results obtained with the PwP scheme implemented for moderately eccentric orbits. Like in the circular orbit case, we have performed computations employing both the penalty method and the direct communication of the characteristic fields (see Section 3.4). In this way, we can cross-check the numerical results of the self-force obtained with both methods.

In Figure 5.4 we show snapshots of the evolution of the $(\ell, m) = (2, 2)$ harmonic mode and its time and radial derivatives, including details near the particle location, that illustrate the ability of our method to capture the structure of the field modes near the particle. The values of the fields have been obtained at $t = 550M_\bullet$ for an eccentric orbit of parameters $(e, p) = (0.5, 7.1)$. This simulation used $D = 10$ subdomains and $N = 100$ collocation points per subdomain. In particular, we can see from the insets how the jumps on the time and radial derivative of the field variables [Eqs. (3.18) (3.21)] are well resolved.

On the other hand, we show in Figure 5.5 the results for the evolution of the components of the gradient of the regularised field obtained for different eccentric orbits, with increasing orbital parameters (e, p). These results have been obtained by choosing $\ell_{\max} = 17$, for which we needed to perform 171
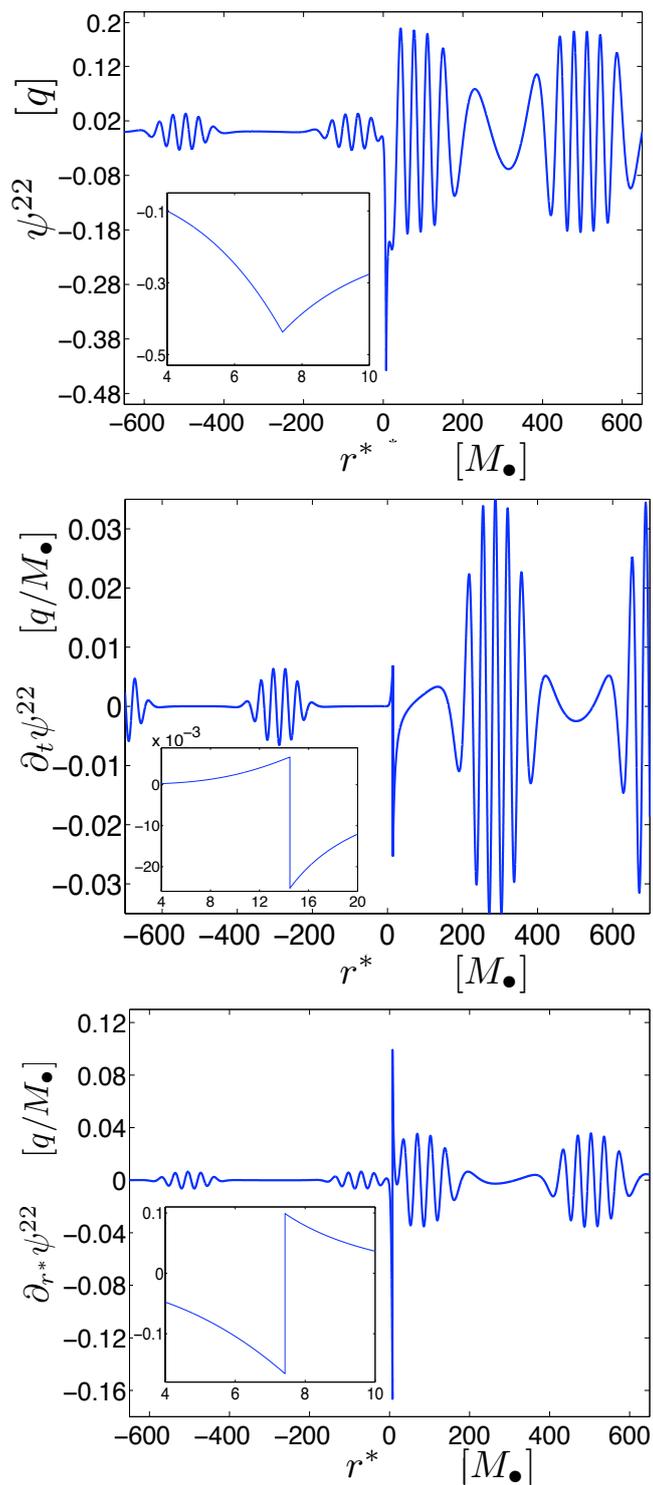
Figure 5.4: *Snapshots of the evolution of a scalar charged particle in eccentric orbits around a non-rotating MBH. They show the variables $\psi^{\ell m}$ (top), $\phi^{\ell m}$ (center), and $\varphi^{\ell m}$ (bottom), for the mode $\ell = m = 2$.*

Table 5.1: *Numerical values of the components of the gradient of the regularised field at the pericentre radius. We present our estimates for different eccentric generic orbits, which correspond to the orbital parameters: (i) $(e, p) = (0.1, 6.3)$; (ii) $(e, p) = (0.3, 6.7)$; and (iii) $(e, p) = (0.5, 7.1)$. The regularised field has been evaluated at the nearest value of the radial coordinate to the pericentre value available in our numerical evolutions, which corresponds to: (i) $6.0M_\bullet$, (ii) $5.1538801M_\bullet$ and (iii) $4.7377989M_\bullet$ respectively. For comparison, we have included the results of Warburton and Barack [Warburton 2010], obtained near the pericenter.*

(e, p)	$\mathcal{F}_\alpha$	PwP	Frequency-Domain	Relative Difference
	$\frac{M_\bullet^2}{q} \Phi_t^{\mathrm{R}}$	$4.517\,196 \cdot 10^{-4}$	$4.517\,994 \cdot 10^{-4}$	0.01%
$(0.1, 6.3)$	$\frac{M_\bullet^2}{q} \Phi_r^{\mathrm{R}}$	$2.125\,049 \cdot 10^{-4}$	$2.125\,7 \cdot 10^{-4}$	0.03%
	$\frac{M_\bullet}{q} \Phi_\phi^{\mathrm{R}}$	$-6.204\,083 \cdot 10^{-3}$	$-6.20\,401 \cdot 10^{-3}$	$3 \cdot 10^{-5}\%$
	$\frac{M_\bullet^2}{q} \Phi_t^{\mathrm{R}}$	$7.698\,048 \cdot 10^{-4}$	$7.177\,3 \cdot 10^{-4}$	0.25%
$(0.3, 6.7)$	$\frac{M_\bullet^2}{q} \Phi_r^{\mathrm{R}}$	$3.63\,3926 \cdot 10^{-4}$	$3.632\,2 \cdot 10^{-4}$	0.04%
	$\frac{M_\bullet}{q} \Phi_\phi^{\mathrm{R}}$	$-9.040\,222 \cdot 10^{-3}$	$-9.0402\,1 \cdot 10^{-3}$	$1.5 \cdot 10^{-5}\%$
	$\frac{M_\bullet^2}{q} \Phi_t^{\mathrm{R}}$	$1.233\,071 \cdot 10^{-3}$	$1.233\,1 \cdot 10^{-3}$	0.015%
$(0.5, 7.1)$	$\frac{M_\bullet^2}{q} \Phi_r^{\mathrm{R}}$	$5.612\,209 \cdot 10^{-4}$	$5.617\,9 \cdot 10^{-4}$	0.1%
	$\frac{M_\bullet}{q} \Phi_\phi^{\mathrm{R}}$	$-1.268\,560 \cdot 10^{-2}$	$-1.2685\,7 \cdot 10^{-2}$	$6.1 \cdot 10^{-4}\%$

evolutions of the retarded field equations (see Section 3.8). The multidomain framework that we have employed for these computations consists of $D = 10$ subdomains and $N = 100$ collocation points per subdomain [Canizares 2010].

Finally, we have computed the self-force components for different types of eccentric orbits. These orbits, in terms of the eccentricity and semilatus rectum, are: (i) $(e, p) = (0.1, 6.3)$; (ii) $(e, p) = (0.3, 6.7)$; and (iii) $(e, p) = (0.5, 7.1)$. We show pieces of the trajectories in Figure 5.6. The multidomain framework employed for these simulations has $D = 80$ and $N = 50$. The results obtained for the self-force components are presented in Table 5.1 and have been computed with the formulation that uses the direct communication of characteristic fields (see Section 3.4.2). These values of the self-force have been computed at the nearest radial location to the pericentre radius (see Eq. (2.102)) available in our evolutions. After the publication of these results [Canizares 2011], Warburton and Barack [Warburton 2010] have arrived at similar results employing frequency-domain methods, suggesting the robustness of the PwP method.

All our calculations have been performed in a computer with two Quad-Core Intel Xeon processors at 2.8 GHz and the time spend for a full self-force
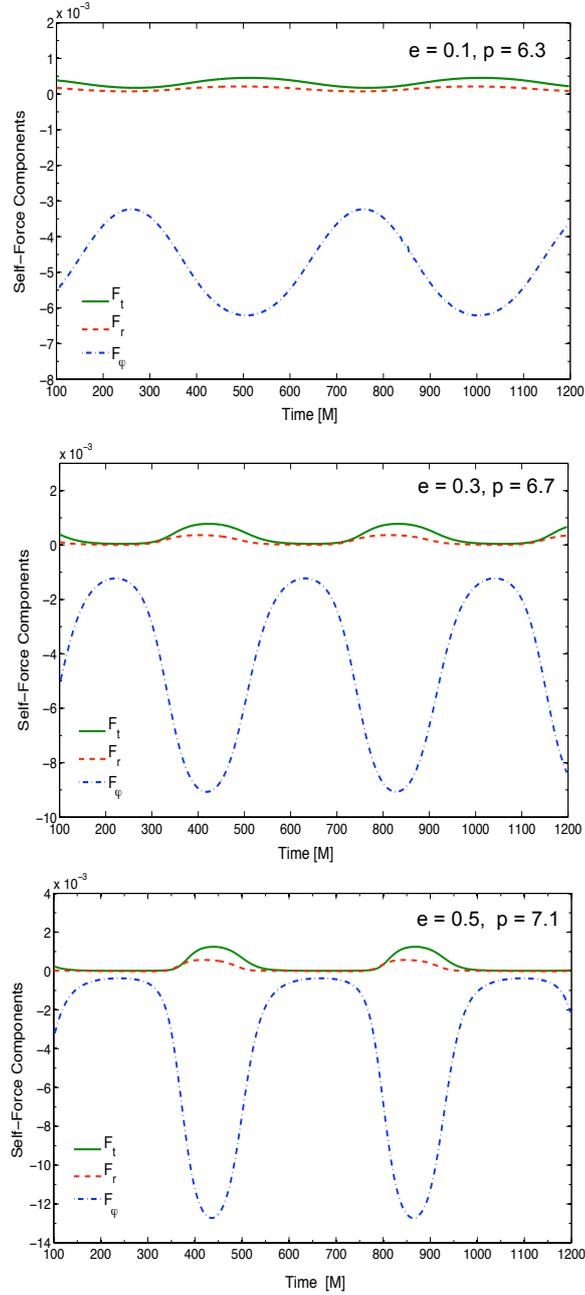
Figure 5.5: *Evolution of the components of the gradient of the regularised field, $\nabla_\alpha \Phi^R$, for a scalar charged particle in eccentric orbits around a non-rotating MBH. From top to bottom, the orbital parameters of the orbits are: (i) $(e,p) = (0.1, 6.3)$; (ii) $(e,p) = (0.3, 6.7)$; and (iii) $(e,p) = (0.5, 7.1)$. For each orbit (frame), the solid line represents the evolution of the dimensionless time component, $\frac{M_\bullet^2}{q} \Phi_t^R$; the dashed line represents the evolution of the dimensionless radial component, $\frac{M_\bullet^2}{q} \Phi_r^R$; and the dot-dashed line represents the evolution of the dimensionless azimuthal component, $\frac{M_\bullet}{q} \Phi_\phi^R$. The numerical setup for these calculations used $D = 10$ subdomains and $N = 100$ collocation points per subdomain.*
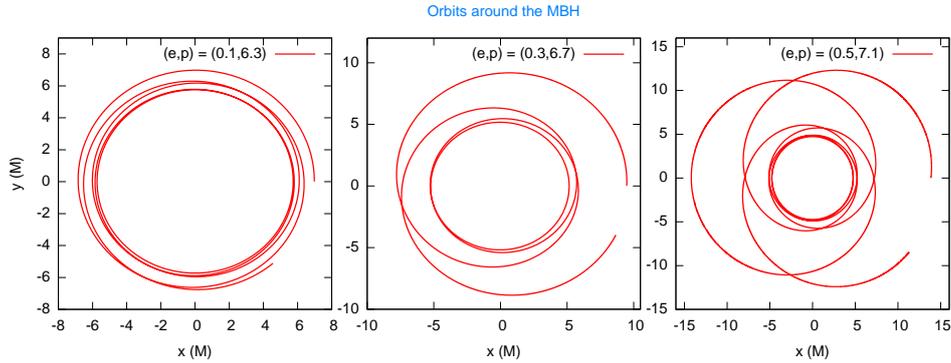
Figure 5.6: *Eccentric orbits considered in the numerical evolutions. From left to right we have: (i) $(e,p) = (0.1, 6.3)$; (ii) $(e,p) = (0.3, 6.7)$; and (iii) $(e,p) = (0.5, 7.1)$. These orbits have been integrated using Eq. (2.107) and Eq. (2.108).*

computation is always in the range 20-30 minutes. Comparing with the time required to obtain a full self-force computation employing circular orbits (see Section 4.6) we can see that the efficiency of the PwP method is maintained.

In summary, we have seen how the PwP scheme can be extended to model EMRIs in generic orbits with moderate eccentricity, maintaining its accuracy and its efficiency. We have also pointed out a possible PwP implementation for performing highly eccentric computations [Canizares 2011]. However, we have not given any result for it, leaving this implementation for future work.

Part II

Testing the Chern-Simons Theory of Gravity

EMRIs in Chern-Simons Gravity

Entities should not be multiplied unnecessarily
William of Ockham.

6.1 General Relativity may not be the last Word on Gravity

The discussion presented in the first part of this thesis has assumed GR as *the theory* underpinning EMRIs. However, in this second part, this is no longer the case and we consider the possibility that these strong field systems can be governed by an alternative theory of gravity. In particular, we shall focus on whether it is possible to distinguish from EMRI detections the theory of gravity, by confronting GR with a particular alternative theory.

Einstein's theory of gravity has successfully passed all the experimental tests to which it has been subjected. However, with the current technology, these tests have been confined to weak gravitational fields, like those of pulsar binaries or within the solar system, leaving strong gravitational regimes unexplored. Aside from this, the main motivation for "pursuing" alternatives to GR stems from unfruitful attempts to unify it with the other forces of Nature, and that there are physical phenomena which could be better described employing alternative theories of gravity. For instance, in this regard there are scalar-tensor theories that are candidates for reproducing inflation, whereas modified Newtonian dynamics is employed to attempt to avoid the problem of dark matter (see [Yunes 2009b] for a review of alternative theories to GR). On the other hand, theories such as string theory predict other physical interactions that are not expected within GR (see, e.g. [Will 2005]) and that may give rise to new kinds of physics.

EMRI GW signals could in principle have different features depending on the theory of gravity that describes the system, and a GW observatory like LISA

could detect them and may be able to distinguish these different features. Then, the question that arises here is which kind of theory do we choose to test? or, alternatively, what kind of phenomena can we expect to test from LISA EMRI observations?. Due to the myriad of alternative theories of gravity available, we choose to focus on DCSMG, which is a $4D$ effective theory that arises in the low-energy limits of *string theory* and can also arise in *Loop Quantum Gravity*. As we shall see, DCSMG enhances the Einstein-Hilbert action through the addition of a dynamical scalar field and a parity-violating term containing the density (see [Weinberg 2008] for a discussion of this term in the context of inflationary cosmology). It has been used to propose an explanation to the cosmic baryon asymmetry [Alexander 2006] and makes predictions for the polarisation of the cosmic microwave background [Lue 1999].

The work presented in the following dissertation is a continuation of previous work by Sopuerta and Yunes [Sopuerta 2009], who have discussed how modifications to the gravitational interaction due to DCSMG can affect the signals emitted by EMRIs and their detectability by LISA. The key idea for this study stems from the fact that if we consider DCSMG instead of GR to model EMRIs, we should change accordingly the spacetime geometry of the MBH and, consequently, this give rise to different equations of motion for the system and, in turn, to different waveforms.

Due to the fact that an EMRI in GR is expected to have a counterpart in DCSMG, this can produce a degeneracy or confusion problem. In the sense that there may be a waveform in GR that matches exactly a waveform in DCSMG, but with different parameters. This confusion problem can be avoided by introducing into the waveforms RR effects (see Section 2.1), which will change the orbital evolution of an EMRI in different ways depending on the theory under consideration. Therefore, including these effects will avoid this degeneracy. In this second part of the thesis we include RR effects for EMRI evolution and use statistical tools to estimate the capability of LISA to constrain DCSMG. In this regard, in [Sopuerta 2009] it has been shown that, at leading order, GW emission in DCSMG takes the form as in GR. This fact simplifies the analysis presented here, since it allows us to employ GR-like expressions for computing the rate of change of constants of motion due to GW emission.

6.2   Dynamical CS Modified Gravity

Following [Sopuerta 2009], we are going to review the main points of the DCSMG formulation employed in our study. In DCSMG, the action of the

system consists of the Einstein-Hilbert term plus the product of a scalar field and the Pontryagin density (the contraction of the Riemann curvature tensor with its dual), and the action of a Chern-Simons (CS) scalar field and/or other matter fields, that is:

$$S = S_{EH} + S_{CS} + S_{\vartheta} + S_{mat} \,, \tag{6.1}$$

where the different terms are:

$$S_{EH} = \kappa \int d^4x \sqrt{-\mathrm{g}} R \qquad\qquad \text{Einstein-Hilbert action}\,,$$

$$S_{CS} = \tfrac{\alpha}{4} \int d^4x \sqrt{-\mathrm{g}}\, \vartheta(^*RR) \qquad \begin{array}{l}\text{CS gravitational}\\ \text{correction}\end{array}$$

$$S_{\vartheta} = -\beta \int d^4x \sqrt{-\mathrm{g}} \left[\, \mathrm{g}^{\mu\nu}(\nabla_\mu\vartheta)(\nabla_\nu\vartheta) \quad \text{CS scalar field action} \right. \tag{6.2}$$

$$\left. +\, 2V(\vartheta)\right]/2 \,,$$

$$S_{mat} = \int d^4 \sqrt{-\mathrm{g}}\, \mathcal{L}_{mat} \qquad\qquad \begin{array}{l}\text{Action of the matter}\\ \text{degrees of freedom}\,,\end{array}$$

here $\kappa = 1/(16\pi G)$ is the gravitational constant; $V(\vartheta)$ is the potential term associated with the CS scalar field ϑ, and α is the coupling constant of this field with the parity violating Pontryagin density, $^*RR$, which is given by:

$$^*RR := {^*R^\alpha}_\beta{}^{\gamma\delta} R^\beta{}_{\alpha\gamma\delta} = \frac{1}{2}\varepsilon^{\gamma\delta\mu\nu} R^\alpha{}_{\beta\mu\nu} R^\beta{}_{\alpha\gamma\delta} \,, \tag{6.3}$$

where * denotes the dual operation, constructed using the antisymmetric Levi-Civita tensor $\varepsilon^{\alpha\beta\mu\nu}$ associated with the spacetime metric. Finally, the coupling constant β in Eq. (6.2) determines the gravitational strength of the CS scalar field stress-energy distribution. The quantities α and β are universal coupling constants that we would like to constrain by employing parameter estimation for EMRI detection.

The field equations in DCSMG are obtained from variation of the action [Eq. 6.1] with respect the metric and the CS scalar, leading to:

$$G_{\mu\nu} + \frac{\alpha}{\kappa}C_{\mu\nu} = \frac{1}{2\kappa}\left(T^{mat}_{\mu\nu} + T^{\vartheta}_{\mu\nu}\right) \,, \tag{6.4}$$

$$\beta\Box\vartheta = -\frac{\alpha}{4}{^*RR} + \beta\frac{dV}{d\vartheta} \,, \tag{6.5}$$

where $T^{mat}_{\mu\nu}$ is the matter stress-energy tensor and $T^{\vartheta}_{\mu\nu}$ is the stress-energy tensor of the CS scalar field given by:

$$T^{\vartheta}_{\mu\nu} = \beta\left[(\nabla_\mu\vartheta)(\nabla_\nu\vartheta)\right] - \frac{1}{2}\mathrm{g}_{\mu\nu}(\nabla^\sigma\vartheta)(\nabla_\sigma\vartheta) - \mathrm{g}_{\mu\nu}V(\vartheta) \,. \tag{6.6}$$

The potential term $V(\vartheta)$ allows us to introduce additional coupling terms to drive the CS scalar evolution [Eq. (6.5)], like for instance a mass term, which would break the shift symmetry of the CS scalar field coming from string theory. For this reason, we henceforth assume that this potential term vanish. Moreover, the C-tensor $C^{\mu\nu}$ can be split into two parts:

$$C^{\mu\nu} = (\nabla_\sigma\vartheta)\varepsilon^{\sigma\delta\beta(\mu}\nabla_\beta R^{\nu)}{}_\delta + (\nabla_\sigma\nabla_\delta\vartheta)^* R^{\delta(\mu\nu)\sigma} \tag{6.7}$$

$$:= C_1^{\mu\nu} + C_2^{\mu\nu} \tag{6.8}$$

Here we mention that in the *non-dynamical* version of CS theory $\beta = 0$ at the level of the action and then, the evolution equations for the CS scalar becomes a differential constraint on the space of the allowed solutions, the so-called Pontryagin constraint $^*RR = 0$ (see discussion in [Sopuerta 2009]).

In order to obtain the metric perturbations in DCSMG, we consider a region of space located several GW wavelengths away from the source, i.e in the radiation zone. In this region both the spacetime metric and the scalar CS field can be split as the sum of two contributions, one is related to a background spacetime and the other is a perturbative quantity. In this way, the global spacetime metric can be regarded as the sum of a background metric $\bar{g}_{\mu\nu}$ and a metric perturbation $h_{\mu\nu}$. Moreover, the scalar field can be decomposed as a background quantity $\bar{\vartheta}$ and a perturbed one $\hat{\vartheta}$. The strengths of $h_{\mu\nu}$ and $\hat{\vartheta}$ are controlled through the perturbative parameter υ, which encodes the weak gravity expansion and serves as a bookkeeping parameter for labelling the different perturbative orders of the metric, that is:

$$g_{\mu\nu} = \bar{g}_{\mu\nu} + \upsilon h_{\mu\nu} + \mathcal{O}(\upsilon^2)\,. \tag{6.9}$$

In a similar way, υ also labels the perturbative orders of the scalar CS field:

$$\vartheta = \bar{\vartheta} + \upsilon\hat{\vartheta} + \mathcal{O}(\upsilon^2)\,. \tag{6.10}$$

In the radiation zone, we can apply the linear approximation (see Section 1.1) and consider that the spacetime background is given by that of a flat space-time. Thus, $\bar{g}_{\mu\nu} = \eta_{\mu\nu}$, and $\upsilon\hat{\vartheta} = 0$. Moreover, we impose the Lorenz gauge [Eq. (1.8)] and the traceless condition [Eq. (1.19)], obtaining that (at leading order) the Riemann, dual Riemann and Ricci tensors are, respectively:

$$R_{\mu\nu\rho\sigma} = \upsilon\left[h_{\sigma[\mu,\nu]\rho} - h_{\rho[\mu,\nu]\sigma}\right] + \mathcal{O}(\upsilon^2)\,, \tag{6.11}$$

$$^*R^{\delta\alpha\beta\gamma} = \upsilon\,\bar{\varepsilon}^{\delta\mu\nu\alpha}h_\nu{}^{[\beta,\gamma]}{}_\mu + \mathcal{O}(\upsilon^2)\,, \tag{6.12}$$

$$R_{\mu\nu} = -\frac{\upsilon}{2}\bar{\Box}h_{\mu\nu} + \mathcal{O}(\upsilon^2)\,. \tag{6.13}$$

In addition, within these approximations the leading-order C tensor is given by:

$$C_{\mu\nu} = -\frac{\upsilon}{2}(\partial_\sigma\vartheta)\bar{\varepsilon}^{\sigma\delta\alpha}{}_{(\mu}\bar{\Box}h_{\nu)\delta,\alpha} \tag{6.14}$$
$$-\frac{\upsilon}{2}(\partial_\sigma^\beta\vartheta)\bar{\varepsilon}^{\sigma\delta\alpha}{}_{(\mu}\left[h_{|\alpha\beta|,\nu)\sigma} - h_{\nu)\alpha,\beta\delta}\right] + \mathcal{O}(\upsilon^2)\,,$$

where the notation $(\mu|\alpha\beta|\nu)$ means symmetrisation with respect to μ and ν only. Employing these expressions, one can see that the modified field equations in the trace-reversed form [Eq. (1.6)] are given by:

$$\bar{T}_{\mu\nu} = -\kappa\upsilon\bar{\Box}h_{\mu\nu} - \alpha(\partial_\sigma\vartheta)\bar{\varepsilon}^{\sigma\delta\alpha}{}_{(\mu}\bar{\Box}h_{\nu)\sigma,\alpha} \tag{6.15}$$
$$-\alpha(\partial^\beta{}_\sigma\vartheta)\upsilon\bar{\varepsilon}^{\sigma\delta\alpha}{}_{(\mu}\left[h_{\alpha\beta,|\nu)\sigma} - h_{\nu)\alpha,\beta\delta}\right] + \mathcal{O}(\upsilon^2)\,,$$

$$\beta\Box\vartheta = -\frac{\alpha}{2}\upsilon^2\bar{\varepsilon}^{\alpha\beta\mu\nu}h_{\alpha\sigma,\gamma\beta}h_\nu{}^{[\gamma,\sigma]}{}_\mu + \mathcal{O}(\upsilon^3)\,, \tag{6.16}$$

where the trace-reversed stress-energy tensor sourcing the metric perturbations is given by $\bar{T}_{\mu\nu} = \bar{T}_{\mu\nu}^{mat} + \bar{T}_{\mu\nu}^\vartheta$. From these equations, one can see that in the radiation zone $\bar{T}_{\mu\nu}$ must be at leading-order $\mathcal{O}(\upsilon)$, whereas the scalar field, which is sourced by the Pontryagin density, goes as $\mathcal{O}(\upsilon^2)$.

Since we are looking for small CS deformations from GR, we can use the *small-coupling approximation* for the CS scalar field, and expand the modified field equations [Eq. (6.15) and Eq. (6.16)] employing the dimensionless parameter:

$$\varpi = \frac{\xi}{M^4}\,, \quad \text{where} \;\; \xi := \frac{\alpha^2}{\beta\kappa}\,, \tag{6.17}$$

where M is the characteristic mass associated with the system that, in the case of an EMRI system, can be set to be $M = M_\bullet$. Here, ϖ is assumed to be a small perturbative parameter associated with the CS gravitational modifications and the physical system under study.

Employing the linear approximation together with the small-coupling approximation, we obtain a two-parameter perturbative scheme in ϖ and υ [Yunes 2009a, Sopuerta 2009], where the metric perturbations $h_{\mu\nu}$ and the CS scalar field ϑ can be expanded as:

$$h_{\mu\nu} = \sum_{a,b}\upsilon^a\varpi^b h_{\mu\nu}^{(ab)}\,, \quad \text{and} \quad \vartheta = \sum_{a,b}\upsilon^a\varpi^b\vartheta^{(a,b)}\,. \tag{6.18}$$

Here, the superindex (a,b) stands for perturbations of order $\mathcal{O}(\upsilon^a, \varpi^b)$ with $a + b \geqslant 1$.

As we are interested in effective small CS deformations towards GR, $\varpi \to 0$ in the GR limit. Consequently, in order to avoid metric perturbations whose dominant behaviour differs from GR in that limit, we shall set $h_{\mu\nu}^{(0,a)} = 0$ for all a. Thus, we allow only metric perturbations that modify the flat-space background in a ϖ−independent manner.

6.3   The Massive Black Hole Geometry

In GR, the geometry of a spinning MBH is given by the Kerr metric, whose non-zero components in Boyer-Lindquist (BL) coordinates (t, r, θ, ϕ) are (see, e.g. [Misner 1973]):

$$\bar{g}_{tt} = -\left(1 - 2M_\bullet r/\rho^2\right), \qquad\qquad \bar{g}_{rr} = \rho^2/\Delta,$$

$$\bar{g}_{\phi\phi} = \Sigma \sin^2\theta/\rho^2, \qquad\qquad \bar{g}_{\theta\theta} = \rho^2, \qquad (6.19)$$

$$\bar{g}_{t\phi} = -\left(2aM_\bullet r \sin^2\theta\right)/\rho^2,$$

where $\Sigma = (r^2 + a^2)^2 - a^2\Delta\sin^2\theta$, $a = |\mathbf{S}|/M_\bullet$ is the spin parameter, $\rho^2 = r^2 + a^2\cos^2\theta$, and $\Delta = r^2 f + a^2$, where f is given by Eq. (2.37).

Employing the slow-rotation approximation ($a/M_\bullet \ll 1$) and the small-coupling approximation, and expanding up to second order in $a/M_\bullet$ and ϖ, the corrections to the gravitational field of a Kerr BH in DCSMG are obtained in [Yunes 2009a]. The form of the non-zero metric components, using coordinates in which the Kerr part of the metric is in Boyer-Lindquist coordinates, are:

$$\bar{g}_{tt} = -\left(1 - 2M_\bullet r/\rho^2\right), \qquad\qquad \bar{g}_{rr} = \rho^2/\Delta,$$

$$\bar{g}_{\phi\phi} = \Sigma \sin^2\theta/\rho^2, \qquad\qquad \bar{g}_{\theta\theta} = \rho^2, \qquad (6.20)$$

$$\bar{g}_{t\phi} = \left[P(M_\bullet, r)\,\xi/M_\bullet^4 - 2M_\bullet^2 r/\rho^2 \right] \sin^2\theta\, a/M_\bullet,$$

where

$$P(M_\bullet, r) = \frac{5}{8}\frac{M_\bullet^5}{r^4}\left(1 + \frac{12M_\bullet}{7r} + \frac{27M_\bullet^2}{10r}\right). \qquad (6.21)$$

Notice that the only metric component that contains the CS parameter ξ is $\bar{g}_{t\phi}$ (i.e. the only metric component that is modified with respect to the GR case) and that it scales as r^{-4} for $M_\bullet/r \ll 1$. Then, it decays faster than the rest of metric terms and hence, its effects become negligible at long distances.

The modified metric given in Eq. (6.20) is still stationary and axisymmetric and then, it has two Killing vectors signaling these properties: a timelike Killing vector $t^\alpha = [1, 0, 0, 0]$ and a spacelike Killing vector $\psi^\alpha = [0, 0, 0, 1]$, which lead to the two following conserved quantities (per unit of SCO mass): The energy,

$$E = -t^\alpha u_\alpha \,, \tag{6.22}$$

and the angular momentum along the spin axis,

$$L = \psi^\alpha u_\alpha \,. \tag{6.23}$$

Here, u^α stands for the four-velocity of the particle in the modified Boyer-Lindquist coordinates, which has components $u^\alpha = dx^\alpha/d\tau = [\dot{t}, \dot{r}, \dot{\theta}, \dot{\phi}]$, where τ denotes proper time.

Employing the same approximations that we have applied to derive the perturbed MBH metric, that is the slow-rotating approximation and the small-coupling approximation, we obtain an expression for the CS scalar field:

$$\bar{\vartheta} = \frac{5}{8} \frac{\alpha}{\beta} \frac{a}{M_\bullet} \frac{\cos\theta}{r^2} \left(1 + \frac{2M_\bullet}{r} + \frac{18M_\bullet^2}{5r^2} \right) \,. \tag{6.24}$$

Notice that the CS scalar decays as r^{-2} in the far-field and hence, it possesses a finite energy.

6.4   Particle Motion in a DCSMG Background

In this section we are going to introduce the equations of motion for an EMRI in DCSMG presented in [Sopuerta 2009], that is, the motion of the SCO in the CS-modified MBH background without RR effects, which are discussed in Section 6.5, i.e. we are going to study geodesic motion around the MBH of DCSMG. This is a key issue in EMRI modelling, since the timing and phase of the GWs emitted depend on the type of orbit performed by the SCO, which in turn depends on the geometry of the MBH spacetime. In order to model these orbits, the SCO can be described as a structureless particle in the MBH geometry (see Section 2.1).

In order to obtain the geodesic equations of motion for the SCO in the CS-modified background, we start by taking the divergence of the stress-energy tensor of the particle [Eq. (2.26)]:

$$\nabla_\beta T_{mat}^{\alpha\beta} = m \int \frac{d\tau}{\sqrt{-g}} \frac{du^\alpha}{d\tau} \delta^4(x - z(\tau)) \,. \tag{6.25}$$

Introducing this expression into the divergence of the field equations [Eq. (6.4)], one obtains:

$$- (\nabla^\nu \vartheta) \left(\beta \Box \vartheta + \frac{\alpha}{4} {}^*RR \right) = m \int \frac{d\tau}{\sqrt{-g}} \frac{du^\alpha}{d\tau} \delta^4(x - z(\tau)) \,. \tag{6.26}$$

Then, taking into account the evolution equation for the CS scalar field [Eq. (6.5)], one can see that the point mass (SCO) must follow geodesics $du^\alpha/d\tau = 0$ of the CS deformed MBH background.

On the other hand, to solve for $\dot{t}$ and $\dot{\phi}$, we employ the energy [Eq. (6.22)] and angular momentum [Eq. (6.23)] definitions obtaining:

$$\dot{t} = \dot{t}_K + L \delta \mathrm{g}_\phi^{CS} \,, \tag{6.27}$$

$$\dot{\phi} = \dot{\phi}_K - E \delta \mathrm{g}_\phi^{CS} \,, \tag{6.28}$$

where $\dot{t}_K$ and $\dot{\phi}_K$ are the corresponding expressions in a Kerr background:

$$\rho^2 \dot{t}_K = - \left(a^2 E \sin^2 \theta - aL \right) + \left(r^2 + a^2 \right) \left(\left(r^2 + a^2 \right) \frac{E}{\Delta} - \frac{aL}{\Delta} \right) \,, \tag{6.29}$$

$$\rho^2 \dot{\phi}_K = - \left(aE - \frac{L}{\sin^2 \theta} \right) + (r^2 + a^2) \frac{aE}{\Delta} - \frac{a^2 L}{\Delta} \,, \tag{6.30}$$

and the CS correction $\delta \mathrm{g}_\phi^{CS}$ is given by [Sopuerta 2009]:

$$\delta \mathrm{g}_\phi^{CS} = \frac{\xi a}{112 r^8 f} \left(70 r^2 + 120 r M_\bullet + 189 M_\bullet^2 \right) \,. \tag{6.31}$$

In addition, to solve for $\dot{r}$ and $\dot{\theta}$, we proceed like in the Kerr case and we look for a third constant of motion, i.e. the Carter constant Q. In [Sopuerta 2009], it was found a symmetric Killing tensor $\xi_{\alpha\beta}$ satisfying the tensor Killing equations (up to the order approximation in which the MBH metric is an approximate solution):

$$\nabla_{(\rho} \mathcal{K}_{\alpha\beta)} = 0 \,. \tag{6.32}$$

This Killing tensor can be written in the same form as in the Kerr case:

$$\mathcal{K}_{\alpha\beta} = -\Delta k_{(\alpha} l_{\beta)} + r^2 \bar{\mathrm{g}}_{\alpha\beta} \,, \tag{6.33}$$

where k^α and l^β are two null vectors given by:

$$k^\alpha = \left[\frac{r^2 + a^2}{\Delta}, -1, 0, \frac{a}{\Delta} - \delta \mathrm{g}_\phi^{CS} \right] \,, \tag{6.34}$$

$$l^\alpha = \left[\frac{r^2 + a^2}{\Delta}, 1, 0, \frac{a}{\Delta} - \delta \mathrm{g}_\phi^{CS} \right] \,, \tag{6.35}$$

which are (again to the level of approximation used for the derivation of the MBH metric) principal null directions of the spacetime. Finally, the Carter constant obtained for our DCSMG background is:

$$\mathcal{Q} = \mathcal{K}_{\alpha\beta}u^{\alpha}u^{\beta} - (L - aE)^2 \,. \tag{6.36}$$

Once we have obtained the expression of the Carter constant in DCSMG (and employing $g_{\alpha\beta}u^{\alpha}u^{\beta} = -1$), we can separate the geodesic equations for r and θ:

$$\dot{r}^2 \;=\; \dot{r}_K^2 + 2ELf\delta g_{\phi}^{CS} \,, \tag{6.37}$$

$$\dot{\theta}^2 \;=\; \dot{\theta}_K^2 \,, \tag{6.38}$$

where, the Kerr part $(\dot{r}_K, \dot{\theta}_K)$ is given by:

$$\rho^4 \dot{r}_K^2 \;=\; \left[(r^2 + a^2)E - aL\right]^2 - \Delta \left[\mathcal{Q} + (aE - L)^2 + r^2\right] \,, \tag{6.39}$$

$$\rho^4 \dot{\theta}_K^2 \;=\; \mathcal{Q} - \cot^2\theta L^2 - a^2 \cos^2\theta(1 - E^2) \,, \tag{6.40}$$

and we recall that the CS correction is given by Eq. (6.31). Then, the geodesic motion of the particle in the geometry of a spinning MBH in DCSMG is obtained by solving the set of ODEs given by Eqs. (6.27)-(6.28) and Eqs. (6.37)-(6.38).

On the other hand, it is well-known (see e.g. [Schmidt 2002, Drasco 2004]) that bound geodesic motion in Kerr is characterised by three fundamental frequencies, namely Ω_r, Ω_θ and Ω_ϕ, which are associated with the radial, polar, and azimuthal motion respectively. Since the orbital motion in a CS-modified spinning MBH is different from that of Kerr in GR [Sopuerta 2009], these frequencies will be different in DCSMG. Then, neglecting RR effects, if DCSMG is the correct theory underlying EMRI systems and we model them employing GR templates, we would obtain systematic errors in the extraction of the EMRI parameters. In other words, since an orbit in GR has a correspondence with an orbit in DCSMG with slightly different parameters, one could detect a GW and not be able to distinguish whether it belongs to GR or DCSMG. However, as we shall see in what follows, including RR effects the orbital parameters will evolve in a different way for the different geometries and we can break this degeneracy.

6.5 Radiation-Reaction in DCSMG

To extract the EMRI parameters successfully, we shall need very accurate waveform templates to cross-correlate them with the detected data stream. This eventually means to take into account the RR effects. As it was discussed in Section 2.2, to account for the RR effects we can introduce a local self-force that deviates the particle from geodesic motion or, alternatively, we can introduce additional approximations, like using only the radiative part of the gravitational perturbations, and derive balance laws associated with the "constants of motion" of the orbit.

Due to the fact that the self-force method has not been fully developed for the gravitational case, nor has it been developed for theories different from GR, and taking into account also that we are only interest in performing a parameter estimation study, we will employ approximate methods to introduce RR in the EMRI dynamics. To that end, it is necessary to understand the propagation of the GWs in DCSMG and obtain their effective stress-energy tensor. We study this question using the *short-wave approximation* [Isaacson 1968a, Isaacson 1968b], where the spacetime geometry is decomposed into a background and an oscillatory part representing the GWs. We can use this method whenever the GW wavelengths are much smaller than the length scale associated with the background curvature (see [Misner 1973] for a detailed account of the shortwave approximation). However, in DCSMG the passage of a GW will also induce oscillations in the CS scalar field ϑ, since it is sourced by the spacetime curvature, as we can see from Eq. (6.5). This is a non-linear effect and to obtain how the nonlinear contribution of the waves shapes the MBH background, we must also decomposed the CS scalar into a background and an oscillatory part $(\tilde{\vartheta})$ induced by the GWs:

$$\vartheta = \bar{\vartheta} + \tilde{\vartheta} \tag{6.41}$$

Applying the short-wave approximation to the field equations [Eq. (6.4)], we describe, in terms of the Isaacson tensor $T_{\mu\nu}^{GW}$ (see, e.g. [Misner 1973]) how the nonlinear contributions of both kind of waves, i.e. the GWs and the CS scalar waves, shape the background [Sopuerta 2009]:

$$\bar{G}_{\mu\nu} + \frac{\alpha}{\kappa}\bar{C}_{\mu\nu} = \frac{1}{2\kappa}\left(T_{\mu\nu}^{mat} + T_{\mu\nu}^{\vartheta}[\bar{\vartheta}] + T_{\mu\nu}^{\vartheta}[\tilde{\vartheta}] + T_{\mu\nu}^{GW}\right), \tag{6.42}$$

where the effective stress-energy tensor of the GWs in DCSMG is given by:

$$\begin{aligned} T_{\mu\nu}^{GW} &= -2\kappa\left\{\langle ^{(2)}R_{\mu\nu}[h]\rangle - \frac{1}{2}\bar{g}\langle ^{(2)}R_{\mu\nu}[h]\rangle \right. \\ &\quad \left. + \frac{\alpha}{\kappa}\left(\langle ^{(2)}C_{\mu\nu}[\bar{\vartheta}, h] + \langle ^{(1)}C_{\mu\nu}[\tilde{\vartheta}, h]\rangle\right)\right\}. \end{aligned} \tag{6.43}$$

Here, the superscript preceding a given quantity denotes the perturbative order of this quantity with respect to metric perturbations, and the angle brackets denote averaging over a small region of the spacetime containing several GWs [Misner 1973]. In [Sopuerta 2009], it was shown that the terms corresponding to the CS correction *vanish exactly* yielding the same expression for the Isaacson tensor as in GR, that is:

$$T_{\mu\nu}^{GW} \;=\; \frac{\kappa}{2}\langle h_{\alpha\beta|\mu} h_{|\nu}^{\alpha\beta}\rangle \,. \tag{6.44}$$

Consequently, the RR to the orbital motion due to GW emission has the same functional dependence in the metric perturbations in DCSMG as in GR. On the other hand, the CS scalar is modified through second-order terms in the GWs:

$$
\begin{aligned}
\beta\bar{\Box}\bar{\vartheta} \;=\; & -\frac{\alpha}{4}\left(1 - \frac{1}{4}\langle h^{\alpha\beta}h_{\alpha\beta}\rangle^{*}\bar{R}\bar{R}\right) \\
& -\frac{\alpha}{4}\bar{\varepsilon}_{\alpha\beta\mu\nu}\langle {}^{(1)}R^{\alpha\beta\rho\sigma\,(1)}R_{\rho\sigma}{}^{\mu\nu}\rangle \,.
\end{aligned}
\tag{6.45}
$$

Finally, from Eq. (6.42), one can obtain the following conservation equation:

$$\bar{\nabla}^{\mu}\tau_{\mu\nu} := \bar{\nabla}^{\mu}\left(T_{\mu\nu}^{mat} + T_{\mu\nu}^{\vartheta}[\tilde{\vartheta}] + T_{\mu\nu}^{GW}\right) = 0 \,, \tag{6.46}$$

where there is a new quantity with respect to GR, the stress-energy tensor $T_{\mu\nu}^{\vartheta}[\tilde{\vartheta}]$ associated with the oscillations induced by the CS scalar field.

In the case of EMRIs, the spacetime background is essentially given by the MBH geometry and, as we discussed in Section 6.3, it is described by two Killing vector fields, t^{μ} and ψ^{μ}. Using these symmetries, we obtain the vector fields describing the total flux of energy $\mathcal{E}^{\mu}$ and angular momentum $\mathcal{L}^{\mu}$:

$$\mathcal{E}^{\mu} = -\tau^{\mu}{}_{\nu}t^{\mu} \,, \qquad \mathcal{L}^{\mu} = \tau^{\mu}{}_{\nu}\psi^{\mu} \,, \tag{6.47}$$

These are divergent-free vector fields and then, they fulfil:

$$\mathcal{E}^{\mu}{}_{|\mu} = 0 \,, \qquad \mathcal{L}^{\mu}{}_{|\mu} = 0 \,. \tag{6.48}$$

Integrating these conditions over a spacetime region $\mathcal{V}$, we can obtain balance laws for the energy and angular momentum that can be employed to account for the DCSMG RR effects. Then, these balance laws can give us the change in the constants of motion (E, L) due to energy and angular momentum contributions of both the GWs and the CS scalar field. We would need in addition a similar balance law for the Carter constant.

In practice, what we will do in this thesis is to use the fact that RR in DCSMG has the same form as in GR and approximate these effects by using GR

formulae, which will account for the leading contribution to the RR effects. Moreover, we are going to neglect in our computations the contribution of the radiative part of the CS scalar field, the term $T^{\vartheta}_{\mu\nu}[\tilde{\vartheta}]$ in Eq. (6.46), which we expect to be a subleading contribution (see [Yunes 2009b] for a discussion). Then, the specific RR effects that we are going to consider in this thesis follow the prescription introduced in Gair and Glampedakis [Gair 2006], which include also an expression for the flux of the Carter constant, $\dot{\mathcal{Q}}$ from Post-Newtonian (PN) approximations. In this way, we consider that the particle is moving in a geodesic of the modified MBH background, where we compute the averaged fluxes of E, L, and $\mathcal{Q}$ from the expressions of [Gair 2006] to subsequently update the orbit parameters. This process is repeated along the full evolution of an EMRI.

Testing DCSMG with EMRIs

Every generalisation is false, including this one.
Mark Twain.

7.1 EMRIs: The Strong Field Emitters

To identify any deviation from GR employing GW detections, one requires long and clean (strong field) signals with good SNRs. EMRIs are an ideal source for this purpose, since the orbits of the SCO are deep into the MBH potential and depend on the details of the MBH geometry. Moreover, they are expected to be very clean astrophysical systems because the SCO barely disturb the MBH geometry and its orbit is not affected by external influences, except in the few per cent of galaxies containing active galactic nuclei where the SCO orbit may be affected due to gravitational effects from other physical mechanisms/objects. In addition, EMRI signals are very long and LISA will detect hundred of thousands of EMRI cycles, which will produce an accumulated SNR (see Section 1.3) above detection levels. Hence, EMRIs are a unique and priceless tool to test the strong field region of MBHs and the theory underpinning them.

The shape of the spacetime of a Kerr BH arises from the structure of its mass M^ℓ and current S^ℓ multipole moments, which fulfil the following relations ($\ell = 0, \ldots, \infty$):

$$M^\ell + iS^\ell = M(ia)^\ell \,. \tag{7.1}$$

To get an idea of the meaning of these quantities, we can compare them with the ones associated with a Newtonian continuous distribution of matter [Hughes 2001]:

$$M^\ell \simeq \int d^3r \, r^\ell \rho(\mathbf{r}) \,, \qquad S^\ell \simeq \int d^3r \, r^{\ell-1} \left[\mathbf{r} \times \mathbf{v}(\mathbf{r}) \rho(\mathbf{r}) \right] . \tag{7.2}$$

Here, $\rho(\mathbf{r})$ is the mass density at a position $\mathbf{r}$ and $\mathbf{v}(\mathbf{r})$ is the velocity of the matter element at that point. Then, the M^ℓ tell us about the distribution of mater and S^ℓ about the distribution of matter flows.

The celebrated *no-hair* conjecture of GR essentially states that independently from the process of formation of a BH, its geometry is given by a Kerr solution of GR and then, the BH geometry is characterised by only two numbers, the mass and spin, which in turn determine all the multipole moments through the relations of Eq. (7.1). In other words, an (uncharged) stationary MBH is completely determined by its mass and its spin angular momentum. Then, given the BH mass $M^0 = M_\bullet$, and spin $S^1 = aM_\bullet$, all the other non-zero BH multipoles can be written in terms of these two. Although there is a wider class of BH solutions endowed with an electric charge, like for instance Kerr-Newman BHs, this charge is not relevant in an astrophysical context since these BHs would discharge very quickly (see e.g. [Wald 1971]).

Ryan [Ryan 1995], employing post-Newtonian waveform models, first showed that the spacetime geometry of a MBH can be imprinted into the EMRI waveforms. Thus, a GW observatory like LISA should be able to test any inconsistency between observations and the multipole relationships of Eq. (7.1), and consequently, determine whether the central object is a Kerr BH or some exotic object [Ryan 1997a, Ryan 1997b], such as a naked singularity, or a boson star, or a soliton star, etc. Here, it is worth mentioning that there are other proposals to test GR using MBHs. In particular, there is a recent investigation which shows that X-ray continuum spectra can potentially be used to constraint small quadrupole deviations away from the Kerr metric, once all the physical effects have been included in the model and all systematics have been understood [Bambi 2011]. In addition, the Kerr nature of astrophysical BHs could be tested with other more conventional observations. Indeed, the BH at the centre of the Milky Way (Sgr *A) could be in principle used to test BH spacetimes (see [Psaltis 2011] for a review of tests of gravity with Sgr *A).

Given that EMRI GWs have high accurate imprints of the structure of the MBH, in such a way that a small deviation from a (a priori) Kerr geometry will build up an observable dephasing from Kerr waveforms, from their detection we could determine whether the theory underlaying BHs is GR or another alternative theory of gravity [Sopuerta 2010]. Indeed, in the work of Sopuerta and Yunes [Sopuerta 2009], where they assumed DCSMG instead of GR as the theory for gravity, it was shown that the CS modified GWs may present an observable dephasing with respect to the GWs of GR after approximately 3 weeks of evolution.

Although the formalism developed by Ryan [Ryan 1995, Ryan 1997a, Ryan 1997b] provides us with a method for mapping EMRI observations with MBH spacetimes, there are two important issues that have to be solved to compute EMRI waveforms in a given MBH background: (i) Precise knowledge of the SCO motion and, once this is achieved, (ii) a description of the GW emission that allows for a precise estimation of waveforms and GW fluxes. In GR, the geodesic motion in a Kerr BH spacetime is well known and has been extensively studied (see, e.g. [Chandrasekhar 1992]), and the GW dynamics is obtained, within the radiative approximation, by employing the Teukolsky formalism [Teukolsky 1972, Teukolsky 1972]. However, up to now there is no theoretical framework that accurately describes the ERMI dynamics in non-Kerr spacetimes. Regarding the modelling of a non-Kerr MBH geometry, apart from Ryan's multipolar expansion, there is another approximation: The *bumpy BH* approach [Collins 2004, Glampedakis 2006, Vigeland 2010]. In this framework, rather than measuring some arbitrary set of multipoles M'_ℓ, S'_ℓ, one measures their deviation from the values that one would expect if the spacetime were a BH described by M_ℓ, S_ℓ, that is: $(\delta M_\ell, \delta S_\ell) = (M'_\ell - M_\ell, S'_\ell - S_\ell)$. The multipole moment deviations $\delta M_\ell, \delta S_\ell$ are non zero, since such objects typically have an event horizon that is distorted from that of a Kerr or a Schwarzschild one. The bumpiness of the spacetime is set by choosing a function that controls how the spacetime describing our BH solution deviates from the BH limit under consideration. Bumpy BHs work well in the strong field regime and include the Kerr limit in a natural way by setting the bumpy parameters to zero. In [Gair 2008], some features of orbits in non-Kerr spacetimes that might lead to observable signatures were explored. As a basis for this analysis, the family of the exact Manko and Novikov [Manko 1992] solutions, which deviate from the Kerr metric in the quadrupole and higher moments, is employed. However, since bumpy BHs assume GR in their construction, using them to map the spacetimes of massive compact objects is not a test of GR but a test of the structure of massive bodies within GR.

The development of a methodology for computing the generation and propagation of EMRI GWs in DCSMG has recently begun [Sopuerta 2009, Pani 2011]. The main motivation of this chapter is to extend the work done in [Sopuerta 2009], where an approximate method for generation and propagation of GWs in DCSMG is proposed for the first time. In the work presented here, we add RR effects (see Section 2.1) to evolve the inspiral and we estimate the ability of LISA to constraint the DCSMG theory by employing Fisher matrix analysis.

7.2   EMRI Waveform Models

In the first part of this thesis we saw that EMRIs are complex systems whose modelling posses a computational challenge. Mainly for this reason, a method for producing accurate waveform templates and extract, in an efficient way, the EMRI parameters has not been fully developed yet (see Section 2.1). This is principally due to their highly relativistic nature and the extreme mass ratios involved. For this reason, it has been necessary to resort to approximate methods and numerical techniques, which are mostly under development and whose performance and efficiency for EMRI parameter extraction have to be still quantified or estimated. All these studies have been mainly developed in GR and, up to now, there is little work related with the study of EMRI waveform templates for modelling non-Kerr BHs or BHs in alternative theories of gravity.

The techniques developed for EMRI modelling have grown in number and much of them have gained complexity and also accuracy in the last years. In what follows, we are going to describe those techniques:

-*Self-force computations*: Due to the extreme mass ratio of EMRIs ($\mu \ll 1$), on short orbital time scales, the SCO motion is well approximated by a geodesic orbit in the MBH background, which is accelerated due to the action of a local self-force (see Section 2.1). In this approach, the Einstein field equations are linearised in the mass-ratio and the equations are solved numerically (see [Barack 2009] for a recent review). Although this approach is still under development, due to their technical complexities self-force computations are not well suited to build the large waveform templates needed for EMRI modelling, since they could become computationally unaffordable.

-*Adiabatic* approximation: Due to the extreme mass ratios of EMRIs, the orbital parameters of the system evolve *adiabatically* under RR, in other words: The time evolution of the orbital parameters is much longer than the time evolution of an orbit $T_{orbital}/T_{inspiral} \sim \mu \ll 1$ (see Section 2.1). This implies that the inspiral trajectory can be described by a flow through a sequence of geodesic orbits. The different geodesics are connected by the evolution of the orbital parameters.

-*Radiative* approximation: Alternatively, in order to connect the different geodesics we can model a slow change of the constants of motion. Traditionally, this is done by solving the Teukolsky equation and using the solution to compute the averaged GW fluxes at the boundaries of the spacetime (horizon and spatial infinity), which tell us how the constants of motion of the SCO orbit evolve (see for instance [Hughes 2000, Hughes 2001, Sundararajan 2008b]).

However, Teukolsky based waveforms are computationally expensive to generate since they require the numerical integration of the Teukolsky equation and summation over all the computed multipole modes. Nevertheless, one can substitute solving the Teukolsky equation by employing GW fluxes computed from other approximation methods, like PN theory. This leads to the so called *kludge* schemes, some of which we summarise below.

-*EMRI Effective-One-Body* (EOB) approximation: In this scheme the two-body EMRI system is mapped to an effective one-body "EMRI" system, which consists of a small object orbiting a PN-deformed Kerr BH [Yunes 2010]. The equations of motion for the object are described in Hamiltonian form and, without taking into account RR, these reduce to geodesic equations of motion in the deformed Kerr background spacetime. In this scheme, the RR is introduced as a dissipative force that is computed from PN results. The formalism also includes free parameters that are adjusted with results obtained from energy and angular momentum fluxes computed with the Teukolsky formalism. Up to now, the EMRI EOB scheme has been developed only for equatorial circular orbits which results agree with the ones obtained with Teukolsky based waveforms.

-*Analytical Kludge* (AK) schemes: Mainly motivated by the difficulties of the self-force and adiabatic approaches to build full families of EMRI waveforms, there was a pressing necessity for the construction of approximate families of waveforms that capture the main features of true EMRI signals and that at the same time can be generated in a quick way. In this regard, Barack and Cutler introduced the dubbed analytical kludge waveforms [Barack 2004]. These are based on the lowest-order, quadrupolar waveforms [Misner 1973] for eccentric-orbit binaries derived by Peters and Matthews [Peters 1963, Peters 1964], but the AK orbits are corrected with PN corrections to account for all the different relativistic effects, such as pericentre precession, Lense-Thirring precession, and GW emission. Analytical kludge waveform models are good enough to provide simple template banks that allow for parameter estimation studies. They have also been employed in the *Mock Data Challenges* aimed at stimulating the development of data analysis techniques and demonstrating their technical readiness for LISA data-analysis purposes.

-*Numerical Kludge* (NK) schemes: The dubbed Numerical Kludge approach has been developed by Babak et al. [Babak 2007]. It can be seen as an alternative approach to AK schemes (in the sense that they are expected to provide more accurate waveform models) and also to the adiabatic approximation (in the sense that they provide a less computationally expensive method for waveform production without degrading much the accuracy). In the NK

scheme, the SCO inspiral is obtained in phase space, that is, it is a trajectory in the space of the constants of motion. This calculation uses the fluxes for Kerr orbits provided in [Gair 2006]. Using the evolution of the constants of motion, the Kerr geodesics are integrated along the inspiral to obtain the Boyer-Lindquist coordinates (t, r, θ, ϕ) of the inspiral trajectory as a function of time. Then, to obtain the gravitational waveforms, the Boyer-Lindquist coordinates of the SCO are identified with standard spherical coordinates in flat-space and then, Cartesian coordinates are computed and introduced in the well-known multipolar expansion of the GWs [Thorne 1980] up to mass octupole and current quadrupole order. In this way, this weak field formula for the waveforms is coupled with a fully relativistic motion, since the trajectory of the particle is computed exactly, up to conservative RR effects and inaccuracies in the phase space trajectory.

- *The Chimera* scheme: This scheme has been recently proposed by Sopuerta and Yunes [Sopuerta 2011] to model the dynamics of EMRIs and to obtain their GWs. The Chimera scheme combines techniques from BH perturbation theory, post-Minkowskian approximations, and post-Newtonian theory. The orbital evolution is approximated as a sequence of osculating Kerr geodesics that shrink due to RR. The RR is modeled via a multipolar expansion in post-Minkowskian theory, here taken up to mass octopole and current quadrupole order. In this scheme, both the orbital evolution and wave generation use a map from the Boyer-Lindquist coordinates of the orbits to the harmonic coordinates used in the post-Minkowskian approximation. Although the Chimera scheme has been initially designed for systems with extreme mass ratios it can also be applied to more moderate mass ratios.

7.3   The GW Model and its Evolution

Our method to model EMRI waveforms in the DCSMG theory follows the lines of the NK scheme described above. In the previous chapter, we already presented the modified geodesic SCO trajectory around the modified MBH geometry. We also studied the introduction of RR effects in DCSMG and concluded that the leading order contribution can be well approximated by using the GR of [Gair 2006] used also in the NK scheme. In principle one can think that using the same RR formulae both in GR and DCSMG cannot break the degeneracy associated with the fact that geodesic trajectories in both theories can be characterised by three fundamental frequencies (see Section 6.4). However, this is not the case because the dependence of the trajectory on the constants of motion $(E, L, \mathcal{Q})$ is different in GR from DCSMG. Then, because

of this, the fundamental frequencies will evolve in a different way despite the fact that we use the same RR formulae.

The only ingredient left to discuss is the computation of the gravitational waveforms themselves. In our analysis we employ the multipolar expansion of the metric perturbations describing the GWs emitted by an isolated system [Thorne 1980], where the transverse-traceless metric perturbation is given by

$$h_{ij}(t) = \frac{2}{r} \left[\ddot{I}_{ij} - 2n^l \dddot{S}_{ljk} + n^l \dddot{M}_{ljk} \right] , \qquad (7.3)$$

where I_{ij} is the mass quadrupole, S_{ijk} is the current quadrupole and M_{ijk} is the mass octopole. Here r is the luminosity distance from the source to the observer in flat space. In this framework, all these multipoles are traceless and defined via

$$I^{ij} = \left[\int dV \, x^i x^j T^{00} \right]^{STF} , \qquad (7.4)$$

$$S^{ijk} = \left[\int dV \, x^i x^j T^{0k} \right]^{STF} , \qquad (7.5)$$

$$M^{ijk} = \left[\int dV \, x^i x^j x^k T^{00} \right]^{STF} , \qquad (7.6)$$

where STF stands for symmetric and trace-free operation (needed to extract the TT part), $T_{\mu\nu}$ is the stress-energy tensor with components $T^{00} = \rho$ and $T^{0j} = \rho v^j$, ρ is the energy density of the matter source (the SCO) given by:

$$\rho(x^i, t) = m \delta^3(x^i - z^i(t)) , \qquad (7.7)$$

where $z^i(t)$ is the spatial trajectory of the SCO and $v^i = dz^i/dt$ is the 3-velocity of the SCO.

In our case, the observer is at the LISA constellation and, in our calculations, we employ the unit vector that points from LISA to the EMRI system written in the Solar System Barycenter (SSB) reference frame (see Table 7.1):

$$\hat{\mathbf{r}}_{SBS} = (\sin \theta_S \cos \phi_S, \sin \theta_S \sin \phi_S, \cos \theta_S) . \qquad (7.8)$$

In order to describe the propagation of the GWs through the spacetime and construct their polarisation tensors, we introduce the polarisation reference frame (see Figure 1.6) given by $\hat{\mathbf{n}}$ and the direction of the MBH spin $\hat{\mathbf{S}}$, which we take pointing in the $\hat{\mathbf{z}}$ direction of the source frame, i.e. $\hat{\mathbf{S}} = S\hat{\mathbf{z}}$. We can

construct an orthonormal basis at the polarisation frame by taking the unit vector $\hat{\mathbf{n}}$ together with the two unit vectors $\hat{\mathbf{p}}$ and $\hat{\mathbf{q}}$, which are defined as:

$$\hat{\mathbf{p}} = \frac{\hat{\mathbf{n}} \times \hat{\mathbf{S}}}{|\hat{\mathbf{n}} \times \hat{\mathbf{S}}|}, \qquad \hat{\mathbf{q}} = \hat{\mathbf{p}} \times \hat{\mathbf{n}}. \qquad (7.9)$$

Moreover, this orthogonal triad $\{\hat{\mathbf{n}}, \hat{\mathbf{p}}, \hat{\mathbf{q}}\}$ can be employed to construct the GW polarisation tensors:

$$\varepsilon_+^{ij} = p_i p_j - q_i q_j, \qquad \varepsilon_\times^{ij} = 2 p_{(i} q_{j)}, \qquad (7.10)$$

where the corresponding GW polarisations are given, using the transverse-traceless gauge, by:

$$h_+(t) = \frac{1}{2}\varepsilon_+^{ij} h_{ij}(t), \qquad h_\times(t) = \frac{1}{2}\varepsilon_\times^{ij} h_{ij}(t), \qquad (7.11)$$

and the converse relation is

$$h_{ij}(t) = \varepsilon_{ij}^+ h_+(t) + \varepsilon_{ij}^\times h_\times(t). \qquad (7.12)$$

Using Eqs. (7.3)-(7.7) we can obtain the following simplified expressions for the GW polarizations in terms of the SCO trajectory:

$$\begin{aligned} h_{+,\times} &= \frac{2m}{r}\varepsilon_{+,\times}^{ij}\left[a_i x_j + v_i v_j + (\mathbf{n} \cdot \mathbf{x})\left(x_i j_j + 3a_i x_j\right) + (\mathbf{n} \cdot \mathbf{v})\left(a_i x_j + v_i v_j\right)\right. \\ &\quad \left. - (\mathbf{n} \cdot \mathbf{a})\, v_i x_j - (\mathbf{n} \cdot \mathbf{j})\frac{1}{2}x_i x_j\right], \end{aligned} \qquad (7.13)$$

where we have introduced the following definitions for the acceleration and jerk: $a_i \equiv \dddot{z}_i$ and $j_i \equiv \dddot{z}_i$ respectively.

Notice that the implementation of the above equations require the use of Cartesian coordinates to cover the SCO motion, whereas the geodesic orbits are written in BL coordinates. Following the procedure followed in the NK scheme described above, we identify the BL coordinates (r, θ, ϕ) with flat-space spherical coordinates and then, we introduce the Cartesian coordinates through the usual relations:

$$x = r \sin\theta \cos\phi, \quad y = r \sin\theta \sin\phi, \quad z = r \cos\theta. \qquad (7.14)$$

In this way, we cover the motion of the SCO and an observer in the radiation zone at the same time [Babak 2007]. Notice that this is an approximation since the multipolar expansions of the waveforms are constructed in a TT gauge, which in principle is not compatible with BL coordinates. However,

we do not expect this to introduce large errors in the waveforms, in particular in the phase.

The response of LISA to an incident GW (see Eq. 1.36) can be written as:

$$h_\alpha(t) = \frac{\sqrt{3}}{2}\left[F_\alpha^+ h^+(t) + F_\alpha^\times h^\times(t)\right], \tag{7.15}$$

where we recall that $\alpha = I, II$ refers to the two independent Michelson-like interferometers that constitute the LISA detector, and where the antenna pattern (response) functions $F_\alpha^{+,\times}$ are given by (see, e.g. [Barack 2004]):

$$
\begin{aligned}
F_I^+ &= \frac{1}{2}(1 + \cos^2\theta)\cos(2\phi)\cos(2\psi) - \cos\theta\sin(2\phi)\sin(2\psi), \\
F_I^\times &= \frac{1}{2}(1 + \cos^2\theta)\cos(2\phi)\cos(2\psi) + \cos\theta\sin(2\phi)\sin(2\psi), \\
F_{II}^+ &= \frac{1}{2}(1 + \cos^2\theta)\sin(2\phi)\cos(2\psi) + \cos\theta\cos(2\phi)\sin(2\psi), \\
F_{II}^\times &= \frac{1}{2}(1 + \cos^2\theta)\sin(2\phi)\sin(2\psi) - \cos\theta\cos(2\phi)\cos(2\psi). \tag{7.16}
\end{aligned}
$$

Here (θ, ϕ) is the sky location of the source in a detector-based coordinate system and ψ is the polarisation angle, which describes the orientation of the "apparent ellipse" given by the projection of the orbit on the sky. However, due to the LISA rotation, it is more convenient to rewrite the response functions in terms of angles defined in a fixed SBS coordinate system (see Table 7.1 for more details). Then, we have to use the relation between the angles (θ, ϕ) and the ones describing the source location in the SBS (θ_S, ϕ_S), which is given by (see, e.g. [Barack 2004]):

$$\cos\theta(t) = \frac{1}{2}\left[\cos\theta_S - \sqrt{3}\sin\theta_S\cos(2\pi(t/T)) - \phi_S\right], \tag{7.17}$$

$$\phi(t) = 2\pi(t/T) + \tan^{-1}\left[\frac{\sqrt{3}\cos\theta_S + \sin\theta_S\cos(2\pi(t/T) - \phi_S)}{2\sin\theta_S\sin(2\pi(t/T) - \phi_S)}\right], \tag{7.18}$$

where T is the time corresponding to the period of the Earth orbit around the Sun, that is, 1 year. On the other hand, ψ can be written in terms of (θ_S, ϕ_S) and the angles describing the direction of the MBH spin with respect to the

SBS frame (θ_K, ϕ_K):

$$
\begin{aligned}
\tan \psi = & \left[\left\{ \cos \theta_K - \sqrt{3} \sin \theta_K \cos(2\pi(t/T) - \phi_K) \right\} \right. \\
& \left. -2 \cos \theta(t) \left\{ \cos \theta_K \cos \theta_S + \sin \theta_K \sin \theta_S \cos(\phi_K - \phi_S) \right\} \right] / \\
& \left[\sin \theta_K \sin \theta_S \sin(\phi_K - \phi_S) - \sqrt{3} \cos(2\pi(t/T)) \left\{ \cos \theta_K \sin \theta_S \sin \phi_S \right. \right. \\
& \left. - \cos \theta_S \sin \theta_K \sin \phi_K \right\} - \sqrt{3} \sin(2\pi(t/T)) \left\{ \cos \theta_S \sin \theta_K \cos \phi_K \right. \\
& \left. \left. - \cos \theta_K \sin \theta_S \cos \phi_S \right\}) \right] .
\end{aligned}
\tag{7.19}
$$

Another thing that we have to take into account in our analysis is that, in general, the time of arrival for a GW will be different when it is computed at the SBS reference frame or at the LISA one, since the time of arrival of the GW to the SBS is given by:

$$
t_{SBS} = t_L + R \sin \theta_S \cos(2\pi t_L - \phi_S) - t_{SBS}^0 ,
\tag{7.20}
$$

where t_L is the time of arrival in the LISA reference frame and t_{SBS}^0 is the initial time in the SBS reference frame. The initial times in both reference frames are related through the following expression:

$$
t_{SBS}^0 = t_L^0 + R \sin \theta_S \cos(2\pi t_L^0 - \phi_S) .
\tag{7.21}
$$

Due to the LISA orbital motion, the phase and frequency of the GW signal are modulated. This spreads an incident monochromatic GW signal across a wide bandwidth, reducing the strength of the signal relative to the instrumental noise. The modulation introduce sidebands at multiples of the orbital frequency $f_m = 1/T$. In order to reduce this effect, the dominant Doppler component of the signal modulation is removed [Cornish 2003]. To that end, we consider the Doppler modulated phase due to the difference of time arrivals between the SSB and LISA:

$$
\Phi(t) = 2\pi f \left[t + R \sin \theta_S \cos(2\pi t/T - \phi_S) \right] ,
\tag{7.22}
$$

where R ($= 1$ AU$/c = 499.00478$s) is the azimuthal velocity of the orbit and $t = t_L$. Then, we seek a new time coordinate measured in the SBS, say $t' = t_{SBS}$, in which the phase is stationary:

$$
\frac{d\Phi}{dt'} = 2\pi f = \frac{d\Phi}{dt} \frac{dt}{dt'} ,
\tag{7.23}
$$

From these expressions we obtain that the difference in the time arrival of the waves due to Doppler modulation is given by:

$$
dt' = dt[1 - 2\pi \sin \theta_S \sin(2\pi t/T - \phi_S)] .
\tag{7.24}
$$

On the other hand, the noise affecting LISA EMRI detections, described in terms of the one-sided noise power spectral density $S_h(f)$, is modelled taking into account three contributions, namely: Instrumental noise $S_h^{\text{inst}}(f)$, confusion noise from short-period galactic binaries $S_h^{\text{gal}}(f)$, and confusion noise from extragalactic binaries $S_h^{\text{exgal}}(f)$ [Barack 2004]:

$$S_h = \min\left\{ S_h^{\text{inst}} \exp\left(\kappa T_{\text{mission}}^{-1} \frac{dN}{df} \right) + S_h^{\text{exgal}} \ , \ S_h^{\text{inst}} + S_h^{\text{gal}} + S_h^{\text{exgal}} \right\} , (7.25)$$

where the different noise contributions are given by:

$$S_h^{\text{inst}}(f) = 9.18 \times 10^{-52} f^{-4} + 1.59 \times 10^{-41} + 9.18 \times 10^{-38} f^2 \ \text{Hz}^{-1}, (7.26)$$

$$S_h^{\text{gal}}(f) = 2.1 \times 10^{-45} \left(\frac{f}{1\text{Hz}} \right)^{-7/3} \text{Hz}^{-1}, (7.27)$$

$$S_h^{\text{exgal}}(f) = 4.2 \times 10^{-47} \left(\frac{f}{1\text{Hz}} \right)^{-7/3} \text{Hz}^{-1}, (7.28)$$

where dN/df is the number density of galactic white dwarf binaries per unit of GW frequency, $T_{mission}$ is the lifetime of the LISA mission, and κ is the average number of frequency bins that are lost when each galactic binary is fitted out. The particular values that we use correspond to:

$$\frac{dN}{df} = 2 \times 10^{-3} \left(\frac{1\text{Hz}}{f} \right)^{11/3} , (7.29)$$

and $\kappa \approx 4.5$ (see, e.g. [Barack 2004]).

The numerical evolution of our system is mainly divided into two parts, namely the computation of the SCO trajectory around the MBH and the computation of the corresponding waveform. As we are considering small deviations from GR and then, the CS parameter is small, the dynamics of the system will be still close to the one of GR.

In GR, the radial r and polar θ coordinates have turning points at $\dot{r} = 0$ and $\dot{\theta} = 0$, leading to different branches during the orbital evolution, which are problematic for numerical integrations (see Section 2.4.1 for the same problem in Schwarzschild). In order to avoid the turning points, we introduce two new coordinates, the angles ψ and χ, which are defined as follows:

$$r = \frac{pM_\bullet}{1 + e \cos\psi} , \qquad \cos^2\theta = \cos^2\theta_{min} \cos^2\chi , (7.30)$$

where p and e are the semilatus rectum and the eccentricity of the orbit respectively, and θ_{min} is the minimum of θ in the orbit, which gives the turning

point of the polar motion. This minimum of θ can be written as

$$\theta_{min} = \text{sign}(L) \left[\frac{\pi}{2} - \theta_{inc} \right] , \tag{7.31}$$

where θ^{inc} is the inclination angle of the orbit in the source frame. Moreover, the sign of L tells us whether the orbit is prograde (positive sign), i.e. the SCO corrotates with the MBH spin, or retrograde (negative sign), i.e. the SCO and the MBH spin rotate in opposite directions. The sign of L is determined by θ_{inc} in the following way:

$$\begin{aligned} \text{for } 0 < \theta_{inc} < \tfrac{\pi}{2} \quad &\Rightarrow \text{sign}(L) = 1 , \\ \text{for } \tfrac{\pi}{2} < \theta_{inc} < \pi \quad &\Rightarrow \text{sign}(L) = -1 . \end{aligned} \tag{7.32}$$

At $\theta = \theta_{min}$ we have that $\dot{\theta} = 0$ and then, the RHS of Eq. (6.38) vanish, leading to an expression for $\mathcal{Q}$:

$$\mathcal{Q} = \cos^2 \theta_{min} \left[\frac{L^2}{\sin^2 \theta_{min}} + a^2 (1 - E^2) \right] . \tag{7.33}$$

We can use this expression for the Carter constant to obtain the energy E and angular momentum L in terms of the orbital parameters (p, e) from the conditions that come from imposing the existence of the turning points of the radial motion, $r_{peri} = pM_\bullet/(1 + e)$ and $r_{apo} = pM_\bullet/(1 - e)$ (see Section 2.4.1 in the context of the bounded geodesics of Schwarzschild), in Eq. (6.37), that is, $\dot{r}(r_{peri}) = 0$ and $\dot{r}(r_{apo}) = 0$.

With the definitions of the new variables ψ and χ, the geodesic equations [Eqs. (6.37)-(6.38)] become ODEs for the variables $(\psi(t), \chi(t), \varphi(t))$ (see e.g [Drasco 2004]) with respect to the BL time t. In order to solve them, we need to introduce in the form of these ODEs the value of the turning points of the radial and polar motions. As it was shown in [Sopuerta 2009], only the equations for the radial turning points are different in DCSMG with respect to GR. Taking all this into account, the scheme for our orbital evolution in DCSMG is as follows: For a given set of initial orbital parameters $(e^{(0)}, p^{(0)}, \theta_{inc}^{(0)})$ we find the associated initial constant of motion $(E^{(0)}, L^{(0)}, \mathcal{Q}^{(0)})$, which differ from the ones that we would obtain in GR. The next step is to compute the time evolution of the "constants" of motion, $(\dot{E}^{(0)}, \dot{L}^{(0)}, \dot{\mathcal{Q}}^{(0)})$, using the same formulae as in the NK scheme introduced in the last section to account for RR effects. More specifically, we use the formulae derived in [Gair 2006]. Then, from the current values of the constant of motion, $(E^{(0)}, L^{(0)}, \mathcal{Q}^{(0)})$, their evolution due to RR, $(\dot{E}^{(0)}, \dot{L}^{(0)}, \dot{\mathcal{Q}}^{(0)})$, and the value of the radial period, T_r (the time to go from the apocenter to

the pericenter and back again to apocenter), we obtain the new constants of motion, $(E^{(1)}, L^{(1)}, \mathcal{Q}^{(1)})$, by applying the following relations:

$$E^{(1)} = E^{(0)} + \delta E^{(1)}, \tag{7.34}$$

$$L^{(1)} = L^{(0)} + \delta L^{(1)}, \tag{7.35}$$

$$\mathcal{Q}^{(1)} = \mathcal{Q}^{(0)} + \delta \mathcal{Q}^{(1)}, \tag{7.36}$$

where:

$$\delta E^{(1)} = \dot{E}^{(0)} N_{periods} T_r, \tag{7.37}$$

$$\delta L^{(1)} = \dot{L}^{(0)} N_{periods} T_r, \tag{7.38}$$

$$\delta \mathcal{Q}^{(1)} = \dot{\mathcal{Q}}^{(0)} N_{periods} T_r, \tag{7.39}$$

where $N_{periods}$ is the number of radial periods that we allow between each update of the constants of motion and orbital parameters. This number is chosen depending on the orbit itself. Finally from $(E^{(1)}, L^{(1)}, \mathcal{Q}^{(1)})$, we obtain the values of the orbital parameters $(p^{(1)}, e^{(1)}, \theta_{inc}^{(1)})$. This algorithm is iterated along the whole EMRI evolution to obtain the SCO orbit and the gravitational waveform. As we have mentioned previously, the EMRIs of interest for doing new science, and in particular for testing a theory like DCSMG, are those that are deep into the strong field region of the MBH. Then, we choose our initial set of orbital parameters $(e^{(0)}, p^{(0)}, \theta_{inc}^{(0)})$ such that the system is not too far from the last stable orbit. Since we expect little deviations from GR, the set of initial orbital parameters $(e^{(0)}, p^{(0)})$ is chosen by looking at the separatrix between stable and unstable orbits for a Kerr BH in GR (we use the slow rotation approximation) [Glampedakis 2002]:

$$p = \left[(6 + 2e) \mp 8a \sqrt{\frac{1+e}{6+2e}} \right] M_\bullet, \tag{7.40}$$

where "$+$" is for prograde orbits, whereas "$-$" is for retrograde orbits. Then, $(e^{(0)}, p^{(0)})$ are set so that their final values after the whole EMRI evolution, (e_f, p_f) fulfil this relation. In practice, since we are working in DCSMG, the value of the final orbit parameters (e_f, p_f) varies from that given by GR. Regarding to the numerical integration of the ODEs for $(\psi(t), \chi(t), \phi(t))$, we use the Bulirsh-Stoer extrapolation method (see, e.g. [Press 1992]).

7.4 Fisher Matrix Analysis

The Fisher matrix (see Section 1.3) plays a fundamental role in forecasting errors from a given experimental set-up, since it estimates the likelihood of

the parameters errors before we do the experiment. Fisher matrices can be computed quickly and then, enables us to explore different experimental set-ups and optimise them. For this reason, it is widely employed to perform survey designs, for example, in cosmology.

Since we have not at hand real GW data to perform parameter estimation, Fisher matrix analysis is employed to characterise the expected parameter estimation accuracy for hypothetical observatories, providing low bounds on the spread of the maximum-likelihood estimator across all possible noise realisations. Moreover, it also provides the leading-order width of the posterior probability density (see, e.g. [Vallisneri 2011]), i.e. the probability of the hypothesis, in our case the particular EMRI model in the DCSMG theory is our hypothesis, given the detected data.

In order to compute the Fisher matrix, we employ the following inner product defined in the frequency domain [Eq. (1.52)]:

$$(\partial_i \mathbf{h}_\alpha | \partial_j \mathbf{h}_\alpha) = 4 \sum_\alpha \Re \int_0^\infty \frac{\partial_i \tilde{\mathbf{h}}_\alpha(f) \partial_j \tilde{\mathbf{h}}_\alpha(f)}{S_h(f)} df \ , \tag{7.41}$$

where we recall that $\alpha = I, II$ stands for each of the LISA interferometers (see Section 1.3). The waveform derivatives, $\partial_i \mathbf{h} = \partial \mathbf{h}/\partial \theta^i$, are computed numerically through the following centered five-point finite-difference expression:

$$\partial_i \mathbf{h}_\alpha \approx \frac{\mathbf{h}_\alpha(\theta^i + 2\delta\theta^i) + 8\left[\mathbf{h}_\alpha(\theta^i + \delta\theta^i) - \mathbf{h}_\alpha(\theta^i - \delta\theta^i)\right] - \mathbf{h}_\alpha(\theta^i - 2\delta\theta^i)}{12\delta\theta^i} \tag{7.42}$$

where $\delta\theta^i$ is a shift on the corresponding parameter. This approximated differentiation rule has an associated numerical error that is proportional to $(\delta\theta^i)^4$. In this way, we need to compute four waveforms for each $\mathbf{h}_\alpha$, that is in total, eight waveforms for each parameter.

A key point in the computation of the Fisher matrix, due to the complications in performing numerical derivatives, is to choose the shift of the system parameters. If we choose a shift too small there will be a lot of cancellations in Eq. (7.42) yielding an incorrect result whereas if we use a shift too big we will simply get a wrong result since we are using points that do not represent the local behaviour of the waveforms. In order to assert that the error estimates obtained are reliable we should find a range of shifts, say $\delta\theta^i \in (\delta\theta^i_A, \delta\theta^i_B)$, such that the corresponding error estimates (given by the diagonal of the covariance matrix $\sqrt{\Gamma_{ii}^{-1}}$ [Eq. 1.53]) converge. To find these ranges one has to explore the parameter space of the EMRI system around the parameters where the errors have to be estimated. To that end, we perform several simulations for a given set of system parameters and for different

Table 7.1: *Summary of the EMRI parameter space employed in our analysis. The angles (θ_S, ϕ_S) and (θ_K, ϕ_K) are spherical coordinates and t_0 stands for the initial time in our computations. For the parameters with physical dimension, we have specified it in terms of the MBH mass $M_\bullet$ within round brackets.*

$M_\bullet$	MBH mass.
$a = \|\mathbf{S}\|/M_\bullet$ $(M_\bullet)$	MBH Spin.
$\mu = m/M_\bullet$	Mass-ratio.
e_0	Eccentricity of the particle orbit at t_0.
p_0	Semilatus rectum at t_0
θ_0^{inc}	Inclination of the orbit at t_0.
$\hat{\xi} = \xi \times S$ $(M_\bullet^6)$	Product of the Chern-Simons parameter and the spin.
θ_S	Polar angle with respect to the ecliptic.
ϕ_S	Azimuthal angle with respect to the ecliptic.
θ_K	Spin polar angle with respect to the ecliptic.
ϕ_K	Spin azimuthal angle with respect to the ecliptic.
D_L (Gyr)	Distance to the EMRI from the ecliptic baricentre.
ψ_0	BL angle associated with the BL coordinate r at t_0.
χ_0	BL angle associated with the BL coordinate θ at t_0.
ϕ_0	BL angle ϕ at t_0.

shifts to determine both $\delta\theta_A^i$ and $\delta\theta_B^i$. However, this is not the end of the story since, as we mentioned in Section 1.3, the error values obtained through the Fisher matrix formalism are only reliable for values of SNR high enough, for which $h(\theta^i)$ is linear in a region around all the parameters θ^i. This is assured if the error estimates obtained fulfil the Eq. (1.56).

In our simulations, we choose the space of EMRI parameters in DCSMG, $\{\theta^i | i = 1, \ldots, N\}$ with $N = 15$, as follows (see Table 7.1 for a description of these parameters):

$$\theta^i = \{M_\bullet, a, \mu, e_0, p_0, \theta_0^{inc}, \hat{\xi}, \theta_S, \phi_S, \theta_K, \phi_K, D_L, \psi_0, \chi_0, \phi_0\}. \qquad (7.43)$$

Due that Fisher matrices use to have very large condition numbers (the ratio of the largest to the smallest eigenvalues), we use a *LU decomposition* to invert it, where the Fisher matrix is written as the product of a lower triangular matrix and an upper triangular matrix, and then we obtain the full covariance matrix [Eq. (1.53)] [Huerta 2009]. In practice, we do the inversion numerically employing the *GSL* library [LU].

7.5   Results

The main goal of our study is to determine to what extent LISA could estimate the EMRI parameters in DCSMG and constrain the CS parameter ξ [Eq. (6.17)] employing Fisher matrix analysis (see Sections 1.3 and 7.4). Following [Sopuerta 2009], we have modeled the motion of the SCO as evolving geodesics in the modified DCSMG MBH geometry. The RR that governs the evolution of the geodesics employs the fact that, at leading-order, the GW emission in DCSMG is the same that in GR [Sopuerta 2009]. Then, we model the inspiral, i.e. the sequence of geodesics, using the philosophy of the NK scheme [Babak 2007] and use the GR expressions of [Gair 2006] for the evolution of the energy E, the angular momentum in the spin direction L, and the Carter constant $\mathcal{Q}$. The GWs are generated with the multipolar formalism given by Thorne [Thorne 1980] up to the quadrupolar order. Finally, the LISA response and the Doppler modulation are computed following [Barack 2004] and [Cornish 2003] respectively (see Section 7.3).

Table 7.2: *Parameter accuracy estimates for the inspiral of a $10M_\odot$ SCO into a $10^6 M_\odot$ MBH. The data have been collected during the last year of inspiral within GR. We compare the results we have obtained using our version of the NK scheme with the results obtained for the same parameters employing AK waveforms [Barack 2004].*

Parameter	This Work	AK
$\Delta \ln M_\bullet$	8.6×10^{-4}	9.2×10^{-4}
$\Delta a/M_\bullet$ $(M_\bullet)$	9.5×10^{-6}	6.3×10^{-4}
$\Delta \ln \mu$	1.4×10^{-4}	9.2×10^{-5}
Δe	2.7×10^{-5}	2.8×10^{-4}
$\Delta \ln D_L$ [(a)] , $\Delta \ln (\mu/D_L)$ [(b)]	6.5×10^{-2} [(a)]	3.7×10^{-2} [(b)]

Employing all the machinery developed along this second part of the thesis, we have computed the error estimates for different systems in DCSMG and their homologous in GR (that is, setting $\xi = 0$). To that end, we first choose a specific point θ^i in the parameter space, to subsequently calculate the EMRI GW and its $2N$ derivatives, where N corresponds to the total number of parameters employed in the simulation (a maximum of 14 in DCSMG) and the 2 accounts for the two LISA channels. Finally, we obtain the variance-covariance matrix of errors through Eq. (1.53), whose corresponding maximum-mismatch criterium [Eq. (1.56)] is typically $|\log r(\delta\theta^k, \text{SNR})| < 0.4$.

As a test of our numerical set-up, we compare our numerical parameter estimates with the ones obtained in [Barack 2004] for the orbital evolution of

Table 7.3: *Parameters of the different systems employed in our simulations, where we have fixed $p = 10$, $\theta_{inc} = 0.85$, $\theta_S = 1.1$, $\phi_S = 0.3$, $\theta_K = 1.4$, $\phi_K = 0.25$, $D_L = 1\,Gyr$, $\psi_0 = 0.25$, $\chi_0 = 1$, and $\phi_0 = 0.1$.*

System	$M_\bullet$	$a/M_\bullet$	μ	e_0	$\hat{\xi}/M_\bullet^6$
A	5×10^5	0.5	2×10^{-5}	0.5	10^{-2}
B	5×10^5	0.5	2×10^{-5}	0.5	0
C	5×10^5	0.25	2×10^{-5}	0.5	10^{-2}
D	5×10^5	0.25	2×10^{-5}	0.5	0
E	10^6	0.25	10^{-5}	0.32	10^{-2}
F	10^6	0.25	10^{-5}	0.32	0

a $10 M_\odot$ SCO into a $10^6 M_\odot$ MBH in GR. As we can see in Table 7.2, the estimation obtained with both methods agree.

Table 7.4: *Error estimates for half a year of evolution ($SNR = 35$) for Systems A, B, C, and D; and for a year of evolution ($SNR = 40$) for Systems E and F.*

Parameter	A	B	C	D	E	F
$\Delta \ln M_\bullet$	1.0×10^{-4}	9.8×10^{-3}	7.8×10^{-4}	7.6×10^{-4}	8.6×10^{-4}	8.4×10^{-4}
$\Delta a \;\; (M_\bullet)$	1.5×10^{-5}	9.5×10^{-6}	7.5×10^{-6}	6.3×10^{-6}	1.8×10^{-5}	9.1×10^{-6}
$\Delta \ln \mu$	1.8×10^{-4}	3.9×10^{-5}	5.7×10^{-5}	2.4×10^{-5}	3.2×10^{-4}	1.2×10^{-4}
Δe_0	9.2×10^{-5}	9.2×10^{-5}	8.4×10^{-5}	8.4×10^{-5}	1.9×10^{-5}	1.7×10^{-5}
$\Delta \theta_0^{inc}$	2.8×10^{-5}	1.7×10^{-5}	2.6×10^{-5}	2.2×10^{-5}	8.1×10^{-5}	3.2×10^{-5}
$\Delta \ln \hat{\xi}$	2.1		4.4×10^{-1}		5.1	
$\Delta \theta_S$	1.8×10^{-2}	1.7×10^{-2}	1.5×10^{-2}	1.4×10^{-2}	1.1×10^{-2}	1.1×10^{-2}
$\Delta \phi_S$	1.7×10^{-2}	1.6×10^{-2}	1.5×10^{-2}	1.5×10^{-2}	2.1×10^{-2}	2.0×10^{-2}
$\Delta \theta_K$	2.8×10^{-2}	2.8×10^{-2}	2.5×10^{-2}	2.5×10^{-2}	2.3×10^{-2}	2.3×10^{-2}
$\Delta \phi_K$	7.2×10^{-2}	7.2×10^{-2}	6.5×10^{-2}	6.5×10^{-2}	8.6×10^{-2}	8.6×10^{-2}
$\Delta D_L \;\; (Gyr)$	2.7×10^{-2}	2.6×10^{-2}	2.2×10^{-2}	2.3×10^{-2}	1.8×10^{-2}	1.9×10^{-2}
$\Delta \psi_0$	9.8×10^{-2}	7.1×10^{-2}	7.2×10^{-2}	6.0×10^{-2}	1.0×10^{-2}	8.6×10^{-2}
$\Delta \chi_0$	8.6×10^{-2}	8.5×10^{-2}	7.7×10^{-2}	7.7×10^{-2}	9.2×10^{-2}	9.0×10^{-2}
$\Delta \varphi_0$	8.6×10^{-2}	8.3×10^{-2}	7.6×10^{-2}	7.5×10^{-2}	1.1×10^{-1}	1.1×10^{-2}

In Table 7.3 we show the different (systems) parameters employed in our simulations, where the distance to the source is give in Gpc the angles are given in radians and the rest of the parameters are given in MBH mass units, but the MBH itself is given in solar masses. The direction of the MBH spin is taken to be parallel to the z-direction of the EMRI reference frame. We have employed two different kind of EMRIs, namely one composed of a MBH with $M_\bullet = 5 \times 10^5 M_\odot$ and a SCO of mass $m = 10 M_\odot$, and the other composed of a MBH with mass $M_\bullet = 10^6 M_\odot$ and SCO mass $m = 10 M_\odot$. The former has been evolved during half a year before plunge (SNR= 35)

and the latter during one year (SNR= 40). In Table 7.4, we show the error estimates obtained in our simulations. As we can see, we find typically that an EMRI observation can determine the extrinsic parameters, namely $\theta_{extrinsic} = \{\theta_S, \phi_S, \theta_K, \phi_k, D_L, \psi_0, \chi_0, \phi_0\}$, within a fractional error of $\sim 10^{-2}$, whereas the intrinsic parameters: $\theta_{intrinsic} = \{M_\bullet, a, \mu, e_0, \theta_0^{inc}, \hat{\xi}\}$, are typically obtained with a fractional error of $\sim 10^{-4}, 10^{-5}, 10^{-5}, 10^{-5}, 10^{-5}, 10^{-1}$. From these results we estimate that a GW observatory like LISA could be able to detect the CS parameter with an error of the order of 0.1 from EMRI observations. Moreover, we obtain that for a fixed value of $\hat{\xi}$, its error is better estimated by the systems with smaller MBH mass, $M_\bullet$, and spin, a. This is not surprising, since the leading factor that contains the CS parameter in the DCSMG metric [Eq. (6.20)] is $\sim \xi a M_\bullet^2$, and then by decreasing the MBH mass and its spin the weight of ξ increases.

Due to computational cost of these computations, a full (including all the parameters) error estimation takes in average time three days using a single processor machine, we have only studied a small sample in the parameter space of all possible EMRI systems that we could detect. In this sense, these results can be improved by performing a more exhaustive study of the parameter space and also using a full Monte Carlo sampling. On the other hand, we could have considered longer gravitational waveforms, in particular waveforms that cover the entire length of the LISA mission, which would improve the error estimation.

Conclusions and Future Prospects

This thesis has two differentiated parts, where we have explored two different lines of research, both related with the science that we expect to perform with EMRIs (and/or IMRIs). In the first part, we have focussed on the development of a novel time-domain technique for computing the self-force. In particular, in Chapters 2 - 5, we have exposed the state of the art of self-force computations, the foundations and implementation of our PwP method and, finally, we have applied it to the computation of the self-force acting on a scalar EMRI model.

The key ingredient of our formulation consist on a multidomain framework, in which the particle (always located at the interface of two subdomains) is replaced by boundary conditions. In this way, the equations solved inside each subdomain are homogeneous wave-type equations for the fields. Consequently, all the problems related with the numerical resolution of a small scale disappear. The work we have presented here can be further improved in terms of computational time, and perhaps in accuracy, by exploring techniques to bring the outer boundaries closer to the particle without degrading the accuracy of the field values near it. This can be done either by improving the outgoing boundary conditions (see, e.g. [Lau 2004]) or by compactifying the physical domain (see, e.g. [Zenginoğlu 2011]). There are two more possibilities for making our computations faster, which are: (i) To reduce the time step of our numerical evolutions, by changing the linear mapping between the physical and spectral representations, and, (ii) to parallelise our numerical code and use computers with many cores (although this does not decrease the CPU time). Since in the Schwarzschild case presented here the different modes are not coupled, this is in principle a simple task. In addition, we can introduce Richardson extrapolation, to improve the estimations of the values of the self-force by using our analytical knowledge of the expansions of the singular field in inverse powers of the harmonic number ℓ, like in [Detweiler 2003a]. These improvements can be perfectly applied to our framework and have significant potential to improve the efficiency of the computations.

Finally, the main goal of the formulation presented in this thesis is to develop an accurate and efficient method to compute the self-force in real physical systems. In particular, for systems of interest for the future observatory LISA.

This means to extend these techniques to the gravitational case and to spinning MBHs. In this sense, we have to mention that while it is straightforward to transfer these techniques discussed here to the gravitational case, to do the same with the case of a spinning black hole may require new technical improvements which we will the subject of future investigations.

On the other hand, in Chapters 6 and 7, we focused on another problem related with EMRI detections, namely the potential ability of LISA to discriminate between GR and alternative theories of gravity. In particular, we have studied the possibility of distinguishing between GR and DCSMG. To that end, we have computed the waveforms emitted by a SCO orbiting in a MBH geometry which have been modified with CS corrections, and the parameter estimation has been performed employing Fisher matrix analysis. We have studied a typical EMRI system in GR and we have found agreement between our results and previous ones found in the literature. Afterwards, we have performed parameter estimation studies to estimate the ability of LISA to distinguish between GR and DCSMG, in particular by estimating the CS parameter ξ. To doing so, we have performed simulations of an EMRI system which falls in the sweet spot of the LISA sensitivity band and we have evolved the system during the last six months before plunge. Our results indicate that, for certain EMRI systems, a detector like LISA may discriminate between GR and DCSMG. We have also seen that the error in estimating ξ decreases with the MBH mass and spin. In order to improve the present results, we would like to perform a more exhaustive study of the parameter space of EMRIs.

In the future, we would like to address topics like to compare or estimate the errors that could arise using GR waveform templates to detect EMRIS in DCSMG. To that end, we can use the formalism developed by Curtler and Vallisneri [Cutler 2007], which allows for the estimation of the magnitude of the model errors. We would like to extend the study presented in this thesis to other GW detectors like, for instance, IMRIs in the Einstein Telescope.

Spherical Harmonics

The expression we use for the scalar spherical harmonics is:

$$Y^{\ell m}(\theta, \varphi) = \sqrt{\frac{2\ell + 1}{4\pi} \frac{(\ell - m)!}{(\ell + m)!}} \, P^{\ell m}(\cos\theta) e^{im\varphi} \, , \qquad \text{(A.1)}$$

where $P^{\ell m}$ are the associated Legendre polynomials [we use the same expressions as in [Abramowitz 1972], equations (8.6.6) and (8.6.18)]

$$P^{\ell m}(x) = \frac{(-1)^{\ell + m}}{2^\ell \, \ell!} (1 - x^2)^{m/2} \frac{d^{\ell + m}}{dx^{\ell + m}} (1 - x^2)^\ell \, , \qquad \text{(A.2)}$$

where ℓ is a non-negative integer and m is an integer restricted to the following range: $m \in (-\ell, -\ell + 1, \ldots, \ell - 1, \ell)$.

Structure of the Singular Field

In the description of the problem in Section 2.4 it was made clear that the computation of the self-force requires the regularisation of the retarded scalar field. This can be done in the framework of the mode-sum scheme, where we need to compute both the harmonic components of the retarded and singular parts of the scalar field at the particle location r_p. The singular part of the retarded field can be computed analytically through Eq. (2.89), here we relate the expressions for the A_α, B_α, C_α, D_α regularisation parameters needed to compute it.

For the case of circular geodesics, the non-vanishing regularisation parameters are A_r, B_r, and D_r [Barack 2002b, Barack 2000b, Detweiler 2003a], [Barack 2002b, Barack 2000b, Detweiler 2003a], which can be written as follows:

$$A_r = -\frac{\sigma_p}{r_p^2} \frac{\sqrt{1 - 3M/r_p}}{1 - 2M/r_p} \, ,$$

(B.1)

$$B_r = -\frac{1}{r_p^2} \sqrt{\frac{1 - 3M/r_p}{1 - 2M/r_p}} \left[F_{1/2} - \frac{1 - 3M/r_p}{2(1 - 2M/r_p)} F_{3/2} \right] \, ,$$

(B.2)

$$
\begin{aligned}
D_r = {} & \frac{1}{r_p^2} \sqrt{\frac{2(1 - 2M/r_p)}{1 - 3M/r_p}} \left\{ -\frac{M}{2r_p} \frac{1 - 2M/r_p}{1 - 3M/r_p} F_{-1/2} \right. \\
& - \frac{(1 - M/r_p)(1 - 4M/r_p)}{8(1 - 2M/r_p)} F_{1/2} \\
& + \frac{(1 - 3M/r_p)(5 - 7M/r_p - 14M^2/r_p^2)}{16(1 - 2M/r_p)^2} F_{3/2} \\
& \left. - \frac{3(1 - 3M/r_p)^2(1 + M/r_p)}{16(1 - 2M/r_p)^2} F_{5/2} \right\} \, ,
\end{aligned}
$$

Another derivation for the regularisation parameters is given in [Haas 2006], where $\nabla_\nu \Phi$ is decomposed in terms of a complex tetrad $e^\alpha_{(\mu)}(x)$, with the index $(\mu) = \{(0), (+), (-), (3)\}$ labelling the different components of this tetrad:

$$e^\alpha_{(0)} = \left[\frac{1}{\sqrt{f}}, 0, 0, 0\right], \tag{B.3}$$

$$e^\alpha_{(3)} = \left[0, \sqrt{f}\cos\theta, -\frac{\sin\theta}{r}, 0\right], \tag{B.4}$$

$$e^\alpha_{(\pm)} = \left[0, \sqrt{f}\sin\theta e^{\pm i\varphi}, \frac{\cos\theta e^{\pm i\varphi}}{r}, \frac{\pm i e^{\pm i\varphi}}{r\sin\theta}\right]. \tag{B.5}$$

The components of the gradient of the retarded field in this tetrad, $\Phi_{(\mu)} \equiv \Phi_\alpha e^\alpha_{(\mu)}$, are scalars. Thus, we can expand $\Phi_{(\mu)}$ in scalar spherical harmonics:

$$\Phi_{(\mu)}(x^\alpha) = \sum_{\ell=0}^\infty \sum_{m=-\ell}^\ell \Phi^{\ell m}_{(\mu)}(t, r) Y^{\ell m}(\theta, \varphi). \tag{B.6}$$

In this way, the components of the gradient of the regular field are given by:

$$\Phi^R_\alpha = \Phi_\alpha - \Phi^S_\alpha = \left\{\Phi_{(\mu)} - \Phi^S_{(\mu)}\right\} e^{(\mu)}_\alpha, \tag{B.7}$$

where, $\Phi_{(\mu)}$ and $\Phi^S_{(\mu)}$, are the tetrad projections of the gradient of the retarded and singular fields. Moreover, the relation between the tetrad and coordinate components of the gradient of the regular field can be written in the form:

$$\Phi^{\ell m}_{(0)} = \frac{1}{\sqrt{f}}\partial_t \Phi^{\ell m}, \tag{B.8}$$

$$\Phi^{\ell m}_{(+)} = -\hat{\alpha}^{\ell m}_{(+)}\left(\Phi^{\ell-1\,m-1}\right) + \hat{\beta}^{\ell m}_{(+)}\left(\Phi^{\ell+1\,m-1}\right), \tag{B.9}$$

$$\Phi^{\ell m}_{(-)} = \hat{\alpha}^{\ell m}_{(-)}\left(\Phi^{\ell-1\,m+1}\right) - \hat{\beta}^{\ell m}_{(-)}\left(\Phi^{\ell+1\,m+1}\right), \tag{B.10}$$

$$\Phi^{\ell m}_{(3)} = \hat{\alpha}^{\ell m}_3\left(\Phi^{\ell-1\,m}\right) + \hat{\beta}^{\ell m}_3\left(\Phi^{\ell+1\,m}\right), \tag{B.11}$$

where $\hat{\alpha}^{\ell m}_{(+)}$, $\hat{\beta}^{\ell m}_{(+)}$, $\hat{\alpha}^{\ell m}_{(-)}$, $\hat{\beta}^{\ell m}_{(-)}$, $\hat{\alpha}^{\ell m}_3$, and $\hat{\beta}^{\ell m}_3$ are linear operators given by the following expressions

$$\hat{\alpha}^{\ell m}_{(+)} = \sqrt{\frac{(\ell+m-1)(\ell+m)}{(2\ell-1)(2\ell+1)}}\left(\sqrt{f}\frac{\partial}{\partial r} - \frac{\ell-1}{r}\right), \tag{B.12}$$

$$\hat{\alpha}^{\ell m}_{(-)} = \sqrt{\frac{(\ell-m-1)(\ell-m)}{(2\ell-1)(2\ell+1)}}\left(\sqrt{f}\frac{\partial}{\partial r} - \frac{\ell-1}{r}\right), \tag{B.13}$$

$$\hat{\alpha}_3 = \sqrt{\frac{(\ell-m)(\ell+m)}{(2\ell-1)(2\ell+1)}}\left(\sqrt{f}\frac{\partial}{\partial r} - \frac{\ell-1}{r}\right), \tag{B.14}$$

$$\hat{\beta}^{\ell m}_{(+)} = \sqrt{\frac{(\ell - m + 1)(\ell - m + 2)}{(2\ell + 1)(2\ell + 3)}} \left(\sqrt{f} \frac{\partial}{\partial r} + \frac{\ell + 2}{r} \right) , \qquad (\text{B.15})$$

$$\hat{\beta}^{\ell m}_{(-)} = \sqrt{\frac{(\ell + m + 1)(\ell + m + 2)}{(2\ell + 1)(2\ell + 3)}} \left(\sqrt{f} \frac{\partial}{\partial r} + \frac{\ell + 2}{r} \right) , \qquad (\text{B.16})$$

$$\hat{\beta}_3 = \sqrt{\frac{(\ell - m + 1)(\ell + m + 1)}{(2\ell + 1)(2\ell + 3)}} \left(\sqrt{f} \frac{\partial}{\partial r} + \frac{\ell + 2}{r} \right) , \qquad (\text{B.17})$$

On the other hand, the tetrad projections of the singular can be written as:

$$\Phi^{\text{s},\ell}_{(\mu)} = q \left\{ (\ell + \tfrac{1}{2}) A_{(\mu)} + B_{(\mu)} + \frac{C_{(\mu)}}{\ell + \tfrac{1}{2}} + \frac{D_{(\mu)}}{(\ell - \tfrac{1}{2})(\ell + \tfrac{3}{2})} + \cdots \right\} . \quad (\text{B.18})$$

The components $A_{(\mu)}$ of the regularisation parameters are given by

$$A_{(0)} = \frac{\varepsilon_p E_p \dot{r}_p}{f_p^{3/2} \left(r_p^2 + L_p^2 \right)} , \qquad (\text{B.19})$$

$$A_{(+)} = \bar{A}_{(-)} = -\varepsilon_p \frac{E_p e^{i\varphi_p}}{\sqrt{f_p} \left(r_p^2 + L_p^2 \right)} , \qquad (\text{B.20})$$

$$A_{(3)} = 0 , \qquad (\text{B.21})$$

where we recall that a dot means differentiation with respect to the coordinate time t; a bar denotes complex conjugate; E_p and L_p are the energy and angular momentum of the particle; $f_p = 1 - 2M_\bullet/r_p$; and ε_p is

$$\varepsilon_p = \text{sign}(r - r_p) = \begin{cases} 1 & \text{if } r > r_p , \\[2mm] -1 & \text{if } r < r_p . \end{cases} \qquad (\text{B.22})$$

On the other hand, the components $B_{(\mu)}$ of the regularisation parameters are:

$$B_{(0)} = \frac{E_p^2 r_p \dot{r}_p}{2 \left[f_p \left(r_p^2 + L_p^2 \right) \right]^{3/2}} \left(F_{1/2} - 2F_{-1/2} \right) , \qquad (\text{B.23})$$

where $F_{1/2}$ and $F_{-1/2}$ are objects defined in terms of hypergeometric functions [Abramowitz 1972] as:

$$F_{1/2} = F(\frac{1}{2}, \frac{1}{2}; 1; \frac{L_p^2}{r_p^2 + L_p^2}) , \qquad (\text{B.24})$$

$$F_{-1/2} = F(-\frac{1}{2}, \frac{1}{2}; 1; \frac{L_p^2}{r_p^2 + L_p^2}), \tag{B.25}$$

and

$$B_{(+)} = \bar{B}_{(-)} = e^{i\varphi_p}(\Re[B_{(+)}] - i\Im[B_{(+)}]), \tag{B.26}$$

where $\Re(z)$ and $\Im(z)$ denote the real and imaginary parts of the complex number z. In the case of $B_{(+)}$, these parts are given by

$$\begin{aligned}
\Re[B_{(+)}] &= \frac{E_p^2 \, r_p \, \dot{r}_p^2}{2 f_p^{5/2} \left(r_p^2 + L_p^2\right)^{3/2}} \left(2F_{-1/2} - F_{1/2}\right) \\
&+ \frac{1}{2 \, r_p \sqrt{r_p^2 + L_p^2}} \left(\sqrt{f_p} \, F_{-1/2} - 2 \left(\sqrt{f_p} - 1\right) F_{1/2}\right), \tag{B.27}
\end{aligned}$$

$$\Im[B_{(+)}] = \frac{\left(2 - \sqrt{f_p}\right) E_p \, \dot{r}_p}{2 L_p \, f_p^{3/2} \sqrt{\left(r_p^2 + L_p^2\right)}} \left(F_{1/2} - F_{-1/2}\right). \tag{B.28}$$

Moreover, we have

$$B_{(3)} = 0, \quad \text{and} \quad C_{(\mu)} = 0. \tag{B.29}$$

Finally, the components $D_{(\mu)}$ of the regularisation parameters are:

$$\begin{aligned}
D_{(0)} &= \frac{E_p^4 \, r_p^3 \, \dot{r}_p^3}{16 \left[f_p \left(r_p^2 + L_p^2\right)\right]^{7/2}} \left\{\left(5r_p^2 - 3L_p^2\right) F_{1/2} - 8 \left(r_p^2 - L_p^2\right) F_{-1/2}\right\} \\
&+ \frac{E_p^2 \, \dot{r}_p}{16 f_p^{3/2} \left(r_p^2 + L_p^2\right)^{5/2}} \left\{\left(F_{1/2} - F_{-1/2}\right) r_p^3\right. \\
&+ M r_p^2 \left(16 \, F_{1/2} - 30 \, F_{-1/2}\right) - r_p L_p^2 \left(3 \, F_{1/2} - 7 \, F_{-1/2}\right) \\
&+ M L_p^2 \left(42 \, F_{1/2} - 114 \, F_{-1/2}\right) \\
&+ \frac{M L_p^4}{r_p^2} \left(18 \, F_{1/2} - 104 \, F_{-1/2}\right) - \left.\frac{36 M L_p^6}{r_p^4} F_{-1/2}\right\}, \tag{B.30}
\end{aligned}$$

$$D_{(+)} = \bar{D}_{(-)} = e^{i\varphi_p} \left(\Re[D_{(+)}] - i\,\Im[D_{(+)}]\right), \tag{B.31}$$

with

$$\Re[D_{(+)}] = \frac{E_p^4 \, r_p^3 \, \dot{r}_p^4}{16 \, f_p^{9/2} \left(r_p^2 + L_p^2\right)^{7/2}} \left\{ 8(r_p^2 - L_p^2) F_{-1/2} - (5r_p^2 - 3L_p^2) F_{1/2} \right\}$$

$$+ \frac{E_p^2 \, r_p \, \dot{r}_p^2}{8 \, f_p^2 \left(r_p^2 + L_p^2\right)^{3/2}} \left(F_{1/2} - 2 \, F_{-1/2} \right)$$

$$+ \frac{E_p^2 \, \dot{r}_p^2}{16 \, f_p^{5/2} \left(r_p^2 + L_p^2\right)^{5/2}}$$

$$\left\{ 4 \left(3r_p^3 + 6Mr_p^2 - L_p^2 r_p + 31ML_p^2 + \frac{26ML_p^4}{r_p^2} + \frac{9ML_p^6}{r_p^4} \right) F_{-1/2} \right.$$

$$\left. - \left(7r_p^3 + 12Mr_p^2 - L_p^2 r_p + 46ML_p^2 + \frac{18ML_p^4}{r_p^2} \right) F_{1/2} \right\}$$

$$+ \frac{\sqrt{f_p}}{16(r_p^2 + L_p^2)^{3/2}} \left\{ \left(3r_p + 8M + \frac{L_p^2}{r_p} + \frac{26ML_p^2}{r_p^2} + \frac{22ML_p^4}{r_p^4} + \frac{8ML_p^6}{r_p^6} \right) F_{-1/2} \right.$$

$$\left. - \left(7r_p + 6M + \frac{6L_p^2}{r_p} + \frac{12ML_p^2}{r_p^2} + \frac{4ML_p^4}{r_p^4} \right) F_{1/2} \right\}$$

$$- \frac{1}{8\sqrt{r_p^2 + L_p^2}} \left\{ \left(\frac{1}{r_p} + \frac{2M}{r_p^2} - \frac{4ML_p^2}{r_p^4} \right) F_{-1/2} - \frac{3F_{1/2}}{r_p} \right\} , \tag{B.32}$$

$$\Im[D_{(+)}] = \frac{(\sqrt{f_p} - 2)E_p^3 \, r_p^2 \, \dot{r}_p^3}{16L_p \, f_p^{7/2} \left(r_p^2 + L_p^2\right)^{5/2}} \left\{ (r_p^2 - 7L_p^2) F_{-1/2} - (r_p^2 - 3L_p^2) F_{1/2} \right\}$$

$$+ \frac{E_p \, \dot{r}_p}{16L_p f_p \left(r_p^2 + L_p^2\right)^{3/2}} \left\{ \left(4r_p^2 + 2Mr_p + 7L_p^2 + \frac{10ML_p^2}{r_p} + \frac{14ML_p^4}{r_p^3} \right) F_{1/2} \right.$$

$$\left. - 2 \left(2r_p^2 + Mr_p + 5L_p^2 + \frac{10ML_p^2}{r_p} + \frac{29ML_p^4}{r_p^3} + \frac{14ML_p^6}{r_p^5} \right) F_{-1/2} \right\}$$

$$+ \frac{E_p \, \dot{r}_p}{8L_p \, f_p^{3/2} \left(r_p^2 + L_p^2\right)^{3/2}} \left\{ 2 \left(r_p^2 - Mr_p + 4L_p^2 - \frac{5ML_p^2}{r_p} + \frac{2ML_p^4}{r_p^3} \right) F_{-1/2} \right.$$

$$\left. - \left(2r_p^2 - 2Mr_p + 5L_p^2 - \frac{8ML_p^2}{r_p} \right) F_{1/2} \right\} , \tag{B.33}$$

and

$$D_{(3)} = 0 . \tag{B.34}$$

The regularisation parameters associated with the coordinate expression of the singular field, see Eq. (2.89), obtained by [Barack 2002b] and [Kim 2004]), are:

$$A_t = -\varepsilon_p \frac{E_p \, \dot{r}_p}{f_p \left(r_p^2 + L_p^2\right)} , \tag{B.35}$$

$$A_r = \varepsilon_p \frac{E_p}{f_p \left(r_p^2 + L_p^2\right)}\,, \tag{B.36}$$

$$A_\varphi = 0\,, \tag{B.37}$$

$$B_t = \frac{E_p^2\, r_p \dot{r}_p \left(F_{1/2} - 2F_{-1/2}\right)}{2\, f_p \left(r_p^2 + L_p^2\right)^{3/2}}\,, \tag{B.38}$$

$$B_r = \frac{E_p^2\, r_p \left[(\dot{r}_p^2 - 2f_p^2)F_{1/2} + (\dot{r}_p^2 - f_p^2)F_{-1/2}\right]}{2\, f_p^3 \left(r_p^2 + L_p^2\right)^{3/2}}\,, \tag{B.39}$$

$$B_\varphi = \frac{E_p\, r_p \dot{r}_p \left(F_{1/2} - F_{-1/2}\right)}{2\, L_p\, f_p \sqrt{r_p^2 + L_p^2}}\,, \tag{B.40}$$

$$C_\alpha = 0\,. \tag{B.41}$$

In this case, the regularisation parameters D_α have not been computed.

Bibliography

[Abramovici 1992] A. Abramovici, W. E. Althouse, R. W. P. Drever, Y. Gursel, S. Kawamura, F. J. Raab, D. Shoemaker, L. Sievers, R. E. Spero and K. S. Thorne. *LIGO - The Laser Interferometer Gravitational-Wave Observatory*. Sci., vol. 256, page 325, 1992. 15

[Abramowitz 1972] M. Abramowitz and I. A. Stegun. Handbook of mathematical functions with formulas, graphs, and mathematical tables. Dover, New R York, 1972. 151, 155

[AdLIGO] AdLIGO.
https://www.advancedligo.mit.edu/. 10

[AdVirgo] AdVirgo.
https://wwwcascina.virgo.infn.it/advirgo/. 10

[Alexander 2006] S. H. Alexander, M. E. Peskin and M. M. Sheikh-Jabbari. *Leptogenesis from gravity waves in models of inflation*. Phys. Rev. Lett., vol. 96, page 081301, 2006. 120

[Amaro-Seoane 2007] P. Amaro-Seoane, J. Gair, M. Freitag, C. M. Miller, I. Mandel, C. Cutler and S. Babak. *Astrophysics, detection and science applications of intermediate- and extreme mass-ratio inspirals*. Class. Quant. Grav., vol. 24, page R113, 2007. 13, 14

[Amaro-Seoane 2011] P. Amaro-Seoane and M. Preto. *The impact of realistic models of mass segregation on the event rate of extreme-mass ratio inspirals and cusp re-growth*. Class. Quant. Grav., vol. 28, page 094017, 2011. 13

[Babak 2007] S. Babak, H. Fang, J. R. Gair, K. Glampedakis and S. A. Hughes. *'Kludge' gravitational waveforms for a test-body orbiting a Kerr black hole*. Phys. Rev. D, vol. 75, page 024005, 2007. 135, 138, 146

[Baker 2006] J. G. Baker, J. Centrella, D. Choi, M. Koppitz and J. van Meter. *Gravitational wave extraction from an inspiraling configuration of merging black holes*. Phys. Rev. Lett., vol. 96, page 111102, 2006. 52

[Bambi 2011] C. Bambi and E. Barausse. *Constraining the Quadrupole Moment of Stellar-mass Black Hole Candidates with the Continuum Fitting Method*. Astrophys. J., vol. 731, page 121, 2011. 132

[Barack 2000a] L. Barack. *Self-force on a scalar particle in spherically-symmetric spacetime via mode-sum regularization: Radial trajectories.* Phys. Rev. D, vol. 62, page 084027, 2000. 28, 44

[Barack 2000b] L. Barack and A. Ori. *Mode sum regularization approach for the self force in black hole spacetime.* Phys. Rev. D, vol. 61, page 061502, 2000. 28, 41, 44, 46, 153

[Barack 2001a] L. Barack. *Gravitational self-force by mode sum regularization.* Phys. Rev. D, vol. 64, page 084021, 2001. 28, 34, 41, 44

[Barack 2001b] L. Barack and A. Ori. *Gravitational self force and gauge transformations.* Phys. Rev. D, vol. 64, page 124003, 2001. 34

[Barack 2002a] L. Barack, Y. Mino, H. Nakano, A. Ori and M. Sasaki. *Calculating the gravitational self force in Schwarzschild spacetime.* Phys. Rev. Lett., vol. 88, page 091101, 2002. 28, 41, 44

[Barack 2002b] L. Barack and A. Ori. *Regularization parameters for the self force in Schwarzschild spacetime. I: Scalar case.* Phys. Rev. D, vol. 66, page 084022, 2002. 28, 41, 44, 46, 153, 157

[Barack 2003] L. Barack and A. Ori. *Regularization parameters for the self force in Schwarzschild spacetime: II. gravitational and electromagnetic cases.* Phys. Rev. D, vol. 67, page 024029, 2003. 44

[Barack 2004] L. Barack and C. Cutler. *LISA capture sources: Approximate waveforms, signal-to-noise ratios, and parameter estimation accuracy.* Phys. Rev. D, vol. 69, page 082005, 2004. xvii, 135, 139, 141, 146

[Barack 2005] L. Barack and C. O. Lousto. *Perturbations of Schwarzschild black holes in the Lorenz gauge: Formulation and numerical implementation.* Phys. Rev. D, vol. 72, page 104026, 2005. 39, 41, 52

[Barack 2007a] L. Barack and D. A. Golbourn. *Scalar-field perturbations from a particle orbiting a black hole using numerical evolution in 2+1 dimensions.* Phys. Rev. D, vol. 76, page 044020, 2007. 52

[Barack 2007b] L. Barack and N. Sago. *Gravitational self force on a particle in circular orbit around a Schwarzschild black hole.* Phys. Rev. D, vol. 75, page 064021, 2007. 41, 52

[Barack 2009] L. Barack. *Gravitational self force in extreme mass-ratio inspirals.* Class. Quant. Grav., vol. 26, page 213001, 2009. 25, 27, 134

[Barack 2010] L. Barack and N. Sago. *Gravitational self-force on a particle in eccentric orbit around a Schwarzschild black hole*. Phys. Rev. D, vol. 81, page 084021, 2010. 28, 41

[Barut 1980] A. O. Barut. Electrodynamics and classical theory of fields and particles. Dover, New York, 1980. 27

[Boyd 2001] J. P. Boyd. Chebyshev and fourier spectral methods. Dover, New York, 2nd édition, 2001. 66, 67, 71, 72, 75, 77, 82

[Brandt 1997] S. Brandt and B. Bruegmann. *Black hole punctures as initial data for general relativity*. Phys. Rev. Lett., vol. 78, page 3606, 1997. 52

[Brown 2007a] D. A. Brown, J. Brink, H. Fang, J. R. Gair, C. Li, G. Lovelace, I. Mandel and K. S. Thorne. *Prospects for Detection of Gravitational Waves from Intermediate-Mass-Ratio Inspirals*. Phys. Rev. Lett., vol. 99, page 201102, 2007. 14

[Brown 2007b] D. A. Brown, H. Fang, J. R. Gair, C. Li, G. Lovelace, I. Mandel and K.S. Thorne. *Prospects for detection of gravitational waves from intermediate-mass-ratio inspirals*. Phys. Rev. Lett., vol. 99, page 201102, 2007. 14

[Burko 2007] L. M. Burko and G. Khanna. *Accurate time-domain gravitational waveforms for extreme-mass-ratio binaries*. Europhys. Lett., vol. 78, page 60005, 2007. 52

[Campanelli 2006] M. Campanelli, C. O. Lousto, P. Marronetti and Y. Zlochower. *Accurate Evolutions of Orbiting Black-Hole Binaries Without Excision*. Phys. Rev. Lett., vol. 96, page 111101, 2006. 52

[Canizares 2009] P. Canizares and C. F. Sopuerta. *Efficient pseudospectral method for the computation of the self-force on a charged particle: Circular geodesics around a Schwarzschild black hole*. Phys. Rev. D, vol. 79, page 084020, 2009. xvii, 78, 79, 92, 96

[Canizares 2010] P. Canizares, C. F. Sopuerta and J. L. Jaramillo. *Pseudospectral Collocation Methods for the Computation of the Self-Force on a Charged Particle: Generic Orbits around a Schwarzschild Black Hole*. Phys. Rev. D, vol. 82, page 044023, 2010. 65, 114

[Canizares 2011] P. Canizares and C. F. Sopuerta. *Tuning time-domain pseudospectral computations of the self-force on a charged scalar particle*. Class. Quant. Grav., vol. 28, page 134011, 2011. 88, 92, 112, 114, 116

[Chandrasekhar 1992] S. Chandrasekhar. The mathematical theory of black holes. Oxford University Press, New York, 1992. 133

[Collins 2004] N. A. Collins and S. A. Hughes. *Towards a formalism for mapping the spacetimes of massive compact objects: Bumpy black holes and their orbits.* Phys. Rev. D, vol. 69, page 124022, 2004. 133

[Cornish 2002] N. J. Cornish. *Detecting a stochastic gravitational wave background with the Laser Interferometer Space Antenna.* Phys. Rev. D, vol. 65, page 022004, 2002. 16

[Cornish 2003] N. J. Cornish and S. L. Larson. *LISA data analysis: Doppler demodulation.* Class. Quant. Grav., vol. 20, page 163, 2003. 140, 146

[Courant 1953a] R. Courant and D. Hilbert. Methods of mathematical physics, vol. 1. Wiley, New York, 1953. 54

[Courant 1953b] R. Courant and D. Hilbert. Methods of mathematical physics. Vol. 2. Wiley, New York, 1953. 55, 58, 76

[Cunningham 1978] C. T. Cunningham, R. H. Price and V. Moncrief. *Radiation from collapsing relativistic stars. I - Linearized odd-parity radiation.* Astrophys. J., vol. 224, page 643, 1978. 37

[Cutler 1994a] C. Cutler and E. E. Flanagan. *Gravitational waves from merging compact binaries: How accurately can one extract the binary's parameters from the inspiral wave form?* Phys. Rev. D, vol. 49, page 2658, 1994. 18

[Cutler 1994b] C. Cutler, D. Kennefick and E. Poisson. *Gravitational radiation reaction for bound motion around a Schwarzschild black hole.* Phys. Rev. D, vol. 50, page 3816, 1994. 47, 51

[Cutler 2007] C. Cutler and M. Vallisneri. *LISA detections of massive black hole inspirals: parameter extraction errors due to inaccurate template waveforms.* Phys. Rev. D, vol. 76, page 104018, 2007. 19, 20, 150

[Davis 1972] M. Davis, R. Ruffini and J. Tiomno. *Pulses of Gravitational Radiation of a Particle Falling Radially into a Schwarzschild Black Hole.* Phys. Rev. D, page 2932, 1972. 51

[Detweiler 1978] S. L. Detweiler. *Black holes and gravitational waves. I - Circular orbits about a rotating hole.* Astrophys. J., vol. 225, page 687, 1978. 51

[Detweiler 1979] S. L. Detweiler and E. Szedenits Jr. *Black holes and gravitational waves. II - Trajectories plunging into a nonrotating hole.* Astrophys. J., vol. 231, page 211, 1979. 51

[Detweiler 2003a] S. Detweiler, E. Messaritaki and B. F. Whiting. *Self-force of a scalar field for circular orbits about a Schwarzschild black hole.* Phys. Rev. D, vol. 67, page 104016, 2003. 28, 46, 149, 153

[Detweiler 2003b] S. Detweiler and B. F. Whiting. *Self-force via a Green's function decomposition.* Phys. Rev. D, vol. 67, page 024025, 2003. 27, 28, 30

[Diaz-Rivera 2004] L. M. Diaz-Rivera, E. Messaritaki, B. F. Whiting and S. Detweiler. *Scalar field self-force effects on orbits about a Schwarzschild black hole.* Phys. Rev. D, vol. 70, page 124018, 2004. xvii, 96, 97

[Dolan 2011] S. R. Dolan, B. Wardell and L. Barack. *Self force via m-mode regularization and 2+1D evolution: II. Scalar-field implementation on Kerr spacetime.* ArXiv gr-qc/1107.0012, 2011. 51, 53

[Drasco 2004] S. Drasco and S. A. Hughes. *Rotating black hole orbit functionals in the frequency domain.* Phys. Rev. D, vol. 69, page 044015, 2004. 127, 142

[Drasco 2006] S. Drasco and S. A. Hughes. *Gravitational wave snapshots of generic extreme mass ratio inspirals.* Phys. Rev. D, vol. 73, page 024027, 2006. 26

[ET]   ET. *The Einstein Telescope.* http://www.et-gw.eu/ . 14

[Field 2010] S. E. Field, J. S. Hesthaven and S. R. Lau. *Persistent junk solutions in time-domain modeling of extreme mass ratio binaries.* Phys. Rev. D, vol. 81, page 124030, 2010. 64

[Finn 2000] L. S. Finn and K. S. Thorne. *Gravitational waves from a compact star in a circular, inspiral orbit, in the equatorial plane of a massive, spinning black hole, as observed by LISA.* Phys. Rev. D, vol. 62, page 124021, 2000. 13, 17, 19, 25

[Fisher 1935] R. A. Fisher. *The Logic of Inductive Inference.* Roy. Stat. Soc. J., vol. 98, page 35, 1935. 20

[Flanagan 2005] E. E. Flanagan and S. A. Hughes. *The basics of gravitational wave theory.* New J. Phys., vol. 7, page 204, 2005. 3, 5, 6

[Flanagan 2010] E. E. Flanagan and T. Hinderer. *Transient resonances in the inspirals of point particles into black holes.* ArXiv gr-gc/1009.4923, 2010. 25

[Frigo 2005] M. Frigo and S. G. Johnson. *The Design and Implementation of FFTW3.* Proceedings of the IEEE, vol. 93, no. 2, page 216, 2005. 74, 77

[Gair 2004] J. R. Gair, L. Barack, T. Creighton, C. Cutler, S. L. Larson, E. S. Phinney and M. Vallisneri. *Event rate estimates for LISA extreme mass ratio capture sources.* Class. Quant. Grav., vol. 21, page S1595, 2004. 13, 19, 25

[Gair 2006] J. R. Gair and K. Glampedakis. *Improved approximate inspirals of test bodies into Kerr black holes.* Phys. Rev. D, vol. 73, page 064037, 2006. 130, 136, 142, 146

[Gair 2008] J. R. Gair, C. Li and I. Mandel. *Observable properties of orbits in exact bumpy spacetimes.* Phys. Rev. D, vol. 77, page 024035, 2008. 133

[Galassi 2006] M. Galassi, J. Davies, J. Theiler, B. Gough, G. Jungman, M. Booth and F. Rossi. Gnu scientific library reference manual. Network Theory Ltd., Bristol, 2nd édition, 2006. 77

[Galley 2009] C. R. Galley and M. Tiglio. *Radiation reaction and gravitational waves in the effective field theory approach.* Phys. Rev. D, vol. 79, page 124027, 2009. 28

[Ganz 2007] K. Ganz, W. Hikida, H. Nakano, N. Sago and T. Tanaka. *Adiabatic Evolution of Three 'Constants' of Motion for Greatly Inclined Orbits in Kerr Spacetime.* Prog. Theor. Phys., vol. 117, page 1041, 2007. 26

[GEO600] GEO600.
    http://www.geo600.org/. 10

[Gerlach 1979] U. H. Gerlach and U. K. Sengupta. *Gauge invariant perturbations on most general spherically symmetric space-times.* Phys. Rev. D, vol. 19, page 2268, 1979. 36

[Gerlach 1980] U. H. Gerlach and U. K. Sengupta. *Gauge invariant coupled gravitational, acoustical, and electromagnetic modes on most general spherical space-times.* Phys. Rev. D, vol. 22, page 1300, 1980. 36

[Glampedakis 2002] K. Glampedakis and D. Kennefick. *Zoom and whirl: Eccentric equatorial orbits around spinning black holes and their evolution under gravitational radiation reaction.* Phys. Rev. D, vol. 66, page 044002, 2002. 143

[Glampedakis 2006] K. Glampedakis and S. Babak. *Mapping spacetimes with LISA: inspiral of a test body in a 'quasi-Kerr' field.* Class. Quant. Grav., vol. 23, page 4167, 2006. 133

[Gralla 2008] S. E. Gralla and R. M. Wald. *A Rigorous Derivation of Gravitational Self-force.* Class. Quant. Grav., vol. 25, page 205009, 2008. 27, 28

[Gustafsson 1995] B. Gustafsson, H. Kreiss and J. Oliger. Time dependent problems. John Wiley & Sons, New York, 1995. 76

[Haas 2006] R. Haas and E. Poisson. *Mode-sum regularization of the scalar self-force: Formulation in terms of a tetrad decomposition of the singular field.* Phys. Rev. D, vol. 74, page 044009, 2006. xvii, 28, 46, 52, 96, 154

[Haas 2007] R. Haas. *Scalar self-force on eccentric geodesics in Schwarzschild spacetime: a time-domain computation.* Phys. Rev. D, vol. 75, page 124011, 2007. xvii, 52, 96

[Hawking 1987] S. W. Hawking and W. Israel. Three hundred years of gravitation, volume Chap. 9. by K. S. Thorne. Cambridge University Press, Cambridge, 1987. 7, 8, 15, 17

[Hesthaven 2000a] J. S. Hesthaven. *Spectral penalty methods.* In Proceedings of the fourth international conference on Spectral and high order methods (ICOSAHOM 1998), page 23, Amsterdam, The Netherlands, The Netherlands, 2000. Elsevier Science Publishers B. V. 61

[Hesthaven 2000b] J. S. Hesthaven. *Spectral penalty methods.* App. Num. Math., vol. 33, page 23, 2000. 61, 87

[Hinderer 2008] T. Hinderer and E. E. Flanagan. *Two timescale analysis of extreme mass ratio inspirals in Kerr. I. Orbital Motion.* Phys. Rev. D, vol. 78, page 064028, 2008. 26

[Holz 2005] D. E. Holz and S. A. Hughes. *Using Gravitational-Wave Standard Sirens*. Astrophys. J., vol. 629, page 15, 2005. 12

[Hopman 2006] C. Hopman and T. Alexander. *The effect of mass-segregation on gravitational wave sources near massive black holes*. Astrophys. J., vol. 645, page L133, 2006. 13

[Hopper 2010] S. Hopper and C. R. Evans. *Gravitational perturbations and metric reconstruction: Method of extended homogeneous solutions applied to eccentric orbits on a Schwarzschild black hole*. Phys. Rev. D, vol. 82, page 084010, 2010. 41

[Huerta 2009] E. A. Huerta and J. R. Gair. *Influence of conservative corrections on parameter estimation for EMRIs*. Phys. Rev. D, vol. 79, page 084021, 2009. 145

[Hughes 2000] S. A. Hughes. *Evolution of circular, nonequatorial orbits of Kerr black holes due to gravitational-wave emission*. Phys. Rev. D, vol. 61, page 084004, 2000. 134

[Hughes 2001] S. A. Hughes. *Gravitational waves from extreme mass ratio inspirals: challenges in mapping the spacetime of massive, compact objects*. Class. Quant. Grav., vol. 18, page 4067, 2001. 131, 134

[Hughes 2003] S. A. Hughes and D. E. Holz. *Cosmology with coalescing massive black holes*. Class. Quant. Grav., vol. 20, page S65, 2003. 12

[Hughes 2005] S. A. Hughes, S. Drasco, E. E. Flanagan and J. Franklin. *Gravitational radiation reaction and inspiral waveforms in the adiabatic limit*. Phys. Rev. Lett., vol. 94, page 221101, 2005. 26

[Hughes 2010] S. A. Hughes. *Probing strong-field gravity and black holes with gravitational waves*. ArXiv gr-qc/1002.2591, 2010. 5

[Hulse 1975] R. A. Hulse and J. H. Taylor. *Discovery of a pulsar in a binary system*. Astrophys. J., vol. 195, page L51, 1975. 1

[Isaacson 1968a] R. A. Isaacson. *Gravitational Radiation in the Limit of High Frequency. I. The Linear Approximation and Geometrical Optics*. Phys. Rev., vol. 166, page 1263, 1968. 128

[Isaacson 1968b] R. A. Isaacson. *Gravitational Radiation in the Limit of High Frequency. II. Nonlinear Terms and the Effective Stress Tensor*. Phys. Rev., vol. 166, page 1272, 1968. 128

[Jackson 1999] J. D. Jackson. *Classical electrodynamics.* J. Wiley & Sons, New York, 3rd édition, 1999. 3, 27

[Jaramillo 2011] J. L. Jaramillo, C. F. Sopuerta and P. Canizares. *Are time-domain self-force calculations contaminated by Jost solutions?* Phys. Rev. D, Rapid communication, vol. 83, page 061503, 2011. 52, 64

[Keidl 2010] T. S. Keidl, A. G. Shah, J. L. Friedman, D. H. Kim and L. R. Price. *Gravitational Self-force in a Radiation Gauge.* Phys. Rev. D, vol. 82, page 124012, 2010. 28

[Kim 2004] D. H. Kim. *Regularization parameters for the self-force of a scalar particle in a general orbit about a Schwarzschild black hole.* ArXiv gr-qc/0402014, 2004. 46, 157

[Konstantinidis 2011] S. Konstantinidis, P. Amaro-Seoane and K. D. Kokkotas. *Kicking massive black holes off clusters: Intermediate-mass ratio inspirals.* ArXiv astro-ph.CO/1108.5175, 2011. 14

[Larson 2000] S. L. Larson, W. A. Hiscock and R. W. Hellings. *Sensitivity curves for spaceborne gravitational wave interferometers.* Phys. Rev. D, vol. 62, page 062001, 2000. 17

[Lau 2004] S. R. Lau. *Rapid evaluation of radiation boundary kernels for time-domain wave propagation on black holes: Implementation and numerical tests.* Class. Quant. Grav., vol. 21, page 4147, 2004. 149

[LIGO] LIGO.
`http://www.ligo.caltech.edu/.` 10

[LISA] LISA. *Laser Interferometer Space Antenna.*
`http://www.esa.int, http://lisa.jpl.nasa.gov.` 10

[LISA International Science Team 2011] LISA International Science Team. *LISA: Unveiling a hidden Universe. Assessment Study Report.* Rapport technique ESA/SRE (2011) 3, European Space Agency, 2011. 10

[Lousto 2008] C. O. Lousto and H. Nakano. *A new method to integrate (2+1)-wave equations with Dirac's delta functions as sources.* Class. Quant. Grav., vol. 25, page 145018, 2008. 52

[LU] *GSL - GNU Scientific Library.*
`http://www.gnu.org/s/gsl/manual/html_node/LU-Decomposition.html.` 145

[Lue 1999] A. Lue, L. M. Wang and M. Kamionkowski. *Cosmological signature of new parity-violating interactions.* Phys. Rev. Lett., vol. 83, page 1506, 1999. 120

[Maggiore 2000] M. Maggiore. *Gravitational wave experiments and early universe cosmology.* Phys. Rep., vol. 331, page 283, 2000. 12

[Manko 1992] V. S. Manko and I. D. Novikov. *Generalizations of the Kerr and Kerr-Newman metrics possessing an arbitrary set of mass-multipole moments.* Class. Quant. Grav., vol. 9, page 2477, 1992. 133

[Martel 2004] K. Martel. *Gravitational waveforms from a point particle orbiting a Schwarzschild black hole.* Phys. Rev. D, vol. 69, page 044025, 2004. 39, 52

[Miller 2009] M. C. Miller. *Intermediate-Mass Black Holes as LISA Sources.* Class. Quant. Grav., vol. 26, page 094031, 2009. 14

[Mino 1997] Y. Mino, M. Sasaki and T. Tanaka. *Gravitational radiation reaction to a particle motion.* Phys. Rev. D, vol. 55, page 3457, 1997. 27, 28, 33, 34

[Mino 2003a] Y. Mino. *Perturbative Approach to an orbital evolution around a Supermassive black hole.* Phys. Rev. D, vol. 67, page 084027, 2003. 26, 27

[Mino 2003b] Y. Mino, H. Nakano and M. Sasaki. *Covariant self-force regularization of a particle orbiting a Schwarzschild black hole: Mode decomposition regularization.* Prog. Theor. Phys., vol. 108, page 1039, 2003. 28, 41, 44

[Mino 2008] Y. Mino. *Modulation of the gravitational waveform by the effect of radiation reaction.* Phys. Rev. D, vol. 77, page 044008, 2008. 26

[Misner 1973] C. W. Misner, K.S. Thorne and J. A. Wheeler. Gravitation. W. H. Freeman & Co., San Francisco, 1973. vii, 2, 4, 5, 124, 128, 129, 135

[Moncrief 1974] V. Moncrief. *Gravitational perturbations of spherically symmetric systems. I. The exterior problem.* An. Phys., vol. 88, page 323, 1974. 35

[Owen 1999] B. J. Owen and B. S. Sathyaprakash. *Matched filtering of gravitational waves from inspiraling compact binaries: Computational cost and template placement.* Phys. Rev. D, vol. 60, page 022002, 1999. 18

[Pani 2011] P. Pani, V. Cardoso and L. Gualtieri. *Gravitational waves from extreme mass-ratio inspirals in dynamical Chern-Simons gravity.* Phys. Rev. D, vol. 83, page 104048, 2011. 133

[Peters 1963] P. C. Peters and J. Mathews. *Gravitational Radiation from Point Masses in a Keplerian Orbit.* Phys. Rev., vol. 131, page 435, 1963. 135

[Peters 1964] P. C. Peters. *Gravitational Radiation and the Motion of Two Point Masses.* Phys. Rev., vol. 136, page 1224, 1964. 135

[Poisson 1995] E. Poisson. *Gravitational radiation from a particle in circular orbit around a black hole. 6. Accuracy of the postNewtonian expansion.* Phys. Rev. D, vol. 52, page 5719, 1995. 51

[Poisson 1997] E. Poisson. *Erratum and Addendum: Gravitational radiation from a particle in circular orbit around a black hole. VI. Accuracy of the post-Newtonian expansion.* Phys. Rev. D, vol. 55, pages 7980–7981, 1997. 51

[Poisson 2004a] E. Poisson. *The motion of point particles in curved spacetime.* Living Rev. Relativity, vol. 7, page 6, 2004. 27, 28, 29, 30, 31, 32, 33

[Poisson 2004b] E. Poisson. *The motion of point particles in curved spacetime.* Living Rev. Rel., vol. 7, page 6, 2004. 30

[Poisson 2005] E. Poisson. *The Gravitational Self-force.* In P. Florides, B. Nolan and A. Ottewill, editeurs, General Relativity and Gravitation, page 119, 2005. 27

[Pound 2005] A. Pound, E. Poisson and B. G. Nickel. *Limitations of the adiabatic approximation to the gravitational self-force.* Phys. Rev. D, vol. 72, page 124001, 2005. 26

[Pound 2008a] A. Pound and E. Poisson. *Multi-scale analysis of the electromagnetic self-force in a weak gravitational field.* Phys. Rev. D, vol. 77, page 044012, 2008. 26

[Pound 2008b] A. Pound and E. Poisson. *Osculating orbits in Schwarzschild spacetime, with an application to extreme mass-ratio inspirals.* Phys. Rev. D, vol. 77, page 044013, 2008. 26

[Pound 2010] A. Pound. *Self-consistent gravitational self-force.* Phys. Rev. D, vol. 81, page 024023, 2010. 27

[Press 1992] W. H. Press, B. P. Flannery, S. A. Teukolsky and W. T. Vetterling. Numerical recipes: The art of scientific computing. Cambridge University Press, Cambridge, 1992. 143

[Pretorius 2005a] F. Pretorius. *Evolution of binary black hole spacetimes.* Phys. Rev. Lett., vol. 95, page 121101, 2005. 41

[Pretorius 2005b] F. Pretorius. *Numerical Relativity Using a Generalized Harmonic Decomposition.* Class. Quant. Grav., vol. 22, page 425, 2005. 41

[Psaltis 2011] D. Psaltis and T. Johannsen. *Sgr A*: The Optimal Testbed of Strong-Field Gravity.* Phys. Conf. J., vol. 283, page 012030, 2011. 13, 132

[Quinn 1997] T. C. Quinn and R. M. Wald. *An axiomatic approach to electromagnetic and gravitational radiation reaction of particles in curved spacetime.* Phys. Rev. D, vol. 56, page 3381, 1997. 27, 28, 33

[Quinn 2000] T. C. Quinn. *Axiomatic approach to radiation reaction of scalar point particles in curved spacetime.* Phys. Rev. D, vol. 62, page 064029, 2000. 30, 45

[Regge 1957] T. Regge and J. A. Wheeler. *Stability of a Schwarzschild Singularity.* Phys. Rev., vol. 108, page 1063, 1957. 28, 34, 35, 37

[Rosenthal 2006] E. Rosenthal. *Second-order gravitational self-force.* Phys. Rev. D, vol. 74, page 084018, 2006. 28

[Ryan 1995] F. D. Ryan. *Gravitational waves from the inspiral of a compact object into a massive, axisymmetric body with arbitrary multipole moments.* Phys. Rev. D, vol. 52, page 5707, 1995. 132, 133

[Ryan 1997a] F. D. Ryan. *Accuracy of estimating the multipole moments of a massive body from the gravitational waves of a binary inspiral.* Phys. Rev. D, vol. 56, page 1845, 1997. 132, 133

[Ryan 1997b] F. D. Ryan. *Scalar waves produced by a scalar charge orbiting a massive body with arbitrary multipole moments.* Phys. Rev. D, vol. 56, page 7732, 1997. 132, 133

[Sago 2005] N. Sago, T. Tanaka, W. Hikida and H. Nakano. *Adiabatic radiation reaction to the orbits in Kerr Spacetime.* Prog. Theor. Phys., vol. 114, page 509, 2005. 26

[Sago 2008] N. Sago, L. Barack and S. Detweiler. *Two approaches for the grav-itational self-force in black hole spacetime: Comparison of numerical results.* Phys. Rev. D, vol. 78, page 124024, 2008. 27, 34

[Schmidt 2002] W. Schmidt. *Celestial mechanics in Kerr spacetime.* Class. Quant. Grav., vol. 19, page 2743, 2002. 127

[Schutz 1999] B. F. Schutz. *Gravitational wave astronomy.* Class. Quant. Grav., vol. 16, page A131, 1999. 9

[Schutz 2009] B. F. Schutz, J. Centrella, C. Cutler and S. A. Hughes. *Will Einstein Have the Last Word on Gravity?* In astro2010: The Astron-omy and Astrophysics Decadal Survey, volume 2010 of *ArXiv Astro-physics e-prints*, page 265, 2009. 12

[Sesana 2011] A. Sesana, J. Gair, E. Berti and M. Volonteri. *Reconstruct-ing the massive black hole cosmic history through gravitational waves.* Phys. Rev. D, vol. 83, page 044036, 2011. 12

[Shah 2011] A. G. Shah, T. S. Keidl, J. L. Friedman, D. H. Kim and L. R. Price. *Conservative, gravitational self-force for a particle in circular orbit around a Schwarzschild black hole in a Radiation Gauge.* Phys. Rev. D, vol. 83, page 064018, 2011. 28

[Sopuerta 2006a] C. F. Sopuerta. *Extreme-Mass-Ratio Binary Systems in the Lorenz Gauge.* Unpublished, 2006. 39, 40

[Sopuerta 2006b] C. F. Sopuerta and P. Laguna. *Finite element computation of the gravitational radiation emitted by a point-like object orbiting a non-rotating black hole.* Phys. Rev. D, vol. 73, page 044028, 2006. 39, 52

[Sopuerta 2006c] C. F. Sopuerta, P. Sun, P. Laguna and J. Xu. *A Toy model for testing finite element methods to simulate extreme-mass-ratio bi-nary systems.* Class. Quant. Grav., vol. 23, page 251, 2006. 52

[Sopuerta 2009] C. F. Sopuerta and N. Yunes. *Extreme- and Intermediate-Mass Ratio Inspirals in Dynamical Chern-Simons Modified Gravity.* Phys. Rev. D, vol. 80, page 064006, 2009. 120, 122, 123, 125, 126, 127, 128, 129, 132, 133, 142, 146

[Sopuerta 2010] C. F. Sopuerta. *A Roadmap to Fundamental Physics from LISA EMRI Observations.* GW Notes, Vol. 4, p. 3-47, vol. 4, page 3, 2010. 14, 132

[Sopuerta 2011] C. F. Sopuerta and N. Yunes. *The Chimera Scheme: Approximate Waveforms for Extreme-Mass-Ratio Inspirals.* ArXiv gr-qc/1109.0572, 2011. 136

[Stroeer 2006] A. Stroeer and A. Vecchio. *The LISA verification binaries.* Class. Quant. Grav., vol. 23, page 809, 2006. 12

[Sundararajan 2007] P. A. Sundararajan, G. Khanna and S. A. Hughes. *Towards adiabatic waveforms for inspiral into Kerr black holes: I. A new model of the source for the time domain perturbation equation.* Phys. Rev. D, vol. 76, page 104005, 2007. 52

[Sundararajan 2008a] P. A. Sundararajan, G. Khanna, S. A. Hughes and S. Drasco. *Towards adiabatic waveforms for inspiral into Kerr black holes: II. Dynamical sources and generic orbits.* Phys. Rev. D, vol. 78, page 024022, 2008. 52

[Sundararajan 2008b] P. A. Sundararajan, G. Khanna, S. A. Hughes and S. Drasco. *Towards adiabatic waveforms for inspiral into Kerr black holes. II. Dynamical sources and generic orbits.* Phys. Rev. D, vol. 78, page 024022, 2008. 134

[Teukolsky 1972] S. A. Teukolsky. *Rotating Black Holes: Separable Wave Equations for Gravitational and Electromagnetic Perturbations.* Phys. Rev. Lett., vol. 29, page 1114, 1972. 133

[Thorne 1980] K. S. Thorne. *Multipole expansions of gravitational radiation.* Rev. Mod. Phys., vol. 52, page 299, 1980. 136, 137, 146

[Thorne 1997] K. S. Thorne. *Probing black holes and relativistic stars with gravitational waves.* ArXiv gr-qc/9706079, 1997. 15

[Vallisneri 2008] M. Vallisneri. *Use and abuse of the Fisher information matrix in the assessment of gravitational-wave parameter-estimation prospects.* Phys. Rev. D, vol. 77, page 042001, 2008. 20, 21

[Vallisneri 2011] M. Vallisneri. *Beyond Fisher: exact sampling distributions of the maximum-likelihood estimator in gravitational-wave parameter estimation.* ArXiv gr-qc/1108.1158, 2011. 144

[van der Sluys 2011] M. van der Sluys. *Gravitational waves from compact binaries.* ArXiv astro-ph.SR/1108.1307, 2011. 12

[Vega 2008] I. Vega and S. Detweiler. *Regularization of fields for self-force problems in curved spacetime: foundations and a time-domain application.* Phys. Rev. D, vol. 77, page 084008, 2008. 52

[Vega 2009] I. Vega, P. Diener, W. Tichy and S. L. Detweiler. *Self-force with (3+1) codes: A Primer for numerical relativists*. Phys. Rev. D, vol. 80, page 084021, 2009. 52

[Vigeland 2010] S. J. Vigeland. *Multipole moments of bumpy black holes*. Phys. Rev. D, vol. 82, page 104041, 2010. 133

[Virgo] Virgo.
`https://wwwcascina.virgo.infn.it`. 10

[Vishveshwara 1968] C. V. Vishveshwara. *The Stability of the Schwarzschild Metric*. PhD thesis, University of Maryland College Park., 1968. 35

[Wald 1971] R. M. Wald. *Final States of Gravitational Collapse*. Phys. Rev. Lett., vol. 26, page 1653, 1971. 132

[Warburton 2010] N. Warburton and L. Barack. *Self force on a scalar charge in Kerr spacetime: circular equatorial orbits*. Phys. Rev. D, vol. 81, page 084039, 2010. xvii, 45, 51, 114

[Weinberg 1972] S. Weinberg. Gravitation and cosmology. principles and applications of the general theory of relativity. J. Wiley & Sons, New York, 1972. 1, 2, 4, 7

[Weinberg 2008] S. Weinberg. *Effective field theory for inflation*. Phys. Rev. D, vol. 77, page 123541, 2008. 120

[Weisberg 2005] J. M. Weisberg and J. H. Taylor. *The Relativistic Binary Pulsar B1913+16: Thirty Years of Observations and Analysis*. In F. A. Rasio and I. H. Stairs, editeurs, Binary Radio Pulsars, volume 328 of *Astrophys. Soc. Pac. Conf. Ser.*, page 25, 2005. 1

[Weisberg 2010] J. M. Weisberg, D. J. Nice and J. H. Taylor. *Timing Measurements of the Relativistic Binary Pulsar PSR B1913+16*. Astrophys. J., vol. 722, page 1030, 2010. 1

[Will 2005] C. M. Will. *The confrontation between general relativity and experiment*. Living Rev. Rel., vol. 9, page 3, 2005. 119

[Yunes 2009a] N. Yunes and F. Pretorius. *Dynamical Chern-Simons Modified Gravity I: Spinning Black Holes in the Slow-Rotation Approximation*. Phys. Rev. D, vol. 79, page 084043, 2009. 123, 124

[Yunes 2009b] N. Yunes and F. Pretorius. *Dynamical Chern-Simons modified gravity: Spinning black holes in the slow-rotation approximation*. Phys. Rev. D, vol. 79, page 084043, 2009. 119, 130

[Yunes 2010] N. Yunes, A. Buonanno, S. A. Hughes, M. C. Miller and Y. Pan. *Modeling Extreme Mass Ratio Inspirals within the Effective-One-Body Approach.* Phys. Rev. Lett., vol. 104, page 091102, 2010. 135

[Zenginoğlu 2011] A. Zenginoğlu. *Hyperboloidal layers for hyperbolic equations on unbounded domains.* Comp. Phys. J., vol. 230, pages 2286–2302, 2011. 149

[Zerilli 1970a] F. J. Zerilli. *Effective Potential for Even-Parity Regge-Wheeler Gravitational Perturbation Equations.* Phys. Rev. Lett., vol. 24, pages 737–738, 1970. 35, 38

[Zerilli 1970b] F. J. Zerilli. *Gravitational Field of a Particle Falling in a Schwarzschild Geometry Analyzed in Tensor Harmonics.* Phys. Rev. D, vol. 2, pages 2141–2160, 1970. 34

Index